Cretaceous-Paleogene evolution of the proto-Paratethys Sea in Central Asia: mechanisms and paleoenvironmental impacts

---

Dissertation

von

Mustafa Yücel Kaya

Kumulative Dissertation
zur Erlangung des akademischen Grades
"doctor rerum naturalium"
(Dr. rer. nat.)
in der Wissenschaftsdisziplin **Geologie**

eingereicht an der
Mathematisch-Naturwissenschaftlichen Fakultät
Institut für Geowissenschaften
der Universität Potsdam

Potsdam, im Juni 2020
Datum der Disputation: 06.11.2020

Hauptbetreuer: Dr. Guillaume Dupont-Nivet

Gutachter: Prof. Dr. Wout Krijgsman
Prof. Dr. Anne Bernhardt

https://doi.org/10.25932/publishup-48329
https://nbn-resolving.org/urn:nbn:de:kobv:517-opus4-483295

ABSTRACT

Unlike today's prevailing terrestrial features, the geologic past of Central Asia witnessed marine environments and conditions as well. A vast, shallow sea, known as proto-Paratethys, extended across Eurasia from the Mediterranean Tethys to the Tarim Basin in western China during Cretaceous to Paleogene times. This sea formed about 160 million years ago (during Jurassic times) when the waters of the Tethys Ocean flooded into Eurasia. It drastically retreated to the west and became isolated as the Paratethys during the Late Eocene-Oligocene (ca. 34 Ma).

Having well-constrained timing and paleogeography for the Cretaceous-Paleogene proto-Paratethys sea incursions in Central Asia is essential to properly understand and distinguish the controlling mechanisms and their link to Asian paleoenvironmental and paleoclimatic change. The Cretaceous-Paleogene tectonic evolution of the Pamir and Tibet and their far-field effects play a significant role on the sedimentological and structural evolution of the Central Asian basins and on the evolution of the proto-Paratethys sea fluctuations as well. Comparing the records of the sea incursions to the tectonic and eustatic events has paramount importance to reveal the controlling mechanisms behind the sea incursions. However, due to inaccuracies in the dating of rocks (mostly continental rocks and marine rocks with benthic microfossils providing low-resolution biostratigraphic constraints) and conflicting results, there has been no consensus on the timing of the sea incursions and interpretation of their records has been in question. Here, we present a new chronostratigraphic framework based on biostratigraphy and magnetostratigraphy as well as a detailed paleoenvironmental analysis for the Cretaceous and Paleogene proto-Paratethys Sea incursions in the Tajik and Tarim basins, in Central Asia. This enables us to identify the major drivers of marine fluctuations and their potential consequences on regional and global climate, particularly Asian aridification and the global carbon cycle perturbations such as the Paleocene-Eocene Thermal Maximum (PETM). To estimate the paleogeographic evolution of the proto-Paratethys Sea, the refined age constraints and detailed paleoenvironmental interpretations are combined with successive paleogeographic maps. Regional coastlines and depositional environments during the Cretaceous-Paleogene sea advances and retreats were drawn based on the results of this thesis and integrated with existing literature to generate new paleogeographic maps.

Before its final westward retreat in the Eocene, a total of six Cretaceous and Paleogene major sea incursions have been distinguished from the sedimentary records of the Tajik and Tarim basins in Central Asia. All have been studied and documented here.

We identify the presence of marine conditions already in the Early Cretaceous in the western Tajik Basin, followed by the Cenomanian (ca. 100 Ma) and Santonian (ca. 86 Ma) major marine incursions far into the eastern Tajik and Tarim basins separated by a Turonian-Coniacian (ca. 92-86 Ma) regression. Basin-wide tectonic subsidence analyses imply that the Early Cretaceous invasion of the sea into the Tajik Basin is related to increased Pamir tectonism (at ca. 130 – 90 Ma) in a retro-arc basin setting inferred to be linked to collision and subduction. This tectonic event mainly governed the Cenomanian (ca. 100 Ma) sea incursion in conjunction with a coeval global eustatic high resulting in the maximum geographic extent of the sea. The following

Turonian-Coniacian (ca. 92-86 Ma) major regression, driven by eustasy, coincides with a sharp slowdown in tectonic subsidence related to a regime change in Pamir tectonism from compression to extension. The Santonian (ca. 86 Ma) major sea incursion was more likely controlled dominantly by eustasy as also evidenced by the coeval fluctuations in the west Siberian Basin. During the early Maastrichtian, the global Late Cretaceous cooling is inferred from the disappearance of mollusk-rich limestones and the dominance of bryozoan-rich and echinoderm-rich limestones in the Tajik Basin documenting the first evidence for the Late Cretaceous cooling event in Central Asia.

Following the last Cretaceous sea incursion, a major regional restriction event, marked by the exceptionally thick (≤ 400 m) shelf evaporites is assigned a Danian-Selandian age (ca. 63-59 Ma). This is followed by the largest recorded proto-Paratethys sea incursion with a transgression estimated as early Thanetian (ca. 59-57 Ma) and a regression within the Ypresian (ca. 53-52 Ma). The transgression of the next incursion is now constrained as early Lutetian (ca. 47-46 Ma), whereas its regression is constrained as late Lutetian (ca. 41 Ma) and is associated with a drastic increase in both tectonic subsidence and basin infilling. The age of the final and least pronounced sea incursion restricted to the westernmost margin of the Tarim Basin is assigned as Bartonian–Priabonian (ca. 39.7-36.7 Ma). We interpret the long-term westward retreat of the proto-Paratethys Sea starting at ca. 41 Ma to be associated with far-field tectonic effects of the Indo-Asia collision and Pamir/Tibetan plateau uplift. Short-term eustatic sea level transgressions are superimposed on this long-term regression and seem coeval with the transgression events in the other northern Peri-Tethyan sedimentary provinces for the 1st and 2nd Paleogene sea incursions. However, the last Paleogene sea incursion is interpreted as related to tectonism. The transgressive and regressive intervals of the proto-Paratethys Sea correlate well with the reported humid and arid phases, respectively in the Qaidam and Xining basins, thus demonstrating the role of the proto-Paratethys Sea as an important moisture source for the Asian interior and its regression as a contributor to Asian aridification.

We lastly study the mechanics, relative contribution and preservation efficiency of ancient epicontinental seas as carbon sinks with new and existing data, using organic rich (sapropel) deposits dated to the PETM from the extensive epicontinental proto-Paratethys and West Siberian seas. We estimate ca. 1390±230 Gt organic C burial, a substantial amount compared to previously estimated global total excess organic C burial (ca. 1700-2900 Gt) is focused in the proto-Paratethys and West Siberian seas alone. We also speculate that enhanced organic carbon burial later over much of the proto-Paratethys (and later Paratethys) basin (during the deposition of the Kuma Formation and Maikop series, repectively) may have majorly contributed to drawdown of atmospheric carbon dioxide before and during the EOT cooling and glaciation of Antarctica. For past periods with smaller epicontinental seas, the effectiveness of this negative carbon cycle feedback was arguably diminished, and the same likely applies to the present-day.

Kreidezeit - Paläogene Entwicklung des Proto-Paratethys-Meeres in Zentralasien: Mechanismen und paläoökologische Auswirkungen

ZUSAMMENFASSUNG

Im Gegensatz zu den heute vorherrschenden kontinentalen Bedingungen war die geologische Vergangenheit Zentralasiens auch Zeuge marin dominierter Phasen. Ein riesiges Schelfmeer, bekannt als Proto-Paratethys, erstreckte sich während der Kreidezeit bis zum Paläogen über Eurasien - von der Tethys im Mittelmeer bis zum Tarimbecken im Westen Chinas. Dieses Meer bildete sich vor etwa 160 Millionen Jahren während der Jurazeit, als das Wasser des Tethys-Ozeans nach Eurasien strömte. Es zog sich drastisch nach Westen zurück und wurde während des späten Eozän-Oligozäns (ca. 34 Ma) als Paratethys isoliert.

Eine gut eingegrenzte zeitliche Einordnung und Paläogeographische Charakterisierung für die kretazisch-paläogenen proto-Paratethys-Meerestransgressionen in Zentralasien ist unerlässlich, um die Kontrollmechanismen und ihre Verbindung mit den paläoökologischen und paläoklimatischen Veränderungen in Asien richtig zu verstehen und zu unterscheiden. Die kreidezeitlich-paläogene tektonische Entwicklung des Pamir und Tibets und ihre Fernfeldeffekte spielen eine bedeutende Rolle für die Entwicklung der zentralasiatischen Becken und der proto-paläozoischen Meeresschwankungen. Aufgrund von Ungenauigkeiten bei der Datierung der Gesteine und widersprüchlichen Ergebnissen gab es jedoch bislang keinen Konsens über den Zeitpunkt der Meerestransgressionen. Die Interpretation der dabei abgelagerten Sedimentfolgen wurde in Frage gestellt. Hier präsentieren wir eine neue, zeitliche Einordung auf Grundlage von Biostratigraphie und Magnetostratigraphie sowie eine detaillierte Paläoumweltanalyse für die Transgressionen des kreidezeitlichen und paläogenen proto-Paratethys-Meeres im tadschikischen und Tarimbecken in Zentralasien. Dies ermöglicht es uns, die wichtigsten Triebkräfte der marinen Fluktuationen und ihre möglichen Auswirkungen auf das regionale und globale Klima zu identifizieren - insbesondere die asiatische Aridifizierung und die Störungen des globalen Kohlenstoffkreislaufs etwa während des paläozän-eozänen thermischen Maximums (PETM).

Beckenweite tektonische Senkungsanalysen deuten darauf hin, dass die frühkretazische Transgressionsphase im Tadschikischen Becken mit einer Intensivierung der Kollisionstektonik im Pamir (zwischen ca. 130 und 90 Ma) und der damit verbundenen Bildung eines Retro-Arc-Beckens in Zusammenhang stehen. Die globale Abkühlung der Spätkreide wird aus dem Verschwinden von molluskenreichen Kalksteinen und der Dominanz von bryozoen- und echinodermenreichen Kalksteinen im Tadschikischen Becken abgeleitet. Dies liefert den ersten Nachweis für das Abkühlungsereignis der Spätkreide in Zentralasien.

Wir interpretieren die langfristige paläogene Regression des Proto-Paratethys-Meeres Richtung Westen ab ca. 41 Ma mit den tektonischen Fernfeldeffekten der indo-asiatischen Kollision und der Hebung des Pamir/Tibetischen Plateaus. Die transgressiven und regressiven Intervalle der proto-Paratethys-See korrelieren gut mit den bekannten feuchten und ariden Phasen im Qaidam- bzw. Xining-Becken, was die Rolle der proto-Paratethys-See als wichtige Feuchtigkeitsquelle für

das asiatische Binnenland und ihren Rückzug als Mitverursacher der asiatischen Aridifizierung verdeutlicht.

Schließlich untersuchen wir die Wirkungsfaktoren, den relativen Beitrag und die Erhaltungseffizienz alter epikontinentaler Meere als Kohlenstoffsenken mit neuen und bestehenden Daten. Dabei verwenden wir organik-reiche Ablagerungen aus den ausgedehnten epikontinentalen Proto-Paratethys- und westsibirischen Meeren, die auf das PETM datiert sind. Wir schätzen eine Einlagerung von ca. 1390±230 Gt organischer Kohlenstoffverbindungen. Das stellt eine beachtliche Menge, verglichen mit der zuvor geschätzten globalen Gesamtmenge an überschüssiger organischer Kohlenstoffeinlagerung (ca. 1700-2900 Gt) dar, welche sich allein auf die Proto-Paratethys und die westsibirischen Meere konzentriert. Für vergangene und zukünftige Perioden mit kleineren epikontinentalen Meeren würde die Wirksamkeit dieser negativen Rückkopplung des Kohlenstoffkreislaufs wohl abnehmen.

Contents

List of Figures

List of Supplementary Figures

List of Tables

List of Supplementary Tables

Chapter 1

1. Introduction

The modern-day geography of Central Asia covers an extremely large region with varied terrestrial features such as mountains and passes, vast deserts and grassy steppes. Its current land-locked setting however contradicts with its geologic past. If you wander in its dry deserts, you can find many marine fossils (e.g. oysters, ammonites, echinoids) which are remnants of a million-year-old lost sea. This lost sea, a shallow, vast epicontinental sea known as proto-Paratethys, formed about 160 million years ago (during Jurassic times) when the waters of the Tethys Ocean flooded into Eurasia. During Cretaceous to Paleogene times the proto-Paratethys extended across Eurasia from the Mediterranean Tethys to the Tarim Basin in western China (Figure 1.1). This sea was also known, at its eastern end in Central Asia, as the Tarim Sea, Tajik Sea, Turan Sea (Tang et al., 1992; Burtman & Molnar, 1993; Burtman, 2000) or regionally as Peri-Tethys (e.g. Gavrilov et al. 1997, 2003) until the Late Eocene when it drastically retreated to the west and became isolated as the Paratethys. The transition from well-oxygenated bottom waters during the Eocene to low-oxygen environments in the Oligocene is generally accepted as the birth of the Paratethys (van der Boon, 2017). Today's remnants of this vast sea are the Black Sea, Caspian Sea and Aral Lake.

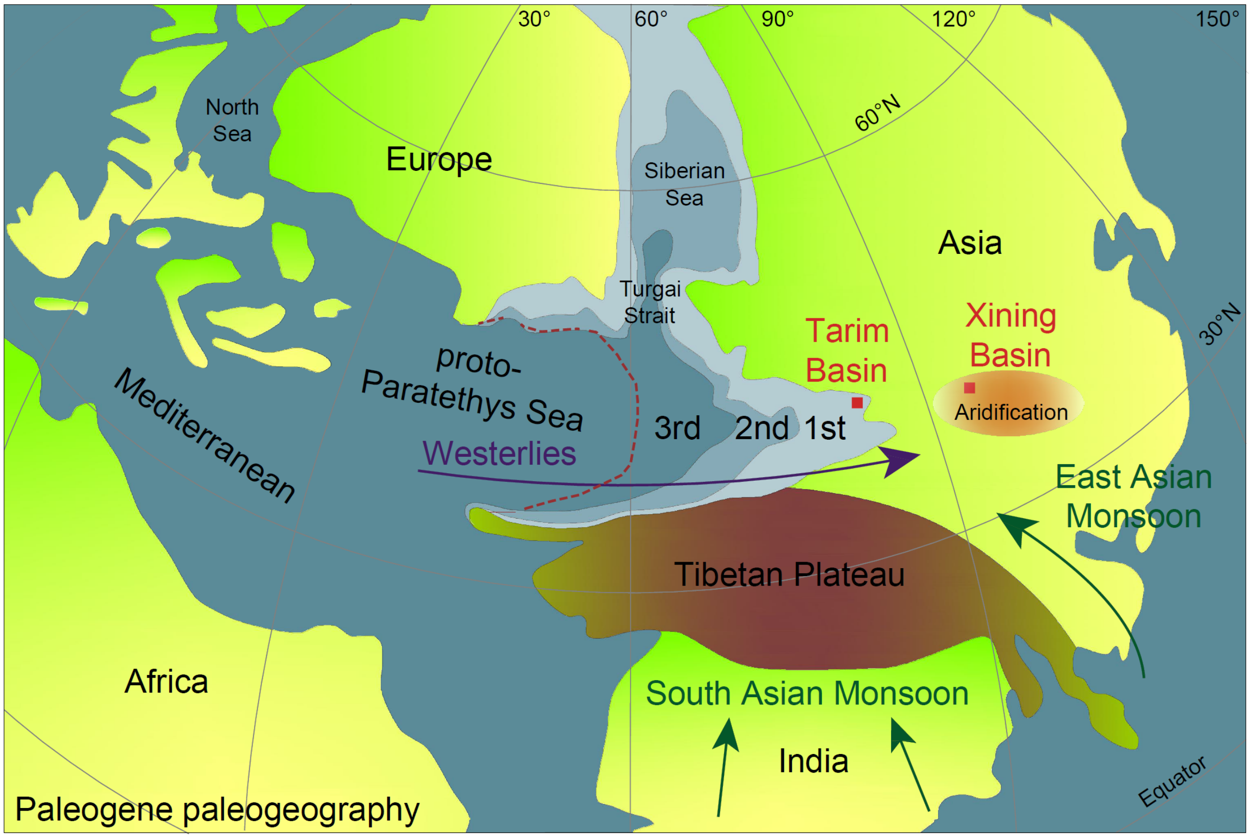

Figure 1.1 Generalized Paleogene paleogeography of Eurasia (modified from Meijer et al., 2019). The maximum spatial extent of the Paleogene proto-Paratethys sea incursiosns are shown on the map. Red dashed line shows the approximate extent of the Paleogene regressions.

Following the pioneering studies of the Soviet and Chinese field geologists (e.g. Markowsky, 1959; Pomazkow, 1972; Naidin et al., 1980; Davidzon et al., 1982; Dzhalilov et al., 1982; Pojarkova, 1984; Yichun et al., 1988; Tang et al.,1989; Bureu of Geology and Mineral Resources of Xinjiang Uygur Autonomous Region, 1993) the Cretaceous-Paleogene sedimentary records of the proto-Paratethys sea in Central Asian basins have attracted more researchers due to their value in bearing the complex history of Asian tectonics and regional paleoenvironmental changes (e.g. Sobel, 1995; Sun & Jiang, 2013; Sun et al., 2016; Zhang et al., 2018, 2019; Bosboom et al., 2017, 2014a, 2014b, 2011, Xi et al., 2016; Guo et al., 2015; Carrapa et al., 2015; Kaya et al., 2019, 2020a; Wang et al., 2016, 2019; Lv et al., 2020). This was particularly after the year of 2010 because since then, it has become easier to have access to these valuable records in the Tajik and Tarim basins, in Tajikistan and China, respectively.

Before its final westward retreat in the Eocene, a total of six Cretaceous and Paleogene major marine incursions have been distinguished from the sedimentary records of the Tajik and Tarim basins in Central Asia (Figure 1.2). It has been previously proposed that the Cretaceous sea fluctuations in the Tajik and Tarim basins were controlled by the global sea-level fluctuations (Xi et al, 2016; Guo et al., 2015; Sobel, 1995; Naidin et al., 1980), whereas the effects of (1) tectonism and associated basin overfilling (Burtman, 2000; Burtman & Molnar, 1993), (2) eustasy (Dupont-Nivet et al., 2007; Sobel & Dumitru, 1997) or (3) combined effects of both tectonism and global sea level (Bosboom et al., 2017, 2014a, 2011; Zhang et al., 2018) have been viewed as the controlling factor for the Paleogene sea incursions.

The Cretaceous-Paleogene tectonic evolution of the Pamir and Tibet and their far-field effects indeed becomes very important for the sedimentological and structural evolution of the Central Asian basins generating subsidence and accommodation space for sedimentation, or otherwise causing uplift, generating structural features and diminishing accommodation space. This might very well relate to the evolution of the proto-Paratethys sea fluctuations in central Asia, therefore comparing the records of the sea incursions to the tectonic and eustatic events has paramount importance to reveal the controlling mechanisms behind the sea incursions (Figure 1.2).

The subsidence of the Tajik and Tarim basins and sea incursions provide insight to the Pamir-Tibetan orogeny and India-Asia collision and associated deformation in central Asia guided by the reactivation of inherited crustal and lithospheric structures (Jolivet, 2017; Robinson, 2015). Not only providing insight on the Asian tectonism and eustasy, the Cretaceous-Paleogene fluctuations of the proto-Paratethys sea across Eurasia also have been shaping Asian paleoenvironments and paleogeography (e.g. Hendrix et al., 1992; Ramstein et al., 1997). Paleogene westward retreat of the proto-Paratethys Sea was viewed as the controlling factor for the aridification by removing a moisture source, and the intensification of the Asian monsoons by increasing the land-sea contrast (Ramstein et al., 1997; Zhang et al., 2007). It has been also proposed recently that the retreat of the proto-Paratethys Sea triggered the onset of the Siberian High driving dust storms and aridification in Central China which results in the intensification of the Asian steppes (e.g. Bosboom et al., 2014b; Meijer et al., 2020a).

What makes more attractive the Cretaceous-Paleogene deposits of the proto-Paratethys Sea in Central Asia for the geoscience community is the sedimentary records of the drastic paleoecological and paleoclimatic events such as the Paleocene-Eocene Thermal Maximum (PETM) or Cretaceous Oceanic Anoxia Events (OAEs) (e.g. Gavrilov et al., 2019). These critical events, particularly the PETM, considered analogous to the present-day climate change, were represented by the extensive accumulation of organic matter-rich deposits (e.g. sapropel beds, shales) which have been the focus of several studies (e.g. Gavrilov et al., 1997, 2003, 2009; Shcherbinina et al., 2016; Dickson et al., 2014, 2015, Bolle et al., 2000) documenting the drastic shifts in the paleoenvironmental/paleoecological conditions.

Consequently, attaining well-constrained timing and paleogeography for the sea incursions in Central Asia is indeed essential to properly understand and distinguish the controlling mechanisms and their link to Asian paleoenvironmental and paleoclimatic change. This might also contribute to our understanding of the interplay between global climate and local environmental and sea-level changes both in the present and future. However, owing to inaccuracies in the dating of rocks (mostly continental rocks and marine rocks with benthic microfossils providing low-resolution biostratigraphic constraints) and conflicting results, there has been no consensus on the timing of the sea incursions and interpretation of these records has been in question.

1.1. Goals

To reveal the timing, extent, controlling mechanisms and effects of Cretaceous-Paleogene proto-Paratethys sea incursions on regional paleoenvironment and paleoclimate in Central Asia we make an integrated sedimentological, stratigraphic and geochemical study. We apply integrated bio- and magnetostratigraphy to date the sea incursions and marine-terrestrial transitions. Marine microfossil assemblages have been identified and studied to obtain age constraints for marine intervals and paleoenvironmental changes as well. Grain associations of carbonate rocks have been studied to reveal the paleoenvironmental and paleoclimatologic changes. Organic and inorganic geochemical proxies are used to reconstruct paleoenvironmental parameters. We combine all these methods to have a reliable and accurate correlation of the paleoenvironmental and paleogeographic changes to the geologic time scale and regional tectonic and paleoclimatic events to be able to improve understanding of the controlling mechanisms behind the sea fluctuations. To estimate the paleogeographic evolution of the proto-Paratethys Sea, the refined age constraints and detailed paleoenvironmental interpretations are combined with successive paleogeographic maps on which the regional coastlines and depositional environments during the Cretaceous-Paleogene sea advances and retreats were drawn based on the results of this thesis and integrated with existing literature.

1.2. Outline

Chapter 2 Paleogene evolution and demise of the proto-Paratethys Sea in Central Asia (Tarim and Tajik basins): Role of intensified tectonic activity at ca. 41 Ma

Mustafa Yücel Kaya, Guillaume Dupont-Nivet, Jean-Noel Proust, Pierrick Roperch, Laurie Bougeois, Niels Meijer, Joost Frieling, Chiara Fioroni, Sevinç Özkan Altıner, Ezgi Vardar, Natasha Barbolini, Marius Stoica, Jovid Aminov, Mehmut Mamtimin and Zhaojie Guo

Basin Research 31, 461-486 (2019) https://doi.org/10.1111/bre.12330

In this chapter a new regional stratigraphic framework is provided for the timing of the Paleogene sea incursions in the SW Tarim and Tajik basins. The long-term westward retreat of the proto-Paratethys Sea starting at ca. 41 Ma is interpreted as being caused by increasing far-field tectonic effects (increased clastics and basin infilling) associated with the Pamir/Tibetan tectonic activity. The transgressive/regressive intervals of the proto-Paratethys Sea in the SW Tarim Basin coincide with the less arid/more arid phases in the Qaidam and Xining basins, establishing the proto-Paratethys as a major important moisture source for the Asian interior and demonstrating its importance as a contributor to Asian aridification.

Author Contributions: MYK performed the fieldwork, sampling, sedimentologic, magnetostratigraphic and sequence stratigraphic analyses. MYK also contributed to data anlysis and interpretation and writing/refinenment of the manuscript. GDN performed the fieldwork and also helped with designing the study, interpreting the data and writing of the manuscript. JNP performed the fieldwork and helped with the sedimentological and sequence stratigraphic interpretations. PR manages the laboratory used for paleomagnetic analysis. LB provided the unpublished geochemical data from her doctoral research. JF, CF, SÖA, EV, NB and MS performed the biostratigraphic analyses. NM, JA and MM helped with fieldwork. ZG helped with the organization of the fieldwork. All co-authors discussed data interpretation.

Chapter 3 Cretaceous evolution of the Central Asian proto-Paratethys Sea: tectonic, eustatic and climatic controls

Mustafa Yücel Kaya, Guillaume Dupont-Nivet, Jean-Noël Proust, Pierrick Roperch, Niels Meijer, Joost Frieling, Chiara Fioroni, Sevinç Özkan Altıner, Marius Stoica, Jovid Aminov, Mehmut Mamtimin and Zhaojie Guo

Tectonics 39, (9) (September, 2020) https://doi.org/10.1029/2019TC005983

This chapter provides new age constraints for the timing of the Cretaceous sea incursions. We document that not only eustasy but also the regional tectonic processes have a major control on the Cretaceous proto-Paratethys Sea incursions in Central Asia. Record of the global Early Maastrichtian cooling event also documented from the carbonate deposits of the proto-Paratethys Sea in the Tajik Basin.

Author Contributions: MYK performed the fieldwork, sampling, sedimentologic, magnetostratigraphic and sequence stratigraphic analyses. MYK also contributed to data anlysis and interpretation and writing/refinenment of the manuscript. GDN performed the fieldwork and also helped with designing the study, interpreting the data and writing of the manuscript. JNP performed the fieldwork and helped with the sedimentological and sequence stratigraphic interpretations. PR manages the laboratory used for paleomagnetic analysis. JF, CF, SÖA and

MS performed the biostratigraphic analyses. NM, JA and MM helped with the fieldwork. ZG helped with the organization of the fieldwork. All co-authors discussed data interpretation.

Chapter 4 The Eurasian Epicontinental Sea, a major carbon sink of the Paleocene-Eocene Thermal Maximum

Mustafa Yücel Kaya, Guillaume Dupont-Nivet, Joost Frieling, Chiara Fioroni, Alexander Rohrmann, Sevinç Özkan Altıner, Ezgi Vardar, Hakan Tanyaş, Birgit Plessen, Mehmut Mamtimin and Zhaojie Guo

(In review in Nature Geoscience)

A new PETM record from the Tarim basin has been presented. The significance and effectiveness of the Eurasian Epicontinental Sea as a carbon sink during the PETM has been proposed and documented implying the role of epicontinental seas as relevant negative feedback to carbon emissions for the present day and other periods in the geologic past.

Author Contributions: MYK performed the fieldwork, sampling, sedimentologic and geochemical analyses. MYK also contributed to data anlysis and interpretation and writing/refinenment of the manuscript. GDN performed the fieldwork and also helped with designing the study, interpreting the data and writing of the manuscript. JF, CF, SÖA and EV performed the biostratigraphic analyses. JF helped with the geochemical analyses. AR performed the biomarker analysis. HT helped the with geospatial analysis. BP manages the laboratory used for geochemical analyses. MM helped with the fieldwork. ZG helped with the organization of the fieldwork. All co-authors discussed data interpretation.

Chapter 5 Discussion

We discuss the main findings of the thesis taking full account of the most recent relevant publications as well. We try to provide the progress and still-existing questions and conflictions on the sea incursions and set out some of the main challenges for the future research as well.

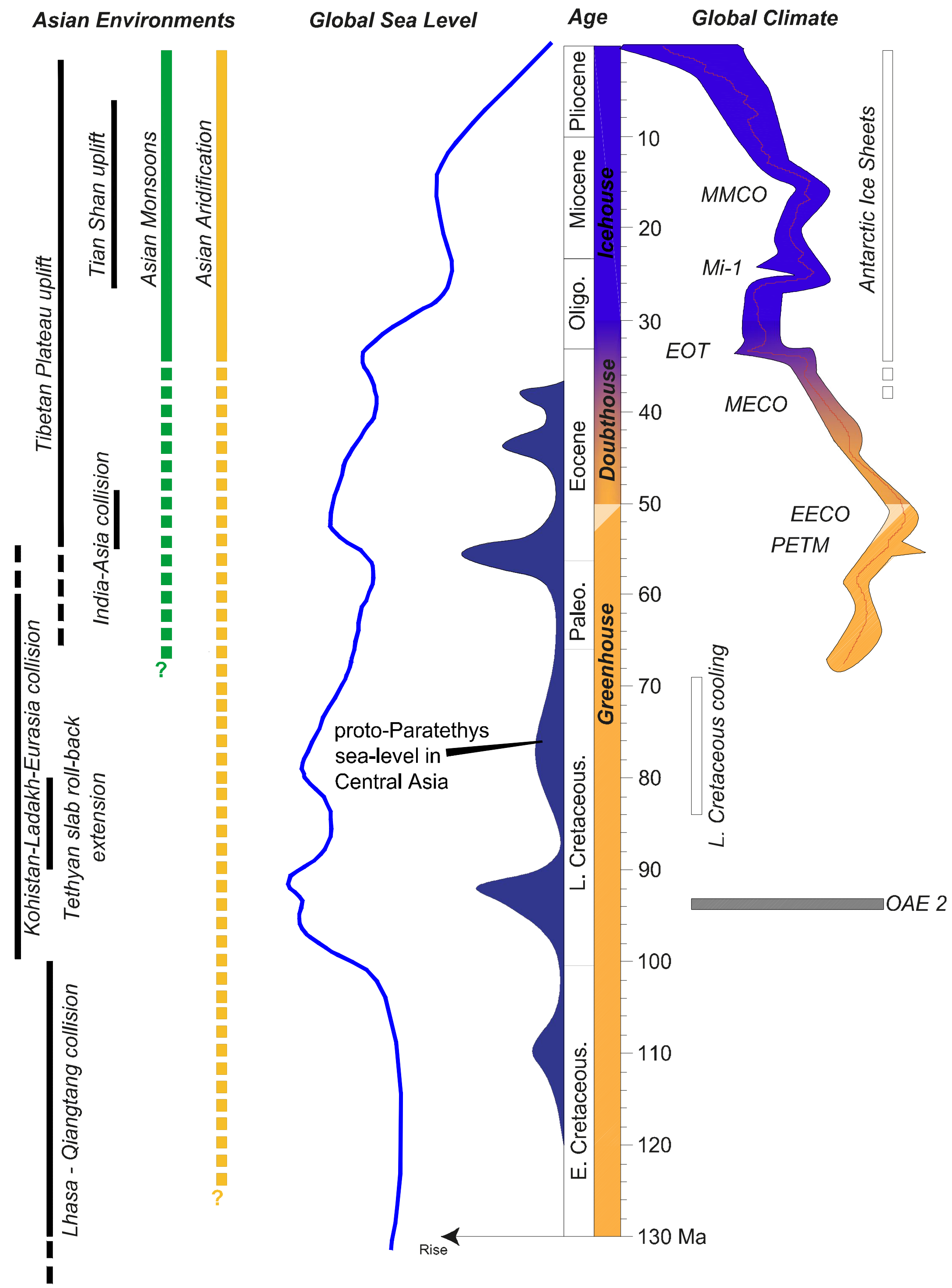

Figure 1.2 Timing of the proto-Paratethys sea incursions with important tectonic, climatic and eustatic events

Chapter 2

2. Paleogene evolution and demise of the proto-Paratethys Sea in Central Asia (Tarim and Tajik basins): role of intensified tectonic activity at ca. 41 ma

Abstract

The proto-Paratethys Sea covered a vast area extending from the Mediterranean Tethys to the Tarim Basin in western China during Cretaceous and early Paleogene. Climate modelling and proxy studies suggest that Asian aridification has been governed by westerly moisture modulated by fluctuations of the proto-Paratethys Sea. Transgressive and regressive episodes of the proto-Paratethys Sea have been previously recognized but their timing, extent and depositional environments remain poorly constrained. This hampers understanding of their driving mechanisms (tectonic and/or eustatic) and their contribution to Asian aridification. Here, we present a new chronostratigraphic framework based on biostratigraphy and magnetostratigraphy as well as a detailed paleoenvironmental analysis for the Paleogene proto-Paratethys Sea incursions in the Tajik and Tarim basins. This enables us to identify the major drivers of marine fluctuations and their potential consequences on Asian aridification. A major regional restriction event, marked by the exceptionally thick (≤ 400 m) shelf evaporites is assigned a Danian-Selandian age (~63-59 Ma) in the Aertashi Formation. This is followed by the largest recorded proto-Paratethys sea incursion with a transgression estimated as early Thanetian (~59-57 Ma) and a regression within the Ypresian (~53-52 Ma), both within the Qimugen Formation. The transgression of the next incursion in the Kalatar and Wulagen formations is now constrained as early Lutetian (~47-46 Ma), whereas its regression in the Bashibulake Formation is constrained as late Lutetian (~41 Ma) and is associated with a drastic increase in both tectonic subsidence and basin infilling. The age of the final and least pronounced sea incursion restricted to the westernmost margin of the Tarim Basin is assigned as Bartonian–Priabonian (~39.7-36.7 Ma). We interpret the long-term westward retreat of the proto-Paratethys Sea starting at ~41 Ma to be associated with far-field tectonic effects of the Indo-Asia collision and Pamir/Tibetan plateau uplift. Short-term eustatic sea level transgressions are superimposed on this long-term regression and seem coeval with the transgression events in the other northern Peri-Tethyan sedimentary provinces for the 1st and 2nd sea incursions. However, the 3rd sea incursion is interpreted as related to tectonism. The transgressive and regressive intervals of the proto-Paratethys Sea correlate well with the reported humid and arid phases, respectively in the Qaidam and Xining basins, thus demonstrating the role of the proto-Paratethys Sea as an important moisture source for the Asian interior and its regression as a contributor to Asian aridification.

2.1. Introduction

The proto-Paratethys Sea, extended across Eurasia from the Mediterranean Tethys to the Tarim Basin in western China during Cretaceous to Paleogene times. The proto-Paratethys Sea fluctuations as well as its long-term incursion and retreat out of Central Asia are well expressed at its eastern end in the Tarim Basin where three Paleogene sea incursions were previously recognized (Mao & Norris, 1988; Tang *et al.*, 1989; Lan & Wei, 1995; Burtman, 2000), but their driving mechanisms remain unresolved. Different controlling factors were suggested: (1) tectonism and associated basin overfilling related to the India-Asia collision (Burtman & Molnar, 1993; Burtman, 2000), (2) global sea level fluctuations (Dupont-Nivet *et al*., 2007; Sobel & Dumitru, 1997) and (3) the combined effects of tectonism and global sea level (Bosboom *et al*., 2011; 2014a; 2017; Zhang *et al*., 2018).

Previous efforts have contributed to constrain the timing, extent and depositional environments of the sea fluctuations (Sun & Jiang, 2013; Wan *et al*., 2014; Wang *et al*., 2014; Sun *et al*., 2016; Zhang *et al*., 2018). In particular, Bosboom *et al*. (2011, 2014a, b, 2017) dated the 2nd and 3rd Paleogene regression events. Despite this, the lack of data for the age and paleogeography of all individual transgression and regression events still hampers understanding the role of tectonics and eustasy on the sea incursions and their paleoclimatic consequences on regional aridification.

Central Asia shifted from a subtropical climate to the onset of inland deserts during the Cenozoic (e.g. Guo *et al*., 2008), however the mechanisms driving this aridification remain elusive. The growth of the Himalaya and Tibetan Plateau in response to the India-Asia collision is one of the proposed mechanisms by forming orographic barriers and creating planetary waves that promote aridity (Manabe & Broccoli, 1990; Kutzbach *et al*., 1993; Li *et al*., in press). Alternatively, it has been suggested that global cooling during the Cenozoic is driving the aridification by weakening the hydrological cycle (Dupont-Nivet *et al*., 2007; Lu *et al*., 2010; Li *et al*., in press). A third view suggests that the westward retreat of the proto-Paratethys sea was the controlling factor for both the aridification by removing a moisture source, and the intensification of the Asian monsoons by increasing the land-sea contrast (Ramstein *et al*., 1997; Zhang *et al*., 2007). However, recent proxy data and climate models show that the sea was too shallow to affect the thermal contrast generating monsoons (Bougeois *et al*., 2014; 2018; Licht *et al*., 2014; 2016; Roe *et al*., 2016; Zhang *et al*., 2012). Recent indications from proxy and model data rather show that Asian aridification since the early Eocene is linked to a decrease in the westerly moisture flux (Caves *et al*., 2015) and that the proto-Paratethys Sea provided moisture via the westerlies which precipitated in Central Asia during wintertime (Bougeois *et al*., 2014; 2018). However, to what extent this westerly moisture is affected by the fluctuating sea incursions and the long-term sea retreat remains mostly unknown and its influence in eastern Asia remains to be explored.

Central Asian moisture records based on pollen, geochemistry and sedimentological data can be found in the terrestrial (fluvio-lacustrine) deposits in the Xining (Abels *et al*., 2011; Bosboom *et al*., 2014a; Meijer *et al*., 2018) and Qaidam (Song *et al*., 2013; Ye *et al*., 2016; Bao *et al*., 2017) basins, both located further east along the northeastern margin of the Tibetan Plateau. Comparing these records with the proto-Paratethys transgressions and regressions could elucidate the marine influence on atmospheric moisture and aridification of the Asian interior. However, this requires constraining the age and extent of the sea level fluctuations.

To better understand the cause and consequences of the proto-Paratethys Sea fluctuations, this study aims to: (1) document the depositional environments during the Paleogene sea incursions and their evolution; (2) provide an improved regional stratigraphic framework, using new biostratigraphic and magnetostratigraphic constraints for the Paleogene transgressive-regressive phases; and (3) discuss their driving mechanisms (tectonic and/or eustatic) and consequences on regional aridification by examining and comparing to regional records of the sea extent, tectonic settings as well as climate records.

2.2. Geologic Setting

2.2.1 Tectonic setting

The Tarim and Tajik basins are part of blocks (or terranes) separated by Paleozoic and Mesozoic fold belts formed by the successive accretion of Gondwanan continental blocks to Laurasia between the Late Triassic and Eocene (Şengör *et al.*, 1988; Yanping, 1990; Hendrix *et al.*, 1992; Yin & Harrison, 2000). Cenozoic northward movement and Eocene accretion of the last continental block (India) to Laurasia created most of the present-day topographies bounding the Tarim and Tajik basins (Figure 2.1).

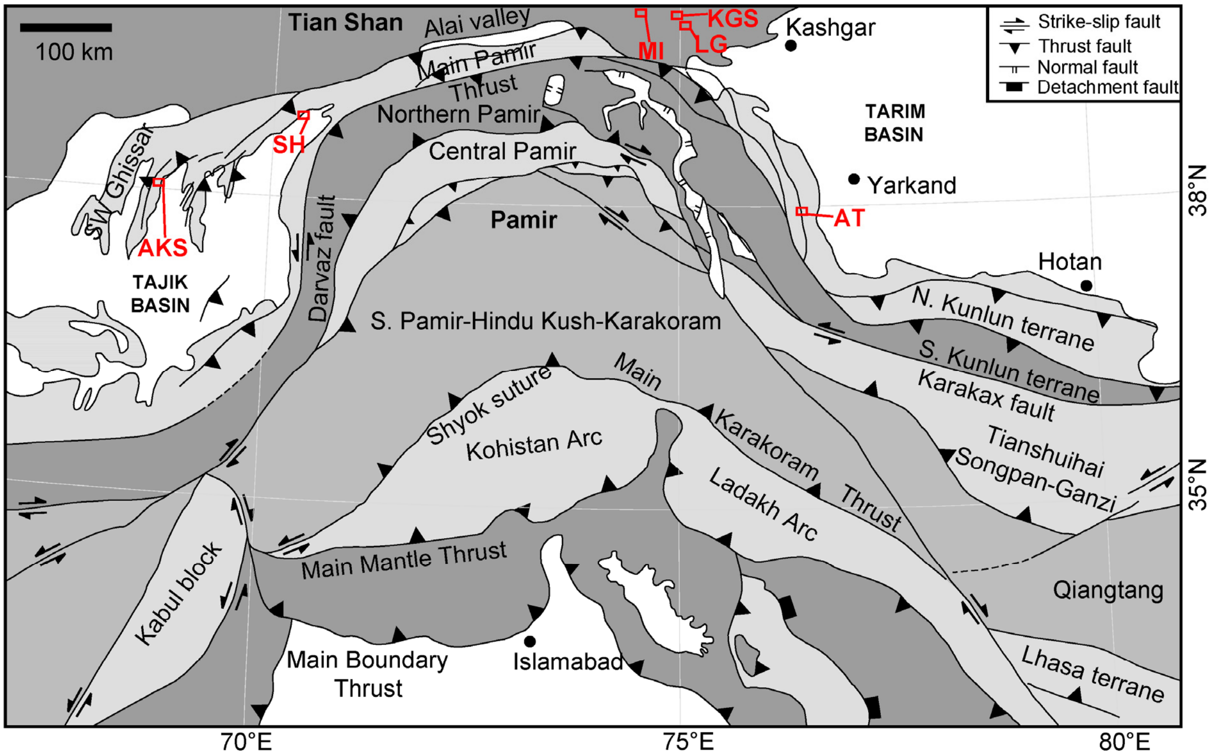

Figure 2.1 Locations of the studied sections in Tarim (KGS: Kangsu, LG: Laghman, MI: Mine, AT: Aertashi) and Tajik (AKS: Aksu, SH: Shuldara) basins on a schematic map of major tectonic domains within the Pamir and western Tibet (modified from Cowgill, 2010).

To the north of the Tajik and Tarim basins, the evolution of the Tian Shan goes back to the Late Paleozoic, initiating during the Carboniferous in an ocean subduction – continental accretion tectonic context (Şengör *et al*, 1993; Jolivet *et al.*, 2013). Its Cenozoic history is still debated with possible early Paleogene tectonic events (e.g. Jolivet *et al.*, 2013) related to propagating deformation from the India-Asia collision. More consensual is the onset of major exhumation well-constrained around the Oligocene-Miocene boundary (Sobel *et al*., 2006; van Hinsbergen *et al*., 2012; Yang *et al*., 2015). Before the early Miocene exhumation, the southwestern Tian Shan foreland remained mostly inactive through the Oligocene, as evidenced by limited exhumation, subsidence and accumulation (Sobel *et al*., 2006; Heermance *et al*., 2007; Yang *et al*., 2015). Since ~25 Ma, the Tian Shan grew through several tectonic pulses (e.g. Yin *et al*., 1998; Sun *et al*., 2009; Qiao *et al*., 2017).

To the south of the Tajik and Tarim basins, early evolution of the Kunlun arc and Karakul-Mazar complex (Kunlun terrane) is associated with closure of the Paleo-Tethys since at least 200 Ma, with exhumation during the Cretaceous, Paleogene and Miocene (e.g. Amidon and Hynek, 2010; Cao *et al*., 2015; Blayney *et al*., 2016). Middle - late Eocene thrusting and exhumation in the West Kunlun Shan and North Pamir, as well as Pamir-Tibetan uplift, magmatism and metamorphism further south in the Qiangtang and Central/South Pamir terranes have been proposed to relate to far field propagation of deformation from the India-Asia collision (Yin *et al*., 2002; Cowgill, 2010; Bershaw *et al*., 2012; Rutte *et al*., 2017; Chapman *et al*., 2018 and references therein). Marked thrusting and exhumation of the West Kunlun Shan has been proposed sometime between the late Oligocene and early Miocene (20-26 Ma) propagating north into the Pamir uplifting mainly ~15 Ma (e.g. Blayney *et al*., 2016 and references therein). The onset of the Pamir indentation and uplift separating the Tarim and the Tajik basins has been constrained at ~25-20 Ma and continued to propagate north from 15 Ma up to the Pliocene (Burtman & Molnar, 1993; Sobel & Dumitru, 1997; Cowgill, 2010; Blayney *et al*., 2016).

2.2.2 Stratigraphic setting

The Precambrian (pre-Neoproterozoic) crystalline basement of the Tarim Basin is covered by Phanerozoic strata consisting of Paleozoic carbonates, marine and non-marine fine clastics, and Mesozoic - Cenozoic red clastics, evaporites and limestones (Li, 1990; Zhang *et al*., 2013). Paleogene deposits in the western Tarim Basin are represented by the Kashi Group, which is composed of the Aertashi, Qimugen, Kalatar, Wulagen and Bashibulake formations.

From the late Cretaceous and to the late Eocene, the Tarim Basin witnessed several transgressions and regressions, resulting in the deepening/shallowing of the epicontinental proto-Paratethys Sea and concomitant transitions from marine to continental depositional environments or vice versa (Burtman, 2000; Bosboom *et al*., 2011, 2014a, 2017; Guo *et al*., 2015; Xi *et al*., 2016; Zhang *et al*., 2018). The easternmost portion of the proto-Paratethys Sea in the western Tarim Basin was connected with the Tajik Basin, as evidenced by the similar stratigraphic and sedimentary successions in both basins (Burtman, 2000; Bosboom *et al*., 2017). Similarities of the fossil assemblages with other basins in Central Asia and Europe indicates that this portion of the Proto-Paratethys in the western Tarim Basin was also a part of the Tethyan Realm (Mao & Norris, 1988; Bosboom *et al*., 2011). It is widely accepted that the first Cretaceous marine incursion in the southwestern Tarim Basin is represented by a Cenomanian transgression, followed by other transgressions during Coniacian and Campanian (Burtman & Molnar, 1993; Burtman, 2000; Guo *et al*., 2015). Thick and extensive early Paleocene evaporites of the Aertashi Formation provide evidence for a regional restriction event. The first Paleogene transgression is characterized by the shelly marls of the lower member of the Qimugen Formation, which represents the maximum extent and deepest environments of the Proto-Paratethys Sea in the Tarim Basin. The succeeding regression is recorded in the gypsiferous mud deposits of the upper member of the Qimugen Formation. The marine Kalatar Formation limestones and silty shales of the Wulagen Formation are associated with the penultimate transgression, whereas the silty shales of the Bashibulake Formation were deposited during the last smaller marine transgression (Bosboom *et al*., 2011 and references therein). Our study focuses mainly on the transgressions represented by the lower member of the Qimugen, Kalatar and Wulagen formations and the regression recorded in the upper member of the Qimugen Formation.

2.3. Material and Methods

We analyzed three detailed sedimentological sections (Aertashi, Mine and Kangsu) and one lithostratigraphic section (Laghman) from the SW and NW Tarim Basin (Figure 2.1). Two lithostratigraphic sections (Aksu and Shuldara) from the Tajik Basin, including the records of the last two marine incursions recognized in the Tarim Basin (Bosboom *et al*., 2017), were re-examined and new biostratigraphic results were obtained from nannofossils and dinoflagellate cysts (dinocysts). Previously published palyno-assemblages from the Tarim Basin together with new palynogical samples provide a reconstruction of the continental paleoenvironments from the late Paleocene to Oligocene.

2.3.1 Sedimentology & sedimentary geochemistry

Based on lithology, thickness and geometry, sedimentary structures and fossil content, we recognized thirteen facies in the field (Table S 2.2). This study was complemented by the analysis of the mineralogical components, fossil assemblages and the texture of the carbonate rocks in thin sections leading to description of sixteen microfacies (MF) (Figure 2.2, S 2.2, S 2.3 and Table S 2.3). Individual facies and microfacies are grouped into facies associations (FA) each of which characterizes a specific depositional environment (Table S 2.1). The facies and microfacies were deposited in alluvial plain, coastal plain, restricted subtidal-shoreface, shoal-high energy shoreface, wave-dominated outer estuarine, offshore and hypersaline evaporitic shelf environments with variable lateral settings and relationships during the regression and transgression events (Figure 2.3a, see supplementary material section 2 for detailed explanation of the lithofacies and depositional environments). Differentiation of gypsum bearing facies as playa, supratidal sabkha and coastal salina settings was not always straightforward due to the lack of diagnostic sedimentary and lithological features on some exposures. This difficulty could also be due to the gradation of evaporite including depositional settings into each other, which produce similar depositional processes and facies in some cases (James & Walker, 1992), accordingly, these type of deposition might have occurred in any of those abovementioned near coast depositional settings. However, stable oxygen and carbon isotopic composition of the carbonate rocks interlayered between gypsum beds can help to identify depositional environments when field observations are insufficient (Hudson, 1977; Nelson & Smith, 1996). For this reason, we analyzed bulk carbon ($\delta^{13}C$) and oxygen ($\delta^{18}O$) isotopic compositions of carbonates from the Mine and Aertashi sections to determine marine and continental influences, which helped with interpretations of depositional environments. (See supplementary material section 3 for the details of the stable oxygen and carbon isotopic analysis).

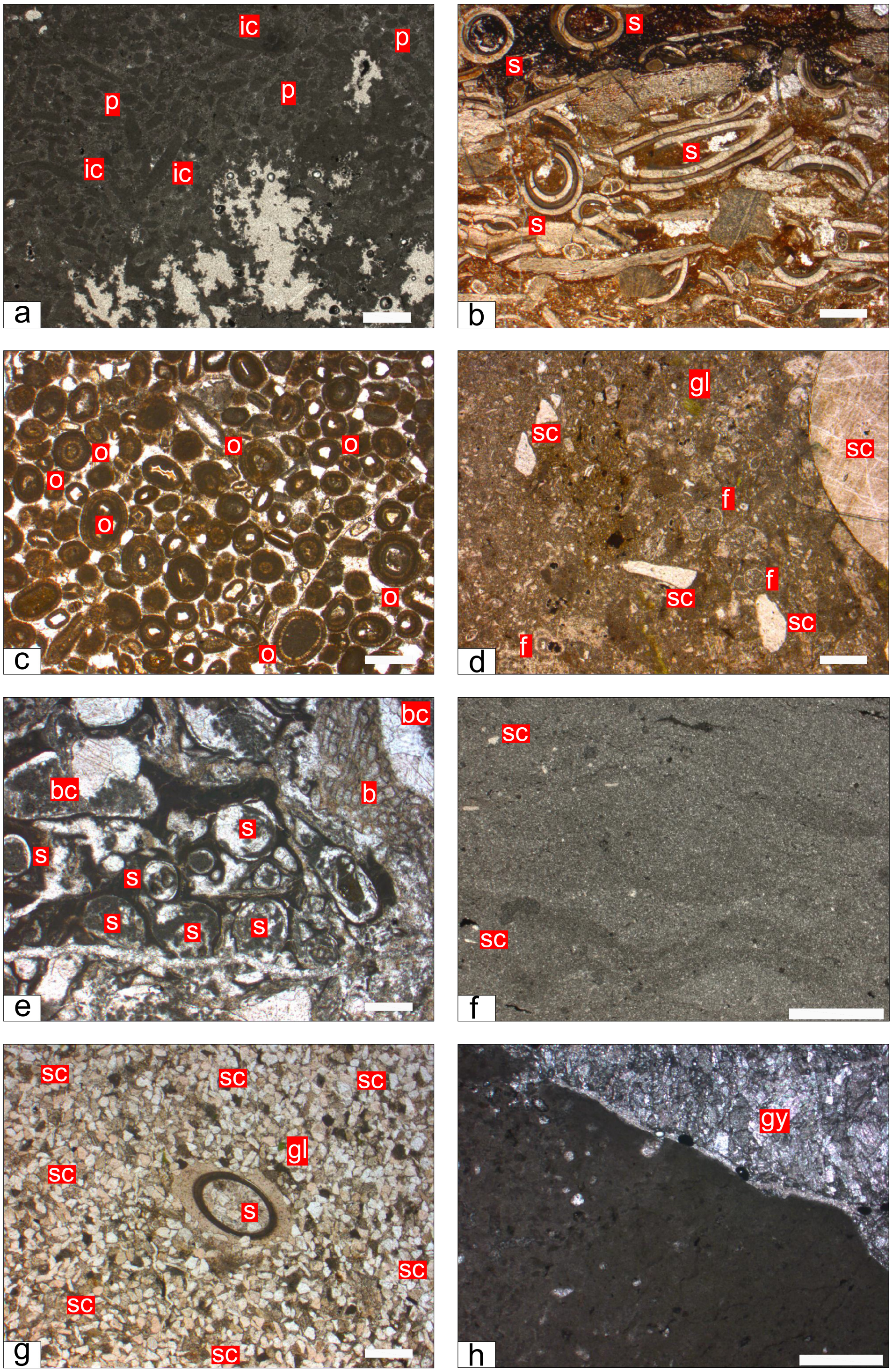

Figure 2.2 Photomicrographs of some microfacies (a) peloidal wacke – to packstone (MF3) KS15-C08; (b) serpulid packstone (MF4) AT13-TS39; (c) ooidal grainstone (MF7) AT13-TS46; (d) distal sandy allochem

limestone (MF11) MI13-TS24; (e) bioclastic packstone (MF6) MI13-TS02; (f) micritic mudrock (MF15) MI15-C22; (g) micritic sandstone with very rare allochems (MF16b) AT13-TS28; (h) mudstone with gypsum (MF12) MI15-C08 - p: peloids, ic: intraclast, s: serpulid, f: foraminifera, bc: bioclast, b: bryozoan, gs: gastropoda, o: ooid, sc: siliciclastic, gl: glauconite, gy: gypsum, for a, b, c, d, e, g and h scale bar is 500 µm, for f scale bar is 1mm.

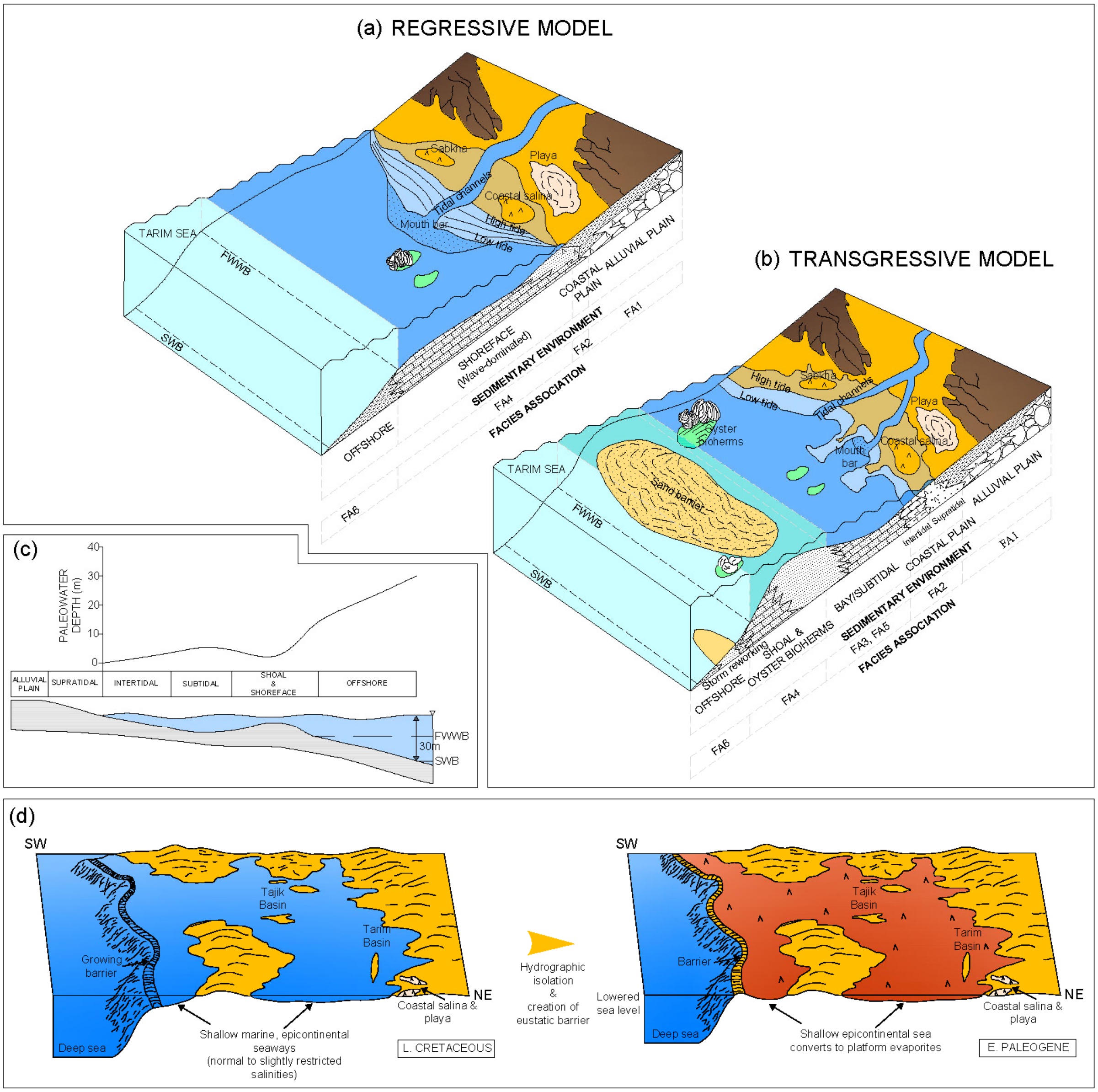

Figure 2.3 Depositional model showing the facies associations and related depositional environments during regressions (a) and transgressions (b). (c) Paleowater depth curve for depositional environments, depths for Fair Weather Wave Base (FWWB; between 10 and 15m) and Storm Weather Wave Base (SWB; 30 m) are taken from Burchette & Wright (1992) and Flügel (2004). (d) Depositional model for the Aertashi Formation, modified from Warren (2010).

2.3.2 Sequence stratigraphy

We used different kinds of surfaces indicative of either a seaward or landward shift of the successive facies belts, i.e. subaerial unconformity, transgressive surface, maximum flooding surface and basal surface of forced regression. These surfaces bound the different systems tracts, i.e. lowstand, transgressive, highstand and falling stage systems tracts, composing the depositional sequences (Catuneanu, 2006 and references therein). The correlations of the surfaces between our different sections led to propose a regional stratigraphic architecture of the Tarim Basin for the Paleogene. (See supplementary material section 4 for the details of the sequence stratigraphic analysis).

2.3.3 Biostratigraphy

Biostratigraphic samples were collected in Paleogene marine deposits from widespread sections in the Tarim Basin (Artashi, Kangsu and Mine sections) and Tajik Basin (Aksu and Shuldara sections; Figure 2.1) to constrain the age of the deposits. Samples of foraminifera, nannofossils and dinoflagellate cysts (dinocysts) were selected for age correlations. We utilize the standard microfossil zonations (Figure 2.8, Table S 2.4, S 2.5, S 2.6, S 2.7, S 2.8, S 2.9, S 2.10, S 2.11, S 2.12 and S 2.13).

2.3.3.1 Palynology

Palynological samples (approximately 50g of rock) were prepared using standard procedures at Palynological Laboratory Service, Holyhead, UK. Briefly, concentrated HCL and HF were used to dissolve carbonates and silicates respectively, followed by neutralization and sieving at 10 µm to remove small particles. In addition, a few samples required short ultrasonic treatment and/or mild oxidation with HNO_3. The concentrated >10 µm fraction was mounted on a microscope slide in glycerine jelly and analyzed at 400x magnification under a light transmitting microscope (Olympus CX41 / Leica DMRB). For biostratigraphy, two slides were scanned entirely and for assemblage studies a minimum of 200 dinoflagellate cysts (dinocysts) were counted and 250 grains for pollen. Dinocyst taxonomy follows Fensome & Williams (2004), and Bijl *et al*. (2016) for Wetzellielloid species.

2.3.3.2 Calcareous nannofossils

Smear slide preparation for calcareous nannofossils followed standard techniques (Bown & Young, 1998) and analyses were performed using a Zeiss Axioskop 40 microscope under crossed-polarized and transmitted light at 1250x magnification, scanning at least three transverses of each slide (~600 fields of view). The nannofossils were identified following the taxonomy given in Perch-Nielsen (1985), and the Nannotax website (Young *et al*., 2017). The biostratigraphic attributions are based on the schemes proposed by Martini (1971) and Okada & Bukry (1980) and on the recognition of secondary nannofossil bioevents (e.g. Bown, 2005; Raffi *et al*., 2005; Fornaciari *et al*., 2010; Agnini *et al*., 2014; Shcherbinina *et al*., 2016).

3.3.3 Foraminifera

For the benthic foraminiferal taxonomy, we basically followed Loeblich & Tappan (1988) at generic level. Due to the state of preservation and low abundance, identification at specific level was fairly limited. Whenever possible, benthic foraminifera species were identified mainly by following the species concepts of Cushman (1951), LeRoy (1953), Berggren & Aubert (1975) and Speijer (1994). The taxonomy and biostratigraphic attribution of planktonic foraminifera were based on Olsson *et al*. (1999), Pearson *et al*. (2006) and Young *et al*. (2018).

2.3.4 Magnetostratigraphy

To further constrain the age, we collected paleomagnetic core samples (25 mm in diameter) from the Laghman, Mine and Shuldara sections by using a standard cordless drill powered by rechargeable batteries and cooled by a water pump. Sampling interval ranged from 0.1 to 9.0 m depending on the suitability of the outcrop. All samples were oriented with a magnetic compass mounted on an orientation stage. Orientations were corrected for local declination. Samples were cut into cylindrical specimens of approximately 2 cm in length. Paleomagnetic analyses were carried out in the magnetically-shielded Archeo-Paleomagnetic Laboratory of the Faculty of Geosciences at the University of Rennes 1.

Following initial measurements of natural remanent magnetization (NRM), the specimens were thermally demagnetized in a shielded oven in 9 to 19 temperature steps of up to 680 ºC. After each demagnetization step, the remanent magnetization was measured by a squid 2G cryogenic magnetometer as well as the bulk magnetic susceptibility to monitor mineral transformation during heating.

2.4. Results

2.4.1 Biostratigraphy

2.4.1.1 Dinoflagellates

Tarim Basin

The presence of *Deflandrea oebisfeldensis* in sample KS33 in the Kangsu section suggests that the analyzed interval of the lower member of the Qimugen Formation is not older than ~59 Ma (Mudge & Bujak, 1996). The Paleocene-Eocene Thermal Maximum (PETM; ~55.8 Ma) is identified in sample KS36 and KS37 in the Kangsu section based on the presence of very abundant *Apectodinium* spp. (Crouch *et al*., 2001) and presence of *Wilsonidium pechoricum* (Iakovleva & Heilmann-Clausen, 2007).

Upon re-examination of the samples used in Bosboom *et al*. (2014b) in the Mine section, we recorded *Dracodinium rhomboideum* in sample B16 at the base of the marine Bashibulake Formation in the Mine section. This marker species is restricted to C18n.2n (40.14-39.7 Ma; Eldrett *et al*. 2004, Bijl *et al*., 2013) and roughly equivalent to the Middle Eocene Climate Optimum (MECO; ~40 Ma). Presence of *Dracodinium rhomboideum* indicates a slightly older age for the third transgressive phase compared to the previous work of Bosboom *et al*. (2014b).

Based on dinocyst biostratigraphy of the samples of the Mine and Kangsu sections, we assigned a Thanetian-Ypresian age for the lower member of the Qimugen Formation and an early Bartonian age to the base of the marine Bashibulake Formation (Figure 4 & 8, see supplementary materials section 1.1 for all dinocyst analyses in the Tarim Basin).

Tajik Basin

Aksu section

A Lutetian age was assigned to the upper member of the Jukar Formation, based on the presence of *Adnatosphaeridium vittatum* in samples AS04 and calcareous nannofossil biostratigraphy. For the Beshkent–Lower Tochar formations in the Aksu section [correlated to the Wulagen Formation in the Tarim Basin (Bosboom *et al*., 2017)], the presence of *H. porosa* (in samples AS08-AS10) indicates an age not older than C20r and not younger than C16r (Eldrett *et al*. 2004). Together with the results from the nannofossils biostratigraphy (see below) the age of the Beshkent –Lower Tochar formations is constrained as Lutetian-lowermost Bartonian (see supplementary materials section 1.1 for all dinocyst analyses in the Tajik Basin).

Shuldara section

A Bartonian – Priabonain age is assigned for the Kushan and Sanglak formations, correlated to the 2nd, 3rd and 4th member of the Bashibulake Formation in the Tarim Basin (Bosboom *et al*., 2017). Few diagnostic species were present, but the short ranging taxon *Dracodinium rhomboideum* was recorded in sample CD10 indicating an age close to or corresponding with C18n.2n (Eldrett *et al*. 2004, Bijl *et al*. 2013). This age assignment is supported by the dinocyst assemblage, which also contains *Lentinia serrata* and *Rhombodinium draco*. We further record the appearance of *Thalassiphora fenestrata* in one sample (CD11), which suggests an age of NP18 (C17n.1n) or younger for the top of the analyzed interval (e.g. Köthe, 2012).

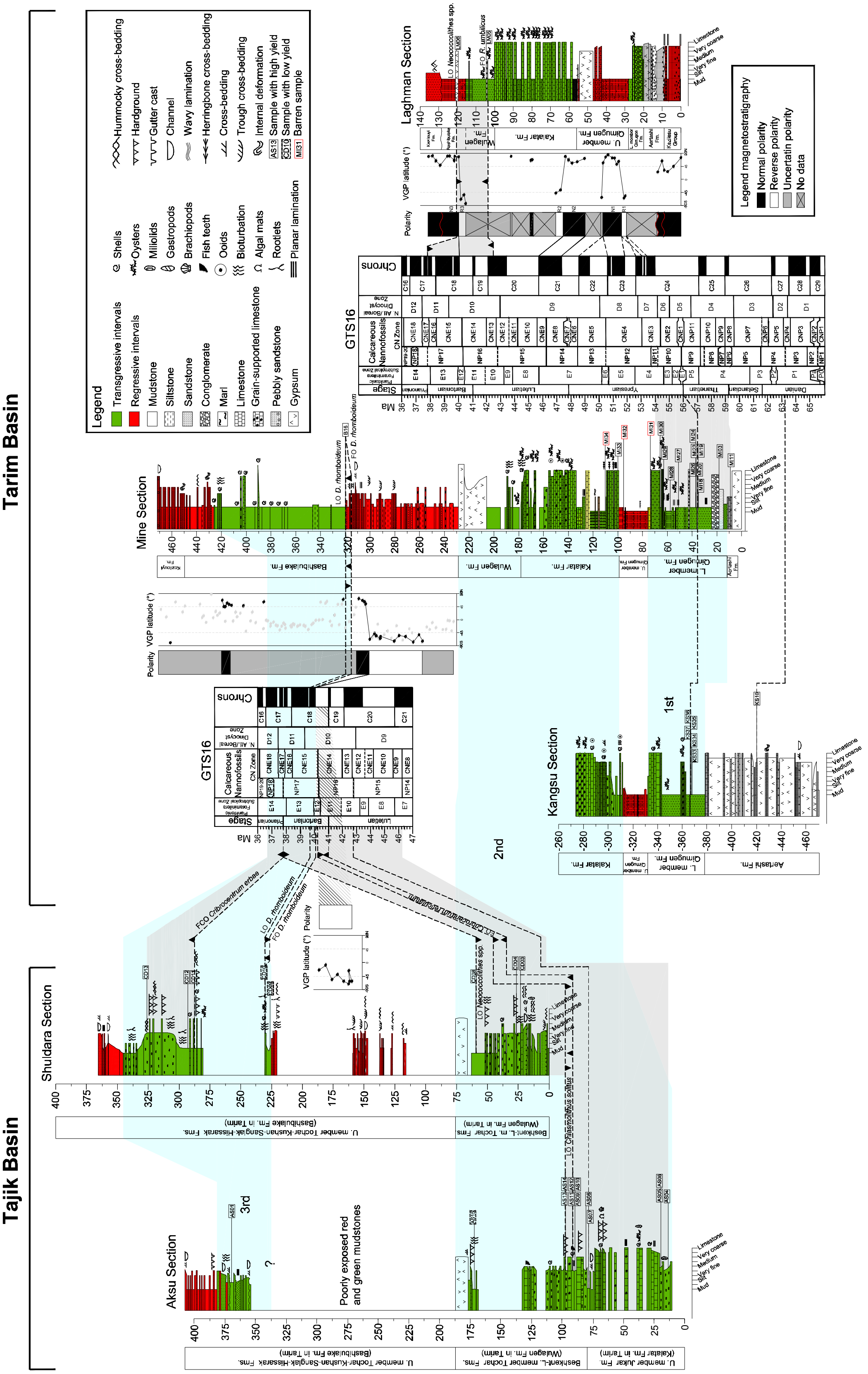

Tajik Basin
Tarim Basin
Aksu Section
Shuldara Section
Mine Section
Kangsu Section
Laghman Section
GTS16
Ma
Stage
Planktonic Foraminifera Subtropical Zone
Calcareous Nannofossils
CN Zone
N. Alt./Boreal Dinocyst Zone
Chrons
Polarity
VGP latitude (°)
Priabonian
Bartonian
Lutetian
Ypresian
Thanetian
Selandian
Danian
1st
2nd
3rd
?
Poorly exposed red and green mudstones
FCO Cribrocentrum erbae
LO D. rhomboideum
FO D. rhomboideum
LO Neococcolithes spp.
LO Cribrocentrum reticulatum
LO Chiasmolithus solitus
FO R. umbilicus
U. member Tochar-Kushan-Sanglak-Hissarak Fms. (Bashibulake Fm. in Tarim)
Beshkent-L. member Tochar Fms. (Wulagen Fm. in Tarim)
U. member Jukar Fm. (Kalatar Fm. in Tarim)
Bashibulake Fm.
Wulagen Fm.
Kalatar Fm.
Qimugen Fm.
U. member
L. member
Aertashi Fm.
Kezilouyi Fm.
Mud
Silt
Very fine
Fine
Medium
Coarse
Very coarse
Limestone
Legend
🟩 Transgressive intervals
🟥 Regressive intervals
Mudstone
Siltstone
Sandstone
Conglomerate
Marl
Limestone
Grain-supported limestone
Pebbly sandstone
Gypsum
Shells
Oysters
Miliolids
Gastropods
Brachiopods
Fish teeth
Ooids
Bioturbation
Algal mats
Rootlets
Planar lamination
Hummocky cross-bedding
Hardground
Gutter cast
Channel
Wavy lamination
Herringbone cross-bedding
Cross-bedding
Trough cross-bedding
Internal deformation
AS13 Sample with high yield
CD10 Sample with low yield
MI31 Barren sample
Legend magnetostratigraphy
■ Normal polarity
☐ Reverse polarity
▨ Uncertain polarity
☒ No data

Figure 2.4 Stratigraphic logs (in meters) of the Aksu, Shuldara (Boosbom et al., 2017), Kangsu, Mine and Laghman sections showing biostratigraphic and magnetostratigraphic correlations to the geological time scale (Ogg et al., 2016). Positive (negative) VGP latitudes represent normal (reversed) polarity indicated in black (white). The thick solid and dashed lines show preferred and other alternative magnetostratigraphic correlations to the geological time scale, respectively. The age correlation based on the microfossil assemblages is shown by light gray shading corresponding dinoflagellate cyst and nannofossil zonations. FO: first occurrence of important age-diagnostic biomarker species, FCO: first common occurrence of important age-diagnostic biomarker species, LO: last occurrence of important age-diagnostic biomarker species.

2.4.1.2 Calcareous nannofossils

Tarim Basin

A Thanetian-Ypresian age is assigned for the lower member of the Qimugen Formation in the Kangsu and Mine sections, based on the presence of several biostratigraphic markers. This notably includes the species *Discoaster multiradiatus* marker of the NP9 zone, ~57.2-55.9 Ma (samples KS34, KS36, KS37 and MI22 to MI27), *Fasciculithus tympaniformis*, which became extinct shortly after the Paleocene-Eocene boundary (56 Ma, samples KS36, KS37, MI22, MI23 and MI26) and *Tribrachiatus* cf. *bramlettei* which has its first occurrence at the base of the Eocene (NP10 zone, sample KS37). A Danian age is assigned to the Aertashi Formation based on the presence of *Fasciculithus* spp. and *F. magnicordis* in sample KS10 in the Kangsu section, however a Danian-Selandian age cannot be excluded based on the Thanetian age assignment for the base of the lower member of the Qimugen Formation. A Lutetian-Bartonian age is assigned to the Wulagen Formation in view of two productive samples (LM05 and LM06) from the Laghman section based on the presence of *Reticulofenestra umbilicus* (first occurrence at the base of the CP14 zone) and the presence of the additional marker *Neococcolithes* spp. (last occurrence at the base of CP15 zone) (Figure 2.4 & 2.8, see supplementary materials section 1.2 for detailed calcareous nannofossil biostratigraphy in the Tarim Basin).

Tajik Basin

Aksu section

The upper member of the Jukar Formation is assigned to the Lutetian based on the relatively common presence of *Lanternithus* sp. and in particular of *L. arcanus*, a species restricted to the CP 13b-CP 13c subzones (Bown, 2005) in samples AS04, coupled with the absence of *Reticulofenestra umbilicus* and *Cribrocentrum reticulatum*, (CP13/~NP15 zones; ~46.2-42.8 Ma), in agreement with previous data from the Tarim Basin (Bosboom *et al*., 2011, 2014a).

The samples (AS08 to AS14) collected from the Beshkent –Lower Tochar formations in the Aksu section, which is correlated to the Wulagen Formation in the Tarim Basin (Bosboom *et al*., 2017), lack *R. umbilicus*. Despite this, the formation has been tentatively correlated with the CP14a/NP16 zone (upper Lutetian-lower Bartonian; ~42.8-40.3 Ma) based on the absence of *L. arcanus* (last occurrence in the CP13c subzone) and the presence of *Neococcolithes* spp. and *Chiasmolithus solitus*, whose last occurrences are in the CP15 zone (Sheldon, 2002) and top of NP16/CP14a, respectively.

Samples collected in the Upper Tochar, Kushan, Sanglak and Hissarak formations, correlated to the Bashibulake Formation in Tarim Basin (Bosboom *et al*., 2017), are almost barren and only at the top of the section, in a low diversity nannofossil assemblage, could the presence of *Cribricentrum reticulatum* be indicative of an age not older than the Bartonian (Figure 2.4 & 2.8, see supplementary materials section 1.2 for detailed calcareous nannofossil biostratigraphy in the Tajik Basin).

Shuldara section

The Beshkent –Lower Tochar formations, correlated to the Wulagen Formation in Tarim Basin (Bosboom *et al*., 2017), are assigned to nannofossil zone CP14 (~NP16/NP17, upper Lutetian – lower Bartonian; ~42.8-37.8 Ma) based on the presence of *Neococcolithes* and *Dictyococcites bisectus* (samples CD03 and CD04) and the absence of *Lanthernithus arcanus*. The Kushan and Sanglak formations, corresponding to the 2nd, 3rd and 4th members of the Bashibulake Formation in Tarim Basin (Bosboom *et al*., 2017), are correlated with the lower Priabonian NP18 zone (~37.8 – 36.7 Ma) based on the presence of *Cribrocentrum reticulatum* and *Cribrocentrum erbae* and the absence of *Neococcolithes* (Figure 2.4 & 2.8, see supplementary materials section 1.2 for detailed calcareous nannofossil biostratigraphy in the Tarim Basin).

2.4.1.3 Foraminifera

A Paleocene to early Eocene age has been assigned to the lower member of the Qimugen Formation, based on benthic foraminiferal assemblages recorded from five samples (KS33-KS37, Kangsu section). Further considerations allow us to more precisely locate the position of the Paleocene-Eocene boundary. The stratigraphic range of *Anomalinoides rubiginosus* (KS36) extends from Campanian to latest Paleocene (P5 zone) (Van Morkhoven *et al*., 1986), thus, the level KS36 cannot be younger than latest Paleocene in age. Since *Acarinina multicamerata* is regarded as an excursion taxon in the PETM interval (Guasti & Speijer, 2008), its presence in the KS37 (E1 zone) define the position of the Paleocene-Eocene boundary between samples KS36 and KS37.

Furthermore, based on the presence of *Acarinina multicamerata* in the early Eocene E1 zone (MI-B22 and MI-B23, Mine section), the Paleocene-Eocene boundary is delineated between samples MI-B21 and MI-B22 (Guasti & Speijer, 2008) (Figure 2.4 & 2.8, see supplementary materials section 1.3 for detailed foraminifera biostratigraphy in the Tarim Basin).

2.4.2 Pollen assemblages

New palynological samples were taken from the Mine and Kangsu sections, but most contained only a few palynomorphs, precluding a quantitative analysis of the material. One productive sample (MI03, numbering 250+ grains) could be counted from the Thanetian-Ypresian lower member of the Qimugen Formation (Mine section) and contained a diverse palynoflora including abundant *Ulmipollenites*, *Inaperturopollenites*, *Graminidites*, *Sparganiaceaepollenites* and rare *Alnipollenites*, *Ephedripites*, *Podocarpidites* and *Chenopodipollis*. Other samples from the

Paleocene–Eocene contained infrequent grains of *Ephedripites*, *Steevesipollenites*, *Polypodiaceaesporites*, *Nitrariadites-Nitraripollis*, *Cicatricosisporites* and *Lophotriletes*.

Taken together with the pollen assemblages examined by Wang *et al*. (1990), late Paleocene and early Eocene continental environments associated with the Tarim Basin were semi-arid and temperate. The middle Eocene was also semi-arid but warmer, and growth of the steppe-desert biome in the late Eocene reflects intensifying aridification in continental Asia following the long-term westward retreat of the proto-Paratethys Sea (Bosboom *et al*., 2014; this paper). These data may also reflect a decrease in seasonality between wetter/cooler winters and dryer/hotter summers. The seasonal moisture influx from the nearby proto-Paratethys during the winter westerlies previously evidenced by Bougeois *et al*. (2018) is expected to decrease as the sea retreats and thereby seasonality in precipitation regime also decreases. Finally, rapid cooling at the Eocene-Oligocene Transition (EOT) is consistent across the Xining and Tarim basins, evidenced by a rapid increase in microthermal–mesothermal Pinaceae pollen (see supplementary materials section 1.4 for detailed analysis on pollen assemblages).

2.4.3 Magnetostratigraphy

2.4.3.1 Thermal demagnetization

The gypsiferous red mudstones of the upper member of the Qimugen Formation display higher initial Natural Remanent Magnetization (NRM) intensities on the order of 10^{-2} A/m. Upon thermal demagnetization, after removal of secondary normal overprint at 200-300 ºC, the trajectories of the remanent magnetization show a linear decay up to ~580 ºC interpreted as a magnetite-type behavior, and then up to ~670 ºC indicating the additional presence of hematite (Figure 2.5a). The carbonates of the Kalatar Formation are characterized by low initial NRM intensities on the order of 10^{-4} – 10^{-5} A/m. A secondary normal overprint is removed by demagnetization up to 300 ºC. This is followed by a linear decay towards the origin for the carbonates with relatively higher initial NRM (10^{-4} A/m) (Figure 2.5b). Carbonates with relatively low magnetization values (10^{-5} A/m) yielded erratic paths after 400 ºC (Figure 2.5b) such that no interpretable directions could be obtained from these samples. Initial NRM intensities of the red mudstones of the Wulagen Formation are on the order of 10^{-3} A/m. Following progressive removal of secondary normal overprints mostly between 250 and 410 ºC, gypsiferous red mudstones of the Wulagen Formation show a linear decay up to ~670 ºC (Figure 2.5c). Similarly, specimens of the red mudstone of the Bashibulake Formation and the red siltstone of the Keziluoyi Formation display higher initial intensities (on the order of 10^{-3} and 10^{-2}, respectively) and show a decay up to ~670 ºC (Figure 2.5e). They are also interpreted to represent a combination of magnetite and hematite.

2.4.3.2 Characteristic Remanent Magnetization (ChRM) directions

ChRM directions were calculated by application of principal component analysis (Kirschvink, 1980) on orthogonal demagnetization plots. The line-fits were applied on a minimum of four temperature steps. In rare cases of clustered directions with a clear normal or reverse orientation but no clear decay, line-fits were anchored to the origin. Most samples have maximum angular deviation (MAD) values of less than 10º. However, MAD values up to 30º were accepted if the polarity for the samples was evident. For a few samples with no linear decay, but a clear demagnetization path along a great circle, great circle ChRM analysis (McFadden & McElhinny, 1988) was performed. Virtual geomagnetic poles (VGPs) were calculated from the ChRM directions (Figure 2.6). The VGPs cluster into two antipodal groups: either normal or reverse. Outliers having a VGP of more than 45º from the means of these two clusters were iteratively removed and were not used for further analysis (Figure 2.6). The mean normal and reverse ChRM directions were respectively calculated from these two clusters by using Fisher statistics (Fisher, 1953).

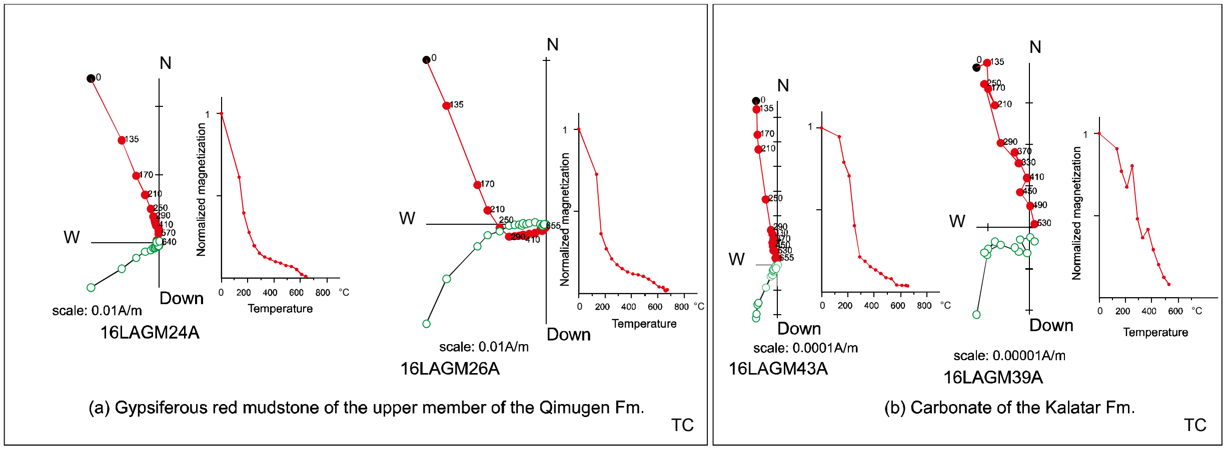

(a) Gypsiferous red mudstone of the upper member of the Qimugen Fm.

(b) Carbonate of the Kalatar Fm.

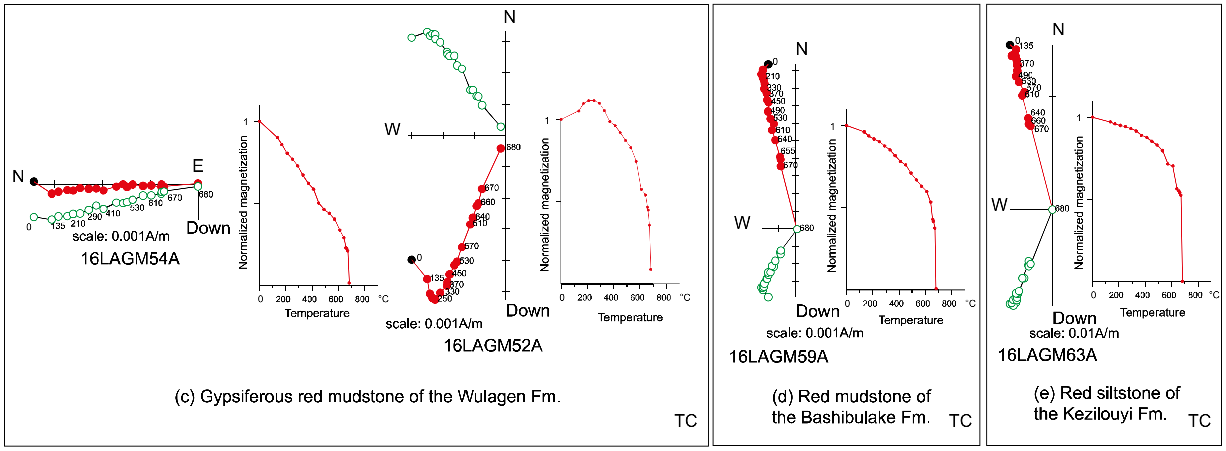

(c) Gypsiferous red mudstone of the Wulagen Fm.

(d) Red mudstone of the Bashibulake Fm.

(e) Red siltstone of the Kezilouyi Fm.

Figure 2.5 Orthogonal plots showing the thermal demagnetization behaviors and decay of intensities of representative specimens of (a) gypsiferous red mudstone of the upper member of the Qimugen Formation, (b) carbonates of the Kalatar Formation, (c) gypsiferous red mudstone of the Wulagen Formation, (d) red mudstone of the Bashibulake Formation, (e) red siltstone of the Kezilouyi Formation in tilt-corrected (TC) coordinates. Numbers next to symbols indicate temperature of demagnetization steps in ºC.

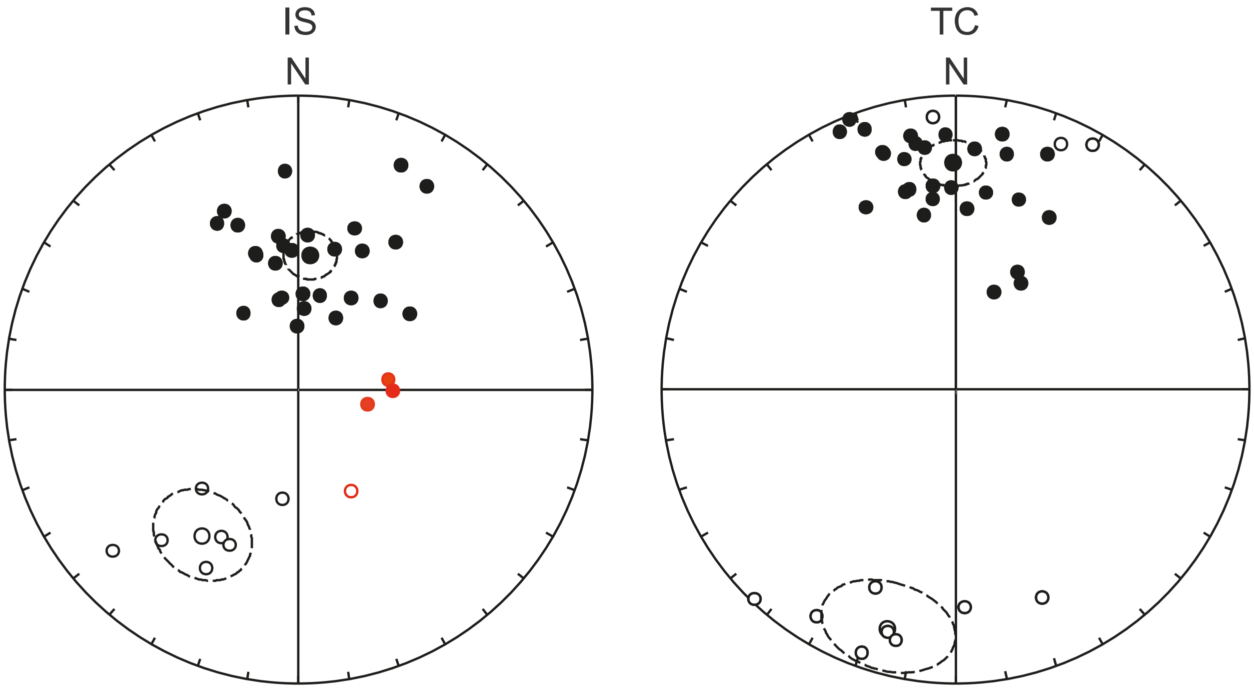

TC after 45° cut-off
N: D = 359.4°; I = 23.2; α95 = 7.6; n = 31 (31)
R : D =195.9°; I = -16.5; α95 = 15.2; n = 8 (8)

Figure 2.6 Equal-area plots of the ChRM directions indicated separately for in situ (IS) and tilt-corrected (TC) coordinates. The plot shows the least square fits and their Fisher means for normal (N) and reversed (R) polarities. ChRM directions rejected after 45º cut-off are shown in red. Solid symbols indicates downward directions, and upward directions are shown as open symbols. The dashed ellipse indicates the alpha95 confidence limit of the Fisher mean directions. D: mean declination and I: mean inclination, n: number of accepted direction, α95; angular radius of 95% confidence on mean direction.

2.4.3.3 Correlation to the Geomagnetic Polarity Time Scale (GPTS)

Magnetic polarity zones were defined by at least two consecutive VGP latitudes of the same polarity. Due to the large sampling gaps in Laghman section (because of outcrops or lithologies unsuitable for paleomagnetism), correlation of a continuously recorded polarity zonation to the geomagnetic polarity time scale (GPTS) (Ogg *et al*., 2016) is prevented. Nevertheless, the combination of available paleomagnetic polarity indications with biostratigraphic constraints from the sections (Bosboom *et al*., 2014; Wan *et al*., 2014 and this study) partially restricts possible correlations. Therefore, instead of matching a series of alternative correlations to the GPTS, we attempted to define reasonable correlations to the GTS for the Laghman section based on the biostratigraphic results (Bosboom *et al*., 2014a; Wan *et al*., 2014 and this study).

The interval including samples LM06 and LM05 in Laghman section correlates to the CP14 zone (corresponding to the NP16/NP17) based on the nannofossil assemblage (Figure 2.4). This implies that the top normal interval zone (N3) around 120 meters in the Bashibulake and Wulagen formations should correlate to C18n (which is the longest normal chron in this interval) whereas the reverse interval below (R3), containing the transitional facies, correlates unambiguously to C18r (Figure 2.4). This correlation implies that the age of the 2nd Paleogene regression is within C18r (41-40.1 Ma) similar to the Aertashi section (Bosboom *et al*., 2014a). It is known from both previous studies (Bosboom *et al*., 2014a; Wan *et al*., 2014) and this study (Figure 2.4) that the Kalatar Formation correlates to the CP13 zone (~NP15 Zone) (Lutetian) based on the macro- and microfossil assemblage. Because NP15 zone span the interval between ~46.2-42.8 Ma and C20r is the only reverse chron during this duration, the reverse interval zone (R2) around 62 meters in the Kalatar Formation should be correlated to C20r. It follows that the normal interval zone (N2) below C20r is correlated to C21n. This constrains the age of the upper member of the Qimugen to Kalatar Formation boundary to within C21n (47.3-45.7 Ma). The youngest possible age for the top of the lower member of the Qimugen Formation is constrained as ~54 Ma based on the stratigraphically highest productive sample (MI29). Therefore, the normal (N1) and reverse (R1) intervals around 30-40 meters in the upper member of the Qimugen Formation should be younger than 54 Ma. Two alternative correlations to the GPTS can be proposed for the reversal (R1) around 30 meters at the base of the upper member of the Qimugen Formation. It may either correlate to the top of chrons C23r (51.8 Ma) or the top of C24n.2r/C24n.1r (53.2 Ma).

The red clastics at the base of the Bashibulake Formation in the Mine section have yielded some interpretable directions guided by the biostratigraphic constraints (this study) (Figure 2.4). The first productive sample (B16) in the marine deposits above the red clastics is dated to C18n.2n (40.14-39.7 Ma). Given this constraint, the normal interval zone and the long reversed interval zone below should correlate to C18n.2n (40.1-39.7 Ma) and C18r (41.0-40.1 Ma), respectively (Figure 2.4). Similarly, in Shuldara section in Tajik Basin, the observed long reversed interval zone in the red clastic deposits of the Upper Tochar-Kushan-Sanglak-Hissarak formations (corresponding to the Bashibulake Formation in Tarim Basin) should correlate to the C18r (41.0-40.1 Ma) based on the sample CD10, which is constrained to C18n.2n (40.1-39.7 Ma) (Figure 2.4).

2.4.4. Sequence stratigraphy overview

Based on our sequence stratigraphic analysis, the studied interval including the three Paleogene sea incursions is divided into four depositional sequences (S) along the western Tarim Basin (Figure 2.7). Facies/microfacies analyses indicate that the transgressive intervals are represented by offshore, shoal, subtidal/bay and intertidal facies bearing distinct fossil assemblages of bivalves, foraminifera, calcareous nannofossils, dinoflagellate cysts and serpulids. The regressive intervals consist mostly of alluvial plain (fluvial and lake) and coastal plain (supratidal) facies preserving fewer (only some bivalves) or no fossils.

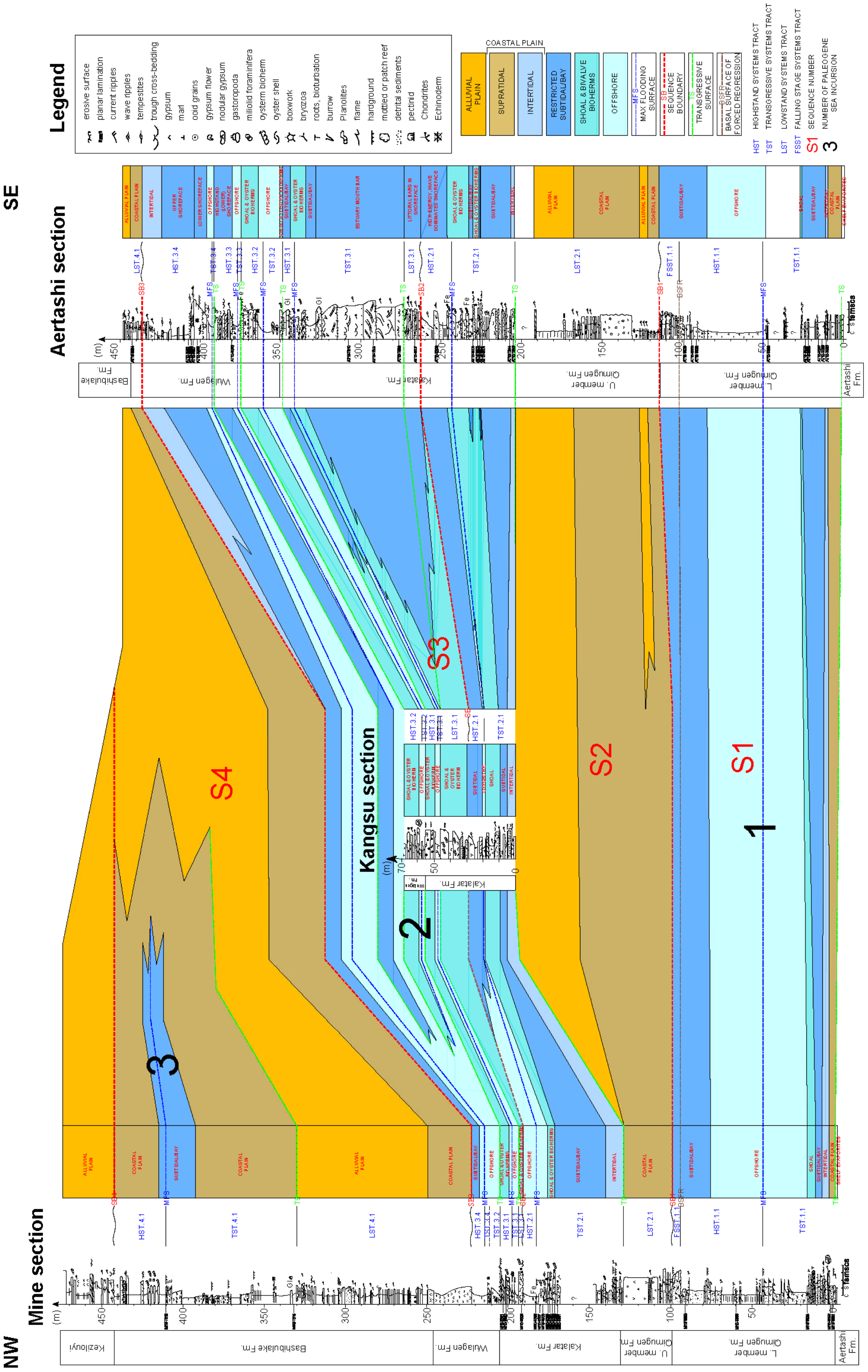NW
SE
Mine section
Kangsu section
Aertashi section
Legend
erosive surface
planar lamination
current ripples
wave ripples
tempestites
trough cross-bedding
gypsum
marl
ooid grains
gypsum flower
nodular gypsum
gastoropoda
miliolid foraminifera
oysterm bioherm
oyster shell
boxwork
bryozoa
roots, bioturbation
burrow
Planolites
flame
hardground
mottled or patch reef
detrital sediments
pectinid
Chondrites
Echinoderm
COASTAL PLAIN
ALLUVIAL PLAIN
SUPRATIDAL
INTERTIDAL
RESTRICTED SUBTIDAL/BAY
SHOAL & BIVALVE BIOHERMS
OFFSHORE
MFS MAX FLOODING SURFACE
SB SEQUENCE BOUNDARY
TS TRANSGRESSIVE SURFACE
BSFR BASAL SURFACE OF FORCED REGRESSION
HST HIGHSTAND SYSTEMS TRACT
TST TRANSGRESSIVE SYSTEMS TRACT
LST LOWSTAND SYSTEMS TRACT
FSST FALLING STAGE SYSTEMS TRACT
S1 SEQUENCE NUMBER
3 NUMBER OF PALEOGENE SEA INCURSION
S1
S2
S3
S4
1
2
3
Kezilouyi
Bashibulake Fm.
Wulagen Fm.
Kalatar Fm.
U. member Qimugen Fm.
L. member Qimugen Fm.
Aertashi Fm.
(m)
450
400
350
300
250
200
150
100
50
0
70
HST 4.1
TST 4.1
LST 4.1
HST 3.4
TST 3.4
HST 3.3
TST 3.3
HST 3.2
TST 3.2
HST 3.1
TST 3.1
LST 3.1
HST 2.1
TST 2.1
LST 2.1
FSST 1.1
HST 1.1
TST 1.1
SB1
SB2
SB3
SB4
MFS
TS
BSFR
Triassic
ESTUARY MOUTH BAR
UPPER SHOREFACE
LOWER SHOREFACE
HIGH ENERGY WAVE DOMINATED SHOREFACE
SHOAL
SUBTIDAL/BAY
SHOAL & OYSTER BIOHERMS

Figure 2.7 Stratigraphic logs of the Mine, Kangsu and Aertashi sections showing sequence stratigraphic interpretations and correlations. Correlation of the identified key bounding surfaces (i.e. SBs, MFs, TSs, BSFR) between the Mine, Kangsu and Aertashi sections enabled us to propose a regional stratigraphic architecture for the Tarim Basin. Four types of systems tracts have been interpreted; LST, TST, HST and FSST (see legend of the figure and section 4 of the supplementary materials for the details).

After the deposition of the Aertashi Formation in a restricted environment, the first Transgressive Surface (TS) is identified at the base of the first Transgressive Systems Tract (TST.1.1, Figure 2.7) represented by the boundary between the Aertashi and Qimugen formations. This is at odds with Zhang *et al.* (2018) interpreting the start of the first transgression at the base of the Aertashi Formation despite the absence of solid evidence for a transgressive event. The first sequence (S1) starts with a Lowstand Systems Tract below, within the Aertashi Formation (Figure 2.7). Therefore, we rather interpret the deposition of the Aertashi Formation as part of regressive phase, which had already started during the deposition of the underlying regressive Tuyiluoke Formation. The regression at the top of the lower member of the Qimugen Formation is interpreted as a forced regression displaying a typical shoreline regression driven by a net base level fall (relative sea-level lowering) represented by the progradational strata in a Falling Stage Systems Tract (FSST.1.1, Figure 2.7).

The next sequence (S2) starts with the transitional to continental deposits of the upper member of the Qimugen Formation marked by a Lowstand Systems Tract (LST.2.1) representing the 1st Paleogene regression. The next transgression starts with a transgressive surface represented by the boundary between the Qimugen and Kalatar formations and followed by the building up of a carbonate ramp system starting with TST.2.1 (Figure 2.7). It is followed in the Kalatar Formation by a Highstand Systems Tract (HST.2.1) at the top of S2 which is interpreted as a normal regression displaying typical shoreline regression driven by sediment supply during the late stage of a base level rise.

The next sequence (S3) is represented in the upper part of the Kalatar and most of the Wulagen formations. The sedimentary architecture of S3 expresses localized drowning of the carbonate ramp system previously developed during the end of S2 in the lower part of the Kalatar Formation. There are clear differences in the expression of S3 between the northwestern and southwestern Tarim Basin. In the north, S3 develops exclusively as a well-developed carbonate ramp system along the southern Tian Shan where the Mine and Kangsu sections are located. In contrast, S3 is more clastic-dominated in southwestern Tarim with higher accumulation after SB2, as observed in the Aertashi section (Figure 2.7) along the eastern Pamir during deposition of the Kalatar Formation as also documented in Yang *et al.* (2014). This suggests a more proximal position of the south Tarim Aertashi section on the ramp system recording the increase in siliciclastic deposition after SB2. In addition, fluctuations between TST.3.2 and TST.3.4 observed in the Aertashi section to the south are not recorded in the Mine section to the north where offshore deposition continued. Together this can be explained by a more distal (outer) position on a ramp for the northern Mine and Kangsu sections compared to the southern Aertashi section during these systems tracts. In S3, the next Highstand Systems Tract.3.2 (HST.3.2), recognized in the Kangsu and Aertashi sections, and HST.3.3, recognized in the Aertashi section, are interpreted as ‘internal’ Highstand Systems Tract (Catuneanu, 2006), where carbonate production is in balance with slow continuous sea level rise (Figure 2.7). In contrast, at the top of S3, represented by the top of the Wulagen Formation, HST.3.4, recognized both in the north Tarim Mine and south Tarim Aertashi sections, is interpreted distinctly as the ‘final’ highstand systems tract (Catuneanu, 2006) marking the return to a siliciclastic-dominated system indicating a regional normal regression displaying shoreline regression driven by sediment supply during the late stage of a base-level rise.

S4 is observed only in the north Tarim Mine section where it includes the deposits of the 3rd Paleogene sea incursion that are mostly continental and transitional with relatively thinner marine deposits only observed near the maximum flooding surface (MFS) (Figure 2.7). This implies a less extensive sea incursion only affecting the outer part of the shelf located in north Tarim.

2.4.5 Age control overview

Aertashi Formation: ~63-59 Ma restriction event

Our biostratigraphic results clearly indicate a Danian (NP4 zone ~63.2-61.5 Ma based on the nannofossil assemblage) age for the Aertashi Formation. A Danian age is in agreement with most previous studies (Chinese Bureau of Stratigraphy, 1981; Hao *et al*., 1982; Tang *et al*., 1989; Jia *et al*., 2004; Wan et al., 2014). In particular, it refines the previous early to middle Paleocene age assignment of Mao & Norris (1988) and Wang *et al*. (1990) based on dinoflagellate cysts and pollen grains. Yet, the age extent of the Aertashi Formation depends on the age assignment of the underlying Tuyiluoke and overlying Qimugen formations.

A Danian age has been generally assigned to the Tuyiluoke Formation, based on the presence of foraminiferal assemblages including genera of *Nonion*, *Cibicides*, *Cibicidoides*, *Quinqueloculina* (Guo, 1990; Hao & Guo, 1990 and Hao *et al*., 2001). Yet, the presence of these genera in the Cretaceous did not enable to restrict the Tuyiluoke Formation to the Danian. However, a Danian age may be confirmed by reports of the Cretaceous-Paleogene (K/Pg; 66 Ma) boundary, 1.4 m stratigraphically above the base of the Tuyiluoke Formation in Aertashi (“Altax”) section based on the alleged presence of an iridium anomaly and the associated trace element, rare earth element anomalies and anomalous change of carbon and oxygen isotopes (Guo, 1990; Ye *et al*., 1992; Tang *et al*, 1992). Together this suggests a Danian age for the Tuyiluoke Formation and therefore that the base of the Aertashi Formation is within the Danian.

Above the Aertashi Formation, the age of the base of the lower member of the Qimugen Formation is well constrained with an oldest possible age of ~59 Ma by our biostratigraphic assemblages which is corroborated by recent zircon U-Pb dating of a tuff (Zhang *et al*., 2018) (see next section). However, we cannot exclude the Aertashi Formation extends into the Selandian (61.6-59.2 Ma). Based on these constraints, we can estimate the age of the Aertashi Formation, representing a major regional restriction event (see discussion below), as Danian (~63.2-61.5 Ma), possibly extending up into the Selandian (61.6-59.2 Ma) (Figure 2.8).

Qimugen Formation: ~59-52 Ma first Paleogene sea incursion

As previoulsy mentioned, our age determination for the base of the lower member of the Qimugen Formation (oldest possible age of ~59 Ma) is also supported by the age constraint based on zircon U-Pb dating of a tuff reported by Zhang *et al.* (2018). They reported the weighted mean U/Pb age of 57.58 ± 0.49 Ma (1σ, n=30) yielded from zircon crystals in the tuff layer occurring 19 m above the base of the Qimugen Formation. Therefore, the boundary between the Aertashi and Qimugen formations can be further constrained to within 59 Ma and 57.5±0.5 Ma providing an age for the 1st transgression at ~59-57 Ma. These assignments update the age of the lower member of the Qimugen Formation as Thanetian-Ypresian which was reported previously as Selandian-Thanetian (Wan *et al.*, 2014) and Thanetian (Zhang *et al.*, 2018) (Figure 2.8). The age of the 1st regression represented by the boundary between the lower and upper members of the Qimugen Formations is here determined as ~53-52 Ma (C23r-C24n.1r).

Kalatar and Wulagen formations: ~47-41 Ma second Paleogene sea incursion

The age of the boundary between the upper member of the Qimugen and Kalatar formations (corresponding to the onset of the 2nd Paleogene marine transgression in the Western Tarim basin) is determined as ~46-47 Ma (within C21n). This constrains the base of the Kalatar Formation to the early Lutetian which is in agreement with the previously suggested age of Wan *et al.* (2014) but at odds with the previously attributed late Ypresian age by Zhang *et al.* (2018) (Figure 2.8). The top of the Wulagen Formation, recording the regression related to the 2nd Paleogene sea incursion, is dated here more precisely at ~41-40 Ma (within C18r) in both Tarim and Tajik basins confirming previous ages by Bosboom *et al.* (2014a; 2014b; 2017).

Bashibulake Formation: ~39.7-36.7 Ma third Paleogene sea incursion

The youngest age for the onset of the 3rd Paleogene sea transgression is determined as ~ 39.7 Ma (within C18n.2n) in the Tajik and Tarim basins based on our biostratigraphic and magnetostratigraphic results. Together with its regression the last sea incursion in the Tarim and Tajik basins is tightly bracketed within 39.7-36.7. This new age constraint updates the previous age estimate of Bosboom *et al* (2014b) where the incursion was dated to within near top C17n.2n to base C16n.2n (38.0 to 36.5 Ma).

In summary, these new age constraints and ages reported by Bosboom *et al.* (2014a; 2014b; 2017) now provide a solid Paleogene chronostratigraphic framework for the proto-Paratethys sea incursions in Central Asia and supersede the previous lower resolution (Wan *et al.*, 2014; Wang *et al.*, 2014; Zhang *et al.*, 2018) and contradictive works (Sun & Jiang, 2013; Sun *et al.*, 2016).

MAIN FOSSIL ASSEMBLAGES / MARKER SPECIES AND GENERA

	TAJIK BASIN	TARIM BASIN	Age	Mao & Norris (1988)	Zhong (1992)	Lan (1997)	Bosboom et al. (2014a)	Bosboom et al. (2014b)	Bosboom et al. (2015) (Tajik Basin)	This study (Tarim Basin)	This study (Tajik Basin)
PALEOGENE FORMATIONS	Hissarak	Bashibulake (5th member)									
	Sanglak Kushan	Bashibulake (2nd, 3rd and 4th members)	Bartonian-Priabonian (~39.7-36.7 Ma)	*Deflandrea intrasphaerula* zone ⚲	*Isthmolithus recurvus-Chiasmolithus oamaruensis* zone ☆	*Ferganea sewerzowii-Cubitostrea-Donax* (4th member) *Ferganea-Lithophaga* (3rd member) *Platygena-Pholadomya* (2nd member) 🐚		*Cribrocentrum reticulatum* ☆ ⚲ *Cordosphaeridium funiculatum* *Lentinia serrata* *Charlesdowniea coleothrypta* subsp. *rotundata* sensu De Coninck (1986) *Glaphyrocysta microfenestrata* *Thalassiphora reticulata* 🐚 *Platygena asiatica* *Ferganea bashibulakeensis* *Cubitostrea tianschanensis*		*Dracodinium rhomboideum* ⚲	*Cribrocentrum reticulatum* *Cribrocentrum erbae* ☆ *Dracodinium rhomboideum* *Thalassiphora fenestrata* *Rhombodinium draco* *Cordosphaeridium funiculatum* *Lentinia serrata* *Thalassiphora fenestrata* ⚲
	U. member Tochar	Bashibulake (1st member)									
	U. member Jukar Beshkent L. member Tochar	Kalatar & Wulagen	Lutetian-Lowermost Bartonian (~47-41 Ma)	*Turbiosphaera filosa* zone (Wulagen Fm.) ⚲	*Reticulofenestra umbilica-Chiasmolithus solitus* zone (Wulagen Fm.) ☆	*Sokolowia buhsii-Kokanostrea kokanensis-Chlamys radiatus* (Wulagen Fm.) *Ostrea (Turkostrea) strictiplicata -Ostrea (Turkostrea) cizancourti* (Kalatar Fm.) 🐚	*Lanternithus arcanus* *Reticulofenestra umbilicus* *Ericsonia formosa* ☆ *Melitasphaeridium pseudorecurvatum*, *Rhombodinium draco* *Areosphaeridium diktyoplokum* *Cordosphaeridium funiculatum* ⚲	*Lanternithus arcanus* ☆ *Rhombodinium draco* ⚲ *Ostrea (Turkostrea) cizancourti* *Ostrea (Turkostrea) striplicata* *Sokolowia-Kokanostrea* assemblage 🐚	🐚 *Ostrea (Turkostrea) afganica* *Ostrea (Turkostrea) strictiplicata* (U. Jukar Fm.)	*Reticulofenestra umbilicus*, *Neococcolithes* spp. ☆	*Coccolithus pelagicus*, *Sphenolithus moriformis*, *Discoaster saipanensis*, *Discoaster septemradiatus*, *Chiasmolithus solitus*, *Chiasmolithus modestus*, *Lanternithus* sp., *Lanternithus arcanus*, *Reticulofenestra umbilicus*, *Cribrocentrum reticulatum*, *Neococcolithes* spp., *Dictyococcites bisectus* ☆ *Adnatosphaeridium vittatum*, *Heteraulacacysta porosa* ⚲
	M. member Jukar	Upper member Qimugen	Ypresian (~52-47 Ma)			*Corbula-Solecurtus-Tellina* *Flemingostrea-Panopea* 🐚					
	Tabakch-Arukfan -Karatag-Givar -L. member Jukar	Lower member Qimugen	Thanetian - Ypresian (~59-52 Ma)	*Phelodinium aniosos* zone ⚲	*Discoaster multiradiatus* *Heliolithus riedelii* ☆ *Heliolithus kleinpellii*	*Ostrea bellovacina - Panopoea corrugata* 🐚 *Pycnodonte (Pycnodonte) camelus-Eomeretrix suzakiensis*			🐚 *Flemingostrea ? hemiglobosa* (Givar Fm.)	*Deflandrea oebisfeldensis*, *Apectodinium* spp., *Wilsonidium pechoricum*, *Alisocysta circumtabulata*, *Melitasphaeridium pseudorecurvatum* and *Deflandrea denticulata*, *Samlandia* spp. ⚲ *Discoaster multiradiatus*, *Fasciculithus tympaniformis*, *Tribrachiatus* cf. *bramlettei*, *Neococcolithes junctus*, *Coccolithus bownii*, *Rhomboaster* spp., *Discoaster araneus*, *Coccolithus pelagicus*, *Toweius* spp. ☆ *Anomalinoides rubiginosus* *Acarina multicamerata* 🌀	
	Akdjar	Aertashi	Danian - Selandian (~63-59 Ma)	⚲ *Cyclonephelium brevispinatum* *Palaeoperidinium* sp. *Leiosphaeridia hyalina*		*Brachidontes-Corbula* 🐚				*Chiasmolithus danicus* *Cruciplacolithus tenius* *Fasciculithus* spp. *Fasciculithus magnicordis* ☆	

Calcareous nanofossils	Dinoflagellates	Bivalves	Foraminifera
☆	⚲	🐚	🌀

Figure 2.8 Depositional ages for the Paleogene formations in the Tarim and Tajik basins based on the fossil assemblage and marker fossil.

2.5. Discussion

2.5.1 Driving mechanisms and Paleogeography

Different driving mechanisms causing the relative sea level fluctuations of the Proto-Paratethys were proposed in previous studies. These include tectonism and associated basin overfilling usually related to the India-Asia collision (Burtman & Molnar, 1993; Burtman, 2000), eustatic sea level changes (Dupont-Nivet *et al*., 2007; Sobel & Dumitru, 1997) and the combined effects of both tectonism and eustasy (Bosboom *et al*., 2011; 2014a; 2017; Zhang *et al*., 2018). However, age control was so far insufficiently resolved to provide unequivocal determination of the controlling factors especially on the 1st and 2nd Paleogene sea incursions.

To elucidate these potential driving mechanisms, we used the refined age constraints and paleoenvironmental interpretations to construct a relative sea level curve and subsidence curves based on the Mine and Aertashi sections (Figure 2.9 and S 2.5). The relative sea level curve was generated by assigning paleo-water depths to the defined facies/microfacies based on their relative positions to the Fair Weather Wave Base (FWWB) and Storm Wave Base (SWB) (Figure 2.9 and Figure 2.3c). The depth of FWWB was assumed as between 10 and 15 m and SWB as 30 m (Burchette & Wright, 1992; Flügel, 2004). It should be noted that assigned paleo-water depth values for the facies/microfacies may not be accurate, however, their relative positions to each other, FWWB and SWB provide insight regarding the relative sea level change during the Paleogene sea incursions in the Tarim Basin. The changes in paleo-water depths were used along with the subsidence curves to derive implication on potential driving mechanisms such as eustatic/tectonic events and related sediment supply.

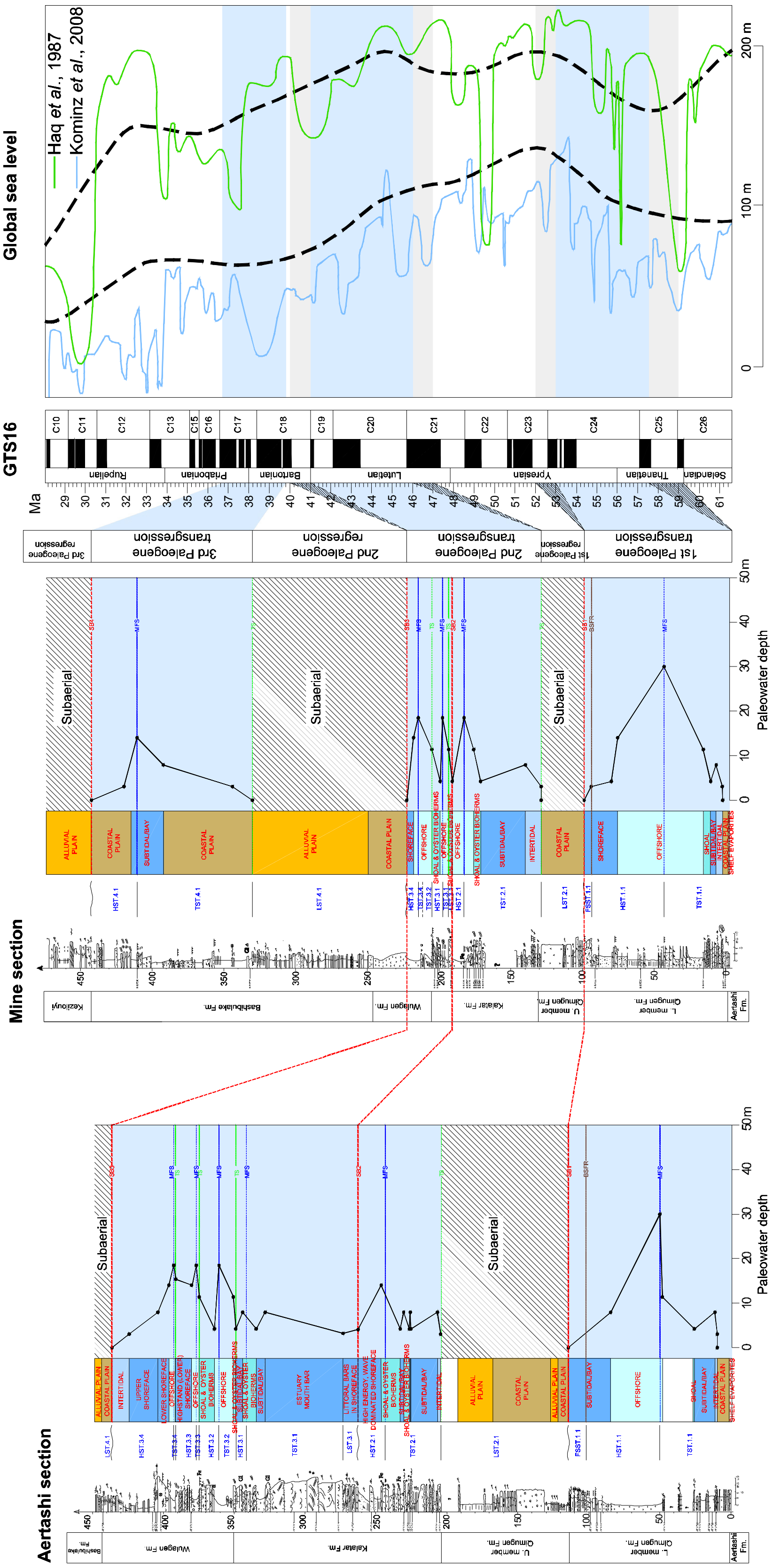
Aertashi section
Mine section
GTS16
Global sea level
Haq et al., 1987
Kominz et al., 2008
Paleowater depth
Subaerial
Ma
1st Paleogene transgression
1st Paleogene regression
2nd Paleogene transgression
2nd Paleogene regression
3rd Paleogene transgression
3rd Paleogene regression
Aertashi Fm.
L. member Qimugen Fm.
U. member Qimugen Fm.
Kalatar Fm.
Wulagen Fm.
Bashibulake Fm.
Keziluoyi
Selandian
Thanetian
Ypresian
Lutetian
Bartonian
Priabonian
Rupelian
0
100 m
200 m
50 m

Figure 2.9 Paleo-water depths & inferred relative sea level curves for the Aertashi and Mine sections compared to the global sea level curve of Kominz et al. (2008) and Haq et al. (1987). The blue shaded areas highlight the sea incursions, which have been accurately dated in this study. Gray shaded parts indicate possible age interval for the onsets of transgressions and regressions.

To estimate the Paleogene paleogeographic evolution of the proto-Paratethys Sea, the refined age constraints and detailed paleoenvironmental interpretations are combined with successive paleogeographic maps based on an extensive review (Figure 2.12). Regional coastlines and depositional environments during the maximum Paleogene sea advances and retreats were drawn based on the results of this study and integrated with existing literature. The updated paleo-reconstructions of Poblete *et al.* (2017) integrating continental reference points, paleotopography and shorelines were updated with data from the Darius project (Barrier *et al.*, 2018), Peri-Tethys atlas (Dercourt et al., 2000), the compilation of Bosboom *et al.* (2017) and paleogeographical changes in the Turgai Strait and West Siberian Sea were drawn based on Radionova *et al.* (2003), Akhmetiev & Beniamovski (2009), Akhmetiev *et al.* (2010; 2012).

Regional restriction event (~63 to 59 Ma)

Both in the Tarim and Tajik basins, the interval between ~63 Ma and ~59 Ma is represented by a major regional restriction event marked by evaporitic deposition in the exceptionally thick Aertashi Formation in the SW Tarim Basin and the equivalent thinner correlative Akdjar Formation in the Tajik Basin. This regional restriction event is interpreted to result from a hydrographic isolation from the open sea by an exposed barrier composed of shoals and (rudist) build-ups due to a relative sea level fall at the end of Cretaceous (Figure 2.3d). There are several lines of evidence to support this inference. (1) The long-term elevated sea levels of Cretaceous greenhouse times would have enabled continuous platform-edge rudist build-ups and shoals to form and grow as platform-edge barriers. (2) The occurrences of rudist bioherms have been reported both in Tajik and Tarim basins and even further west in Uzbekistan (Scott *et al.*, 2010). (3) With the subsequent sea level fall, well-established at the end of Cretaceous period, these barriers most likely would have been subaerially exposed, hydrographically isolating the back-barrier part of the platform/shelf with limited marine seepage supplying water for the deposition of the evaporites (Warren 2010). (4) The presence of a widespread uppermost Cretaceous unconformity evidencing subaerial exposure within the western Tajik Basin was reported by Sobel (1995 and references therein). (5) Similar formation of platform evaporites is common, reported from the Middle East (Jurassic Hith Anhydrite), Saudi Arabia, Qatar and the Emirates (Permian Khuff Anhydrite), Gulf of Mexico (Cretaceous Ferry Lake Anhydrite), West Texas and New Mexico (Permian San Andres Fm. and equivalents) and Australia (Cambrian Red Heart Dolomite and equivalents) (Warren, 2010 and references therein). A similar model for the isolation of the Tarim basin during the deposition of the Aertashi evaporites has been proposed by Zhang *et al.* (2018), yet driven by a tectonic barrier related to far-field effects at the onset of the India-Asia collision. However, the onset of the deposition of the Aertashi evaporites is now constrained to NP4 zone ~63.2-61.5 Ma (see previous section) which predates even the oldest estimates for the India-Asia collision onset such as 59 ± 1 Ma by Hu et al. (2016). In addition, the presence of thick gypsum deposition (Akdjar Formation) west of Pamir in the Tajik Basin, makes the tectonic barrier hypothesis unlikely. The tectonic hypothesis was supported by the presence of conglomerates found locally at the base of the Aertashi Formation in the Wuyitake section (Sobel 1995; Bershaw *et al*., 2012) and in the Akqiy section of Tarim Basin (Zhang *et al*., 2018). However, these conglomerates (<100 meter-thick) can equally relate to channel extension during the sea-level fall with the braid-plain extending seaward resulting in more extensive fluvial deposition (Blum & Törnqvist, 2000).

1st sea incursion (~59 Ma to 53-52 Ma)

This represents the largest Paleogene sea incursion with a maximum water depth based on our relative sea-level curve represented by the offshore facies and microfacies of the lower member of the Qimugen Formation (Figure 2.9). Consistently, the maximum eastward extent of the Proto-Paratethys sea was also reached during this 1st Paleogene sea incursion (e.g. Burtman, 2000) (Figure 2.12). During subsequent sea incursions, the extent and paleo-water depths were progressively smaller until the ~37 Ma sea retreat out of the Tarim and Tajik basins (Bosboom *et al*., 2014b).

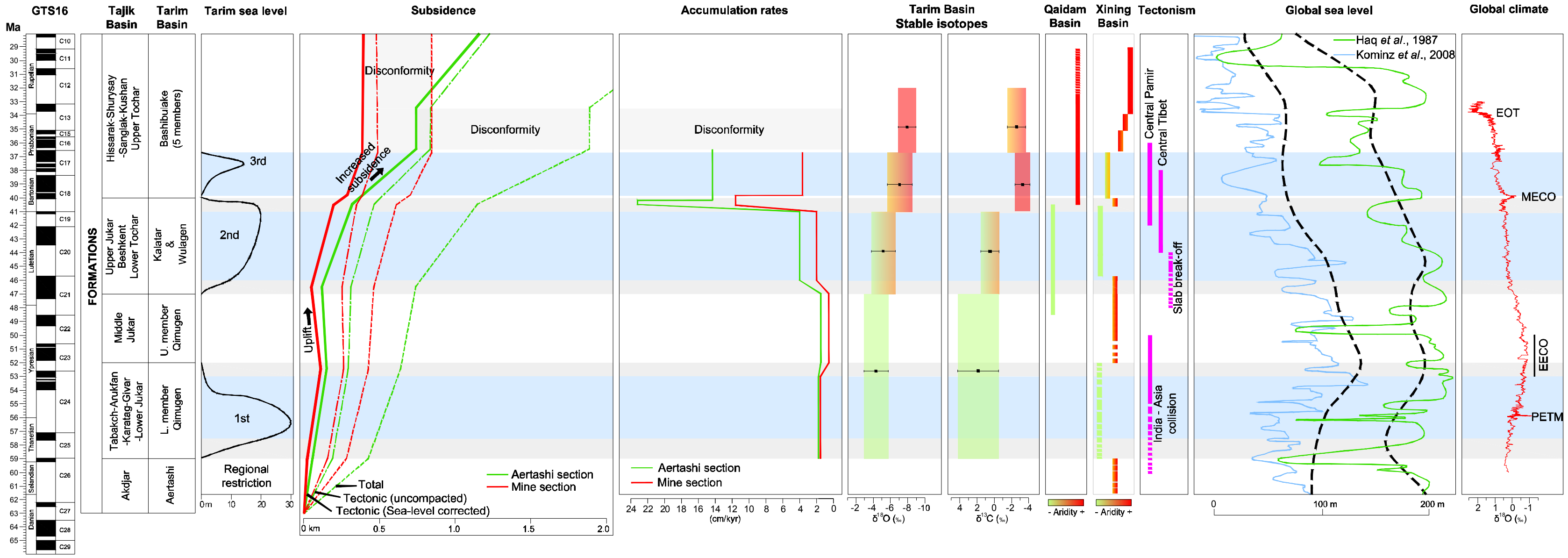
Ma
GTS16
29
30
31
32
33
34
35
36
37
38
39
40
41
42
43
44
45
46
47
48
49
50
51
52
53
54
55
56
57
58
59
60
61
62
63
64
65
Rupelian
Priabonian
Bartonian
Lutetian
Ypresian
Thanetian
Selandian
Danian
C10
C11
C12
C13
C15
C16
C17
C18
C19
C20
C21
C22
C23
C24
C25
C26
C27
C28
C29
FORMATIONS
Tajik Basin
Tarim Basin
Hissarak-Shurysay -Sanglak-Kushan Upper Tochar
Bashibuake (5 members)
Upper Jukar Beshkent Lower Tochar
Kalatar & Wulagen
Middle Jukar
U. member Qimugen
Tabakch-Arukfan -Karatag-Givar -Lower Jukar
L. member Qimugen
Akdjar
Aertashi
Tarim sea level
3rd
2nd
1st
Regional restriction
0m
10
20
30
Subsidence
Disconformity
Disconformity
Increased subsidence
Uplift
Total
Tectonic (uncompacted)
Tectonic (Sea-level corrected)
Aertashi section
Mine section
0 km
0.5
1.0
1.5
2.0
Accumulation rates
Disconformity
Aertashi section
Mine section
24
22
20
18
16
14
12
10
8
6
4
2
0
(cm/kyr)
Tarim Basin Stable isotopes
-2
-4
-6
-8
-10
δ18O (‰)
4
2
0
-2
-4
δ13C (‰)
Qaidam Basin
- Aridity +
Xining Basin
- Aridity +
Tectonism
Central Pamir
Central Tibet
Slab break-off
India - Asia collision
Global sea level
Haq et al., 1987
Kominz et al., 2008
0
100 m
200 m
Global climate
EOT
MECO
EECO
PETM
2
1
0
-1
δ18O (‰)

Figure 2.10 Simplified regional lithostratigraphic framework of the Paleogene sea incursions in the Tarim and Tajik basins, compared temporally with the regional tectonic events and related magmatism (Chapman et al., 2018 and references therein; slab break-off data from Negredo et al., 2007), paleoenvironmental changes recorded in the Qaidam (Song et al., 2013; Ye et al., 2016; Bao et al., 2017) and Xining (Abels et al., 2011; Hoorn et al., 2012; Meijer et al., 2018) basins, global sea level curve (Kominz et al., 2018 and Haq et al., 1987) and global climate events (benthic $\delta^{18}O$ record of Cramer et al., 2009). The approximate relative changes in sea level in the Tarim Basin are shown by thick solid lines. The blue shaded areas highlight the sea incursions, which have been accurately dated in this study. Gray shaded parts indicate possible age interval for the onsets of transgressions and regressions. The subsidence curves for the Mine and Aertashi sections were produced by performing backstripping analysis using BasinVis 1.0 (Lee et al., 2016). Stable isotopic composition data for the Tarim Basin is from Bougeois et al. (2018).

The 1st Paleogene sea incursion at ~59 Ma appears coeval with the Thanetian transgression in the northern Peri-Tethys sedimentary provinces (Radionova *et al.*, 2003) (Figure 2.12) and the onset of a long-term global sea level high (black dashed lines in Figure 2.9) suggesting eustatic forcing of the 1st sea incursion. Subsequent Thanetian-Ypresian short-term global sea level fluctuations (blue curve on Figure 2.9) (Kominz *et al.*, 2008) and the Ypresian fluctuations in the West Siberian Sea (Radionova *et al.*, 2003) have not (yet) been identified in the Tarim Basin. The following ~53 - 52 Ma regression fits with the Siberian Sea retreat but does not match the long-term global sea level reconstructions indicating a maximum sea level high (black dashed lines in Figure 2.9). We therefore speculate tectonic effects were likely more important driver for this retreat in the Tarim which is further corroborated by coeval uplift observed in subsidence curves (Figure 2.10). Unfortunately, major tectonic activity in this particular area and time period remains insufficiently constrained to couple specific tectonic activity to this regression. The timing of the regression may have roughly coincided with the initial early Eocene Indo-Asia collision and it has been previously speculated that its far-field deformation may have propagated to the northern part of the proto-Tibetan plateau at this time (Jolivet *et al.*, 2001; 2013 Dayem *et al.*, 2009; Clark *et al.*, 2010; Jin *et al.*, 2018) despite the ca. 3000 km of separation (Dupont-Nivet et al., 2010). We conclude that this relatively small regression might have been tectonically driven but does not represent a major tectonic event in the area based on the small decrease in associated subsidence.

2nd sea incursion (~47-46 Ma to ~41-40 Ma)

The 2nd Paleogene sea incursion in the Tarim Basin appears also coeval with the fluctuations in the Siberian Sea where a transgression during the Lutetian (starting at ~47 Ma) is reported by Radionova *et al.* (2003) (Figure 2.12). During this interval, an increase is indicated in the global sea level reconstruction curve of Haq *et al.* (1987). Together, these suggest an eustatic control on the long-term trend of the 2nd Paleogene sea incursion in the Tarim Basin and West Siberian Sea.

For the following regression, the subsidence curves indicate an increase in tectonic subsidence at the initial deposition of the Kalatar Formation after a brief uplift event starting with the upper member of the Qimugen Formation deposition, discussed above (Figure 2.10). The regression seems at odds with increased subsidence. However, the regressive interval also corresponds to a prominent increase in accumulation rates between 41 and 40 Ma suggesting a normal regression driven by excess sediment supply (Figure 2.10, 2.11b). A net sea-level fall during this interval, also recorded in the West Siberian Sea and long-term eustatic curve (Figure 2.10 and 2.12), must have also induced an additional but less prominent component of forced regression. We therefore interpret the 2nd Paleogene regression to have been controlled by a combination of normal regression driven by excess sediment supply related to tectonism and a forced regression related to a net eustatic sea-level fall during this interval. In detail, we identify here that the onset of the increasing tectonic subsidence corresponds to sequence boundary 2 (SB2) in the marine deposits of the Kalatar Formation considering the increase in depositional thicknesses and accumulation rates thereafter (Figure 2.9 and S 2.5). Based on the presented age constraints on SB2, the onset of this increase in tectonic subsidence occurred within ~47 and ~41 Ma (Figure 2.9, 2.11a). The strong increase in tectonic subsidence is associated with a short interval of very fast accumulation rates of continental clastic sediment from ~41 to ~40 Ma. This ~41-40 Ma event is interpreted to relate to fast infilling of the previously under-filled marine basin. It is followed by more steady deposition in a continental foreland basin setting increasing up to the Miocene (Blayney *et al*., in revision) (Figure 2.11b). This marked tectonic phase coincides with the onset of regional deformation reported at similar ages further south in the Kunlun and Qiangtang as well as Northern and Central Pamir terranes (e.g. Wang *et al*., 2008; Amindon and Hynek, 2010; Bershaw *et al*., 2012; Rutte *et al*., 2017). This regional event has been related to Pamir and Tibetan Plateau uplift, regional magmatism initiating around 44-42 Ma (Chapman *et al*., 2018 and references therein) and more generally to the effects of "hard collision" following the Neo-Tethyan slab break-off or flattening ca. 45-40 Ma (Negredo *et al*., 2007; Replumaz *et al*., 2010; DeCelles *et al*., 2011; Smit *et al*., 2014; van Hinsbergen *et al*., 2018).

3rd sea incursion (~ 39.7 to 36.7 Ma)

Our subsidence curve indicates the 3rd marine incursion occurs during increased tectonic subsidence directly after the ~41-40 Ma short infilling event described above (Figure 2.10). The 3rd incursion occurred in the Tajik Basin and the northwestern Tarim Basin from ~39.7 to 36.7 Ma but did not reach south Tarim where basin infilling was particularly strong (Figure 2.10, 2.11c). The 3rd Paleogene sea incursion does not correspond in timing with the last Siberian Sea incursion (Akhmetiev *et al*., 2010; 2012) or the early Priabonian eustatic fluctuations (Kominz *et al*., 2008; Haq *et al*., 1987; Bosboom *et al*., 2014b) (Figure 2.10). These together suggest that the 3rd Paleogene sea incursion was not primarily driven by eustasy. It is thus interpreted to relate to tectonic subsidence creating accommodation space overcoming basin infilling in the Tajik and northern Tarim basins after the initial ~41 to 40 Ma excess sediment supply (Figure 2.11c). The following ~36.7 Ma regression is not expressed in the Siberian Sea records and does not correspond to a clear eustatic drop (Figure 2.10) although it is apparently synchronous from the northern Tarim Basin to the Tajik Basin. We thus rather interpret this regression to result from the ongoing tectonism and related to increased aggradational basin infilling prograding from the southern to northern Tarim Basin and into the Tajik Basin (Figure 2.11d).

We note that after the 3rd sea regression, marine facies are not recorded in the Tajik and Tarim basins that have higher accumulation rates of continental clastics and typical features of foreland basin deposits with little expression of eustasy (Figure 2.12). However, a long disconformity well dated from ~35.6 to ~33.3 Ma in south Tarim at the Aertashi section, correlates well with the Siberian Sea regression occurring at ~34 Ma (Akhmetiev *et al.*, 2010; 2012) and has been previously interpreted to relate to the ca. 100 m sea level drop at the Eocene-Oligocene transition (Bosboom *et al.*, 2014a). This indicates that although tectonism was the major driving factor of long-term and possibly short-term fluctuations since ~41 Ma, the basins preserved an oceanic connection allowing for some eustatic influence.

(a) Onset of tectonics ~47 & 41 Ma

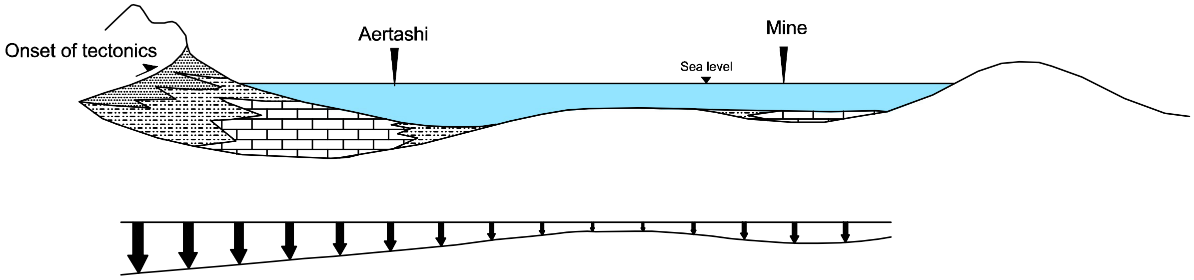

(b) 2nd regression ~41-40 Ma

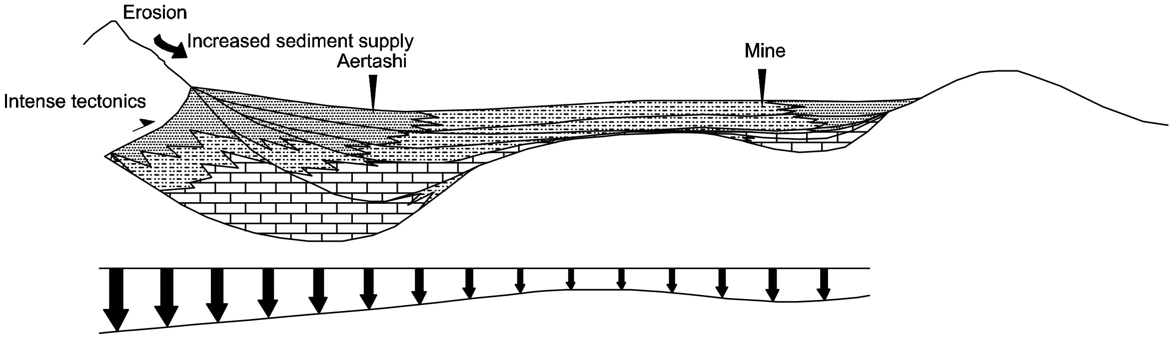

(c) 3rd transgression ~39 Ma

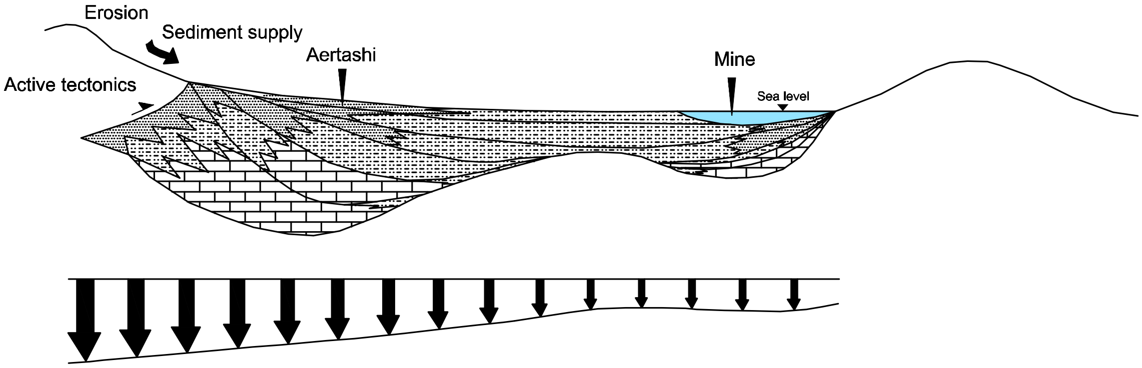

(d) 3rd regression ~37-34 Ma

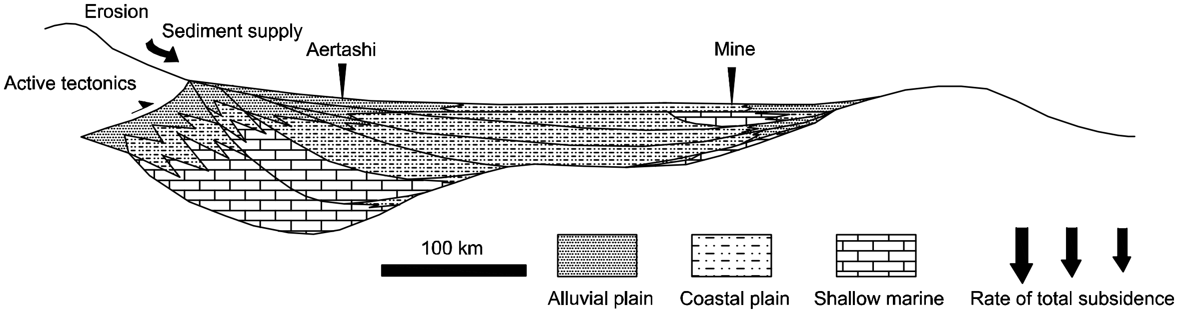

Figure 2.11 Model showing total subsidence and stratigraphic fill of the Tarim Basin associated with the tectonic activity intensifying at ~41 Ma. This model refers to the foreland model of Catuneanu (2006). (a) Onset of the tectonic activity between ~47-41 Ma. Subsidence due to mainly tectonic loading and dynamic subsidence. (b) Intensification of the tectonic activity at ~41-40 Ma and the related increase in sediment supply and aggradation outpacing accommodation and resulting in the 2nd regression throughout the basin. Subsidence due to tectonic loading, sediment loading and dynamic (c) Total subsidence outpaces the sediment infilling that has decreased in the north Tarim causing the 3rd transgression. In the south however, the infilling still outpaces accommodation, therefore no sea incursion occurs. Subsidence due to tectonic loading, sediment loading and dynamic subsidence. (d) The last regression is explained by northward propagation of aggradation outpacing subsidence.

2.5.2 Effects on regional paleoclimate

Recent studies have established that the westerlies constitute a major moisture source to Central Asia and played a significant role in the aridification of the area since the Eocene (Caves *et al.*, 2015; Bougeois *et al.*, 2014; 2018). The long-term westward retreat of the Proto-Paratethys Sea during the Paleogene (starting ~52-53 Ma and ending ~36.7 Ma) likely removed a potentially significant moisture source to Central Asia (Ramstein *et al.*, 1997; Graham *et al.*, 2005; Kent-Corson *et al.*, 2009; Zhang *et al.*, 2012; Bosboom *et al.*, 2014a; Bougeois *et al.*, 2014; 2018) and therefore could have had a profound effect on progressive aridification in Central Asia. At shorter time scales, Paleogene sea transgressions and regressions may have modulated moisture supply provided by the westerlies to Central and East Asia. To test this, we compared our results constraining the evolution of the proto-Paratethys sea to the long-term and short-term humid and arid phases existing in the paleoenvironmental records further east in the Tarim Basin (this study), Qaidam Basin (Song *et al.*, 2013; Ye *et al.*, 2016; Bao *et al.*, 2017) and the Xining Basin (Meijer *et al.*, 2018).

In the Tarim Basin, well-dated continental paleoenvironmental records from the Paleogene are rare and usually poorly constrained in age but suggest a long-term Paleogene to Neogene aridification (Wang, 1990; Wang *et al.*, 2013). The pollen assemblages reported here confirm this long-term aridification now dated from Paleocene to Eocene. Similarly, the late Paleocene to late Eocene decrease in marine $\delta^{13}C$ and $\delta^{18}O$ values is also likely related to the long-term sea retreat and increasing effects of runoff by Bougeois *et al.* (2018) (Figure 2.10). The resolution of those datasets, however, does not allow for deciphering the shorter-term effects of the sea fluctuations.

In the Qaidam Basin the timing of reported warmer and more humid climate conditions between ~48 Ma and 40 Ma (Song *et al.*, 2013; Bao *et al.*, 2017) is coeval with the 2nd Paleogene sea incursion (~47-40 Ma) in the Tarim Basin (Figure 2.10). An aridification and cooling event has been proposed at ~40 Ma (Song *et al.*, 2013; Ye *et al.*, 2016) that may be linked to the 2nd Proto-Paratethys sea regression (~41-40 Ma) and the related reduction of moisture transport from the sea eastward into Asia. Note, however, that age constraints on the Qaidam stratigraphy are controversial and may have to be radically limited to Neogene times (Wang *et al.*, 2017).

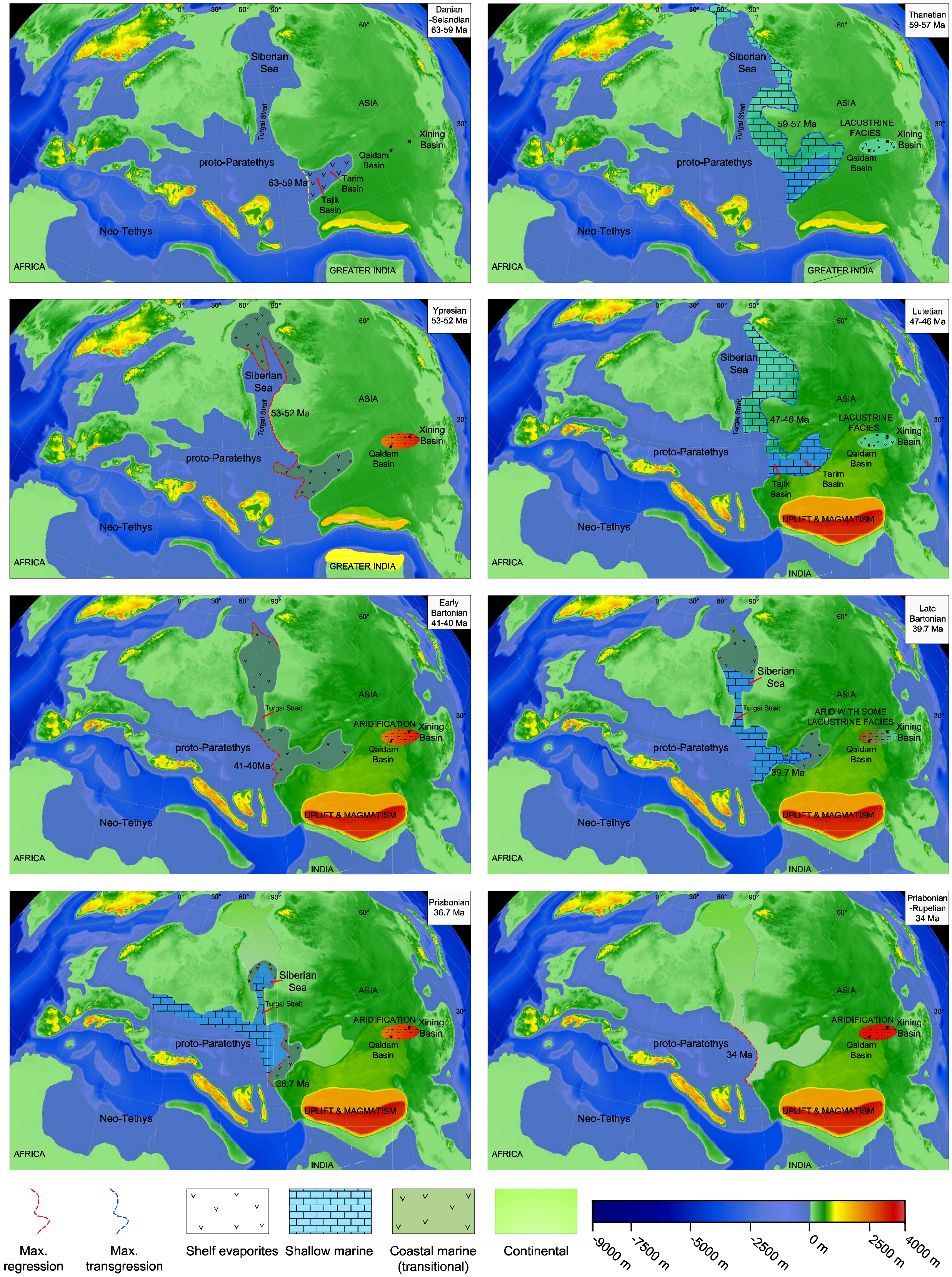Danian -Selandian 63-59 Ma
Siberian Sea
Turgai Strait
ASIA
Xining Basin
Qaidam Basin
Tarim Basin
Tajik Basin
63-59 Ma
proto-Paratethys
Neo-Tethys
AFRICA
GREATER INDIA
Thanetian 59-57 Ma
59-57 Ma
LACUSTRINE FACIES
Ypresian 53-52 Ma
53-52 Ma
Lutetian 47-46 Ma
47-46 Ma
UPLIFT & MAGMATISM
INDIA
Early Bartonian 41-40 Ma
ARIDIFICATION
41-40Ma
Late Bartonian 39.7 Ma
ARID WITH SOME LACUSTRINE FACIES
39.7 Ma
Priabonian 36.7 Ma
36.7 Ma
Priabonian -Rupelian 34 Ma
34 Ma
0°
30°
60°
90°
Max. regression
Max. transgression
Shelf evaporites
Shallow marine
Coastal marine (transitional)
Continental
-9000 m
-7500 m
-5000 m
-2500 m
0 m
2500 m
4000 m

Figure 2.12 Paleogeographic maps displaying the early Paleogene regional restriction event and sea incursions. Numerical ages in the figures show the onset of individual transgressions and regressions whereas the paleogeographies show the maximum transgressions and regressions. Coastline for the 3rd regression is based on Bosboom et al. (2017). All other coastlines during the Paleogene sea incursions were drawn based on the results of this study and Peri-Tethys atlas (Dercourt et al., 2000). Paleogeographical changes in the Turgai Strait and Siberian Sea were drawn based on Radionova et al. (2003), Akhmetiev & Beniamovski (2009), Akhmetiev et al. (2010; 2012), and our new results. Corresponding facies during the transgressions and regressions can also be seen on the paloegeographic maps. Note also that transgressions and regressions are coeval with the humid and arid phases reported from the Xining and Qaidam basins.

In the Xining Basin further east, deposition of the late Paleocene – early Eocene thick carbonaceous gypsum may coincide with the transgression of the 1st Paleogene sea incursion (~59-57 Ma) in the SW Tarim Basin (Meijer *et al*., 2018). The subsequent sudden increase in lacustrine deposits at ~45.7 Ma is closely linked with the transgression of the 2nd Paleogene sea incursion (Bosboom *et al*., 2014a; Meijer *et al*., 2018). An aridification step at ~41-40 Ma is then indicated by regional disappearance of this perennial lake system and shift to a more arid flora (Bosboom *et al*, 2014c). This has been previously linked to the regression of the 2nd Paleogene sea incursion by Bosboom *et al*. (2014a) (Figure 2.10). Finally, the last sea incursion in the Tarim Basin now dated in this study as ~39.7 – 36.7 Ma (C17n.1n) corresponds to the more gypsiferous interval before the aridification step 1 and the appearance of *Picea* associated with a drastic environmental change (Abels *et al*, 2011; Hoorn *et al*., 2012). This suggests that this interval was relatively humid due to the sea incursion and followed by aridification and possibly cooling at ~ 36.7 Ma corresponding to the *Picea* appearance in the Xining Basin (Figure 2.10).

Tectonic control on the long-term aridification of the basins north of the growing Tibetan Plateau is well established (Graham *et al*., 2005). However, shorter term changes of wet/arid depositional systems are unlikely related to the influence of local tectonics (in particular uplift) but rather represent fluctuations in atmospheric moisture (Dupont-Nivet *et al*., 2007; Abels *et al*., 2011; Meijer *et al*., 2018). Indeed, episodic local tectonic events would require associated variations in depositional environments with fluctuations in accumulation rates and coarsening trends that are not observed. In the Paleogene, the Qaidam and Xining basins record slow and constant sediment accumulation before the dominantly Neogene exhumation of local mountain ranges (Ji *et al*., 2017: Meijer *et al*., 2018). The short-term change of depositional systems representing moisture shifts in the Qaidam and Xining Basin also do not correspond with global climate events (e.g. Meijer et al., 2018). Therefore, these findings of moisture fluctuations in the Xining and Qaidam basins coeval with sea transgressions and regressions in the Tarim Basin strengthen the hypothesis that the proto-Paratethys Sea was an important mechanism influencing the westerly flux of moisture into Asia during the Paleogene.

2.6. Conclusions

Our new regional stratigraphic framework provides solid age constraints for the early Paleogene sea incursions in the SW Tarim and Tajik basins. Based on our results, a major regional restriction event represented by the thick and extensive gypsum deposits occurred between ~63 Ma and ~59-57 Ma (Danian to possibly Selandian). This was followed by the 1st transgression event around 59-57 Ma (base of Thanetian), possibly driven by eustasy, resulting in the maximum geographic extent and deepest offshore marine environment of the proto-Paratethys. The 1st Paleogene regression occurred around 53-52 Ma (Ypresian; C24n.1r-C23r) and was likely caused by far-field tectonic effects, possibly due to the coeval early Eocene Indo-Asia collision deformation. The age of the 2nd Paleogene transgression, represented by the establishment of a carbonate ramp system, is determined as ~47-46 Ma (C21n) and, similar to the first transgression, may be related to eustatic fluctuations. The subsequent regression starting at ~41 Ma and followed by a dramatic increase in tectonic subsidence can be related to regional tectonic events reported in the Pamir and Tibetan Plateau around 45-40 Ma. The last sea transgression event driven by the combined effects of increased tectonic subsidence and decreased accumulation rates occurred at ~39.7 Ma (within C18n.2n). The following westward final retreat of the proto-Paratethys Sea (at ~36.7 Ma) is thus interpreted as being caused by increased basin infilling associated with the Pamir/Tibetan tectonic activity. These interpretations for the Paleogene sea incursions support the assessment that far field tectonic effects of India-Asia collision and early Pamir/Tibetan activation intensifying at ~41 Ma forced the long-term westward retreat of the proto-Paratethys Sea by driving the Paleogene regressions. Although tectonism was the primary driver since ~41 Ma, short-term as well as long-term sea level fluctuations may have contributed as well. Palynofloral assemblages indicate semi-arid and temperate environments in the late Paleocene and early Eocene, which then warmed in the middle Eocene and became drier in the late Eocene. The transgressive/regressive intervals of the proto-Paratethys Sea in the SW Tarim Basin coincide with the less arid/more arid phases in the Qaidam and Xining basins, establishing the proto-Paratethys as a major important moisture source for the Asian interior and demonstrating its importance as a contributor to Asian aridification.

2.7. Supplementary Information

2.7.1. Biostratigraphy

2.7.1.1. Dinoflagellates

Tarim Basin

Five samples of the lower member of the Qimugen Formation from the Kangsu section were analyzed (KS33 to KS37) for the presence of biostratigraphic marker species (Figure 2.4). The samples yielded common to very abundant dinocysts, of which KS36 was the most productive. The dinocyst assemblages are similar to those recorded in the North Atlantic, Arctic and Peri-Tethys in the Paleogene, confirming these basins are in open connection to one another (Iakovleva *et al*., 2012). We thus compare our results to existing work from these basins (e.g. Heilmann-Clausen, 1985; Mudge & Bujak, 1996; Powell *et al*., 1996; Iakovleva & Heilmann-Clausen, 2010). The presence of *Deflandrea oebisfeldensis* in the lowermost sample (KS33) suggests that the analyzed interval is not older than ~59 Ma (Mudge & Bujak, 1996). The Paleocene-Eocene (P-E) boundary interval is identified in sample KS36 and KS37 based on the presence of abundant *Apectodinium* spp. and *Wilsonidium pechoricum* (Iakovleva & Heilmann-Clausen, 2007). We interpret this abundance of *Apectodinium* to represent the quasi-global acme event of the genus at the Paleocene-Eocene Thermal Maximum (PETM; 56 Ma) (e.g. (Crouch *et al*., 2001; Sluijs *et al*., 2007). Although the marker species for the PETM, *Apectodinium augustum* (Schmitz *et al*., 2004; Sluijs *et al*., 2006), is not recorded, some specimens transitional between this species and *A. hyperacanthum* are present in sample KS36.

Samples from the Mine Section (Figure 2.4) yielded abundant dinocysts, particularly in the interval from samples MI20 to MI30. The lowermost analyzed samples (MI03, MI11) contain sparse *Alisocysta circumtabulata*, *Melitasphaeridium pseudorecurvatum* and *Deflandrea denticulata*. *A. circumtabulata* in the North Sea has a last appearance in the uppermost Paleocene. *M. pseudorecurvatum* had a calibrated first appearance in the early Eocene (~55 Ma) (e.g. Williams *et al*. 2004), but this species has also been recorded in the upper Paleocene of the New Jersey shelf (Sluijs & Brinkhuis, 2009), equatorial Atlantic (Awad & Oboh-Ikuenobe, 2016) and Southeast Australia (Frieling *et al*., 2018). *Deflandrea denticulata* has a first occurrence at the base of the Thanethian (~59 Ma) in the North Sea (Powell, 1992). The assemblages here recorded are very similar to those in the North Atlantic and North Sea, and we therefore argue that these species definitively establish the presence of upper(most) Paleocene (Thanetian) sediments.

Subsequently, *Apectodinium* dominates assemblages in sample MI20, and the co-occurrence of *Wilsonidium pechoricum* suggests this interval is equivalent to the quasi-global *Apectodinium* acme that marks the PETM. As in the Kangsu section, the PETM marker species *A. augustum* is not recorded.

Sample MI33 contains a few specimens tentatively assignable to *Samlandia* spp., which has a first occurrence around 52.5 Ma in nearby Peri-Tethyan sedimentary deposits (Iakovleva &

Heilmann-Clausen, 2010). However, we record no Wetzellielloids other than *Apectodinium* or other early Eocene markers, and we find no concrete indication for sediment accumulation between the P-E boundary interval and 52.5 Ma. Furthermore, the presence of several morphotypes of *Thalassiphora* and abundant amorphous organic material, which signal restricted, anoxic, conditions (Pross, 2001), coupled with and relatively poor preservation, implies the age assignment of the topmost sample should be treated with some caution.

Upon re-examination of the samples used in Bosboom *et al*. (2014b), we found a few specimens of the C18n.2n (40.14-39.7 Ma) marker species *Dracodinium rhomboideum* (Eldrett *et al*. 2004, Bijl *et al*., 2013) in sample B16, at the base of the marine Bashibulake Formation in the Mine section. This suggests a slightly older age for the third transgressive phase compared to previous work (see also subsequent paragraphs on the Aksu and Shuldara sections).

Tajik Basin

Aksu section

For the Paleogene of the Aksu section, 14 samples were analyzed for the presence of important dinocyst marker taxa. Detailed dinocyst assemblage studies were not conducted for these samples. A few important taxa were recorded, most notably *Rhombodinium draco*, *Adnatosphaeridium vittatum, Heteraulacacysta porosa* and *Enneadocysta pectiniforme*. Specimens tentatively assigned to *Adnatosphaeridium vittatum* are found in AS04, the lowermost analyzed sample. These specimens may indicate an age equivalent to C21n or older. *H. porosa* (samples AS08-AS10) indicates an age not older than C20r and not younger than C16r (Eldrett *et al*. 2004). It is important to note that markers suggesting an age of C19 or younger are not present below the topmost productive sample (AS01). The topmost analyzed sample (AS01) is assigned an age based on the presence of *Rhombodinium draco* and *Cordosphaeridium funiculatum*, which indicate an age older than C16 (LO of *C. funiculatum*) and younger than C19 (FO of *R. draco*). Despite relatively poor preservation, we also note the presence of a few specimens bearing strong resemblance to *Dracodinium rhomboideum* in this sample. This short-ranging species is considered a marker species for C18n.2n (40.14-39.7 Ma) (Eldrett *et al*. 2004, Bijl *et al*. 2013).

Shuldara section

Fourteen samples were analyzed spanning the Shuldara section. As for the Aksu section, assemblage studies were not conducted for these samples. Only few diagnostic species were present at the Shuldara section, but the short ranging taxon *Dracodinium rhomboideum* was recorded in sample CD10. This species indicates an age close to or corresponding with C18n.2n (Eldrett *et al*. 2004, Bijl *et al*. 2013), and roughly equivalent to the Middle Eocene Climate Optimum (MECO; ~40 Ma). The age assignment is supported by the dinocyst assemblage, which also contains *Lentinia serrata* and *Rhombodinium draco*. It should be noted that we here deviate from the work of Iakovleva & Heilmann-Clausen (2010), who placed the occurrence of *D. rhomboideum* in C16, much later than found elsewhere (Eldrett *et al*., 2004, Bijl *et al*., 2013). In contrast to the work of Iakovleva & Heilmann-Clausen (2010), we argue for an older age assignment for this specific interval in their magnetic reversal pattern. Specifically, the FOs of *L. serrata*, *H. porosa* and first consistent occurrence of *Cordosphaeridium funiculatum*, are also supposedly much younger than observed elsewhere (e.g. Eldrett *et al*. 2004), and the number of reversals in this interval is higher than expected based on the geomagnetic polarity time scale (GPTS) (Ogg *et al*., 2016). This is an important difference as the FO of *C. funiculatum* and *L. serrata* were used as markers in earlier work in this basin. Although this inference also implies some uncertainty exists in the local first and last occurrences of species and does not take into account any diachroneity between basins, the assigned ages in this study appear more consistent with calcareous nannofossil biostratigraphy (see next section) and magnetostratigraphy from the same sections (Figure 2.4). We further record the appearance of *Thalassiphora fenestrata* in one sample (CD11), which suggests an age of NP18 (C17n.1n) or younger for the top of the analyzed interval (e.g. Köthe, 2012).

2.7.1.2. Calcareous nannofossils

Tarim Basin

Three samples from the Aertashi Formation were analyzed, but only one yielded nannofossils (KS10, midway through the Aertashi Formation in the Kangsu section, Figure 2.4). The presence of *Chiasmolithus danicus* and *Cruciplacolithus tenuis* indicates a Paleocene age and the occurrence in the same sample of *Fasciculithus* spp. and *F. magnicordis* enables a biostratigraphic correlation with the NP4 zone (~63.2-61.5 Ma) of Martini (1971), within the upper part of the lower Paleocene (Danian), in accordance with the results reported in Lan & Wei (1995) based on bivalves and the review of Yin *et al*. (2002) for this formation.

The samples collected in the lower member of the Qimugen Formation in the Kangsu section (KS33 to KS37; Figure 2.4), yielded very few nannofossils. Nevertheless, presence of some biostratigraphic markers enable us to narrow the age down to the late Paleocene (based on the presence of *Discoaster multiradiatus*, marker of the NP9 zone, ~57.2-55.9 Ma) up to the earliest Eocene (based on the presence of *Fasciculithus tympaniformis*, which became extinct shortly after the Paleocene-Eocene boundary (56 Ma) (Agnini *et al*., 2014). Furthermore, very rare specimens of *Tribrachiatus* cf. *bramlettei* were recovered in sample KS37. This species has its first occurrence at the base of the Eocene (NP10 zone) and often is associated with the PETM (e.g. Gavrilov *et al*., 2003; Raffi *et al*., 2005, Self-Trail *et al*., 2012, Aubry & Salem, 2012). In the same sample (KS37), *Neococcolithes junctus* has a relatively high abundance. It is considered an opportunist species that appears to thrive under eutrophic conditions (Jiang & Wise, 2006; Self-Trail *et al*., 2012), suggesting a high-nutrient environment.

The abundance and preservation of the samples collected in the lower member of the Qimugen Formation in the Mine section are very limited. Nevertheless, the occurrence of *Discoaster multiradiatus* (in samples MI18 to MI27; Figure 2.4) suggests an age that is not older than the late Paleocene for the lower member of the Qimugen Formation. The presence of *Coccolithus bownii* from sample MI19 upwards and the concurrent presence of “long arm” *Rhomboaster* and “malformed” *Discoaster* (*D.*cf. *araneus*) in samples MI23 and MI24 allow us to refer this part of the section to the PETM (e.g. Bown & Pearson, 2009; Self-Trail *et al*., 2012; Agnini *et al*., 2016). In fact, the *Rhomboaster* lineage and the asymmetrical *Discoaster araneus* are restricted to the PETM interval (Bybell & Self-Trail,1995; Kahn & Aubry, 2004; Tremolada & Bralower, 2004; Cao *et al*., 2018) and *C. bownii* is considered an excursion species (Bown & Pearson, 2009).

The stratigraphically higher samples of the lower member of the Qimugen Formation (MI26 to MI29), though very poor, still seem to indicate the lower Eocene (NP10 zone, ~55.9-54.2 Ma), being dominated by *Coccolithus pelagicus*, associated with specimens of *Toweius* spp. and *D. multiradiatus*. Based on the presence of these forms, the youngest possible age for the top of this interval (MI26 to MI29) of the lower member of the Qimugen Formation is estimated as ~54 Ma (Figure 2.4).

Samples LM05 and LM06 from the Wulagen Formation in the Laghman section are characterized by a fairly diversified assemblage and can be correlated to the CP14 zone (approximately corresponding to the NP16/NP17, ~42.8-37.8 Ma) (Figure 2.4). This correlation is based on the presence of *Reticulofenestra umbilicus* (first occurrence at the base of the CP14 zone) and the presence of the additional marker *Neococcolithes* spp. (last occurrence at the base of CP15 zone). Furthermore, in sample LM06 the very common presence of *Pontosphaera* spp. is indicative of a shallow, stressed environment (Lozar *et al*., 2010; Auer *et al*., 2014); this is also confirmed by the common presence of *Neococcolithes* spp. and *Lanternithus* spp., regarded as indicative of nearshore eutrophic conditions.

Tajik Basin

Aksu section

Samples (AS04, AS05, Aksu section) collected in the Jukar Formation, correlated to the Kalatar Formation in the Tarim Basin (Bosboom *et al*., 2017), contain common *Coccolithus pelagicus* and *Sphenolithus moriformis*. Throughout the upper part of the formation, the assemblage is also characterized by the presence of *Discoaster saipanensis* and the rosette-shaped *Discoaster* group (AS07), *D. septemradiatus*, *Chiasmolithus solitus*, and *Chiasmolithus modestus*, indicating a middle Eocene age. The relatively common presence of *Lanternithus* sp. and in particular of *L. arcanus*, a species restricted to the CP 13b-CP 13c subzones (Bown, 2005), coupled with the absence of *Reticulofenestra umbilicus* and *Cribrocentrum reticulatum*, permits us to refer the upper member of the Jukar Formation to the Lutetian (CP13/~NP15 zones; ~46.2-42.8 Ma), in agreement with previous data from the Tarim Basin (Bosboom *et al*., 2011, 2014a).

The samples (AS08 to AS14) collected from the Beshkent –Lower Tochar formations in the Aksu section [correlated to the Wulagen Formation in the Tarim Basin (Bosboom *et al*., 2017)] lack *R. umbilicus*, nevertheless the formation has been tentatively correlated with the CP14a/NP16 zone (upper Lutetian-lower Bartonian; ~42.8-40.3 Ma) based on the absence of *L. arcanus* (last occurrence in the CP13c subzone) and the presence of *Neococcolithes* spp. and *Chiasmolithus solitus*, whose last occurrences are in the CP15 zone (Sheldon, 2002) and top of NP16/CP14a, respectively. The presence of one specimen of *Cribrocentrum reticulatum* in the best preserved sample (AS11) should confirm a Bartonian age assignment, as its first rare occurrence was detected at the top of Chron C19n (Fioroni *et al*., 2015) or in Chron C18r (Fornaciari *et al*., 2010).

Shuldara section

In the Shuldara section, seven of the 15 samples collected are barren and two contain a very limited assemblage. The Beshkent–Lower Tochar formations, correlated to the Wulagen Formation in Tarim Basin (Bosboom *et al*., 2017), lack the markers included in the standard zonations, and biostratigraphic attribution is tentatively based on additional bioevents. The genus *Neococcolithes* was detected in all the fossiliferous samples. Its' last occurrence is reported at the base of the CP15/NP18 zone (~37.8 Ma) (Sheldon, 2002, Varol, 1998). On the basis of this event the Beshkent –L. Tochar formations should be older than the lowermost Priabonian. In addition, the absence of *Lanthernithus arcanus* suggests a correlation with the CP14 zone, and the presence of *Dictyococcites bisectus* supports this biostratigraphic correlation: its occurrence is reported from the upper NP16/CP14a or NP17 zones (Bartonian) in the Indian and Pacific equatorial sites respectively (Fioroni *et al*., 2015; Bown & Dunkley Jones, 2012), confirming the previously assigned age (Bosboom *et al*., 2011, 2014a).

The relatively common presence of *Lanthernithus* sp. and *Zigrablithus bijugatus* is indicative of a nearshore environment.

Samples collected in the overlying Kushan and Sanglak formations (CD11, CD12, CD13) contain common specimens of *Cribrocentrum reticulatum*, pointing to an age not older than the Bartonian. The absence of the genus *Neococcolithes*, along with the presence of *Cribrocentrum erbae*, enables a correlation with the CP15a/NP18 zone (lower Priabonian). The first common occurrence of *C. erbae* (Agnini *et al*., 2014) has been proposed as an alternative biohorizon for the base of zone NP18 (~CP15a), and the definition of the GSSP for the base of the Priabonian Stage. The relatively abundant and diversified assemblage indicates more open marine conditions.

2.7.1.3. Foraminifera

Five samples (KS33-KS37, Kangsu section) from the lower member of the Qimugen Formation yielded rare to common, poorly preserved benthic foraminiferal assemblages in low to moderate diversity (Table S 2.8).

Based on benthic foraminiferal assemblages recorded from these samples a Paleocene to Early Eocene age has been assigned to this part of the Kangsu section. The stratigraphic range of *Anomalinoides rubiginosus* (KS36) extends from Campanian to Paleocene (P5 zone) (Van Morkhoven *et al*., 1986), thus, the level KS36 cannot be younger than Paleocene in age. Since *Acarinina multicamerata* is regarded as an excursion taxon in the Paleocene-Eocene Thermal Maximum interval (Guasti & Speijer, 2008), its presence in the KS37 (E1 zone) allows us to define the Paleocene-Eocene boundary between samples KS36 and KS37.

The samples from the lower member of the Qimugen Formation in the Mine section (MI20 to MI30) yielded a rare to common foraminiferal assemblage in very low to low diversity (Table S 2.9). The preservation of specimens is very poor and the identification of foraminifers at some level is difficult.

A precise age could not be assigned to samples based on benthic foraminifers because of the long stratigraphic ranges of the recorded taxa. However, based on the presence of *Acarinina multicamerata* in the Early Eocene E1 zone (MI-B22 and MI-B23), the Paleocene-Eocene boundary is delineated between samples MI-B21 and MI-B22 (Guasti & Speijer, 2008) (see section 1.3 of the supplementary materials for the paleoecological considerations).

2.7.1.4. Pollen assemblages

Wang *et al*. (1990) reported a comprehensive study of Upper Cretaceous and Cenozoic palynofloras from the Tarim Basin (Shache, Kuche, Wuqia and Kashi regions), but age control was of relatively low resolution. This can now be refined through our new bio- and magneto-stratigraphic results. Biomes are assigned using the Nearest Living Relatives (NLR) approach followed by Hoorn *et al*. (2012). The Thanetian–Ypresian Qimugen Formation palynoflora is dominated by the steppe-desert taxon *Ephedripites*, with the deciduous tree taxa *Quercoidites*, *Cupuliferoipollenites* and *Ulmipollenites*, and conifers *Abietineaepollenites* and *Piceapollenites* also present. *Normapolles* pollen, previously thought to be indicative of the Paleocene, is common, while *Schizaeoisporites*, *Rhoipites*, *Nanlingpollenites*, and *Proteacidites* are more infrequent elements (Wang *et al*., 1990).

The xerophyte *Ephedripites,* as well as deciduous trees *Quercoidites* and *Cupuliferoipollenites* dominate the Lutetian Kalatar Formation palynoflora. Other common elements include temperate and warm broad-leaved forest: *Betulaceoipollenites*, *Alnipollenites*, *Momipites*, *Celtispollenites*, *Rutaceoipollenites*, *Labitricolpites* and *Euphorbiacites*, while *Ulmipollenites* and *Pinuspollenites* are rare.

The Wulagen Formation palynoassemblage, of Lutetian-earliest Bartonian age, is very similar to that of the underlying Kalatar Formation, with many subordinate temperate and warm broad-leaved forest taxa. Pollen assemblages are dominated by *Ephedripites* and *Meliaceoidites* (temperate–sub-tropical).

The Bartonian–Priabonian Bashibulake Formation pollen assemblage is dominated by xerophytic *Ephedripites* in even greater numbers than previously, with *Quercoidites* and *Cupuliferoipollenites* also being very abundant. *Chenopodipollis* (steppe-desert) and *Salixipollenites* (temperate–sub-tropical) are common while *Caryapollenites*, *Engelhardtioipollenites* and *Juglanspollenites* (temperate and warm broad-leaved forest) are rare.

The overlying Oligocene Keziluoyi Formation palynoflora is markedly different, being dominated by Pinaceae pollen (*Pinuspollenites* with underlying components of *Abietineaepollenites* and *Piceapollenites*). Also present are xerophytic *Ephedripites* and temperate broad-leaved forest: *Quercoidites*, *Cupuliferoipollenites*, *Ulmoideipites* and

Celtispollenites. This sudden upswing of microthermal–mesothermal pollen is also seen at the Eocene-Oligocene Transition (EOT) in the Xining Basin (Page et al., under review). This suggests the hiatus generally observed between the Bashibulake to Keziluoyi formations includes the Eocene-Oligocene boundary as previously indicated (Bosboom *et al.*, 2014a; Yang *et al.*, 2015).

2.7.2. Lithofacies and depositional environments

We describe in the following the various facies associations and their respective depositional environment interpretations (Table S 2.1, Figure 2.3). The facies and microfacies composing the facies associations can be found in Tables S 2.2 and S 2.3. The evolution of these environments is illustrated along the logs of the studied stratigraphy in Figure 2.7.

2.7.2.1. Facies association 1 (FA1) – Reddish brown sandstones, siltstones and claystones of fluvial and playa lake environments

Description - FA1 consists mainly of facies Sl, Sc, Sa, Ch, Ml, Ms, Mp and Mg (Table S 2.1 and S 2.2). It crops out in the fine clastics of the Upper Qimugen and Bashibulake formations of the Aertashi section, in the lower part of the Bashibulake Formation and in the Kezilouyi Formation of the Mine section. FA1 typically shows dm to m-thick and 10's of meters large medium to coarse-grained, trough cross-bedded (Sc) sandstone channels (Ch) with few bioturbation and dewatering structures. The channels are overlain by 1 to 5 m-thick, fine-grained cross or parallel-bedded sandstones (Sc, Sl) showing asymmetrical ripples (Sa). Mudstones and siltstones interbedded with fine sands (Ms) include asymmetrical ripples, occasional bioturbation, carbonate nodules and wood debris (Figure S 2.1a). This sedimentary sequence is encased into meter-scale, massive, by place horizontally laminated and bioturbated red siltstone and claystone with very rare root traces (Ml) and alternated with gypsum nodules/layers (Mg). No fossil fauna or macroflora is observed in this facies association.

Interpretation - The concave-up, erosive based, fining upward, medium to coarse-grained sandstone succession observed in FA1 corresponds to channel deposits. The trough cross bedding and the medium to coarse granulometry in these channels are indicative of the migration of high energy, 3D megaripples in unidirectional flow direction of probable fluvial origin (Harms *et al.*, 1982). In such a context, the red siltstone and claystone with rare root traces and bioturbation are interpreted as flood plain deposits. The small size of the sandstone channels encased in thick red mudstones points to episodic/ephemeral flow in an aggradational alluvial plain. Adjacent to the channel beds, laterally extensive thin beds of fining upward, medium to fine sands with asymmetrical ripples and occasional bioturbation encased in the red siltstones and mudstones are interpreted as rapid deposition from unconfined flow in overbank or waning flood, therefore as crevasse splay deposits (e.g. Gulliford *et al.*, 2017) (Figure S 2.1a). Planar laminated red claystone and siltstone with occasional bioturbation represent the settling of fine-grained particles from suspension in a standing body of water such as a pond/lake on the flood plain. The overall scarcity of root traces and bioturbation together with the reddish brown color and episodic functioning of the fluvial channels point to semi-arid conditions in which the growth of vegetation is limited by the irregular and high energy supply of water (Collinson 1996). The presence of gypsum nodules/layers within these fine-grained deposits also implies a semi-arid/arid climatic setting with small ponds in a continental playa (Figure 2.3, Figure S 2.1b).

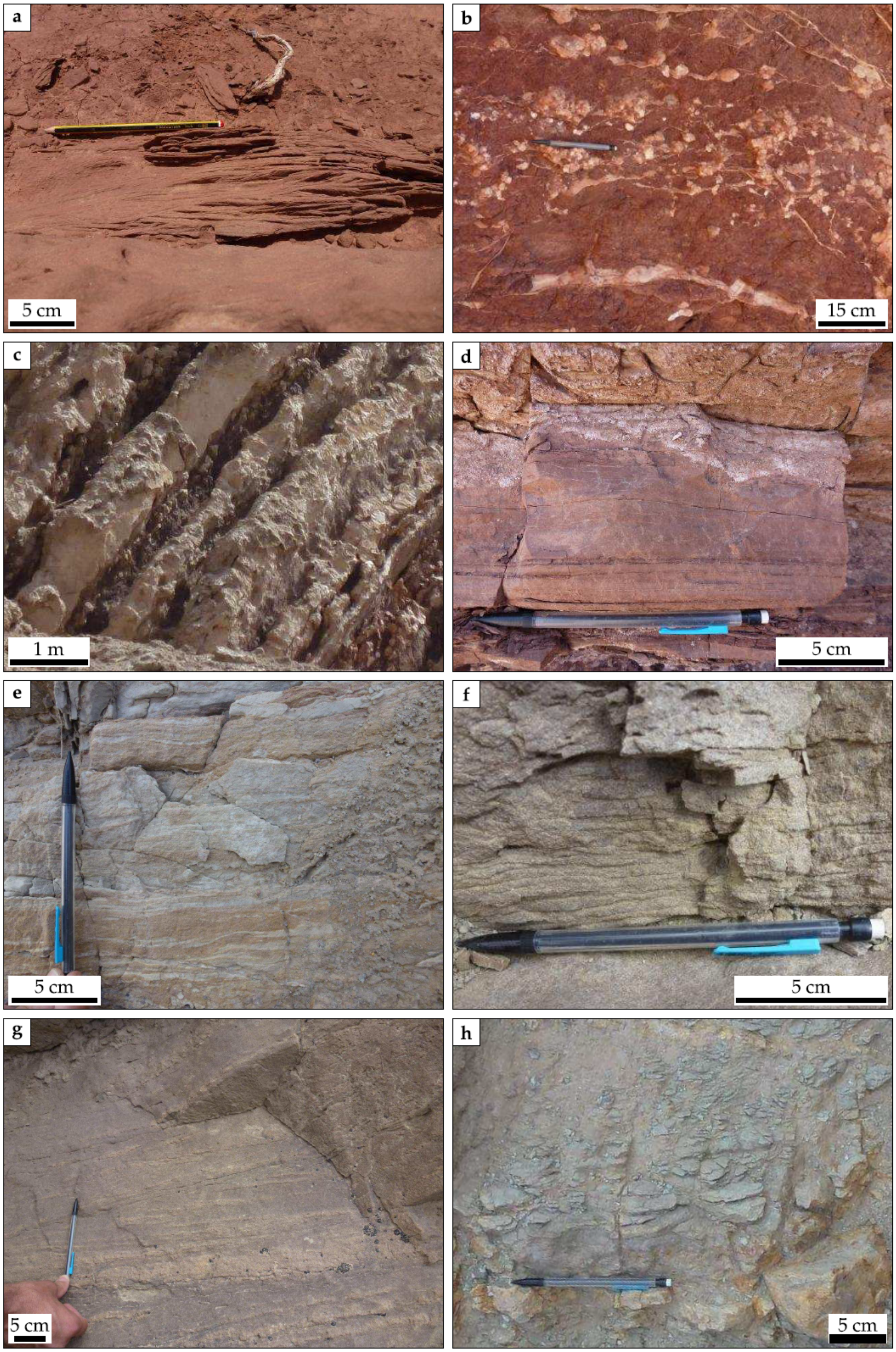
a
5 cm
b
15 cm
c
1 m
d
5 cm
e
5 cm
f
5 cm
g
5 cm
h
5 cm

Figure S 2.1 Paleogene sedimentary facies and depositional environments (pictures from Bougeois et al., 2018). (a) crevasse splay deposits in alluvial flood plain: reddish brown rippled very fine sand and clayey silt alternation. (b) playa: claystones and nodular gypsum. (c) sabkha: massive gypsum alternating with red claystones. (d) coastal plain: bioturbated, planar laminated very fine grained pinkish sandstones with clay drapes by places. (e) tidal flat: thick-thin, cm-scale sets of doublets of fine to coarse grained deposits with current ripples (neap-spring tide alternations). (f) shoal: ooidal grainstone with wave ripples. (g) shoal: grainstone with through cross-bedding and low angle truncations. (h) offshore: blue-green laminated marls with lenticular grainstone storm beds.

2.7.2.2. Facies association 2 (FA2) – Massive-layered gypsum, red-brown claystones, siltstone and sandy calcareous beds of coastal plain environment

Description - FA2 consists of facies Mp, Mg, Gl and microfacies MF9, MF10 and MF16 (a) (Table S 2.1, S 2.2 and S 2.3). It crops out at the base of the Lower Qimugen Formation, in most parts of the Upper Qimugen Formation, at the top of the Wulagen Formation and in the Bashibulake Formation. FA2 comprises of dm to m-scale, massive, locally layered gypsum strata (Gl) interbedded at random with cm-scale or m-scale, red-brown claystone (Mp), red-brown laminated siltstone and very fine grained siliciclastic, sandy calcareous or dolomitic sandstone beds with occasional intense bioturbation, desiccation cracks, gypsum nodules (Mg) (Figure S 2.1c). The siliciclastic, very fine sandstone can be fining upward and planar laminated with clay drapes at the top (Figure S 2.1d) while the red-brown claystone and siltstones show more consistent lamina/interlamina couplets. The sandy calcareous beds show trough cross bedding, herringbone structures and cm-scale sets of fine and coarse-grained doublets with current ripples. The dolomitic beds show a crystal-supported planar-e dolomite texture (Sibley & Gregg, 1987) in which most dolomite crystals are euhedral rhombs and where intercrystalline area is filled by micrite (MF9, Figure S 2.2c). The siliciclastic sandy calcareous beds are either rich in allochems including bryozoan fragments, benthic foraminifera, bivalves and glauconite (MF10, Figure 2.2d, e) or devoid of any allochems instead including predominantly siliciclastic grains (MF16 (a), Figure S 2.3e, f). Disarticulated shells of the oysters *Platygena asiatica* and *Cubitostrea plicata* were observed in the claystone and red-brown siltstone beds of the Bashibulake Formation in the Mine section. In the uppermost red-brown claystones and siltstones of the Bashibulake Formation, oyster bioherms of *Cubiostrea tianshanensis* and *Donax chion* are common.

Interpretation – Deposition in a nearshore setting is evidenced by the presence of desiccation cracks, dolomitization, intense bioturbation and lamina/interlamina couplets in the siltstone and claystone, as well as herringbone structures in the sandstone beds formed by bidirectional currents in tidal channels characteristic of intertidal deposition. In places, cm-scale, thick-thin sets of relatively coarse to fine-grained doublets with current ripples represent tidal rythmites deposited on a tidal flat (Tessier, 1993) as a result of neap-spring tide alternations (Figure S 2.1e). The massive locally layered gypsum is interpreted to be deposited in a subaqueous environment close to the sea such as a coastal salina [see e.g. the modern marine evaporites of Warren & Kendall (1985) occurring in subaqueous salina setting]. However, red-brown gypsiferous silts, clays and desiccation cracks imply subaerial deposition as a result of fluctuating ground water levels, probably in a sabkha environment (Warren & Kendall, 1985).

This indicates deposition in a near shore, coastal plain environment with a semi-perennial water table including supratidal sabkhas and salinas, and intertidal settings similar to the Facies Zone 9A of Wilson (1975) defined for an arid, evaporitic platform interior setting including calcareous, dolomitic mud or sands with nodular, wavy gypsum and interlayers of red beds.

2.7.2.3. Facies association 3 (FA3) – Micrite-dominated carbonates and gray siltstones and mudstones of restricted subtidal lagoon/bay environment

Description - FA3 is composed of facies Mp, Sa, Ss, Cq and decimetric to plurimetric fine calcareous beds represented by microfacies MF1, MF4, MF5, MF10, MF14 (a), MF15 and MF16 (a, b) (Table S 2.1, S 2.2 and S 2.3). It crops out in the Lower Qimugen, Kalatar, Wulagen and Bashibulake formations. FA3 includes (1) m-scale, gray, bioturbated siltstones and mudstones with planar lamination and ripple-forms (Mp), (2) poor to moderately sorted, fine-grained, dm to m-scale sandstones with ripple laminations and bioturbation (Sa, Ss) interbedded with (3) calcareous beds and m-scale patchy oyster bioherms (boundstones and floatstones, Cq) of *Ostrea (T.) strictiplicata*. Other oysters found in FA3 are *Ostrea (Turostrea) cizancourti*, *Chlamys* sp. and *Fergana bashibulakeensis*, which appear in the mudstones and siltstones of the Bashibulake Formation. Calcareous beds interbedded with the fine clastics are composed either of micritic mudstone including some dolomite crystals (MF1) (Figure S 2.2a), serpulid wackestone to packstone (MF4) (Figure S 2.2e, Figure 2.2b), bioclastic wackestone to packstone including miliolid foraminifera (MF5) (Figure S 2.2f) and some mixed siliciclastic-carbonate microfacies [MF10, MF14 (a), MF15, MF16] (see Figure S 2.3g for MF10; Figure S 2.3b for MF14(a); Figure 2.2f for MF 15; Figure 2.2g and Figure S 2.3e, f for MF16).

Interpretation – Planar laminated fine-grained clastics and micrite-dominated carbonates with occasional intense bioturbation are characteristic of deposition in a low-energy, quiet environment rich in nutrients. Meter-scale boundstone lenses of *Fergana bashibulakeensis* and *Ostrea (T.) strictiplicata* occurring in the fine-grained calcareous beds represent oyster patch reefs. These reefs, due to the preferential occurrence of these two oyster species, are characteristic of a restricted, low-energy subtidal marine environment (Bougeois *et al*., 2016). Serpulid fossils in MF4 are classified as the members of the *Ditrupa* community of Yang *et al*. (2012) who documented their occurrence in a semi-restricted lagoonal environment. The presence of dolomite crystals, peloids, miliolid foraminifera and biota with a reduced diversity also indicate a restricted, low-energy environment. We interpret FA3 as a low energy, subtidal lagoon or bay-like restricted depositional environment (Figure 2.3). Such an environment is very common on shallow ramps between a rim of shoals (on the seaward side) and a coastal plain (on the landward side).

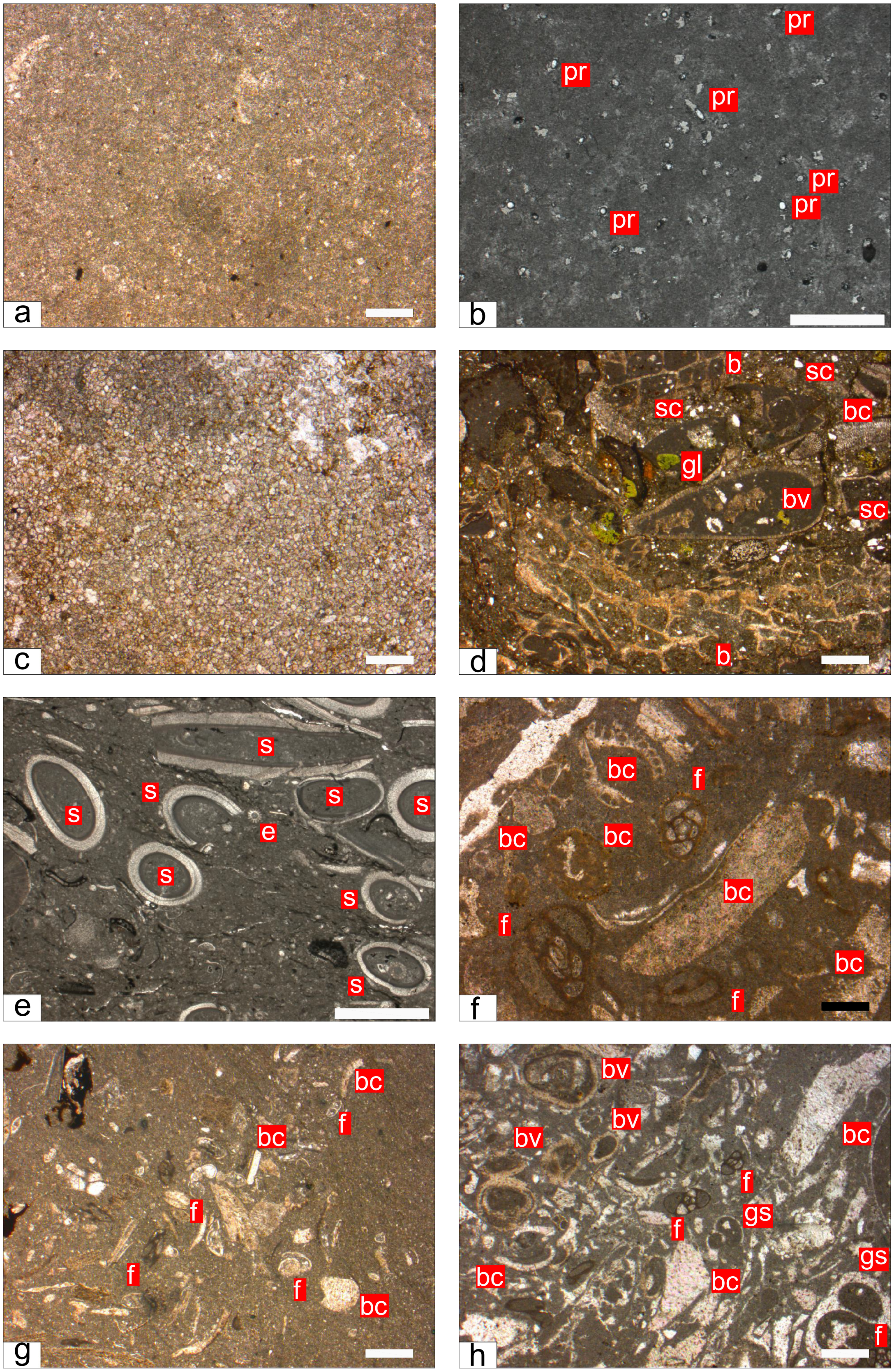
a
b
pr
pr
pr
pr
pr
pr
c
d
b
sc
sc
bc
gl
bv
sc
b
e
s
s
s
s
s
e
s
s
s
f
bc
f
bc
bc
bc
f
bc
f
g
bc
f
bc
f
f
f
bc
h
bv
bv
bv
bc
f
gs
f
gs
bc
bc
f

Figure S 2.2 Photomicrographs of the microfacies - (a) mudstone (MF1) AT13-TS26; (b) porous mudstone (MF2) MI15-C10; (c) dolomite (MF9) MI13-TS21; (d) proximal sandy allochem limestone (MF10) AT13-TS49; (e) serpulid wackestone (MF4) MI15-C18; (f) bioclastic wacke to packstone (MF5) AT13-TS5; (g) bioclastic wackestone (MF5) AT13-T32; (h) bioclastic packstone (MF6) MI13-TS09 – pr: pores, p: peloids, s: serpulid, f: foraminifera, bc: bioclast, b: bryozoan, bv: bivalve, gs: gastropoda, e: echinoderm fragment, gl: glauconite, sc: siliciclastic, e: echinoderm fragment, for a, b, c, d, f, g and h scale bar is 500 µm, for e scale bar is 1 mm.

2.7.2.4. Facies association 4 (FA4) – Grain-supported carbonates, oyster bioherms of a high-energy shoreface to shoal/beach environment

Description - FA4 consists of metric to pluri-metric interbedding of detrital carbonate beds and m-scale oyster bioherms with *Ostrea bellovacina*, *Ostrea strictiplicata*, and *Ostrea cizancourti* (Cq). It crops out in the carbonates of the Kalatar Formation, Lower Qimugen and Wulagen formations in the Mine, Aertashi and Kangsu sections. The detrital carbonates are bioclastic packstones to grainstones (MF6) and oolitic grainstones (MF7) while the oyster bioherms are boundstones and floatstones. The detrital carbonates show wave ripples, hummocky to swaley cross stratification, trough cross-beddding and intense bioturbation including vertical burrows and box-works of the *Skolithos* ichnofacies. The packstone to grainstone beds (MF6) at the base of the succession include foraminifera, serpulids, bryozoa, echinoderm fragments, gastropoda and peloids (Figure S 2.2h and Figure 2.2e) while the overlying oolitic grainstone (MF7) beds include well-sorted abundant concentric, spherical ooids, foraminifera, bryozoa and broken shells of oyster *Pycnodonte nomada* (Figure 2.2c).

Interpretation – The abundance of concentric, spherical ooids in hummocky to swaley cross stratified and trough cross-bedded detrital carbonates is indicative of a shallow marine, high energy, wave-dominated environment such as in shoreface to shoal and beach/barrier settings (Strasser, 1986; Flügel, 2004) (Figure S 2.1g). Boundstones and floatstones (Cq) with largely dominated *Ostrea* species either bounded together in situ or disarticulated are interpreted as small patch bioherms seated downdip of the wave-dominated shoals.

2.7.2.5. Facies association 5 (FA5) – Wave rippled, cross bedded mixed siliciclastic-carbonate beds of a mouth bar in a wave-dominated estuarine environment

Description - FA5 consists of thick, plurimetric mixed siliciclastic-carbonate beds. It crops out in the deposits of the Kalatar Formation only in the Aertashi section. The calcareous sandstone beds with micritic matrix show trough and herringbone cross bedding, wave ripples and appear as fining-upward, occasionally erosive-based successions including some mud pebbles with intensely bioturbated tops. These mixed siliciclastic-carbonate beds can be either rich in allochems including bivalves, gastropoda, foraminifera, bryozoa, serpulids, ooids (MF10) or devoid of any allochems [MF16 (a)].

Interpretation – The thick, fining upward, trough and herringbone cross-bedded, erosive-based calcareous sandstone beds with mud pebbles are interpreted as mouthbars formed at the outlet of tidal channels in a high energy, wave-dominated estuarine environment (Dalrymple *et al.*, 1992) (Figure 2.3). Its sandy character with cross bedding and wave ripples together with its microfossil content suggest a depositional setting corresponding to an outer zone of an estuarine dominated by marine processes (waves and/or tidal currents) where sediment is derived mostly from the sea (Reading, 1996).

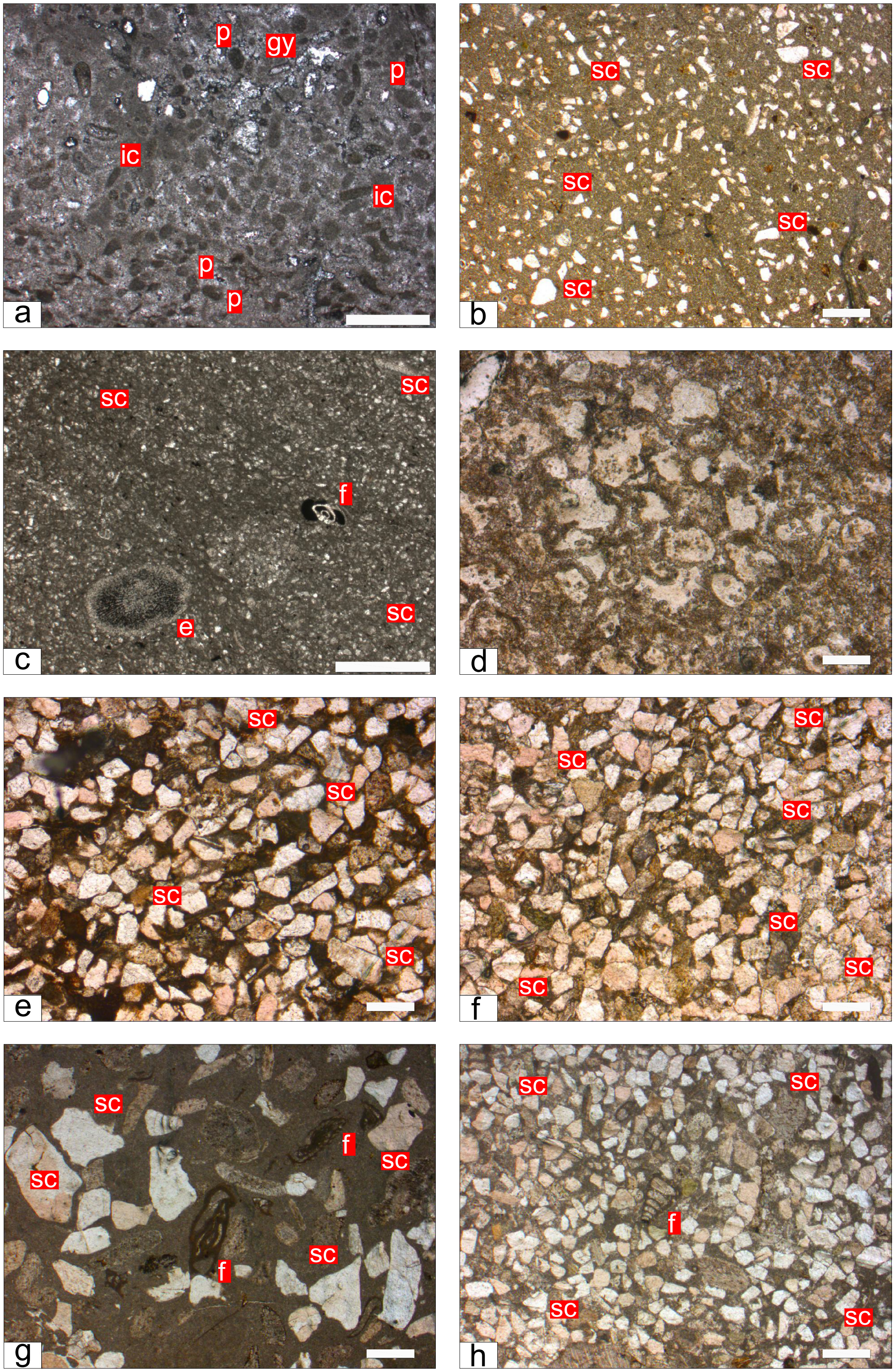
p
gy
p
ic
ic
p
p
a
sc
sc
sc
sc
sc
b
sc
sc
f
sc
e
c
d
sc
sc
sc
sc
e
sc
sc
sc
sc
sc
sc
f
sc
f
sc
sc
sc
f
g
sc
sc
f
sc
sc
h

Figure S 2.3 Photomicrographs of the microfacies - (a) peloidal wackestone with gypsum (MF13) MI15-C09; (b) sandy micrite (MF14a) MI13-TS08; (c) sandy micrite with very rare allochems (MF14b) MI15-C12; (d) dolomitic limestone (MF8) MI13-TS30; (e, f) micritic sandstone (MF16a) AT13-TS03 (e), AT13-TS06 (f); (g) proximal sandy allochem limestone (MF10) MI13-TS14; (h) micritic sandstone with very rare allochems (MF16b) AT13-TS33 – e: echinoderm fragment, p: peloid, gy: gypsum, ic: intraclast, sc: siliciclastic, f: foraminifera, s: serpulid, scale bar is 500 µm for all.

2.7.2.6. Facies association 6 (FA6) – Laminated dark mudstones, bluish marls and fine calcareous beds of offshore environment

Description – FA6 consists of interlayering of (1) m-scale, finely laminated, locally calcareous and shelly, bioturbated dark mudstones (Mr), (2) decametric to plurimetric bluish marls (Mr), (3) m-scale calcareous beds and (4) dm to m-scale poorly bedded to massive oyster bioherms (Cq). FA5 crops out in the Lower Qimugen Formation in the Mine and Aertashi sections and in the transitional interval from the Kalatar to Wulagen formations in the Mine, Kangsu and Aertashi sections. The sandy limestone beds are fining upward and they include fine-grained siliciclastics on a micritic matrix. They show erosive bases with gutter casts and bioturbated tops with iron oxide-impregnated hardground layers. The hardground layers act as a substrate for colonization of the oyster species *Kokanostrea kokanensis* observed in the Wulagen Formation (Cq). The other oyster species found in the Wulagen Formation, *Sokolowia buhsii*, prefers soft, muddy substrates. These sandy calcareous beds also include low angle lamination and hummocky cross stratifications (Ts). These beds may contain considerable bioclastic allochems as bivalves, gastropoda, serpulids, bryozoa, planktonic foraminifera and echinoderm fragments indicating a diverse community (MF11) (Figure 2.2d) or they may contain a lesser quantity of allochems as shell fragments together with planktonic and benthic foraminifera [MF14 (b)] (Figure S 2.3c). Other calcareous beds interbedded with the mudstones and marls are bioclastic wackestones (MF5) including bivalves, foraminifera, serpulids, echinoderm fragments, gastropoda, bryozoa, unidentified bioclasts, and peloids. Oyster bioherms (Cq) observed in the Qimugen Formation include mostly specimens of *Flemingostrea hemiglobosa* and may show evidences of partial dolomitization (MF8) (Figure S 2.3d).

Interpretation - Fine-grained siliciclastics and micrite-dominated carbonates indicate a quiet, low-energy marine environment below the fair weather wave base, which is also corroborated by the macro- and micro- fossil assemblages. Both *F. hemiglobosa* and *S. buhsii* prefer a low energy, offshore environment (Bougeois *et al.*, 2016). The presence of highly diverse fossil assemblages containing bivalves, gastropoda, serpulids, bryozoan, echinoderm fragments, planktonic and benthic foraminifera also supports an open marine, offshore environment. Erosive-based sandy calcareous beds with low angle laminations and hummocky cross stratification are interpreted to be the result of episodic storm wave action on the sea-floor (Handford, 1986) or tempestites (Ts) indicating an upper offshore environment between the storm wave base and fair weather wave base (Figure S 2.1h).

2.7.2.7. Facies association 7 (FA7)- Hypersaline evaporitic shelf/basin marginal deposits

Description – FA7 consists of predominantly massive or locally layered white gypsum deposits with occasional cross-laminations and ripple forms interbedded with m-scale red mudstones, grey siltstones and calcareous beds (Gl). The latter are peloidal wackestone to packstones with dissolution vugs (MF3, Figure 2.2a), massive dolomites, sandy micrites (MF14), gypsiferous peloidal mudstones (MF12, Figure 2.2h; MF13, Figure S 2.3a) and micritic mudstones with birdeyes (MF2, Figure S 2.2b). These deposits crop out in the Aertashi Formation. The thickness of massive gypsiferous deposits varies from ca. 20 m to 400 m.

Interpretation - The thickness and widespread distribution of the evaporite deposits, the presence of dolomites, peloids and a biota with a reduced diversity [although we couldn't identify any micro/macro fossils from the collected carbonate samples, the presence of interbedded fossiliferous carbonate beds (miliolid foraminifera *Qinquloculina* spp., bivalve *Brachidontes elegans*, gastropod *Potamides* sp.) with gypsum was previously reported (Chinese Bureau of Stratigraphy, 1981; Hao *et al*., 1982; Tang *et al*., 1989; Jia *et al*., 2004)] suggests a restricted marine environment on a shelf. The presence of ripples and cross-laminations indicates a shallow subaqueous wave and current influenced environment (Schreiber *et al*., 1976). Red mudstones, birdeyes and dissolution vugs indicate occasional emergence of the shallow shelf. Lagoons and widespread shallow shelfs/platforms may become restricted and hypersaline with or without a barrier in which case the entire inner shelf may become evaporitic or evaporite-accumulating (James & Walker, 1992; Reading, 1996). However, shoals and organic buildups of bivalves may have played a barrier role to isolate the marginal parts of the Tarim Basin as a hypersaline evaporite shelf with a brine depth of a few meters. Shoals and organic buildups of bivalves (rudists bioherms) are also reported further west in the Tajik Basin and Uzbekistan (Scott *et al*., 2010). Sea level fall at the end of the Cretaceous may have also restricted the complete or partial movement of marine waters onto the shelf, which increases the possibility of occurrence of shelf evaporites.

2.7.3. Sedimentary geochemistry: Effects of depositional setting on the bulk stable C and O isotope compositions

To corroborate our facies and depositional environmental interpretations, we analyzed bulk carbon and oxygen isotopic compositions of marine and continental carbonates from the Mine and Aertashi sections. High frequency changes in $\delta^{18}O$ and $\delta^{13}C$ values indicate that the isotopic system was closed relatively early during lithification hampering the interaction with meteoric fluids during diagenesis (Bougeois *et al*., 2018). Therefore, the effects of diagenesis were likely limited and the primary signal should have been preserved. $\delta^{18}O$ values in marine systems are influenced significantly by ice volume, temperature and runoff in coastal environments whereas they controlled primarily by the ratio of precipitation to evapotranspiration in continental environments. Similarly depending on the different carbon sources $\delta^{13}C$ values differ for marine and continental systems (Bougeois *et al*., 2018). Therefore, there should be a clear distinction between the isotopic signature of marine and continental environments, which has proven helpful to distinguish equivocal environment attributions when sedimentological observations are not sufficient alone.

As can be seen in Figure S 2.4a, carbonates interlayered with gypsum beds of the Upper Qimugen Formation in the Mine section show less negative values indicating a more marine (supratidal sabkha or salina) influence/origin. On the other hand, sediments in the Upper Qimugen Formation interlayered with gypsum beds in the Aertashi section display more negative isotopic values implying a continental (playa) influence/deposition which is consistent with our interpretations.

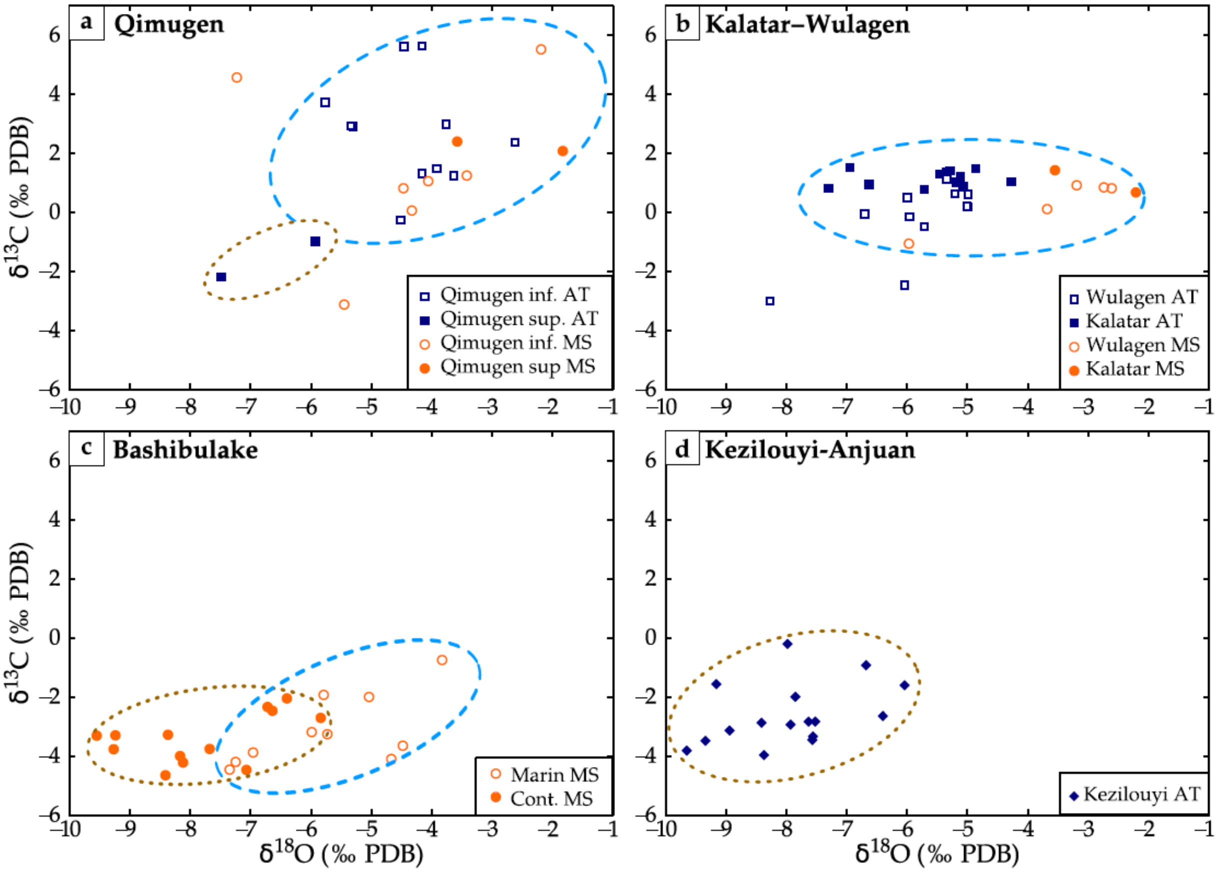

Figure S 2.4 Bulk carbon and oxygen isotopic compositions of the carbonate rocks from the Aertashi and Mine sections. (a) Qimugen Formation (3rd sea incursion), (b) Kalatar and Wulagen formations (4th sea incursion), (c) Bashibulake Formation (last sea incursion), (d) Kezilouyi Formation.

The difference in the δ^{18}O values of samples from the Kalatar and Wulagen formations between the Mine and Aertashi sections (Figure S 2.4b) can be interpreted as primarily reflecting variation in continental runoff. A marine environment in the Mine section with less continental runoff or a large river influence in the Aertashi section could explain this difference. This is precisely what have been observed and interpreted sedimentologically in those two sections (Figure 2.7).

As seen in Figure S 2.4c, distinction between marine and continental carbonates of the Bashibulake Formation is relatively straightforward, with higher values in δ^{18}O and δ^{13}C during submerged periods. However, there exists an area where mixed δ^{18}O and δ^{13}C values can be seen for both marine and continental carbonates. The variation of marine and continental environments in the Bashibulake Formation is relatively restricted to alluvial plain, coastal plain and subtidal environments during the last sea incursion (Figure 2.7). Therefore, transition from marine to continental environment seems to be reflected by the isotopic compositions of carbonates during the associated regression event. In this very shallow environment, evaporation may also result in less negative values for $\delta^{18}O$. This is another potential explanation for the $\delta^{18}O$ values around -6 and -7‰ for the continental carbonates of the Bashibulake Formation.

2.4. Sequence Stratigraphy

We identified key bounding surfaces as erosional (subaerial) unconformities, which are interpreted as Sequence Boundaries (SBs), Maximum Flooding Surfaces (MFSs), Transgressive Surfaces (TSs) and Basal Surface of Forced Regression (BSFR). The key surfaces bound specific facies assemblages called systems tracts (Catuneanu, 2006). We have interpreted four types of systems tracts: (1) Lowstand Systems Tract (LST); (2) Transgressive Systems Tract (TST); (3) Highstand Systems Tract (HST); (4) Falling Stage Systems Tract (FSST).

2.4.1. Key bounding surfaces

Erosional (subaerial) unconformities

The erosional unconformities are characterized by an erosion surface underlined by an abrupt facies change, marking a clear downward (seaward) shift in the overlying facies belts. They can be subaerial in a landward direction or marine and conformable in a seaward direction.

The erosional unconformities are exposed in the field as (1) a sharp, erosive surface at the base of fluvial channel belts downcutting the red-brown silty claystones of the alluvial environment [e.g. sequence boundary 4 (SB4) in the Mine section] (Figure 2.7); (2) an irregular, crinkled ferruginous hardground surface separating the underlying shoreface deposits from the overlying coastal plain deposits (e.g. SB1 in the Mine section) (Figure 2.7).

SB3 showing a sharp facies contrast between the shoreface/intertidal and coastal deposits (in the Mine and Aertashi sections) was interpreted as the conformable portion of the subaerial unconformities recognizable landward due to lack of a clear exposure/erosion surface (Figure 2.7). Similar to SB3, SB2 was also interpreted as a conformable surface separating different facies in all sections (Figure 2.7).

Maximum flooding surfaces (MFSs)

Maximum flooding surfaces are underlined by ferruginous and phosphatic hardgrounds (e.g. MFSs at the top of TST.1.1 and TST.2.1 - the first Transgressive Systems Tract in the first and second sequence respectively- in the Mine section; MFS at the top of the TST.4.1 in the Mine section) or represented as sharp changes from deepening up to shallowing up facies tracts (MFSs at the top of the TST.3.2 and TST.3.4 in the Aertashi section) (Figure 2.7).

Transgressive surfaces (TSs)

Transgressive surfaces are sharp, in places erosional surfaces, characterized by an abrupt deepening or landward shift of the overlying facies belt. In the field they were observed as: (1) surfaces marking the sharp facies change from coastal (supratidal) or alluvial plain to intertidal calcareous sand deposition with bioturbation and oysters (e.g. TS overlying the LST.2.1 in all sections, which displays the onset of 2nd Paleogene transgression); (2) surfaces displaying the first offshore sediment deposition on top of the shoal deposits (e.g. TS at the base of the TST.3.1 in the Mine and Kangsu sections); (3) wave erosional surface (e.g. TS at the base of the TST.3.1 in the Aertashi section (4) hardground surfaces displaying a change from shallowing up to deepening up facies tracts (e.g. TS at the base of the TST.3.3 in the Aertashi section); (5) surfaces displaying the onset of the glauconite-bearing coastal plain deposition on top of the alluvial plain deposits (e.g. TS on top of the LST.4.1 in the Mine section, which represents the onset of the 3rd Paleogene transgression) (Figure 2.7).

Basal surface of forced regression (BSFR)

Basal surfaces of forced regression are recognized as either a sharp erosion surface (e.g. BSFR at the base of the FSST.1.1 in the Mine section) or a conformable surface (BSFR at the base of the FSST.1.1 in the Aertashi section) overlain by coarse shoreface sands indicative of a sharp seaward shift of the shoreface facies belt (Figure 2.7).

2.4.2. Sedimentary architecture

The lowstand systems tracts are bounded below by an erosional unconformity or its lateral conformity and above by a transgressive surface. LSTs are composed of progradational to aggradational sets of deposits represented by (1) coastal plain (supratidal) gypsiferous deposits of FA2 and alluvial plain fine clastics of FA1 (e.g. LST.2.1 and LST.4.1 in the Mine and Aertashi sections); (2) shoal deposits of FA4 (e.g. LST.3.1 in the Mine and Kangsu sections); (3) upper shoreface mouth bar sand deposits with large trough cross beds of FA5 (e.g. LST.3.1 in the Aertashi section) (Figure 2.7).

The transgressive systems tracts are bounded below by a transgressive surface and above by a maximum flooding surface. TSTs are composed of deepening upward, retrogradational sets of deposits and represented by (1) shallow intertidal (FA2) and subtidal facies (FA3) capped by shoal and bioherm (FA4) and offshore facies (FA6) (e.g. TST.1.1 in the Mine and Aertashi sections and TST.2.1 in the Mine and Aertashi sections); (2) an upsection deepening in the offshore facies of FA6 (e.g. TST.3.1 and TST.3.2 in the Mine and Kangsu sections); (3) an upsection deepening represented by the successive deposition of shoal and bioherm facies of FA4 and offshore facies of FA6 (TST.3.2. in the Aertashi section); (4) coastal plain deposits of FA2 and overlying subtidal deposits and FA3 (TST.4.1 in the Mine section) (Figure 2.7).

The highstand systems tracts are bounded below by a maximum flooding surface and above by an erosional unconformity (or its lateral conformity surface) or a basal surface of forced regression. The HSTs consists of shallowing upward, progradational sets of deposits and represented by (1) offshore marls of FA6 overlaid by shoreface calcareous mudstones of FA3 (e.g. HST.1.1 in the Mine and Aertashi section, HST.3.4 in the Mine section); (2) an upsection shallowing in the offshore marls of FA6 (e.g. HST.2.1 in the Mine section); (3) shoal & oyster bioherm facies of FA4 overlaid by wave dominated shoreface deposits of FA5 (e.g. HST.2.1 in the Kangsu and Aertashi sections); (4) offshore marls of FA6 capped by shoal and bioherm facies of FA4 (e.g. HST.3.1. in the Mine and Kangsu sections); (5) shoal and bioherm deposits of FA4 overlaid by shoreface facies of FA3 (e.g. HST.3.1 in the Aertashi section); (6) offshore marls of FA6 overlaid by shoreface calcareous mudstones of FA3 and intertidal deposits of FA2 (e.g. HST.3.4. in the Aertashi section) (Figure 2.7).

The falling stage systems tracts are limited below by a basal surface of forced regression and above by an erosional unconformity (or its lateral conformity surface). FSSTs are composed of shoreface calcareous sands displaying a sharp and high angle progradational trend (e.g. FSST.1.1 in the Mine and Aertashi sections (Figure 2.7).

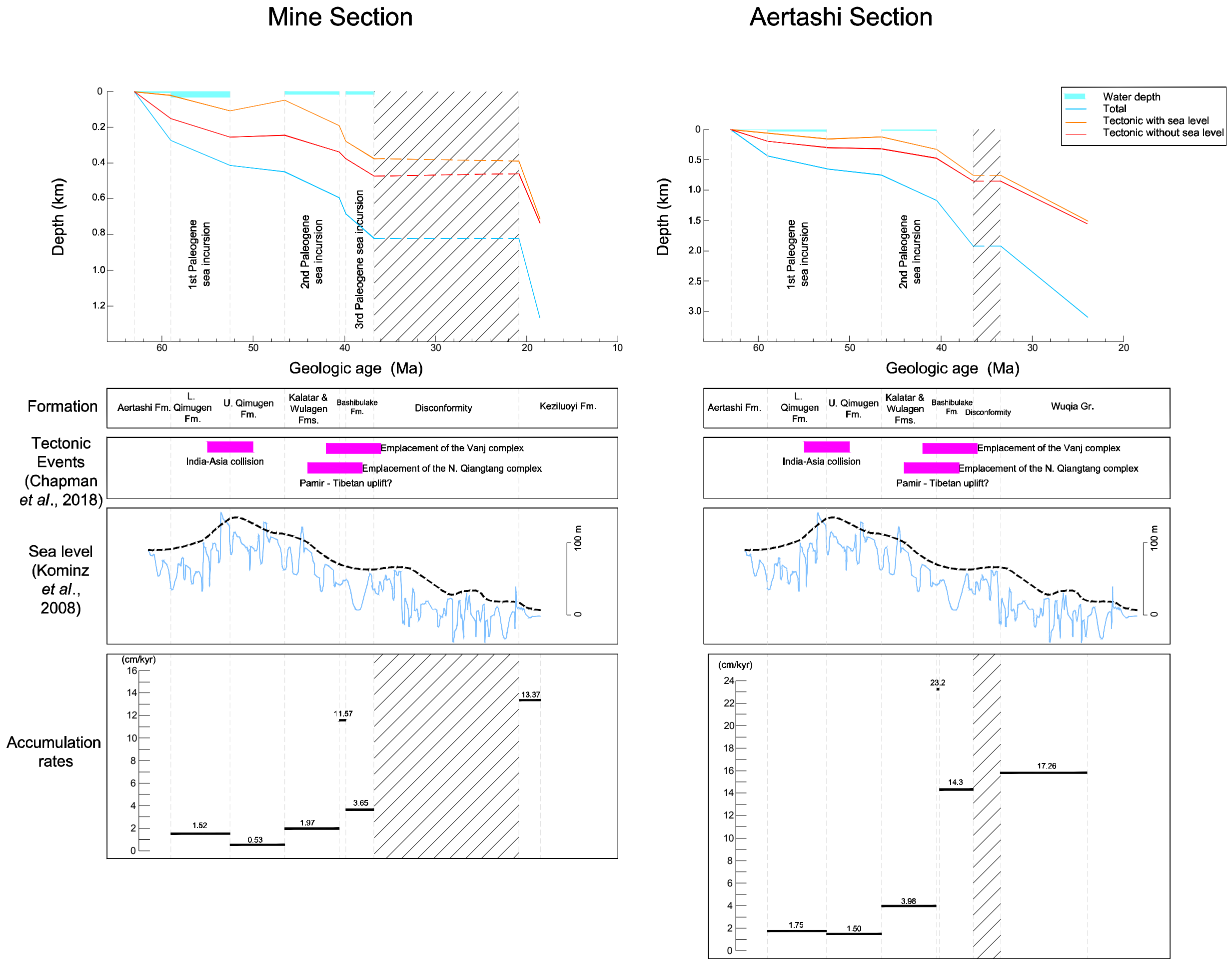
Mine Section

Aertashi Section

Figure S 2.5 The subsidence curves for the Mine and Aertashi sections were produced by performing backstripping analysis using BasinVis 1.0 (Lee et al., 2016) and then compared to the main tectonic events (Chapman et al., 2018) and global sea level curve of (Kominz et al., 2008). Data for the uppermost part of the Mine Section (unconformity and Keziluoyi Fm.) were obtained from Yang et al. (2015) and data for the uppermost part of the Aertashi section (Bashibulake Formation, unconformity and Wuqia Group) were obtained from Bosboom et al. (2014a) and Blayney et al (2016).

Sedimentary environment	Facies association	Facies/Microfacies
Alluvial plain (Fluvial, pond, playa)	FA1	Sl, Sc, Sa, Ch, Ml, Ms, Mp, Mg
Coastal plain (Supratidal including Sabkha and coastal salina, Intertidal)	FA2	Mp, Mg, Gl, MF9, MF10, MF16(a)
Restricted subtidal lagoon or bay	FA3	Mp, Sa, Ss, Cq, MF1, MF4, MF5, MF10, MF14 (a), MF15, MF16(a, b)
High-energy shoreface to shoal/beach	FA4	Cq, MF6, MF7, MF10, MF16(a)
Wave-dominated outer estuarine	FA5	MF10, MF16 (b)
Offshore	FA6	Ts, Cq, Mr, MF5, MF8, MF11, MF14 (a,b)
Hypersaline evaporitic shelf	FA7	Gl, MF2, MF3, MF12, MF13, MF14

Table S 2.1 Facies associations and their related facies/microfacies and depositional environments

Facies code	Lithology	Sedimentary structures/Other features	Interpretation
Sl	Poorly to moderately sorted coarse to medium grained sandstones	Horizontal lamination	Saltation transport of sand in rivers at high flow velocities in the upper flow regime
Sc	Poorly to moderately sorted coarse to medium grained sandstones	Cross bedding	Migration of dunes in rivers at high flow velocities in the lower flow regime
Ss	Poorly to moderately sorted fine grained sandstones	Symmetrical ripples, bioturbation, lenticular bedding	Wave reworking, migration of ripples
Sa	Poorly to moderately sorted fine grained sandstones	Asymmetrical ripples	Current reworking, migration of ripples
Ch	Poorly sorted medium to coarse sandstone	Erosive base, Scour-fill structures, rip-up clasts, megaripples, cross bedding	Deposition in channels
Mp	Siltstone, claystone, mudstone	Horizontal lamination, ripples, bioturbation, dewatering structures	Suspension settling out of fine-grained sediments in a subaqueous (pond, lake)/submarine environment
Ml	Siltstone, mudstone	Horizontal lamination or massive, traction features, rare root traces	Suspension settling out of fine-grained sediments from flood waters carried into the flood plain
Mg	Siltstone, claystone, mudstone with gypsum nodules or/and gypsum layers	Horizontal lamination or massive, some sand layers	Suspension settling out of fine-grained sediments with gypsum precipitation
Ms	Siltstone, mudstone alternating with fine sands	Sometimes with carbonate nodules, bioturbation, ripples	Crevasse splay deposits, sedimentation from both saltation and suspension on flood plain and levees
Gl	Thick gypsum (occasionally interbedded with limestones and muds)	Occasionally massive, sometimes with lamination or cross-lamination, nodular structures and ripples	Gypsum precipitation in a hypersaline lagoon/shelf with occasional carbonate precipitation and suspension settling of fine material
Cq	Coquina shell bed/bioherms	Poorly bedded to massive, calcareous cement-matrix	Abundant bivalves forming a bioherm both in high and low energy environments
Ts	Tempestites, alternation of storm and shelf muds	Graded shell beds and detrital carbonates with low angle laminations, lenticular bedding, intense bioturbation in shelf muds	Suspension settling of fine material during fair weather phase and storm influenced deposition during storms
Mr	Mudstones, marls	Horizontal lamination or massive, some shelly layers at some levels, some carbonate layers	Suspension settling out of fine-grained sediments with carbonate precipitation in marine, low energy environment

Table S 2.2 Descriptions of siliciclastic facies

Facies code	Type	Lithology	Main components	Interpretation	Sample
MF1	**Pure carbonates**	Mudstone	Micrite, rare dolomite crystals, rare unidentified allochems and bivalves	Low energy environment, deposition below wave base or in a protected environment	MI13-TS18, AT13-TS26
MF2		Mudstone with pores	Micrite with pores, very rare or no allochems	Low energy environment, deposition below wave base or in a protected environment, dissolution	MI15-C10
MF3		Peloidal wacke- to packstone	Micritic intraclasts and abundant peloids, dissolution vugs	Syn-sedimentary and post-sedimentary reworking of carbonate mud and micrite	MI15-C07, KS15-C03, KS15-C04, KS15-C07, KS15-C08, KS15-C09
MF4		Serpulid wackestone, packstone	Abundant serpulids, echinoderm fragments, foraminifera, thin bivalve shell fragments	Low energy environment, both individual and colonial serpulids	MI15-C18, AT13-TS39
MF5		Bioclastic wackestone	Bivalves, shell fragments, foraminifera, serpulids, echinoderm fragments, gastropoda, bryozoa, unidentified bioclasts, peloids	Low energy environment, deposition below wave base or in a protected environment	MI15-C23, MI13-TS01, MI13-TS06, MS13-TS33, AT13-TS05, AT13-TS32
MF6		Bioclastic packstone	Gastropoda, foraminifera, peloids, serpulids (colonial), echinoderm fragments, shell fragments, bryozoa, glauconite	Deposition in varying energy levels	MI15-C26, MI13-TS02, MI13-TS03, MI13-TS04, MI13-TS09
MF7		Oolitic grainstone	Abundant ooids, shell fragments, foraminifera, unidentified bioclasts, bryozoa	High energy environment, deposition above wave base	MI15-C20, MI15-C27, AT13-TS01, AT13-TS46
MF8	**Dolomite bearing**	Dolomitic limestone	Partly dolomitization of the cement, calcite is still the common mineral	Secondary dolomitization	MI13-TS30
MF9		Dolomite	Dolomite is the common mineral	Complete or nearly complete dolomitization	MI13-TS21, MI13-TS22 AT13-TS25
MF10	**Mixed with siliciclastics**	Proximal sandy allochem limestone	Bivalves, gastropoda, foraminifera, bryozoa, serpulids, glauconite, ooids and siliciclastics	Mixing of siliciclastics and carbonates, transport of near shore siliciclastics into intertidal and relatively deeper proximal subtidal environments by storm-surge ebb, wind forcing etc. (Punctuated mixing of Mount, 1984)	MI13-TS05, MI13-TS07, MI13-TS10, MI13-TS11, MI13-TS14, AT13-TS07, AT13-TS08, AT13-TS09 AT13-TS17, AT13-TS21, AT13-TS27, AT13-TS30, AT13-TS43, AT13-TS44, AT13-TS48, AT13-TS49
MF11		Distal sandy allochem limestone	Bivalves, gastropoda, serpulids, bryozoa, planktonic foraminifera, echinoderm fragments, glauconite and siliciclastics	Mixing of siliciclastics and carbonates, transport of tidal flat and near shore siliciclastics into deeper, distal subtidal or offshore environments by storm-surge ebb, wind forcing etc. (Punctuated mixing of Mount, 1984)	MI15-C17, MI15-C19, MI13-TS24
MF12		Mudstone with gypsum	Micrite and gypsum crystals	Carbonate and gypsum precipitation	MI15-C08, MI15-CO25

MF13		Peloidal wackestone with gypsum	Peloids, micritic intraclasts, micrite, gypsum crystals	Carbonate and gypsum precipitation	MI15-C09, MI15-C21
MF14		(a) Sandy micrite	Micrite with siliciclastic sands	Mixing of siliciclastics and carbonates, transport of tidal flat and near-shore siliciclastics into relatively deeper, subtidal or offshore environments by storm-surge ebb, wind forcing etc. (Punctuated mixing of Mount, 1984)	MI13-TS08, AT13-TS02, AT13-TS19
		(b) Sandy micrite with very rare allochems	Micrite with siliciclastic sand, a few planktonic foraminifera and shell fragments in some samples		MI15-C11, MI15-C12, MI15-C13, MI15-C14, MI15-C15, MI15-C16, MI15-C24
MF15		Micritic mudrock	Micrite and fine siliciclastics	Mixing of siliciclastics and carbonates, transport of tidal flat and near-shore siliciclastics into deeper, subtidal environments by storm-surge ebb, wind forcing etc. (Punctuated mixing of Mount, 1984)	MI15-C22
MF16		(a) Micritic sandstone	Micrite, siliciclastic sand	Mixing of siliciclastics and carbonates, transport of near-shore siliciclastics into intertidal and relatively deeper proximal subtidal environments by storm-surge ebb, wind forcing etc. (Punctuated mixing of Mount, 1984)	AT13-TS03, AT13-TS06, AT13-TS10, AT13-TS15, AT13-TS54
		(b) Micritic sandstone with very rare allochems	Micrite, siliciclastic sand, glauconite, serpulids, shell fragments, foraminifera		AT13-TS16, AT13-TS28, AT13-TS29, AT13-TS33,

Table S 2.3 Descriptions of carbonate microfacies

Formation	Sample number	Abundance	*Braarudosphaera bigelowi*	*C. dela*	*Coccolithus pelagicus*	*D. nobilis*	*Discoaster multiradiatus*	*Ericsonia* sp.	*Fasciculithus* sp.	*Fasciculithus ?magnicordis*	*Fasciculithus magnus*	*F. tympaniformis*	*Fasciculithus cf. richardii*	*Lanternithus minutus*	*Neochiastozygus junctus*	*Markalius* sp.	*Neochiastozygus* sp.	*Sphenolithus primus*	*Toweius* sp.	*Toweius rotundus*	*Tribrachiatus ?bramlettei*
L. member Qimugen	KS37	VR	2	1	5		4	1	3			2			4	1			2	1	2
	KS36	VR			2	1	2	1				3	1					1	2		
	KS35	VR															1				
	KS34	VR			1		2		3	1	1							2			
	KS33	VR			1				1				1								

Table S 2.4 Kangsu section nannofossil biostratigraphy chart

Formation	Sample number	Abundance	*Bomolithus supremus*	*Braarudosphaera* spp.	*Coccolithus bownii*	*Coccolithus pauxillus*	*Coccolithus pelagicus*	*Discoaster araneus*	*Discoaster delicatus*	*Discoaster multiradiatus*	*Discoaster nobilis*	*Ericsonia cf. subpertusa*	*Ericsonia* sp.	*Fasciculithus gr. shaubii*	*Fasciculithus involutus*	*Fasciculithus tympaniformis*	*Markalius* sp.	*Micrantholithus* sp.	*Neococcolithes junctus*	*Neococcolithes* sp.	*?Rhomboaster cf calcitrapa*	*Pontosphaera cf exilis*	*Sphenolithus moriformis*	*Toweius rotundus*	*Toweius pertusus*	*Toweius* sp.	*Zygrablithus bijugatus*	*Zygodiscus plectopons*
Kalatar	MI34	barren																										
	MI33	barren																										
U. member Qimugen	MI32	barren																										
L. member Qimugen	MI31	barren																										
	MI30	barren																										
	MI29	VR		1			3											3							1	1		
	MI28	almost barren		1														1	1				1					
	MI27	VVR					4			2												1	3	1				
	MI26	VR		1		1	2			2						1			1	1		1	2	7				
	MI25	barren																										
	MI24	VR			1	4	5	1	1	C					1						1				3		1	
	MI23	VR	1	8		3	9	1		6	1 + 1 cf			1 cf		2	1	6	5					3	1	1		1
	MI22	VR		C			7			3	1	1	1			1		C	4	1								
	MI21	barren																										
	MI20	barren																										
	MI04	barren																										
	MI03	barren																										
Aertashi	MI11	barren																										

Table S 2.5 Mine section nannofossil biostratigraphy chart

Formations	Bashibulake	Bashibulake	Wulagen	Wulagen	Wulagen	Wulagen	Wulagen
Sample code	AS01	AS02	AS15	AS14	AS13	AS12	AS11
Abundance	VR	barren	barren	R	R	R	Few
Blackites spinosus							
Braarudosphaera bigelowi				x	x	x x	x
Chiasmolithus modestus							
Chiasmolithus solitus				x			
Chiasmolithus sp.						x	
Coccolithus pelagicus	x			x		x	x x
Cribrocentrum reticulatum	x						x
Cruciplacolithus edwardsii							x
Cruciplacolithus sp.						x	x x
Cyclagelosphaera sp.							
Cyclicargolithus floridanus							
Dictyococcites bisectus	1						
Dictyococcites spp.(< 3μm)						x	x
Discoaster barbadiensis				x	x		
Discoaster saipanensis	x						
Discoaster septemradiatus							
Discoaster spp.				x	x	x	x
Eiffellithus turriseiffelii							
Ericsonia formosa							x
Lanternithus arcanus							
Lanternithus sp.							
Micrantholithus crenulatus							
Micula praemurus							
Micula cf.*prinsii*							
Micula sp.							
Monomarginatus quaternarius							
Nannotetrina sp.					1		
Neococcolithes protenus					x		
Neococcolithes dubius					x		
Pontosphaera duocava				x			
Pontosphaera exilis				x		x	
Pontosphaera sp.				x x			x
Reticulofenestra daviesii						x	
Reticulofenestra samodurovii	x					x	x
Reticulofenestra sp.(3-5 μm)	x				x		x
Sphenolithus moriformis							
Sphenolithus sp.							
Transversopontis pulcheroides				x			x
Uniplanarius gothicus							
Uniplanarius sissinghii							
Watnaueria barnesae							
Zigrablithus bijugatus				x x	x	x	

Qimugen	Kalatar	Kalatar	Kalatar	Kalatar	Wulagen	Wulagen	Wulagen
AS03	AS04	AS05	AS06	AS07	AS08	AS09	AS10
barren	R	VR	VR	R	R	R	VR
							x
				x		x x	x x
				x			
				x	x		
	x x	x	x	x		x	x
					x		
						x	
						x	x
				x	x		
				x			
				x x	x x		x
						x	
	x						
	x						
						x	x
							x
						x	x
	x	x					
	x						x
						x	x

Table S 2.6 Aksu section nannofossil biostratigraphy chart

Formations	Sample code	Abundance	*Braarudosphaera bigelowi*	*Clausicoccus* sp.	*Coccolithus pelagicus*	*Cribrocentrum erbae*	*Cribrocentrum reticulatum*	*Cyclicargolithus floridanus*	*Dictyococcites bisectus*	*Dictyococcites scrippsae*	*Discoaster barbadiensis*	*Discoaster sp.*	*Ericsonia formosa*	*Lanternithus arcanus*	*Lanthernithus minutus*	*Lanternithus* sp.	*Neococcolithes dubius*	*Pontosphaera spp.*	*Reticulofenestra daviesii*	*Reticulofenestra dictyoda*	*Reticulofenestra samodurovii*	*Reticulofenestra umbilicus*	*Reticulofenestra* spp. < 3μ	*Reticulofenestra* spp. 3-5μ	*Zigrablithus bijugatus*
Bashibulake	CD15	barren																							
Bashibulake	CD14	barren																							
Bashibulake	CD13	VR			x	x	x														x		x	x	
Bashibulake	CD12	VR		1	x	x	x x	x								x		x			x		x	x	x
Bashibulake	CD11	R			x	x x	x x					x			x	x									x
Bashibulake	CD10	VVR			x																				
Bashibulake	CD09	VVR			x																x		x	x	
Wulagen	CD08	VR			x							x					x	x			x	1		x	
Wulagen	CD07	barren																							
Wulagen	CD06	barren																							
Wulagen	CD05	barren																							
Wulagen	CD04	VR			x				x								x				x				x
Wulagen	CD03	R	x		x x			x	x	x	x		x			x	x		x	x	x x				x x
Wulagen	CD02	barren																							
Wulagen	CD01	barren																							

Table S 2.7 Shuldara section nannofossil biostratigraphy chart

Formation	L. member Qimugen				
Sample number	KS33	KS34	KS35	KS36	KS37
Acarinina multicamarata					x
Acarinina soldadonensis					x
Acarinina spp.					x
Ammobaculites spp.			x		
Ammobaculites midwayensis				x	
Ammobaculites espansus				x	
Ammodiscus sp.	x			x	
Ammomarginulina sp.				x	
Anomalinoides acutus	x		x		
Anomalinoides rubiginosus	x	x	x	x	
Anomalinoides spp.	x	x	x	x	x
Astacolus ? sp.			x		
*Baggina*spp.					x
Bolivina sp.					x
Cancris sp.					x
Cibicidoides spp.	x	x	x	x	
Evolutinella sp.				x	
Gaudryina sp.	x			x	
Globanomalina ? sp.					x
Lagenammina sp.				x	
Lenticulina sp.			x		
Lenticulina aff. *pseudomamilligera*				x	
Marssonella sp.				x	
Morozovella aequa					x
Morozovella subbotinae					x
Nonion sp.					x
Nonionella spp.					x
Osangularia aff. *plummerae*				x	
Psammosphera sp.				x	
Pyramidulina sp.				x	
Pyrulinoides sp.			x	x	
Saccammina sp.					x
Spiroplectinella laevis				x	
Textularia ? sp.				x	
Trochammina sp.			x	x	

Table S 2.8 Kangsu section foraminifera biostratigraphy chart

L. member Qimugen										**Formation**
MI20	MI21	MI22	MI23	MI24	MI25	MI26	MI27	MI29	MI30	**Sample number**
		x	x							*Acarinina multicamarata*
		x	x	x	x					*Acarinina* spp.
x			x	x	x	x	x	x		*Anomalinoides*spp.
				x	x					*Anomalinoides aegyptiacus*
x		x	x							*Baggina*spp.
		x								Bolivina sp.
						x				*Cancris* spp.
							x			*Cibicidoides* spp.
							x			*Eponides* sp.
x										*Haplophragmoides* sp.
x		x	x							*Lagenammina* sp.
x		x	x							*Morozovella* spp.
			x							*Morozovella aequa*
			x							*Morozovella subbotinae*
		x				x				*Nonionella africana*
		x	x			x				*Nonionella* spp.
						x				*Nonion* sp.
							x			*Osangularia* sp.
		x								*Parasubbotina inaequispira*
x										*Recurvoides*? sp.
							x			*Spiroplectinella* sp.
		x	x			x				*Stainforthia* sp.
		x								*Subbotina* sp.
x						x				*Trochammina* sp.
x	x									Trochamminids with flattened test

Table S 2.9 Mine section foraminifera biostratigraphy chart

Sample	Formation name	Dinocyst abundance	Pollen abundance	Dinoflagellate age estimate	Based on:
KS37	L. member Qimugen	xx		PETM	*Wilsonidium pechoricum*
KS36	L. member Qimugen	xxx		PETM	Abundance of *Apectodinium*, some specimens close to *A. augustum*
KS35	L. member Qimugen	xx		late Paleocene?	*Melitasphaeridium pseudorecurvatum*
KS34	L. member Qimugen	o		late Paleocene?	*Deflandrea oebisfeldensis*
KS33	L. member Qimugen	o		late Paleocene	*Deflandrea oebisfeldensis*

Table S 2.10 Kangsu section dinocyst biostratigraphy chart

Sample	Formation name	Dinocyst abundance	Dinoflagellate age estimate	Based on:	Notes
MI34	Kalatar FM		`		barren
MI33	Kalatar FM	x	younger than ~52.5 Ma	*Samlandia* spp. (cf. Iakovleva & Heilmann-Clausen 2010)	
MI32	U. member Qimugen FM	-			almost barren
MI31	L. member Qimugen FM	-			almost barren
MI30	L. member Qimugen FM	xxx	earliest Eocene	as below, no *Wetzeliella* recorded	
MI29	L. member Qimugen FM	xxx	earliest Eocene	as below	
MI28	L. member Qimugen FM	xxx	earliest Eocene	*Melitasphaeridium pseudorecurvatum*	
MI27	L. member Qimugen FM	xxx	earliest Eocene	some *Apectodinium, Muratodinium fimbriatum*	
MI26	L. member Qimugen FM	xxx	PETM/earliest Eocene	*Polysphaeridium subtile, Apectodinium*, but no other Wetzellioideae	Abundant low-salinity tolerant dinocysts
MI25	L. member Qimugen FM	xxx	PETM/earliest Eocene	*Apectodinium*, but no other Wetzellioideae	
MI24	L. member Qimugen FM	xxx	PETM	*Eocladopyxis* spp., multiple *Apectodinium* species, *Muratodinium fimbriatum*	PETM marker *A. augustum* not recorded
MI23	L. member Qimugen FM	xxx	PETM	High abundance of multiple *Apectodinium* species	PETM marker *A. augustum* not recorded
MI22	L. member Qimugen FM	xxx	PETM	High abundance of multiple *Apectodinium* species	PETM marker *A. augustum* not recorded
MI21	L. member Qimugen FM	xx	PETM	common *Apectodinium*, common Areoligeraceae	PETM marker *A. augustum* not recorded
MI20	L. member Qimugen FM	xx	PETM	Very abundant *Apectodinium*	Some specimens that are morphologically close to *A. augustum*

Table S 2.11 Mine section dinocyst biostratigraphy chart

Sample no.	**Dinocyst yield**	**Approximate age**	**Based on:**	**Dominant/Important secondary species**
AS01		Tentatively assigned to MECO	*Dracodinium rhomboideum**	*Rhombodinium draco*
AS02	barren			
AS15		middle-late Eocene (likely still older than C19)	general absence of *R. draco*, *Thalassiphora reticulata/fenestrata*, *Cordosphaeridium funiculatum*	
AS14		few diagnostic, see samples above and below		
AS13		few diagnostic, see samples above and below		
AS11		few diagnostic, see samples above and below		
AS10		younger than C20r	*Heteraulacacysta porosa*	*Wetzeliella astroides*, *W. irthychiensis*, *Cerebrocysta bartonensis*
AS9		younger than C20r	*Heteraulacacysta porosa, Turbiosphaera magna*	*Charlesodowniea coleotrypta*, *Thalassiphora pelagica*
AS8		younger than C20r	*Heteraulacacysta porosa*	
AS7	barren			
AS6		middle Eocene	*Rhombodinium pentagonum* (abundant), diverse *Phthanoperidinium*	
AS5		middle Eocene	*Rhombodinium pentagonum* (abundant), diverse *Phthanoperidinium*	Assemblage dominated by low-salinity tolerant species and stratification indicators
AS4		middle Eocene (C20) or older	*Adnatosphaeridium vittatum**	Assemblage dominated by low-salinity tolerant species and stratification indicators
AS3		Paleogene	*Diphyes colligerum*	Assemblage dominated by low-salinity tolerant species

Table S 2.12 Aksu section dinocyst biostratigraphy chart

Sample no.	Dinocyst yield	Approximate age	Based on:	Other remarks	Dominant/Important secondary species
CD02	barren				
CD03	barren				
CD04	barren				
CD05	barren				
CD06	barren				
CD07	barren				
CD08	barren except few fragments				
CD09		mid-late Eocene	*Areosphaeridium michoudii, Rhombodinium* cf. *draco*	*Charlesdowniea coleotrypta*	
CD10		Tentatively assigned to MECO	*Dracodinium rhomboideum*	*Lentinia* spp., *Rhombodinium draco*	
CD11		late Eocene (C17n.1n / NP18 or younger)	*Thalassiphora fenestrata*		
CD12		see above			
CD13		see above		Restricted?	*Homotryblium tenuispinosum*
CD14	barren except few *Homotryblium*		Restricted?	*Homotryblium tenuispinosum*	
CD15	barren				

Table S 2.13 Shuldara section dinocyst biostratigraphy chart

Chapter 3

3. Cretaceous evolution of the Central Asian proto-Paratethys Sea: tectonic, eustatic and climatic controls

Abstract

The timing and mechanisms of the Cretaceous sea incursions into Central Asia are still poorly constrained. We provide a new chronostratigraphic framework based on biostratigraphy and magnetostratigraphy together with detailed paleoenvironmental analyses of Cretaceous records of the proto-Paratethys Sea fluctuations in the Tajik and Tarim basins. The Early Cretaceous marine incursion in the western Tajik Basin was followed by major marine incursions during the Cenomanian (ca. 100 Ma) and Santonian (ca. 86 Ma) that reached far into the eastern Tajik and Tarim basins. These marine incursions were separated by a Turonian-Coniacian (ca. 92-86 Ma) regression. Basin-wide tectonic subsidence analyses imply that the Early Cretaceous sea incursion into the Tajik Basin was related to increased Pamir tectonism. We find that thrusting along the northern edge of the Pamir at ca. 130–90 Ma resulted in an increased subsidence in a retro-arc basin setting. This tectonic event and coeval eustatic highstand resulted in the maximum observed geographic extent of the sea during the Cenomanian (ca. 100 Ma). The following Turonian-Coniacian (ca. 92-86 Ma) major regression, driven by eustasy, coincides with a sharp slowdown in tectonic subsidence related to a regime change in Pamir tectonism from compression to extension. The Santonian (ca. 86 Ma) major sea incursion was likely controlled by eustasy as also evidenced by the coeval fluctuations in the west Siberian Basin. An early Maastrichtian cooling (ca. 71-70 Ma), potentially connected to global late Cretaceous trends, is inferred from the replacement of mollusk-rich limestones by bryozoan-rich and echinoderm-rich limestones.

3.1. Introduction

The proto-Paratethys Sea was a shallow epicontinental sea that extended across Eurasia from the Mediterranean Tethys to China. The proto-Paratethys sea incursions occurred during the Cretaceous and Paleogene until its drastic retreat during the late Eocene, followed by its isolation as the Paratethys during the Oligocene and Miocene (e.g. Kaya et al., 2019; Naidin et al, 1980; Popov et al., 2004). The fluctuations of this sea across Eurasia have not only shaped Asian paleoenvironments, but also provide a valuable record of Asian tectonism and eustatism (e.g. Bosboom et al 2017; 2014; Carrapa et al., 2015; Hendrix et al., 1992; Kaya et al., 2019; Ramstein et al., 1997; Sun et al., 2016; Wang et al., 2019). We focus here on the onset and early history of these fluctuations during the Cretaceous and early Paleogene because the timing and drivers of the sea incursions into Central Asia still remain unclear. This ambiguity can be attributed to the lack of consensus on the extent, timing and depositional environments of the sea incursions despite numerous previous studies (e.g. Guo et al., 2015; Hao et al., 1988; Hao & Zeng, 1984; He, 1991; Lan & Wei, 1995; Mao & Norris, 1988; Naidin et al., 1980; Pan, 1991; Pojarkova, 1984; Sobel, 1995; Sun, 1991; Tang et al., 1992b, 1989; Wang et al., 1990; Wang et al., 2014; Xi et al., 2016; Yang, 1991; Yang et al., 1995; Yang et al., 1983; Zhang, 1992). While numerous, these studies propose different interpretations on the age, importance and even the number of the sea incursions across Central Asia (e.g. Guo, 1991; Hao et al. 1998). These differences may result from the spatially-limited observations and from published biostratigraphic ages relatively low in resolution, often based on the benthic fossils carrying significant uncertainty. Recently published reviews of regional geology and radiochronological ages result in contrasting interpretations (e.g. Chapman et al., 2019; Xi et al., 2019 and references therein). The lack of higher resolution age constraints and comprehensive paleogeographic reconstructions implies that the controlling factors for the Cretaceous sea incursions and their potential consequences on Asian environments remain unresolved.

It is often suggested that the Cretaceous transgressions and regressions in the Tajik and Tarim basins were controlled by global sea-level fluctuations (Guo et al., 2015; Naidin et al., 1980; Sobel, 1995; Wang et al., 2014; Xi et al, 2016). Yet, three prominent geodynamic events, while distant to the south, are usually considered to have governed the Cretaceous subsidence of the Tajik and Tarim basins. As a consequence, it is likely also far-field tectonics influenced the Cretaceous sea incursions. The geodynamic events include (1) the collision of the Lhasa and Qiangtang blocks (e.g. Hendrix et al., 1992; Jolivet, 2017; Sobel, 1999), (2) the collision of the Central Afghan blocks with the southern Eurasian margin (e.g. Montenat, 2009; Tapponnier et al., 1981), and (3) the Kohistan-Ladakh-Eurasia collisions (e.g. Aminov et al., 2017; Bouilhol et al., 2013). These events are important to understand the India-Asia collision, Pamir-Tibetan orogeny and associated deformation in Central Asia in the form of reactivation of inherited crustal and lithospheric structures (Jolivet, 2017; Robinson, 2015). Better constraints on the geodynamic driving mechanism behind basin formation are also required to differentiate tectonic from climatic and eustatic signals recorded in the sedimentary rocks.

The Cretaceous marine record from the Tajik Basin, yet poorly dated and documented, is exceptionally well preserved and exposed, providing an excellent opportunity to assess marine fluctuations and their connections to global climate events. In particular, the early Late Cretaceous period (late Cenomanian-early Turonian, ca. 95-90 Ma) witnessed one of the warmest climates of the past 140 million years followed by a transition to significant global cooling spanning from the late Turonian to the Maastrichtian, ca. 90-66 Ma (Linnert et al., 2014). These multimillion-year global temperature fluctuations in ice-free conditions are generally thought to be driven by a combination of $p\mathrm{CO}_2$ and ocean gateway evolutions (Clarke & Jenkyns, 1999; Friedrich et al., 2012; Linnert et al., 2014; Miller et al., 2005). Short-lived (<1 Ma) Oceanic Anoxic Events (OAEs) associated with episodes of organic carbon burial characterized by the widespread deposition of black shales were also documented in a variety of marine settings under the warm climate of the Aptian-Turonian (ca. 125-90 Ma) (e.g. Schlanger & Jenkyns, 1976). The thick, mollusk- and bryozoa-rich Late Cretaceous carbonate deposits of the Tajik Basin are excellent candidates for the examination of these global climate events. These carbonate-producing organisms react sensitively to changes in the environment (e.g. water depth, light intensity, nutrient input, water temperature, hydrodynamic energy) and neritic carbonates can hence be used as excellent proxies to reveal environmental changes (e.g. Jaramillo-Vogel et al., 2013; Pomar et al., 2004).

To better understand the timing, cause and effect of the proto-Paratethys sea fluctuations across Central Asia during Cretaceous times, we studied a suite of sedimentary sections throughout the Tajik and Tarim basins. We analyzed the depositional environments and their evolution to interpret the marine transgressions and regressions and developed an improved regional stratigraphic framework using new biostratigraphic and magnetostratigraphic constraints. The comparison of regional environmental records to established geodynamic/tectonic and global climate events allowed us to discuss the controlling mechanisms behind the sea incursions in the proto-Paratethys sedimentary records.

3.2. Geological setting

3.2.1. Tectonic setting

The Tajik and Tarim basins are parts of continental fragments successively accreted to each other along a system of sutures mainly related to the Cimmeride and Alpide orogenies (e.g. Robinson, 2015; Şengör, 1984) (Figure 3.1). The Mesozoic Tajik basin has been interpreted differently as a (1) foreland basin (Chapman et al., 2019; Hamburger et al., 1992; Şengör, 1984), (2) cratonic basin (Burtman & Molnar, 1993; Burtman, 2000; Nikolaev, 2002), (3) passive margin (Leith, 1985) or (4) back-arc basin (Tapponnier et al., 1981; Thomas et al., 1999), whereas the Mesozoic Tarim Basin has been mostly explained as a foreland basin (Hefu, 1986; Hendrix et al., 1992; Watson et al., 1987).

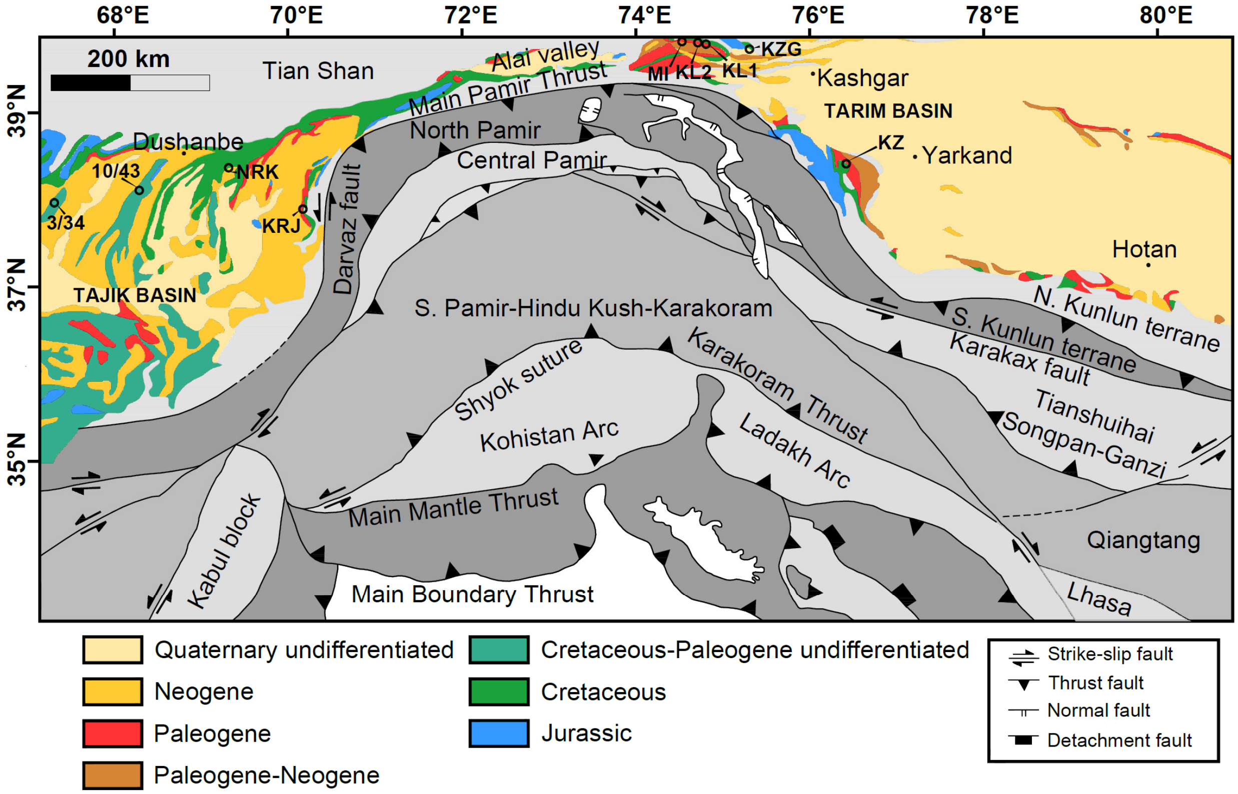

Figure 3.1 Locations of the studied sections in the Tarim (MI: Mine, KL1: Ka Latale 1, KL2: Ka Latale 2, KZG: Kuzigongsu, KZ: Kezi) and Tajik (NRK: Nurek, KRJ: Khirmanjo) basins on a schematic geologic map with major tectonic domains (shaded in grey) within the Pamir and western Tibetan Plateau in Central Asia (modified from Carrapa et al., 2015 and Cowgill, 2010). Locations of the two sections, 3/34 and 10/43 from Burtman (2000) on which subsidence analysis was performed for the west and central Tajik Basin, are also shown.

The Pamir separates the Tajik and Tarim basins and forms the western extension of the Tibetan Plateau in an arcuate convex salient (Figure 3.1). It has generally been divided into three tectonic domains: the North Pamir, Central Pamir, and South Pamir (e.g. Burtman & Molnar, 1993) (Figure 3.1). The North Pamir is composed of mainly Paleozoic and Triassic (meta)sedimentary and metavolcanic rocks intruded by Triassic-Jurassic granitoids (Schwab et al., 2004). The Central Pamir consists of Paleozoic, Mesozoic (Triassic, Jurassic and Cretaceous) and Cenozoic (Oligocene) (meta)sedimentary rocks, gneiss domes of various protolith types and ages (He et al., 2019; Schwab et al., 2004) and Late Cretaceous, Eocene and Miocene igneous rocks (Chapman et al., 2018b). The South Pamir is composed of Paleozoic, Triassic and Jurassic (meta)sedimentary rocks affected by Cretaceous and Cenozoic magmatism and metamorphism (Schwab et al., 2004). To the south, the Karakoram block consists of deep crustal metamorphics, Cretaceous to Cenozoic intrusive and sedimentary rocks and the Kohistan-Ladakh block comprises predominantly Cretaceous oceanic island arc rocks (e.g. Blayney et al., 2016). The complex tectonic evolution of the Pamir has been discussed in many studies with several proposed processes such as slab roll-back, subduction erosion, subduction accretion and marginal slab-tear (e.g. Burtman & Molnar 1993; Hamburger et al., 1992; Kufner et al., 2016; Replumaz et al., 2010; Sobel et al., 2013). The formation of the arcuate shape of the Pamir has been interpreted by two end-member models, including the Neogene gradual deformation and the inherited, pre-existing arcuate Pamir that was formed by the successive accretions of Paleozoic-Mesozoic continental fragments onto southern Eurasia prior to the India-Asia collision (Blayney et al., 2019; Chen et al., 2018 and references therein).

Before the Paleogene India-Asia collision, several accretionary events might have governed successive regional tectonic regimes, but the timing of these accretionary events and tectonic regime shifts remain poorly constrained. The collision of the Lhasa and Qiangtang blocks, represented by the closure of the Meso-Tethys Ocean, has been controversially dated between mid-late Jurassic and Late Cretaceous (Bian et al., 2017; Kapp et al., 2007; Ma et al., 2017; Sun et al., 2019; Wang et al., 2016; Yang et al., 2019). Diachronous suturing has also been suggested such that the collision between the Lhasa and Qiangtang blocks appeared earlier in the east during the mid-Jurassic, while initial collision towards the west would have taken place during the late Early Cretaceous to early Late Cretaceous (Guo et al., 2019; Kapp & DeCelles, 2019). To the west, in Afghanistan, a Late Jurassic-Early Cretaceous age has been proposed for the suturing of the Central Afghan blocks to the southern Eurasian margin (e.g. Montenat, 2009; Otto, 1997; Tapponnier et al., 1981). The collision-age between the Kohistan Arc and the southern margin of Eurasia is also highly uncertain and estimates range from 100-80 Ma (Aminov et al., 2017; Borneman et al., 2015; Faisal et al., 2014; Fraser et al., 2001; Robertson & Collins, 2002) to 50-40 Ma (Bouilhol et al., 2013; Khan et al., 2009).

In addition to the commonly accepted Cenozoic thickening that formed the 90 km thick continental crust (Rutte et al., 2017a, b; Stübner et al., 2013a, b), pre-Cenozoic deformation involving significant Mesozoic upper-crustal shortening and related crustal thickening in the Central and South Pamir has also been proposed (e.g. Aminov et al., 2017; Robinson, 2015). Late Jurassic and mid-Cretaceous crustal shortening and thickening in the North Pamir and Karakoram regions to the north and south of the Central and South Pamir have also been evidenced, suggesting that the Central and South Pamir were similarly affected by the same deformation events (e.g. He et al., 2019; Imrecke et al., 2019; Robinson et al., 2004, 2012; Robinson, 2015).

The evolution of the Tian Shan located north of the Tajik and Tarim basins initiated during the Carboniferous in an ocean subduction-continental accretion complex (Jolivet et al., 2013; Şengör et al., 1993). Limited activity has been reported in the Cretaceous-Paleogene before the major exhumation and uplift of the Tian Shan during the Oligocene-Miocene (Sobel et al., 2006; Yang et al., 2015).

3.2.2. Stratigraphic setting

Jurassic to Paleogene marine, transitional (mixed terrestrial-marine) and terrestrial sedimentary rocks unconformably overlay the basement in the Tajik Basin. The Jurassic to Paleogene rocks, in turn, are unconformably overlain by Paleogene-Neogene syn- and post-orogenic continental clastics. The Mesozoic-Cenozoic strata have been classified and organized in a complex nomenclature of numerous formations (e.g. Brookfield & Hashmat, 2001; Dzhalilov et al., 1982; Nikolaev, 2002). The Tarim Basin Precambrian basement is covered by marine and terrestrial Paleozoic carbonates and fine-grained clastics. The Mesozoic-Cenozoic strata contain terrestrial red clastics and marine carbonates, clastics and evaporites (e.g. Klocke et al., 2017; Zhang et al., 2013). Cretaceous successions in the western Tarim Basin are classified into groups of formations defined by their predominantly marine or terrestrial depositional environments. The Lower Cretaceous Kezilesu Group consists of red clastics of conglomerates, sandstones and mudstones (Guo et al., 2015). The Upper Cretaceous Yingjisha Group is composed of gray marls, mudstones and carbonates of the Kukebai Formation, red gypsiferous mudstones of the Wuyitake Formation, beige, gray carbonates and calcareous mudstones of the Yigeziya Formation and red gypsiferous mudstones of the Tuyiluoke Formation.

We followed mostly the nomenclature used in Dzhalilov et al. (1982) for the stratigraphy of the Tajik Basin. To simplify the stratigraphic classification, we established groups for the local formations in the Tajik Basin based on appropriate geographic names (Table 3.1). Geographic locations near which the aggregated local formations are present as complete successions were used for naming. The Shirabad-Akkapghigai-Luchak-Derbent-Karakuz-Kaligrek-Okuzbulak-Kizyltash-Almurad Karabil formations were classified together to be the Gashion Group. The Dazgiriak-Talhab-Gazdahana-Tagara-Karikansai-Tjubegatan formations were aggregated into the Baldzhuvon Group, and the Bulgary-Udantu-Daralitau-Sarykamish-Kattakamysh-Akrabat-Modun formations were aggregated into the Argankun Group. A regional correlation across the Tajik and Tarim basins for the Cretaceous deposits (Table 3.1) is proposed based on our lithostratigraphic, biostratigraphic and sequence stratigraphic interpretations presented in detail later in this paper, along with a review of existing lithostratigraphic descriptions, correlations and nomenclatures (e.g. Dzhalilov et al., 1982). The Kezilesu Group is correlated to the Gashion Group in the Tajik Basin. The Kukebai Formation is interpreted to be correlative to the Baldzhuvon Group within the Tajik Basin. The Wuyitake and Yigeziya formations are correlated to the Muzrabat Formation and the Argankun Group in the Tajik Basin, respectively. The Tuyiluoke Formation is correlated to the red gypsiferous mudstone unit at the base of the Akdjar Formation in the Tajik Basin. The underlying correlations of the proposed nomenclature are justified in this study.

For the Tajik Basin, a different formation nomenclature has been recently proposed by Chapman et al. (2019) based on their observations and age controls from the Dashtijum section in the southeast Tajik Basin (Table 3.1). In detail, they defined the Hasarak-bolo, Schuchi-poyon, Sangoba and Bukhara formations and correlated them with the local formations. The local Dazgiriak-Talhab-Gazdahana-Tagara-Karikansai-Tjubegatan formations are, as described by Dzhalilov et al. (1982), mainly composed of marine strata of grey mudstones, marls with bivalves and ammonites, coquina limestones and sandstones. These lithologies are very different from the Schuchi-poyon Formation of Chapman et al. (2019) that consists of sandstones, dark red siltstones and conglomerates interpreted as fluvial channel and overbank deposits. The

Hasarak-bolo Formation consists of siltstone and sandstone interpreted as marginal marine deposits (Chapman et al., 2019). Similarly, the Kattakamysh-Akrabat-Modun formations that contain grey mudstones, marls and limestones and coquina beds (Dzhalilov et al., 1982) are different from the Hasarak-bolo Formation of Chapman et al. (2019). These newly described formations in Chapman et al. (2019) have been interpreted to be time correlative with the local formations of Dzhalilov et al. (1982) mostly based on new age control. The abovementioned lithology differences suggest significant lateral facies change that we have not observed in the field. These discrepancies of correlation were resolved by new age determinations in the present study.

<table>
<tr><th rowspan="3">Age</th><th rowspan="3">Lithology</th><th>Tarim Basin</th><th colspan="3">Tajik Basin</th></tr>
<tr><th colspan="2">This study</th><th>Dzhalilov et al. (1982)</th><th>Chapman et al. (2019)</th></tr>
<tr><th colspan="4">Formation/Group</th></tr>
<tr><td>Danian-Selandian</td><td>Gypsum and dolomites</td><td>Aertashi</td><td colspan="2" rowspan="2">Akdjar</td><td rowspan="3">Bukhara</td></tr>
<tr><td>Maastrichtian-Danian?</td><td>Red mudstones with interbeds of red siltstones, sandstones and gypsum</td><td>Tuyiluoke</td></tr>
<tr><td rowspan="3">Santonian - Maastricthian</td><td rowspan="3">Limestones, sandy limestones, coquinas, grey and variegated sandstones, marls, mudstones and siltstones bearing bivalves, ammonites, echinoderms with some gypsum interlayers</td><td rowspan="3">Yigeziya</td><td rowspan="3">Argankun Group</td><td rowspan="3">Bulgary
Udantu
Daralitau
Sarykamish
Kattakamysh
Akrabat
Modun</td></tr>
<tr><td>Sangoba</td></tr>
<tr><td rowspan="3">Hasarak-bolo</td></tr>
<tr><td>Late Turonian - Coniacian</td><td>Grey mudstones bearing brackish-water ostracods with interbeds of limestones, gypsum, red siltstones and sandstones</td><td>Wuyitake</td><td colspan="2">Muzrabat</td></tr>
<tr><td rowspan="2">Cenomanian - Early Turonian</td><td rowspan="2">Grey, dark-grey mudstones bearing ammonites, echinoids and bivalves with interbeds of marls, coquinas, limestones, sandy limestones, sandstones, siltstones and gypsum</td><td rowspan="2">Kukebai</td><td rowspan="2">Baldzhuvon Group</td><td rowspan="2">Dazgiriak
Talhab
Gazdahana
Tagara
Karikansai
Tjubegatan</td></tr>
<tr><td rowspan="2">Schuchi-poyon</td></tr>
<tr><td>Early Cretaceous</td><td>Red terrigenous sandstones and siltstones alternating with claystones, gypsum, dolomites and marls</td><td>Kezilesu Group</td><td>Gashion Group</td><td>Shirabad
Akkapghigai
Luchak
Derbent
Karakuz
Kaligrek
Okuzbulak
Kizyltash
Almurad
Karabil</td></tr>
</table>

Table 3.0.1 Depositional ages, simplified lithological descriptions and lithostratigraphic correlations for the Cretaceous formations and groups in the Tajik and Tarim basins

3.3. Materials and methods

The Nurek (38° 21.898'N, 69° 19.997'E) and Khirmanjo (37° 54.389'N, 70° 9.174'E) sections were analyzed in detail to establish the stratigraphic framework of the Cretaceous sea fluctuations in the Tajik Basin (Figure 3.1). We also examined five sections (Kuzigongsu 39° 44.970'N, 75° 17.935'E; Kezi 38° 25.078'N, 76° 23.229'E; Mine 39° 50.860'N, 74° 30.124'E; Ka Latale 1 39° 49.336'N, 74° 41.246'E and Ka Latale 2 39° 50.217'N, 74° 39.033'E) from the Tarim Basin (Figure 3.1). In total, ca. 4.5 km stratigraphic thickness was measured and logged. Field observations include lithologies, facies, sedimentary structures, fossil content and discontinuity surfaces. Fine-grained siliciclastic (samples labeled with "B") and carbonate rock samples (labeled with "C") were collected from all sections for biostratigraphic and microfacies analyses. Foraminifera, calcareous nannofossils, ostracods and dinoflagellate cysts (dinocysts) were identified and used for age correlations based on their previously established age ranges (Figure 3.2, Table 3.2 & Supporting Information Text S6 for details). In total, 562 carbonate thin sections were analyzed for microfacies analysis which were used to determine depositional environments. Microfacies analysis in combination with facies descriptions from the field also enabled us to define depositional sequences and their bounding surfaces. Carbonate grain abundances were estimated using charts of Bacelle & Bosellini (1965). The percentages of components of bryozoa, mollusk, echinoderm and non-skeletal ooid grains were determined to mechanistically resolve the biotic changes within the Nurek and Khirmanjo sections (Figure 3.5). We also collected paleomagnetic core samples from the Khirmanjo (82 samples), Mine (60 samples), and Ka Latale 1 (42 samples) sections for magnetostratigraphic analyses. In addition to intra-basinal correlations, inter-basinal correlation was conducted by using the sequence stratigraphic interpretations and biostratigraphic constraints from the Nurek, Khirmanjo, Mine, Ka Latale 2 and Ka Latale 1 sections. Details of the sedimentological, sequence stratigraphic and magnetostratigraphic methods are provided in Supporting Information (Text S1 to S5).

We produced subsidence and relative sea-level curves (Figure 3.6 & S 3.6) based on the results from the sections in the Tajik and Tarim basins to derive implications on the potential controlling mechanisms of the sea incursions. Relative sea-level curves were generated by assigning paleo-water depths to the defined facies/microfacies based on their relative positions to each other on the epeiric ramp (Figure 3.3). Maximum water depth was assumed as 50 m and 30 m for distal ramp offshore and proximal ramp subtidal facies, respectively as proposed for epeiric ramps (Lukasik et al., 2000) (Figure S 3.6). Even though there are uncertainties of the assigned paleo-water depth values for the facies/microfacies, their relative position to each other provides solid qualitative insight for the relative sea level change during the Cretaceous sea incursions.

The subsidence curves for the Khirmanjo and Nurek sections in the east Tajik Basin and Kezi and Kuzigongsu sections in the Tarim Basin were produced by performing subsidence analysis using BasinVis 1.0 (Lee et al., 2016). The subsidence analysis integrates the sedimentological, biostratigraphic and magnetostratigraphic results obtained in this study (see Supporting Information Table S 3.13 for details of the input data for the subsidence analysis). In addition, subsidence analysis for the west and central Tajik Basin was performed on two sections (3/34 &

10/43) from Burtman (2000) (Figure 3.1). The porosity and compaction coefficients for different lithologies were adopted from Sclater and Christie (1980). Eustatic changes in sea level (Kominz et al., 2008) were included during analysis. The thickness of the red gypsiferous mudstone unit of the Akdjar Formation, correlated to the Tuyiluoke Formation in the Tarim Basin was taken from Burtman & Molnar (1993). The thickness of the Gashion Group, correlated to the Kezilesu Goup in the Tarim Basin, at the Nurek section was adopted from Leith (1985). The thickness of the Gashion Group at the Khirmanjo section was taken from Burtman and Molnar (1993), whereas that of the Kezilesu Group at the Kuzigongsu and Kezi sections was adopted from Sobel (1995) and Sobel (1999). Subsidence curves display both the total (basement) subsidence and tectonic subsidence calculated by using decompaction and backstripping techniques, respectively.

The local fluctuations in the relative sea-level were used along with the subsidence curves to elucidate the potential tectonic and/or eustatic driving mechanisms (Figure 3.6). Furthermore, the refined age constraints and paleoenvironmental interpretations are combined to generate detailed paleogeographic maps based on the results of this study and existing literature (Figure 3.8). The maps from the Darius project (Barrier et al., 2018) were updated with data from Kontorovich et al. (2014) for the West Siberian Sea and with data from Kapp and DeCelles (2019) for the Southern Tibet areas.

3.4. Results & Interpretations

3.4.1. Biostratigraphy

3.4.1.1. Calcareous nannofossils

Tajik Basin

Nurek (NR) section

In sample NR-B25, the presence of *Gartnerago segmentatum* suggests a correlation with the base of the UC2 biozone (Burnett, 1998), early Cenomanian in age (Figure 3.2).

The assemblage of sample NR-B27 is characterized by the occurrence of *Microrhabdulus decoratus, Rotelapillus biarcus* and *Eprolithus octopetalus*. The first occurrence of this latter species marks the base of subzone UC5c, allowing a correlation with the uppermost Cenomanian.

Sample NR-B30 yields few specimens of *M. decoratus*, and very few specimens of *Eprolithus moratus,* suggesting a correlation with the UC6b subzone of the lowermost Turonian. In sample NR-B35 *E. moratus* is common, indicating an early Turonian age. For sample NR-B36, a Turonian age is also assigned on the basis of the occurrence of *Quadrum gartneri*, marker of the base of UC7 zone. Based on these results, the Baldzhuvon Group in the Nurek section which is correlated to the Kukebai Formation in the Tarim Basin, might be Cenomanian to early Turonian in age.

In sample NR-B44, the occurrence of *Calculites obscurus* yields an age not older than the late Santonian. This species marks the base of zone CC17 (Sissingh, 1977), which has a calibrated age of 84.08 Ma (Gradstein et al., 2012). In the same sample, single specimen of *Uniplanarius* cf. *sissinghi*, marker of the UC15b subzone, could suggest a Campanian age.

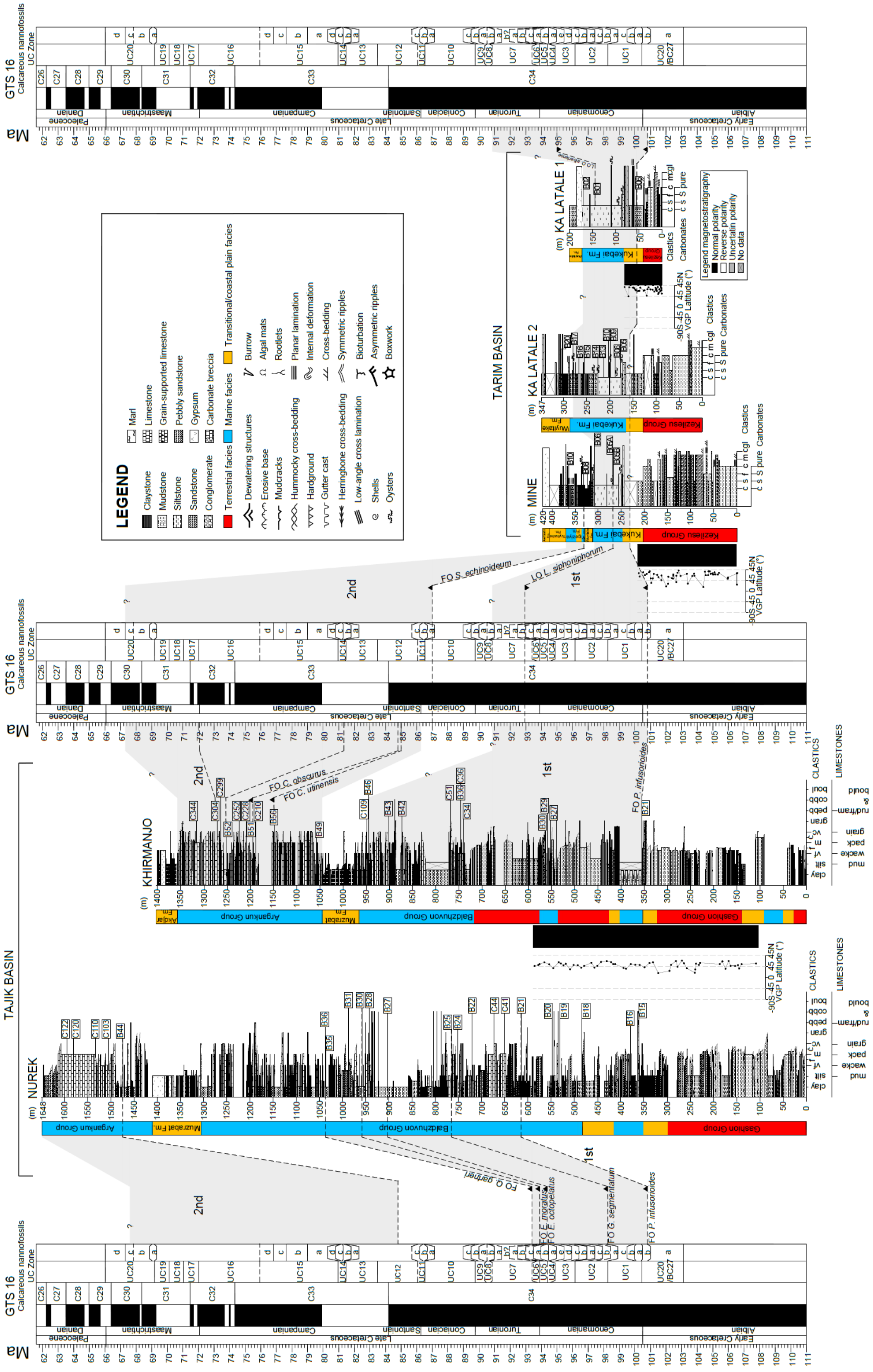
TAJIK BASIN
TARIM BASIN
NUREK
KHIRMANJO
MINE
KA LATALE 2
KA LATALE 1
GTS 16
Calcareous nannofossils
UC Zone
Ma
Paleocene
Danian
Maastrichtian
Campanian
Late Cretaceous
Santonian
Coniacian
Turonian
Cenomanian
Albian
Early Cretaceous
Arganikun Group
Muzrabat Fm.
Baldzhuvon Group
Gashion Group
Kezilesu Group
Kukebai Fm.
Wuyitake Fm.
1st
2nd
FO O. gartneri
FO E. moratus
FO E. octopetalus
FO G. segmentatum
FO P. infusorioides
FO C. obscurus
FO C. ultinensis
FO S. echinoideum
LO L. siphoniphorum
VGP Latitude (°)
CLASTICS
LIMESTONES
clay silt vf f m c vc gran pebb cobb boul
mud wacke pack grain rud/fram & bould
Clastics
Carbonates
LEGEND
Claystone
Mudstone
Siltstone
Sandstone
Conglomerate
Marl
Limestone
Grain-supported limestone
Pebbly sandstone
Gypsum
Carbonate breccia
Terrestrial facies
Marine facies
Transitional/coastal plain facies
Dewatering structures
Erosive base
Mudcracks
Hummocky cross-bedding
Hardground
Gutter cast
Herringbone cross-bedding
Low-angle cross lamination
Shells
Oysters
Burrow
Algal mats
Rootlets
Planar lamination
Internal deformation
Cross-bedding
Symmetric ripples
Bioturbation
Asymmetric ripples
Boxwork
Legend magnetostratigraphy
Normal polarity
Reverse polarity
Uncertain polarity
No data

Figure 3.2 Stratigraphic logs of the Nurek, Khirmanjo, Mine, Ka Latale 1 and Ka Latale 2 sections showing biostratigraphic and magnetostratigraphic correlations to the geological time scale (Ogg et al., 2016). The age correlations based on microfossil assemblages are shown by light grey shading corresponding to the stratigraphic ranges of dinoflagellate cysts and nannofossils. FO: first occurrence of important age-diagnostic biomarker species, LO: last occurrence of important age-diagnostic biomarker species.

Khirmanjo (KR) section

Sample KR-B51 yields very rare specimens of *Calculites obscurus*, *Micula staurophora*, *Eiffellithus gorkae*, *Lucianorhabdus cayeuxii* and *Uniplanarius gothicus*, indicating an age not older than the late Santonian.

The assemblage of sample KR-B52 is characterized by the occurrence of very rare specimens of *Eiffellithus eximius* and *Arkangelskiella cymbiformis*, rare specimens of *Chiastozygus litterarius, Cribrosphaera ehrenbergii*, *Micula staurophora* and *W. barnesiae*. The occurrence of *Broinsonia parca constricta*, marker of the base of subzone UC14b, indicates for this sample a Campanian age.

3.4.1.2. Dinoflagellates cyst

Tarim Basin

Mine (MI) Section

The lowermost productive samples (MI-B05A, MI-B05B) contain both *Litosphaeridium siphoniphorum* (Last occurrence, LO, Cenomanian-Turonian, ca. 93 Ma, e.g. Pearce et al., 2009) and abundant *Palaeohystrichophora infusorioides* (First occurrence, FO, ca. 100 Ma, Albian-Cenomanian), suggesting Cenomanian-early Turonian ages. Sample MI-B08 from the Yigeyiza Formation contains a more diverse assemblage, including *Xenascus ceratoides*, diverse *Florentinia* spp., *Alterbidinium* spp. and a few specimens of *Spinidinium echinoideum.* The data constrain the top of the section to an oldest possible age of ca. 87 Ma (late Coniacian) (Lebedeva, 2006; Williams et al., 2004).

Ka Latale 1 (KL1) Section

Samples KL1-B01 and KL1-B06 contain abundant *P. infusorioides*, *Oligosphaeridium pulcherrimum*, and *O. albertense* (LO, Cenomanian ca. 95 Ma). However, no species confidently indicate an age older than the Cenomanian. We therefore assign a Cenomanian age to these samples.

Ka Latale 2 (KL2) Section

P. infusorioides is very abundant, and the dinocyst assemblages are seemingly similar to those recorded in the Kukebai Formation elsewhere in the Tarim Basin. The presence of *Apteodinium deflandrei* in sample KL2-B15 suggests an age not older than the Cenomanian. Although few age diagnostic species are present, we note that Turonian or younger marker species appear to be absent.

Tajik Basin

Nurek Section

The productive samples suggest a Cenomanian age for most of the section, with abundant *P. infusorioides* and some *O. albertense*. A more diverse assemblage containing mostly Peridinioid cysts, specifically *Alterbidinium*, *Isabelidinium* and *Chatangiella*, likely indicates a younger (Turonian) age for the top of the section (sample NR-B31 and above) (Lebedeva et al., 2013; Williams & Bujak, 1989). The topmost productive sample (NR-B44) yields a few *Spinidinium echinoideum* specimens, and we tentatively assign an age not older than ca. 87 Ma. The presence of *Pediastrum*, a fresh water alga, and abundant plant debris in some samples is noteworthy as it indicates strong fresh water influence in some intervals.

Khirmanjo Section

A few diagnostic species were identified, including *P. infusorioides* and *P. paleoinfusa* at the bottom of the analyzed interval (sample KR-B21). We recorded *Epilosphaeridia spinosa* in samples KR-B27 and KR-B29, indicating the lower part of the section has a Cenomanian age. The interval represented by samples KR-B42 and KR-B43 contains few diagnostic species, that are similar to the previously published dinocyst assemblages in Spain (Peyrot, 2011), which may suggest a similar age for the samples KR-B42 and KR-B43 (Cenomanian-Turonian). The top of the section (sample KR-B56) is marked by rare occurrences of the genus *Dinogymnium* which has a first occurrence around or slightly before 90 Ma (Williams et al., 2004). We also recorded a single specimen that can be tentatively assigned to *Cannosphaeropsis utinensis* (FO ca. 85 Ma, top of C34n, late Santonian, Williams et al., 2004) in the same sample.

3.4.1.3. Foraminifera

Tajik Basin

Nurek Section

The first assemblage from the interval between the sample NR-C41 and sample NR-C44 contains *Charentia cuvillieri, Nezzazatta simplex, Cuneolina sp., Quinqueloculina* sp., nodosarids, discorbids, miliolids. Based on this foraminiferal assemblage, a Cenomanian age has been assigned to this interval (Figure 3.2).

The second assemblage from the interval between samples NR-C103 and NR-C110 mainly consists of calcisphaerulids, and very few planktonic foraminifera, such as *Planoheterohelix reussi* and *Muricohedbergella holmdelensis*. Considering the age constraint from the nannofossils analysis of sample NR-B44 (oldest possible age of late Santonian), coexistence of these species in this interval might suggest a late Santonian - early Campanian age.

The third assemblage at the top of the section, between samples NR-C120 and NR-C122 is characterized by *Sirtina orbitoidiformis, Sulcoperculina* sp., *Goupilloudina* sp., *Cibicidoides* ? sp., miliolid forms and unidentified larger agglutinated forms. This foraminiferal assemblage indicates a Campanian-early Maastrichtian age.

Khirmanjo Section

Few age diagnostic species, such as *Charentia cuvillieri* and *Cuneolina pavonia*, were recorded in the interval between sample KR-C36 and sample KR-C51. Coexistence of these species in this interval suggests a Cenomanian age (Figure 3.2).

A Turonian-Santonian age might be assigned to the interval between sample KR-C210 and KR-C228 based on the presence of *Calcisphaerula innominate*; however, a late Santonian age could be assigned more precisely considering the age constraint from the other microfossil analyses (Figure 3.2).

The third assemblage from the interval represented by the samples KR-C252 and KR-C344 contains larger benthic foraminifera indicating a Santonian-Maastrichtian age. *Praesiderolites douvillei* recorded in sample KR-C252 suggests a Santonian-Campanian age, whereas the assemblage of *Pseudosiderolites vidali, Sirtina orbitoidiformis, Vaughanina* sp. from sample KR-C299 yields a late Campanian age. The presence of *Pseudosiderolites vidali, Sivasella* sp., *Pseudorbitoides* sp. in sample KR-C304 suggests Campanian-Maastrichtian boundary interval. An early Maastrichtian age is assigned to sample KR-C344 based on the presence of *Sirtina orbitoidiformis, Siderolites* cf. *calcitrapoides, Lepidorbitoides* sp. (Figure 3.2).

3.4.1.4. Ostracods

Tajik Basin

Khirmanjo section

Samples KR-B36, KR-B42 and KR-B46 contain ostracod assemblages indicating a Cenomanian-early Turonian age whereas sample KR-B49 above contains taxa indicating a Turonian-Maastrichtian age (see text S6 in supporting information and Table 3.2 for the details list of ostracod fauna).

Tarim Basin

Mine section

Sample MI-B08 from the base of the Yigeziya Formation contains abundant ostracods with most common taxon belonging to *Fossocytheridea* sp. aff. *F. longielliptica* indicating a Santonian-Campanian age (Tibert et al., 2003).

MAIN FOSSIL ASSEMBLAGES / MARKER SPECIES AND GENERA

FORMATION / GROUP TAJIK BASIN	FORMATION / GROUP TARIM BASIN	Age	Mao & Norris (1988) (Tarim Basin)	Hao & Zeng (1984) (Tarim Basin)	Hao & Guo (1990) (Tarim Basin)	Yang et al. (1995) (Tarim Basin)	Lan & Wei (1995) (Tarim Basin)	This study (Tarim Basin)	This study (Tajik Basin)	Chapman et al. (2019) (Tajik Basin)
Akdjar	Aertashi	Danian-Selandian								
	Tuyiluoke	Maastrichtian -Danian			*Cibicides* sp., *Cibicidoides* sp., *Florilus* sp., *Anomalina* sp., *Quinqueloculina* sp., *Ammobaculites* sp., *Meloris* sp. ֍					
Argankun Group	Yigeziya	Santonian -Maastrichtian (ca. 86-68? Ma)	*Canningia reticulata* zone (middle part of the Wuyitake Fm. and Yigeziya Fm.) ✢		*Quinqueloculina* sp., *Triloculina* sp., *Spiroloculina* sp., *Massilina* sp., *Aerenoturrispirillina* sp., *Florilus* sp., *Brizalina* sp., *Bolivina* sp. ֍	*Cythereis* sp., *Bronsteiniana* sp., *Pontocyprella facilis*, *Veenia* sp., *Sarlatina yigeziyaensis*, *Ovocytheridea* sp. ○	*Leptosolen* sp., *Pholadomya* sp. 🐚	*Xenascus ceratoides*, *Florentinia* spp., *Alterbidinium* spp., *Spinidinium echinoideum* ✢ *Fossocytheridea* sp., *F.* aff *longielliptica*, *Xestoleberis* sp., *Dolocytheridea* sp. ○	*Spinidinium echinoideum*, *Pediastrum* sp., *Dinogymnium* spp., *Cannosphaeropsis utinensis* ✢ *Siderolites* cf. *calcitrapoides*, *Praesiderolites douvillei*, *P. vidali*, *Pseudorbitoides* sp., *Orbitoides* sp., *Sivasella* sp., *Lepidorbitoides* sp., *Historbitoides* sp., *Planorbulina* sp., *Vaughanina* sp., *Nummoallotia* sp., *Planoheterohelix reussi*, *Muricohedbergella holmdelensis*, *Sirtina orbitoidiformis*, *Sulcoperculina* sp., *Goupilloudina* sp., *Cibicidoides* ? sp., *Calcisphaerula innominate* ֍ *Eifeellithus eximius*, *Arkangelskiella cymbiformis*, *Chiastozygus litterarius*, *Cribrosphaera ehrenbergii*, *Watznaueria barnesiae*, *Broinsonia parca constricta*, *Calculites obscurus*, *Micula staurophora*, *Eiffellithus gorkae*, *Lucianorhabdus cayeuxii*, *Uniplanarius gothicus*, *Uniplanarius* cf. *sissinghi*, ☆ *Veenia donzei*, *Cytherelloidea granulosa*, *Veeniacythereis begudensis*, *Imhotepia marssoni multipapillata*, *Paijenborchella* (*Eopaijenborchella*) *marssoni*, *Neocythere* aff. *verbosa*, *Dolocytheridea* (*Paracytheridea*) sp., *Paracypris* sp. ○	*Omphalocyclus* sp., *Lafitteina* sp. ֍ *Watznaueria barnesiae*, *Micula staurophora*, *Lucianorhabdus cayeuxii*, *Eiffellithus turriseiffellii*, *Prediscosphaera cretacica*, *Arkalgelskiella cymbiformis*, *Broinsonia* sp., *Eiffelliths eximius*, *Zeughrabdothus* sp., *Staurolites ellipticus*, *Cretarhabdus surirellus*, *Cretarhabdus angustiforatus* ☆
Muzrabat	Wuyitake	Late Turonian -Coniacian (ca. 92?-86 Ma)			*Quinqueloculina* sp., *Massilina* sp., *Triloculina* sp., *Spiroloculina* sp., *Pararotalia* sp., *Nonionella* sp., *Cibicidina* sp., *Cibicides* sp., *Nonionellina* sp., *Heterohelix* sp., *Hedbergella* sp., *Guembelitria* sp. ֍					
Badzhuvon Group	Kukebai	Cenomanian -Early Turonian (ca. 100-92? Ma)	*Alterbidinium emulatum* zone (upper part of the Kukebai Fm.) *Cyclonephelium brevispinatum* zone (middle part of the Kukebai Fm.) ✢	*Migros asiatica*, *M. spiritensis*, *M. oryzanus*, *M. hectori*, *M. lobatulus*, *M. guttiformis*, *Yuanaia xinjiamggensis*, *Y.* sp., *Discorbis vescus*, *D.* sp., *Nonion* sp., *Cibicides* sp. (upper part of the Kukebai Fm.) *Migros asiatica*, *M. spiritensis*, *M. oryzanus*, *M. hectori*, *M. lobatulus*, *M.* sp. (middle part of the Kukebai Fm.) ֍	*Discorbis* sp., *Nonionella* sp., *Pullina* sp., *Gavelinella* sp., *Loxoconcha* sp., *Bythocypris* sp., *Ammobaculites* sp., *Hedbergella* sp., *Guembelitrie* sp., *Heterohelix* sp. (upper part of the Kukebai Fm.) ֍ *Ammobaculites* sp., *Reophax* sp. *Ammomarginulina* sp. (middle part of the Kukebai Fm.) *Discorbis* sp., *Quinqueloculina* sp., *Ammobaculites* sp., *Haplophragmoides* sp., *Ammotium* sp., *Ammomarginulina* sp. (lower part of the Kukebai Fm.)	*Ovocytheridea* sp., *Pontocyprella* sp., *Cytherella* sp., *Schuleridea irinae*, *Loxoconcha* sp., *Bythocypris* sp., *Paracypris* cf. *princeps* (upper part of the Kukebai Fm.) *Pontocyprella* sp., *Cytherella* sp. (middle part of the Kukebai Fm.) *Ovocytheridea* sp., *Pontocyprella* sp., *Cytherella* sp. (lower part of the Kukebai Fm.) ○	*Lima marrotiana*, *Pycnodonte costei*, *Cyprimeria* ? *faba* (upper part of the Kukebai Fm.) *Ostrea vatonnoides*, *Ostrea oxiana*, *Lima* aff. *subrigida* (middle part of the Kukebai Fm.) *Flaventia ovalis*, *Ostrea oxiana*, *Lima* aff. *subrigida* (lower part of the Kukebai Fm.) 🐚	*Lithosphaeridium siphoniphorum*, *Palaeohystrichophora infusorioides*, *Apteodinium deflandrei*, *Oligosphaeridium pulcherrimum*, *Oligosphaeridium albertense* ✢	*Palaeohystrichophora infusorioides*, *P. paleoinfusa* *Oligosphaeridium albertense*, *Alterbidinium* spp., *Isabelidinium* spp., *Chatangiella* spp., *Epilosphaeridia spinosa* ✢ *Charentia cuvillirti*, *Nezzazatta simplex*, *N.* sp., *Cuneolina pavonia*, *C.* sp., *Quinqueloculina* sp., Textularia sp. Lenticulian sp. ֍ *Watznaueria barnesiae*, *Gartnerago segmentatum*, *Microrhabdulus decoratus*, *Rotelapillus biarcus*, *Eprolithus octopelatus*, *E. moratus*, *Quadrum gartneri*, *Braarudosphaera bigelowii* ☆ *Cytherella ovata*, *Cytherelloidea hindei*, *Bairdia* aff. *pseudoseptentrionalis*, *Schuleridea* aff. *jonesiana*, *Dolocytheridea* (*Paracytheridea*) aff. *crassa*, *Hamocythere harrsiana*, *Cornicythereis bonnemai*, *Isocythereis grossouvrensis*, *Neocythere* aff. *inornata* ○	
Gashion Group	Kezilesu Group	Early Cretaceous								

Calcareous nanofossils	Dinoflagellates	Bivalves	Ostracods	Foraminifera
☆	✢	🐚	○	֍

Table 3.0.2 Depositional ages of the Cretaceous formations/groups in the Tarim and Tajik basins based on the fossil assemblage and marker fossils and their comparison with different studies.

3.4.2. Magnetostratigraphy

3.4.2.1. Characteristic Remanent Magnetization (ChRM) directions

Natural Remanent Magnetization (NRM) intensities of the red fine-grained clastics of the Gashion and Kezilesu groups from three sampled sections (Khirmanjo, Mine and Ka Latale 1) in the Tajik and Tarim basins have mean values of ca. 3 10^{-3} Am^{-1} (Figure S 3.4). The means of the magnetic susceptibility are comparable in the Khirmanjo section in the Tajik Basin (ca. 13 10^{-5} SI) and in the Mine and Ka Latale 1 sections in the Tarim Basin (ca. 8 10^{-5} SI). These relatively low values suggest detrital magnetite is absent in the measured samples. Progressive thermal demagnetization was applied to determine the characteristic remanent magnetization (ChRM). In the Mine and Ka Latale 1 sections, the ChRMs were defined in a temperature range ca. 240º-660ºC. The vectors were not anchored to the origin because in several samples an ill-defined magnetization was also observed above 660ºC. The negative inclination for the in situ direction of the samples from the Mine section demonstrates that the ChRM is a pre-tectonic magnetization. In the Tajik Basin, the unblocking temperatures are slightly higher enabling to define ChRMs most likely carried mainly by hematite. The ChRM directions were anchored to the origin. For the Tajik samples, isothermal remanent magnetization (IRM) acquisition and subsequent thermal demagnetization of the IRMs clearly confirm that hematite is the main magnetic carrier in these rocks (Figure S 3.5b). In the Tarim sections, the large unblocking temperature range suggests magnetization mainly carried by pigmentary hematite demagnetized at lower temperatures while the highest unblocking temperatures observed in the Khirmanjo section in the Tajik Basin suggest more detrital hematite. The maximum angular deviation (MAD) values are less than 15º with half of the samples having MAD values less than 5º.

The mean direction for each section was calculated after removing outliers at more than 45º from the mean (Figure S 3.4). After bedding correction, the Khirmanjo section records a significant counterclockwise direction in agreement with the previous results in the Tajik Basin (e.g. Thomas et al., 1994). The low inclination recorded in the Khirmanjo section compared to the one observed in the Ka Latale 1 and Mine sections suggests inclination shallowing due to detrital hematite in the Khirmanjo section while the ChRMs in the Mine and Ka Latale 1 section are more likely of chemical origin and carried by pigmentary hematite (e.g. Butler, 1998).

3.4.2.2. Age correlation

Consistent with our biostratigraphic age constraints, exclusively normal polarities forming a single long normal polarity zone in the Khirmanjo, Mine and Ka Latale 1 sections indicate deposition within the Cretaceous normal polarity superchron (C34n; ca. 126-84 Ma, Ogg et al., 2016) (Figure 3.2). However, determination of the upper and lower limits of correlation is not possible.

3.4.3. Sedimentology and sequence stratigraphy overview

The recognized facies and microfacies were deposited on a ramp composed of alluvial plain, coastal plain-supratidal, intertidal, high-energy shoreface-shoal/beach, low-energy and high-energy subtidal, and offshore environments (Figure 3.3, see Supporting Information Text S5 for details). These depositional environments display variable lateral settings and relationships during marine regression and transgression events. The ramp had a width of several hundreds of kilometers extending from the Tarim Basin to the Tajik Basin to the west. With a low bathymetric slope and maximum water depths of tens of meters it is analogous to the "epeiric ramp" of Lukasik et al. (2000). The epeiric ramp had distal and proximal portions. The offshore-outer ramp facies were deposited in the distal portion, whereas grain-supported high-energy ramp facies, and the low-energy subtidal and tidal flat facies were deposited in the proximal ramp (Figure 3.3).

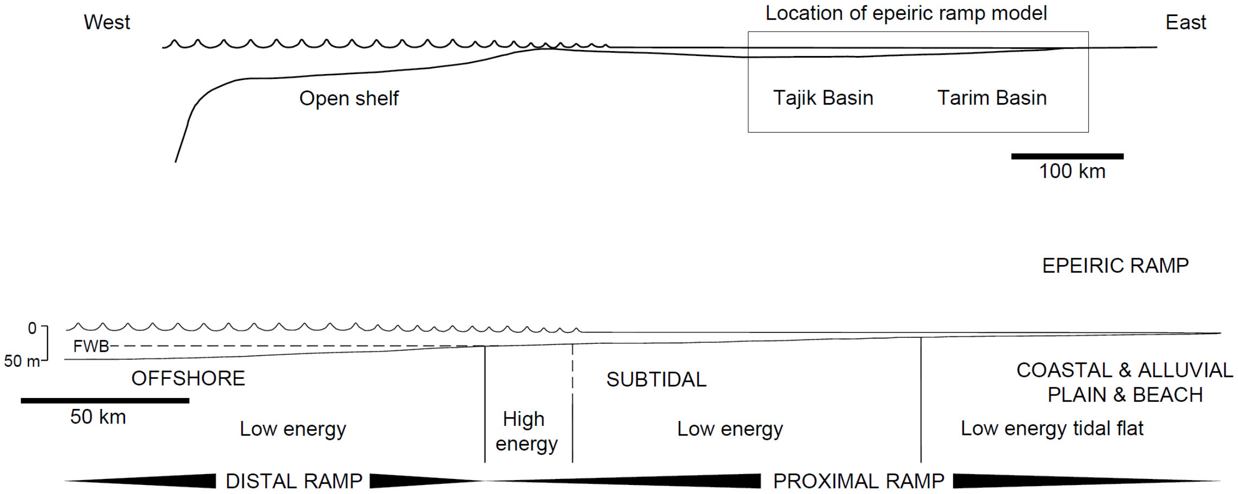

Figure 3.3 (a) The epeiric ramp model proposed for the Tarim and Tajik Basins (modified from Lukasik et al., 2000). Note that epeiric ramp is located in the east, whereas in the west open shelf conditions prevail. (b) Epeiric ramp model with distal (offshore) and proximal (subtidal, coastal plain, alluvial plain, occasional beach) parts and their energy conditions. FWB: Fair weather wave base.

The studied interval is divided into six and four depositional sequences (S) in the Tajik and Tarim basins, respectively (Figure 3.4). Facies/microfacies analyses indicate that the transgressive intervals are represented by offshore, high-energy and low-energy subtidal and intertidal facies bearing distinct fossil assemblages of ostracods, bivalves, gastropods, bryozoa, benthic and planktonic foraminifera, calcareous nannofossils, dinoflagellate cysts, echinoderms, ammonite fragments and serpulids (see Text S5 for the fossil content of different facies). The regressive intervals are composed of mostly alluvial plain (fluvial and lacustrine) and coastal plain (supratidal) facies including fewer (gastropods, bivalves and some benthic foraminifera) or no fossils.

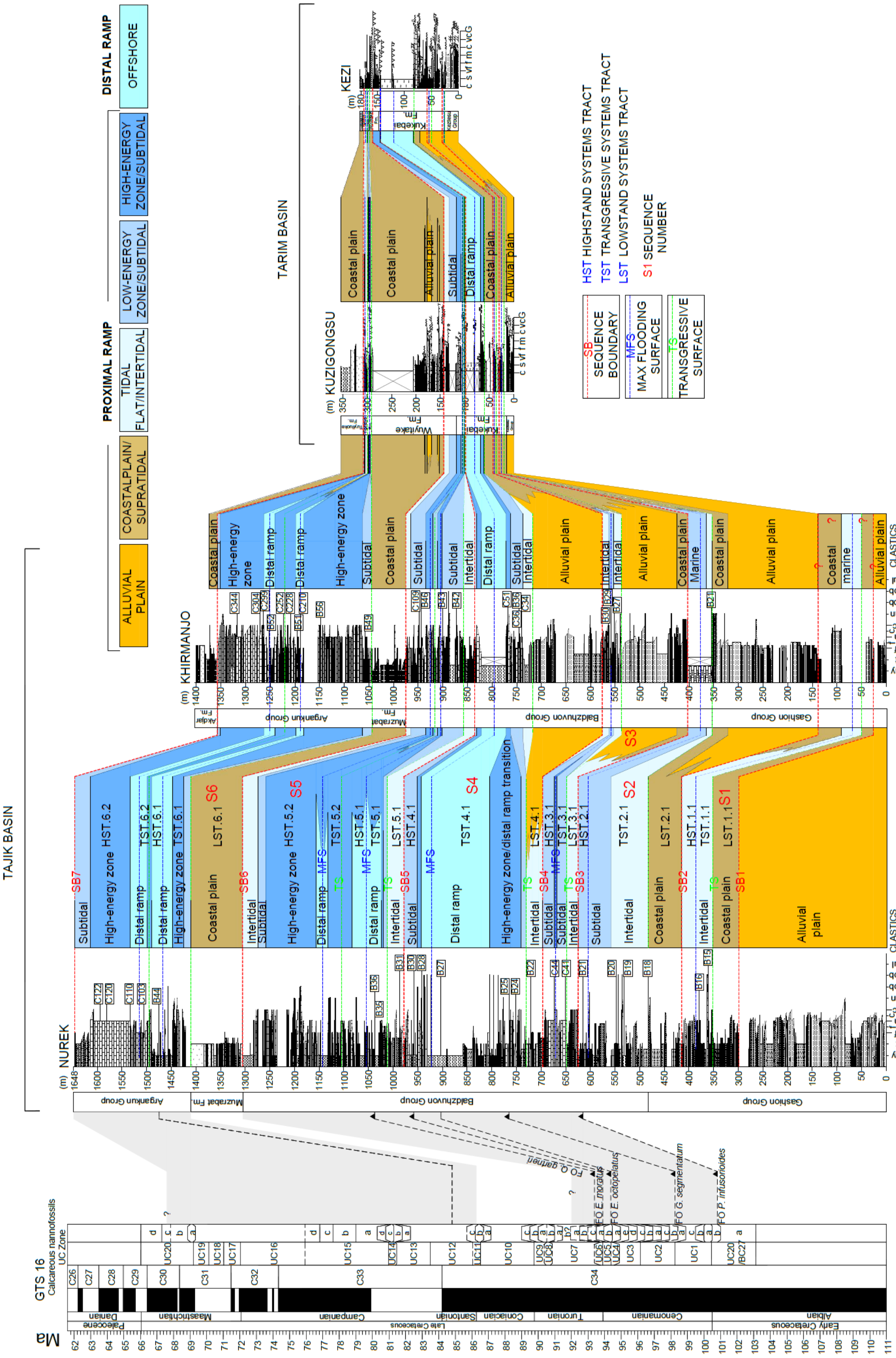
Ma
GTS 16
Calcareous nannofossils UC Zone
Early Cretaceous
Albian
Late Cretaceous
Cenomanian
Turonian
Coniacian
Santonian
Campanian
Maastrichtian
Paleocene
Danian
C26
C27
C28
C29
C30
C31
C32
C33
C34
FO P. infusoroides
FO G. segmentatum
FO E. octopetalus
FO E. moratus
FO Q. gartneri
TAJIK BASIN
NUREK
KHIRMANJO
TARIM BASIN
KUZIGONGSU
KEZI
Gashion Group
Baldzhuon Group
Muzrabat Fm.
Arganklun Group
Akdjar Fm.
Wuyitake Fm.
Kukebai Fm.
clay silt mud
vf f m c vc wacke pack grain
gran pebb cobb boul rud/fram & bould
CLASTICS
LIMESTONES
SB1
SB2
SB3
SB4
SB5
SB6
SB7
TS
MFS
S1
S2
S3
S4
S5
S6
LST.1.1
TST.1.1
HST.1.1
LST.2.1
TST.2.1
HST.2.1
LST.3.1
TST.3.1
HST.3.1
LST.4.1
TST.4.1
HST.4.1
LST.5.1
TST.5.1
HST.5.1
TST.5.2
HST.5.2
LST.6.1
TST.6.1
HST.6.1
TST.6.2
HST.6.2
Alluvial plain
Coastal plain
Intertidal
Subtidal
Distal ramp
High-energy zone
High-energy zone/distal ramp transition
Coastal marine
ALLUVIAL PLAIN
COASTALPLAIN/ SUPRATIDAL
PROXIMAL RAMP
TIDAL FLAT/INTERTIDAL
LOW-ENERGY ZONE/SUBTIDAL
HIGH-ENERGY ZONE/SUBTIDAL
DISTAL RAMP
OFFSHORE
SB SEQUENCE BOUNDARY
MFS MAX FLOODING SURFACE
TS TRANSGRESSIVE SURFACE
HST HIGHSTAND SYSTEMS TRACT
TST TRANSGRESSIVE SYSTEMS TRACT
LST LOWSTAND SYSTEMS TRACT
S1 SEQUENCE NUMBER

Figure 3.4 Correlations between the Tajik and Tarim Basins. Stratigraphic logs of the Nurek, Khirmanjo, Kuzigongsu and Kezi sections are correlated by the sequence stratigraphic relationships and interpretations. Correlation of the identified key bounding surfaces (i.e. sequence boundaries, maximum flooding surfaces, transgressive surfaces) between the sections enabled us to propose a regional stratigraphic architecture for the Tajik and Tarim basins. Three types of systems tracts have been interpreted; LST, TST and HST (see legend of the figure the text for the details).

The first sequence (S1) starts with a Lowstand Systems Tract (LST) at the top of the Gashion Group in the Nurek section (Figure 3.4). This sequence represents the first marine incursion in the eastern Tajik Basin. The first incursion in the Khirmanjo section is based on the presence of marine dinocyst fragments at the base of the section (ca. 30 m). However, due to poor outcrop exposure and lack of high-resolution age constraint, definition of a sequence with its bounding surfaces and its correlation to the Nurek section was arbitrary for this interval in the Khirmanjo section.

An Early Cretaceous sea incursion in the Kangsu area in the Tarim Basin was proposed by Hao et al. (1998) and Guo (1991) based on the presence of marine trace fossils *Ophiomorpha* and *Thalassinoides*, foraminifera *Saccammina globose* and glauconite abundance data. During fieldwork, we did not find any evidence of this sea incursion in any of our studied sections. Therefore, we argue that, even if this Early Cretaceous sea incursion did occur in the Tarim Basin and might be correlated to the first sea incursion in the eastern Tajik Basin mentioned above, it appears to be absent from our studied sections.

The transgressive surface above the LST of sequence 2 (LST.2.1) represents the second Cretaceous marine incursion during the early Cenomanian with limited geographical extent in the eastern Tajik Basin. This sea incursion did not reach into the Tarim Basin where time-equivalent coastal plain and alluvial plain deposits were found.

The next sequence (S3) presents at the base of the Kukebai Formation and the equivalent Baldzhuvon Group in the Tajik Basin. It starts with the LST.3.1 consisting of alluvial plain and coastal plain deposits in the Khirmanjo, Kuzigongsu and Kezi sections and intertidal deposits in the Nurek section. S3 represents another Cenomanian marine incursion with limited geographical extent, which like the early Cenomanian transgression did not reach the Tarim Basin.

LST.4.1 at the base of the next sequence (S4) is represented with similar depositional environments as in the LST.3.1 in all sections. The transgressive surface at the base of the Transgressive Systems Tract (TST) 4.1 marks the onset of the first major Cretaceous proto-Paratethys Sea incursion in Central Asia followed by the build up of an epeiric mixed siliciclastic-carbonate ramp system in S4 and S5 during the Cenomanian-early Turonian. The proto-Paratethys Sea reached its easternmost extent into the Tarim Basin during this sea incursion. The deepest Cretaceous marine environments of the proto-Paratethys sea appear in the Transgressive Systems Tracts of sequence 4 (TST.4.1) and sequence 5 (TST.5.1). Remarkably, the marine deposits of the first major sea incursion were not reported from the nearby Dashtijum section (Chapman et al., 2019) despite their occurrence in the Khirmanjo section (this study) and elsewhere in the Tajik Basin (e.g. Naidin et al., 1980; Pojarkova, 1984).

The following sequence (S6) starts with an extended coastal plain deposition during the late Turonian-Coniacian in LST.6.1. This coastal plain deposition was recorded both in the Tajik and Tarim basins representing a major regression in Central Asia. The transgressive surface at the base of the TST.6.1 marks the second major Cretaceous sea incursion during the Santonian displaying a shift to a carbonate-dominated system on the epeiric ramp both in the Tarim and Tajik basins. S6 ends with shallowing in a Highstand Systems Tract (HST.6.2) and then transition into coastal plain deposition in the following sequence during the Maastrichtian.

3.4.4. Facies evolution based on predominant biota

The Late Cretaceous succession in the Nurek and Khirmanjo sections shows a pronounced evolutionary trend (Figure 3.5). The majority of the fossil-bearing carbonate rocks in the Nurek and Khirmanjo sections are dominated by mollusks (bivalves and gastropods) and small benthic foraminifera, i.e. foramol grain association type of Lees and Buller (1972) or molechfor grain association type of Carannante et al. (1988) (Figure 3.5). Echinoderm-, bryozoa- and calcisphaerulid-rich or reefal (coral, rudists and red algae bearing) carbonate lithofacies are also present but less frequent (Figure S 3.3). Lithofacies contains primarily mollusks and benthic foraminifera are abruptly replaced by bryozoan-dominated limestones (bryomol grain association type of Nelson, 1988) at ca. 1260 m in the Khirmanjo section and by echinoderm-rich limestones at ca. 1560 m in the Nurek section (Figure 3.5). The proportion of echinoderm and bryozoan bioclasts rapidly increases up to ca. 60% and dominates the carbonate lithofacies in the Nurek and Khirmanjo sections, respectively. At the top of the Khirmanjo section, ca. 1325 m, there is a shift from heterozoan bryozoa-rich to photozoan reefal biota (bearing corals, rudists and red algae).

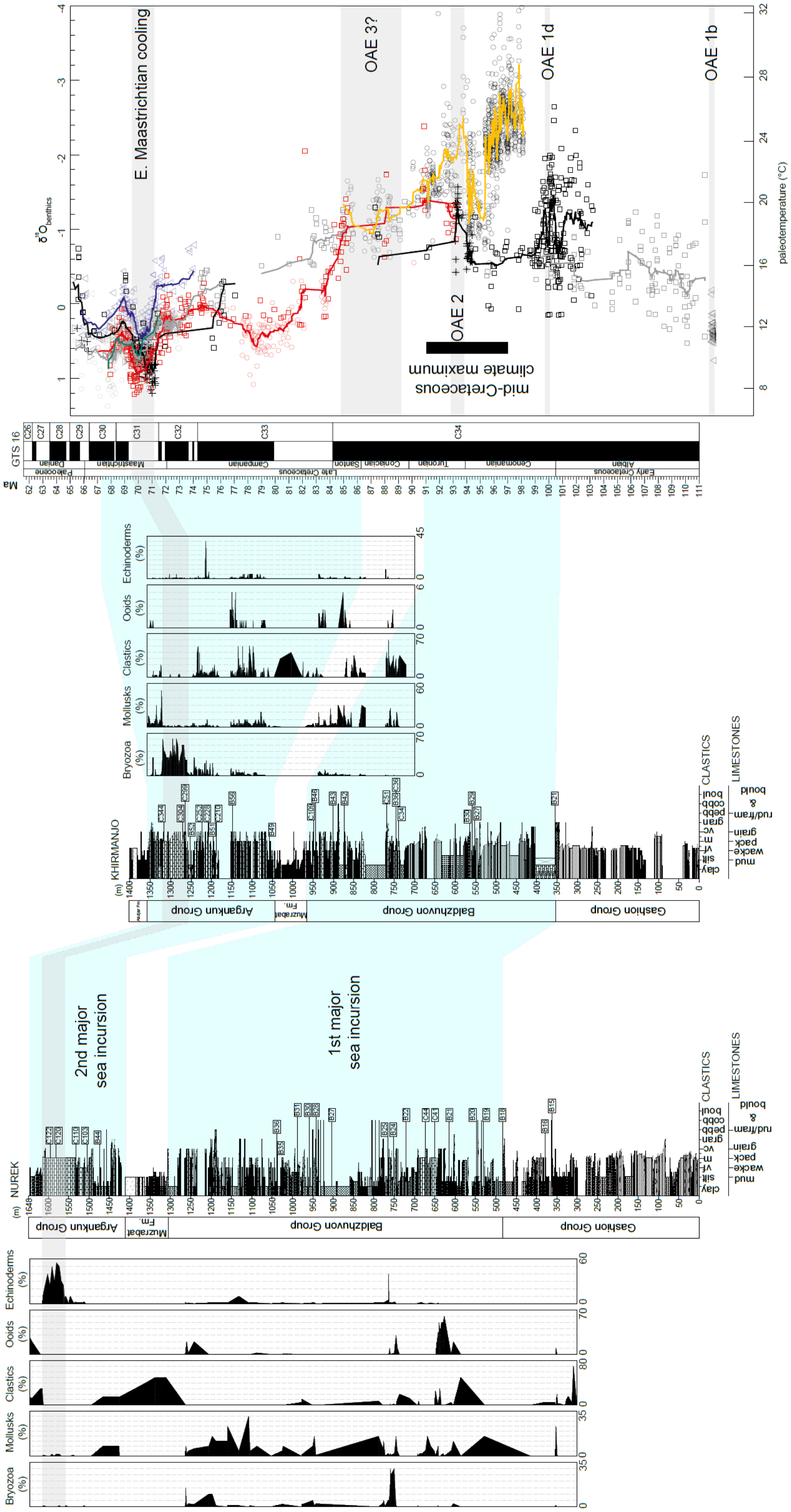

E. Maastrichtian cooling
OAE 3?
OAE 2
OAE 1d
OAE 1b
mid-Cretaceous climate maximum
$\delta^{18}O_{benthics}$
paleotemperature (°C)
GTS 16
Ma
Paleocene
Danian
Maastrichtian
Campanian
Santon
Coniacian
Turonian
Cenomanian
Albian
Late Cretaceous
Early Cretaceous
C26
C27
C28
C29
C30
C31
C32
C33
C34
Echinoderms (%)
Ooids (%)
Clastics (%)
Mollusks (%)
Bryozoa (%)
KHIRMANJO
NUREK
(m)
Arganakun Group
Muzrabat Fm.
Baldzhuvon Group
Gashion Group
Akdar Fm
CLASTICS
LIMESTONES
clay
silt
vf
f
m
c
vc
gran
pebb
cobb
boul
mud
wacke
pack
grain
rud/fram
&
bould
2nd major sea incursion
1st major sea incursion

Figure 3.5 Logs of the Nurek and Khirmanjo sections displaying the changes in the carbonate grain relative abundancies (data showing are percentages of bioclasts, siliciclastics grains and ooids). The bryozoa- and echinoderm-rich levels (grey shaded areas) show cooler intervals at the top of the Nurek and Khirmanjo sections, respectively (see section 5.3 for explanations). They are correlated to the early Maastrichtian cooling event on the diagram to the far-right (paleotemperature vs. age) showing stable oxygen isotope compilation of benthic foraminifera modified from Friedrich et al., 2012. On this diagram, thick lines show trends through data of different individual ocean basins (black: North Atlantic, orange; Demerara Rise, grey: southern high latitudes, red: Pacific, blue: subtropical South Atlantic, green, Indian Ocean. OAE: Ocean Anoxic Event).

3.4.5. Age control overview

Kezilesu & Gashion groups: Early Cretaceous

The ages of the Kezilesu Group in the Tarim Basin and the correlated Gashion Group in the Tajik Basin (Table 3.1) were poorly constrained to the Early Cretaceous (ca. 145 – 100 Ma), mainly relying on lithostratigraphic correlations and relative age determinations (e.g. Baratov et al., 1976). Our magnetostratigraphic results indicate that the deposition of some part of the Kezilesu Group clastics and its Tajik Basin equivalent Gashion Group is younger than the base of C34n at ca. 126 Ma (Ogg et al., 2016) and older than the ca. 100 Ma based on the biostratigraphic constraint of the overlying marine strata (see next paragraph). Recently Chapman et al. (2019) interpreted the maximum depositional age of the Schuchi-poyon Formation (including the Gashion Group and the base of the overlying Baldzhuvon Group, see Table 3.1) as 99±6 Ma based on the detrital Zircon Fission Track (ZFT) data from the base of the Dashtijum section, only 15 km north of the Khirmanjo section. Compared to the ca. 100 Ma age of the overlying Baldzhuvon Group, this ZFT age is within error.

1st major sea incursion in the Kukebai Formation – Baldzhuvon Group: Cenomanian – early Turonian (ca. 100 – 92? Ma)

The age of the Kukebai Formation, correlated to the Baldzhuvon Group in the Tajik Basin, representing the 1st major transgression extended into the Tarim Basin, is determined to be Cenomanian-early Turonian based on the analyzed microfossil assemblages. This age constraint is in agreement with several previous studies (Guo et al., 2015; Hao et al., 1982; He, 1991; Pa, 1991; Sobel, 1995; Wang et al., 1990; Yang, 1991; Zhang 1992), but differs from the previously attributed Cenomanian-Coniacian age by Xi et al. (2016; 2019). With the present data, the base of the Kukebai Formation is relatively well constrained to the early Cenomanian (ca. 100 Ma), and the age of the top of the Kukebai Formation remains less well defined to the early Turonian.

1st major regression in the Wuyitake-Muzrabat formations: late Turonian–Coniacian (ca. 92?-86 Ma)

The age of the Wuyitake Formation and the time-correlative Muzrabat Formation in the Tajik Basin, corresponding to the 1st major regression, could be designated as late Turonian-Coniacian based on the constraints from the overlying and underlying Yigeziya (see below) and Kukebai formations. This age estimate is in agreement with the suggested age of He (1991) and Wang et al (1990), however, more difficult to reconcile with age estimates of Xi et al. (2016; 2019 – late Coniacian-Early Campanian) and Guo et al. (2015) and Sobel (1995) (Turonian).

2^nd^ major sea incursion in the Yigeziya Formation - Argankun Group: Santonian – Maastrichtian (ca. 86-68? Ma)

The age of the Yigeziya Formation, correlated to the Argankun Group in the Tajik Basin, representing the 2nd major transgression in the Tajik and Tarim basins is constrained to Santonian-Maastrichtian, which is different from the previously suggested ages that range from the Coniacian to Maastrichtian (Chapman et al., 2019; Guo et al., 2015; Pan, 1991; Sobel, 1995; Sun, 1991; Wang et al., 1990; Xi et al., 2016; 2019; Yang, 1991; Zhang, 1992). Based on our age constraint, the onset of the 2nd sea incursion should be during the early Santonian (ca. 86 Ma). The onset of the subsequent regression, however, cannot be further constrained than Maastrichtian.

The Bukhara Formation of Chapman et al. (2019), correlated to the Argankun Group and Yigeziya Formation (Table 3.1), has previously been assigned a Maastrichtian-Paleogene age. Crucially, these authors also reported the presence of rudist-bearing units near the top of the Bukhara Formation (sample DSH-16-28 ca. 2110 m in Dashtijum section, see their supplementary files 4), which cannot be *in situ* if the sediments were indeed deposited after the Cretaceous-Paleogene extinction event. The rudists in the correlative limestone beds in the Khirmanjo section (Figure S 3.2i; see also Dedow et al., 2020) are, however, clearly *in situ*, excluding a Paleogene age for these successions (e.g. Ogg et al., 2016). The base of the Bukhara Formation of Chapman et al. (2019) has been assigned a Maastrichtian age based on the presence of the benthic foraminifera *Omphalocyclus* and *Laffitteina* in sample DSH16-26 (ca. 1890 m in Dashtijum section). However, this identification is questionable as the images showing longitudinal sections and details of the forams (Plate 2, figure f-h and i in supplementary files 4 of Chapman et al., 2019) appear to lack diagnostic features of *Omphalocyclus* and *Laffitteina.* Specifically, the illustrated specimens lack diagnostic features of *Omphalocyclus*, including a central depression and concave test shape. Normally, *Omphalocyclus* is characterized by a discoidal, centrally depressed biconcave test consisting of a median layer of chamberlets, which doubles and/or then trebles in late ontogenetic stages (Loeblich & Tappan, 1988; Özcan, 2007). Similarly, for *Laffitteina*, the lack of lenticular, planispiral to trochospiral test shape and other diagnostic features (see Loeblich & Tappan, 1988 for details) does not support this identification. The alternative would be that these microfossils are bryozoan fragments.

2^nd^-major regression in the Tuyiluoke-Akdjar formations: Maastrichtian –Danian

Most of our samples from the Tuyiluoke Formation, correlated to the red gypsiferous mudstone/siltstone unit at the base of the Akdjar Formation in the Tajik Basin, corresponding to the 2nd major regression in the Tajik and Tarim basins were barren or yielded only a few fossils. However, a Maastrichtian - Danian age could be assigned to the Tuyiluoke Formation representing the 2nd major regression based on the foraminiferal assemblages (Guo, 1990; Hao & Guo, 1990; Hao et al., 2001) and the presence of the Cretaceous-Paleogene boundary, identified near the base of the Tuyiluoke Formation in the Tarim Basin (see Kaya et al., 2019 for more discussion; see also Guo, 1990; Tang et al., 1992a; Ye et al., 1992).

3.4.6. Subsidence history

Subsidence curves highly depend on age assignments that are well-constrained except for the onset of deposition of the Kezilesu and Gashion clastics during the Early Cretaceous. The onset of deposition may be estimated as old as 145 Ma for the Kezilesu Group in the Tarim Basin and the correlated Gashion Group in the Tajik Basin (e.g. Baratov et al., 1976). Using this estimate would result in relatively slow tectonic subsidence through the Early Cretaceous followed by a marked increase from 100 Ma to 90 Ma (Figure 3.6). However, the onset of the deposition may be as young as the abovementioned maximum depositional age (99±6 Ma) of Chapman et al. (2019). This would imply a very short time period of deposition of the Gashion Group (a few million years) implying this entire clastic group marks a sudden and drastic increase in tectonic subsidence (Figure 3.6). In either case, we interpret this subsidence increase as due to tectonism and the related increase in sediment supply, rather than longer lithospheric cooling, isostatic or dynamic processes because of the concave-down shape of the subsidence curve. Tectonism is also suggested by the variability in depositional thickness and subsidence in the Tajik and Tarim basins indicating partitioning of the basins discussed in detail in section 5.1. This fast subsidence is followed by a slowdown at ca. 100 Ma first, and then at ca. 90 Ma, resulting in a concave-up subsidence curve, which is apparent in all the sections in the Tajik and Tarim basins (Figure 3.6).

3.5. Discussion

3.5.1. Driving mechanisms of tectonic subsidence

The subsidence, both total and tectonic, during the Cretaceous is generally higher in the Tajik Basin compared to the Tarim Basin (Figure 3.6). Within the Tajik Basin, the subsidence increases to the southeast, in the sections close to the Pamir, and the lowest subsidence occurs in the central part of the basin. Considering the Cenozoic counterclockwise rotation (e.g. Thomas et al., 1994), this basin-wide subsidence pattern is consistent with a subsidence in a foreland basin with the foredeep in the southeast, the backbulge in the northwest and a central forebulge. Similarly, for the southwestern Tarim Basin, published isopach maps for the Cretaceous sedimentary units show a mirror SW-NE trend, i.e. thicker units close to the Pamir in the southwest and northeast, thinner units in the center (e.g. Lee, 1985; Sobel, 1995). This pattern suggests that the Tajik and Tarim basins have been the locus of tectonic subsidence associated with crustal thickening in the Pamir since Early Cretaceous time. Supporting this interpretation is the asymmetrical distribution of the Early Cretaceous rocks in the Tajik Basin showing increased thicknesses and marine proportions from northwest to southeast towards the Pamir. In addition, the presence of clastic rocks bearing lithic fragments derived from the North Pamir (Zone VI of Burtman & Molnar, 1993) is indicative of a foreland Tajik Basin with a Pamir hinterland during the Early Cretaceous (Burtman & Molnar, 1993; Chapman et al., 2019). Similarly, the Tarim Basin was also interpreted as a Jurassic–Cretaceous foreland basin based on the occurrence of basin-vergent thrusting during the latest Jurassic (Cobbold et al., 1993; Sobel, 1999).

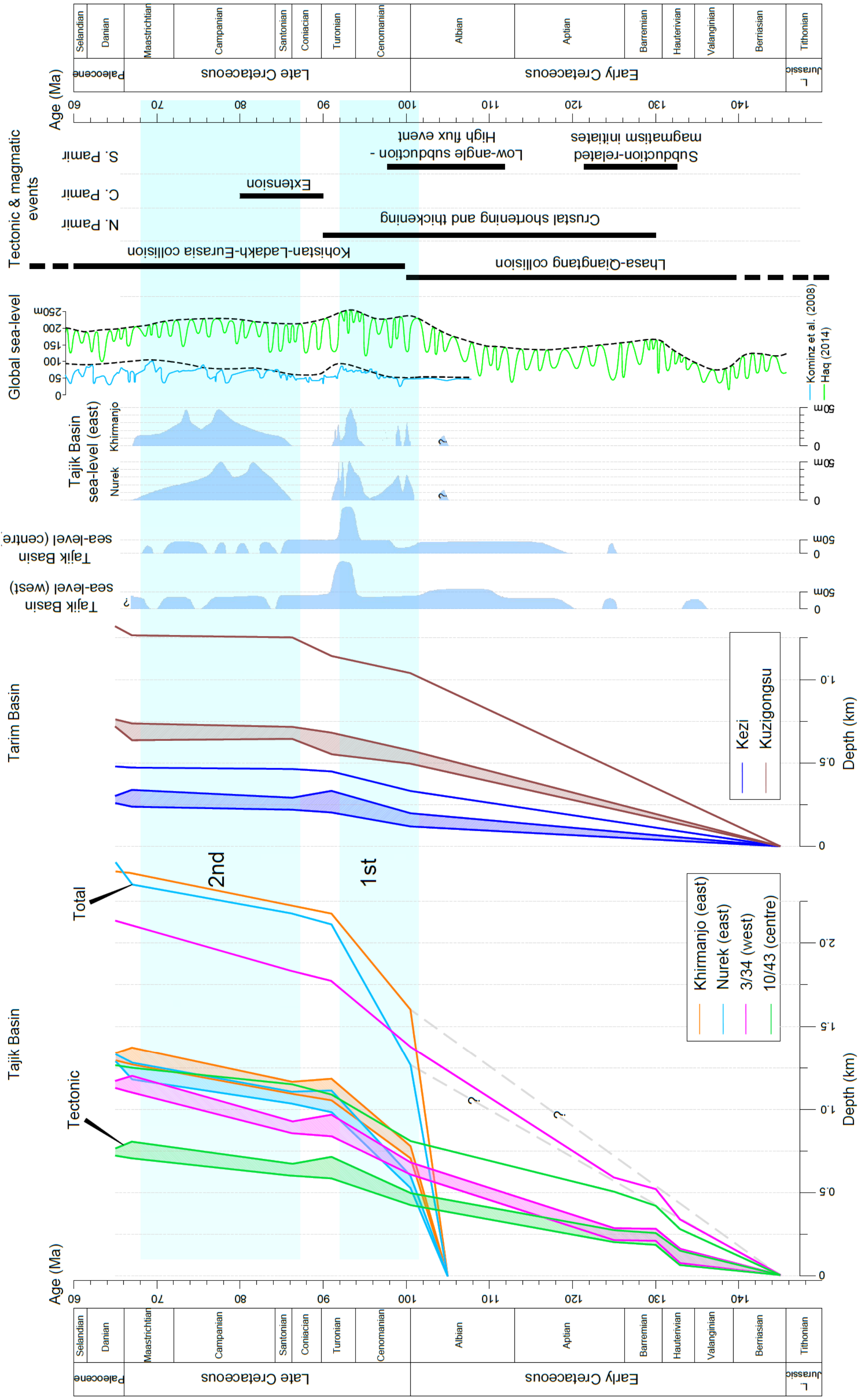
Tajik Basin
Tarim Basin
Tajik Basin sea-level (west)
Tajik Basin sea-level (centre)
Tajik Basin sea-level (east)
Nurek
Khirmanjo
Global sea-level
Tectonic & magmatic events
Age (Ma)
Depth (km)
Tectonic
Total
1st
2nd
Khirmanjo (east)
Nurek (east)
3/34 (west)
10/43 (centre)
Kezi
Kuzigongsu
Kominz et al. (2008)
Haq (2014)
Lhasa-Qiangtang collision
Kohistan-Ladakh-Eurasia collision
N. Pamir
Crustal shortening and thickening
C. Pamir
Extension
S. Pamir
Low-angle subduction - High flux event
Subduction-related magmatism initiates
Paleocene
Late Cretaceous
Early Cretaceous
L. Jurassic
Selandian
Danian
Maastrichtian
Campanian
Santonian
Coniacian
Turonian
Cenomanian
Albian
Aptian
Barremian
Hauterivian
Valanginian
Berriasian
Tithonian
60
70
80
90
100
110
120
130
140
0
0.5
1.0
1.5
2.0
50m
0
50
100
150
200
250m
?

Figure 3.6 Cretaceous subsidence curves (left) and major sea incursions (cyan shades labelled as 1st and 2nd) constrained in this study, compared temporally with the Tajik Basin sea-level curves, the global sea level curves of Kominz et al. (2008) and Haq (2014) and the regional tectonic and magmatic events (Chapman et al., 2018b). The sea-level curves for the west, central and east Tajik Basin are shown separately; data for the east are from this study and data for the west and central Tajik Basin are from Naidin et al. (1980).

With the recently proposed age constraints on the Early Cretaceous Gashion Group in the Tajik Basin (e.g. Chapman et al., 2019), and the equivalent Kezilesu Group in the Tarim Basin, we can compare the age of the increase in tectonic subsidence in the two foreland basin settings to other reported regional tectonic events in order to infer potential driving mechanisms.

Several studies in the Pamir (e.g. He et al., 2019; Imrecke et al., 2019; Robinson et al., 2004; 2012; Robinson, 2015) attempted to constrain the age of the Cretaceous tectonic deformation. Crustal thickening and shortening in the North Pamir have been evidenced by metamorphic and rapid exhumation events during the mid-Cretaceous (130-100 Ma) by Robinson et al. (2004). During this time, shortening in the North Pamir resulted in north-directed thrusting of the Karakul-Mazar terrane over the Kunlun terranes along the northern edge of the Pamir (Robinson et al., 2012). It has also been documented that retro-arc shortening related to Neo-Tethys subduction resulted in the development of the Tanymas-Baoziya-Torbashi thrust as a regionally extensive thrust nappe (He et al., 2019) ca. 120-100 Ma. This regionally extensive thrust nappe development resulted in the imbrication of the Karakul-Mazar and its emplacement on Central Pamir rocks (Imrecke et al, 2019; Robinson et al., 2012). Robinson et al. (2012) suggested that south directed emplacement of the Karakul-Mazar terrane over the Central Pamir was coeval with Cretaceous shortening to the north. To the south, the U-Pb data from the South Pamir batholith suggest that most subduction-related magmatism occurred between 120 and 90 Ma with a higher volumetric output ca. 105 Ma (Aminov et al., 2017; Chapman et al., 2018b). Similarly, the oldest and youngest ages of the Karakoram batholith have been given as 130 Ma and 95 Ma by Chapman et al. (2018b). Taken together, these data suggest a mid-Cretaceous subduction related, mostly likely compression dominated, tectonic regime with arc development to the south and retro-arc deformation to the north around ca. 130-90 Ma (Figure 3.7; Robinson et al., 2012).

The Tajik and Tarim basins located to the north of the Pamir orogen, have generally been interpreted as retro-arc foreland basins due to the widespread shortening and crustal thickening within the Pamir related to Neo-Tethyan subduction and collisional events along the southern margin of Eurasia (e.g. Chapman et al., 2018a, 2019; Hamburger et al., 1992; Hendrix et al., 1992; Robinson 2015; Sobel, 1999; Şengör, 1979, 1984). These events include the Lhasa-Qiangtang collision leading to the inception of a new subduction zone in the Neo-Tethys (Guilmette et al., 2012) or protracted underthrusting of the Lhasa terrane beneath the Qiangtang block (Kapp et al., 2003) or intrusion of large granitic and granodioritic batholiths onto the southern Pamir (Chapman et al., 2018b). In addition, the collision of the Central Afghan blocks with the south Eurasian margin that occurred during the Late Jurassic-Early Cretaceous, may have contributed to the increased tectonic subsidence and controlled the deposition of the

Kezilesu and Gashion clastics in the Tarim and Tajik basins, respectively (e.g. Montenat, 2009; Otto, 1997; Tapponnier et al., 1981).

Collectively, we argue that the Early Cretaceous elevated tectonic subsidence is likely due to the crustal thickening and shortening along the northern margin of the Pamir (ca. 130-90 Ma) related to the Lhasa-Qiangtang collision (Robinson et al., 2004) and the collision of the Central Afghan blocks with the south Eurasian margin (e.g. Montenat, 2009; Otto, 1997; Tapponnier et al., 1981). The deformation event in the Northern Pamir is also documented to the south in the Karakoram-Hindu Kush and accordingly it has been interpreted that the South and Central Pamir would have been similarly affected (Robinson, 2015).

Another remarkable result from our subsidence curves is the synchronous slowdown in subsidence at ca. 90 Ma, apparent in all the sections in the Tajik and Tarim basins (Figure 3.6). This slowdown might be related to a change in the tectonic regime along the southern margin of Eurasia (Figure 3.7). At this time approximately, a shift to lower volume magmatism in the Central Pamir, Karakoram and within the Kohistan arc has been related to a Neo-Tethyan slab roll-back event and associated with extension in the Central Pamir (Burg, 2011; Chapman et al., 2018b; Jagoutz et al., 2007). Similarly, an extensional regime resulting in intra-arc rifting has been explained by a southward roll-back of a northward subducting slab beneath the Kohistan arc at ca. 90-80 Ma (Burg et al., 2006; Burg, 2011). During the late Early Cretaceous and Late Cretaceous, a back-arc extension due to a southward roll-back of the subducting Neotethys slab controlling the formation of the Xigaze forearc basin and the emplacement of the Gangdese magmatic arc has been also proposed in the southern Tibet (Jolivet, 2017; Zhang et al., 2004). A more precise estimation has been provided recently by proposing the roll-back of the northward subducting Neo-Tethys slab beneath southern Tibet at ca. 90 Ma inducing an upper-plate extension and resulting in the opening of the Xigaze back-arc basin (Kapp & DeCelles, 2019).

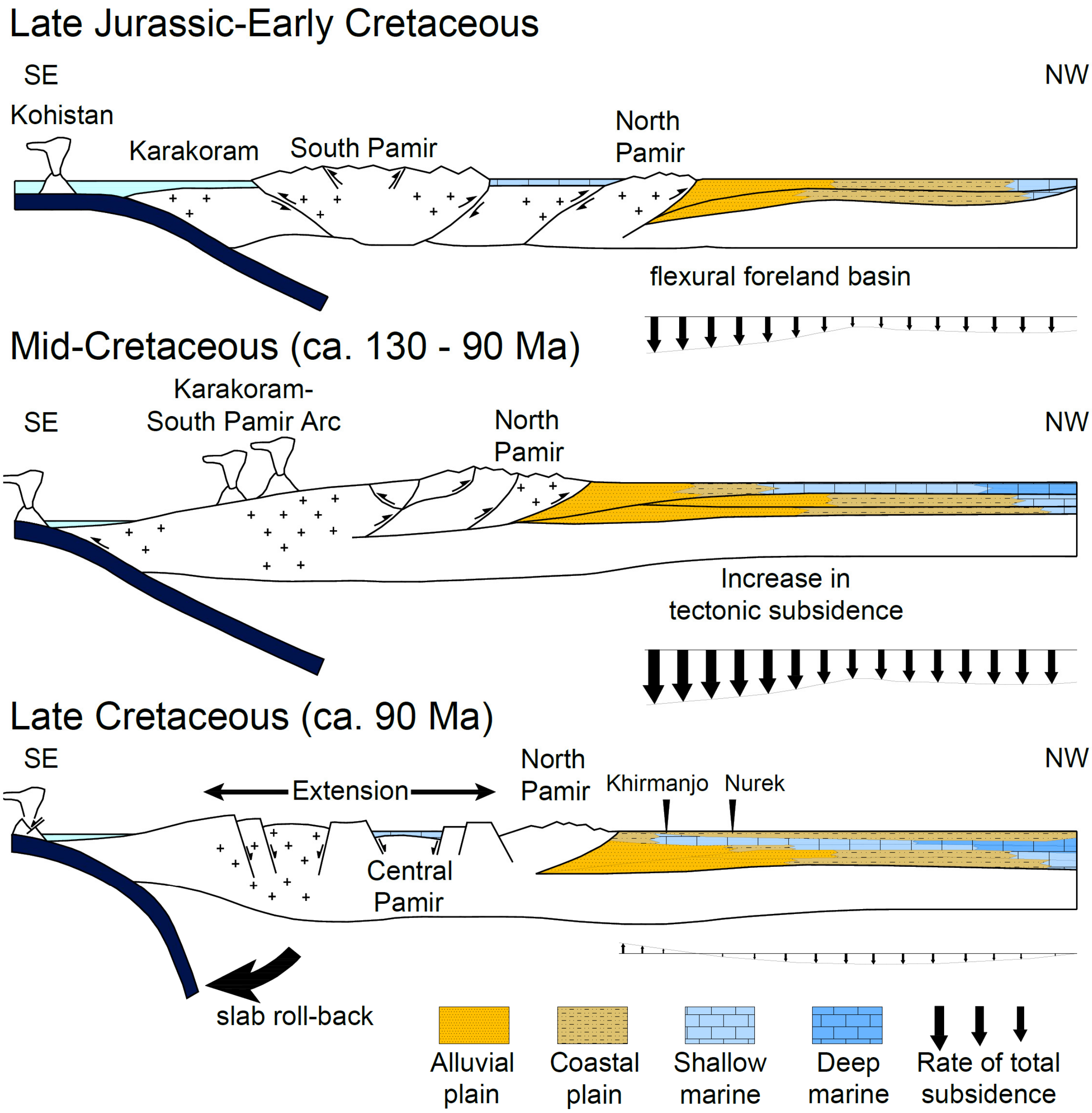

Figure 3.7 Schematic tectonic evolution of the Pamir and Tajik Basin during the Late Jurassic and Late Cretaceous (Modified from Robinson, 2015; Chapman et al., 2019; 2018b).

We thus propose that this ca. 90 Ma change in tectonic subsidence in the Tarim and Tajik basins might relate to a shift from a compressional to an extensional regime in the Central Pamir related to slab roll-back. However, the extensional tectonics due to the Neo-Tethyan slab roll-back does not seem to be expressed as extension in the Tajik and Tarim basins where such structures are not observed (e.g. Chapman et al., 2019, Sobel, 1999) but rather as a period of overfilled basin with limited thrusting and relative decrease in tectonic subsidence (Figure 3.7). This is reminiscent of the overfilled period in the foreland basin model of Yang (2011). Further support for this inference comes from the symmetrical regional depositional thickness patterns during the Late Cretaceous. The maximum thickness of the Late Cretaceous deposits in the central Tajik basin (Burtman, 2000, Chapman et al. 2019) suggests the available accommodation shifted from the southern edge to the center of the basin. This pattern of deposition indicates that the Tajik basin was lacking a forebulge during this period, suggesting that the deposition took place in an overfilled basin that was already filled by the deposition of early Cretaceous terrigenous clastic and Cenomanian-Turonian marine strata. Following the cessation of intense tectonic activity marked by the slowdown in subsidence, the observed late Turonian-Coniacian regression may have resulted from increased sediment supply (due to continuous erosion of the uplifted thrust belt) and rebound of the proximal part of the basin (e.g. Catuneanu, 2004; Yang, 2011). However, no obvious evidence for increased sediment supply or rebound of the proximal part in the studied stratigraphic records has been found.

Finally, we note that Chapman et al. (2019) alternatively interpreted the concave up subsidence pattern with slowdown in the Tajik Basin as an indicator to an extensional basin in response to lithospheric stretching and followed by slow cooling initiated by the onset of Neo-Tethyan slab roll-back. However, there is no clear evidence for a significant extensional event in the Tajik Basin in the Early Cretaceous (ca. 130-90 Ma) (e.g. Hamburger et al., 1992). We hence relate the large initial increase in subsidence to a compressional regime, principally because of the regional compressional context at this time (ca. 130-90 Ma) and the lack of extensional features expressed in the related Tajik Basin and Tarim Basin strata.

3.5.2. Driving mechanisms for sea level fluctuations

Due to lack of high-resolution age constraint for the sea incursion at the base of the Khirmajo and Nurek sections, it was not possible to correlate this sea incursion with the global sea-level constructions and regional tectonic events (Figure 3.6). Therefore, the driving mechanism of this marine incursion will remain elusive.

Our regional compilation (Figures 3.6 and 3.7) indicates a major proto-Paratethys sea incursion into the Tajik foreland basin for the first time during the Early Cretaceous (Aptian, ca. 120 Ma) from the west, shortly after the initiation of the subduction related magmatism (Naidin et al., 1980) (Figure 3.6). However, the incursion did not reach the eastern Tajik Basin due to the infilling of the basin represented by the alluvial and coastal plain deposition of the Gashion Group units (Figure 3.7). During this period, reconstructed global sea level decreased (Figure 3.6). Considering the very large (several 100 meters) increase in tectonic subsidence in the east and marine incursion during an apparent eustatic lowstand from the west (Figure 3.6), we conclude that tectonism must have been the main driver for the mid-Cretaceous (ca. 120 - 90 Ma) evolution of the proto-Paratethys Sea fluctuations (i.e. for the Early Cretaceous and 1st major sea incursions). However, an eustatic component becomes increasingly likely during the Cenomanian-Turonian hothouse climate, and we find it likely this climatic factor amplified highstands and enabled the proto-Paratethys Sea to reach its easternmost extent into the Tarim Basin during the 1st major sea incursion.

The subsequent major regression after the first major sea incursion coincides with a drop in eustatic sea level curves of Haq (2014) and Kominz et al. (2008) during the late Turonian-Coniacian (Figure 3.6). There is no evidence for a coeval increase in sediment supply causing a normal regression, which would present itself as extensive alluvial deposition with coarsening trends. Instead, this major regression is likely related to relative sea-level lowering and extensive coastal plain deposition in both basins. Therefore, we interpret that this regression more likely corresponds to a long-term decrease in the global sea level curves of Haq (2014) and Kominz et al. (2008).

Following the tectonic regime change and relatively low tectonic subsidence during the overfilled period, eustasy started to play a more dominant role in the proto-Paratethys Sea fluctuations. This is evidenced by their parallel trends with global sea-level reconstructions (Figure 3.6). Eustatic sea-level curves of Haq (2014) and Kominz et al. (2008) indicate a slight increase following the lowstand during the late Turonian-Coniacian, which can also be observed for the proto-Paratethys Sea fluctuations. Eustatic control is also evidenced by the 2nd major Late Cretaceous sea incursion, which appears coeval with the fluctuations in the West Siberian Basin. If these incursions are indeed coeval, this would support a eustatic driving mechanism (Kontorovich et al., 2014) (Figure 3.8). The 2nd major Late Cretaceous sea incursion extended up to the Tarim Basin, producing carbonate-dominated epeiric ramp environments until the subsequent regression. The subsequent regression event in the Tajik and Tarim basins appears also coeval with the Maastrichtian regression causing general shallowing and gradual expansion of alluvial and coastal plains in the West Siberian Basin (Kontorovich et al., 2014), which strengthens the interpretation that the 2nd sea incursion was mainly driven by eustasy (Figure 3.8).

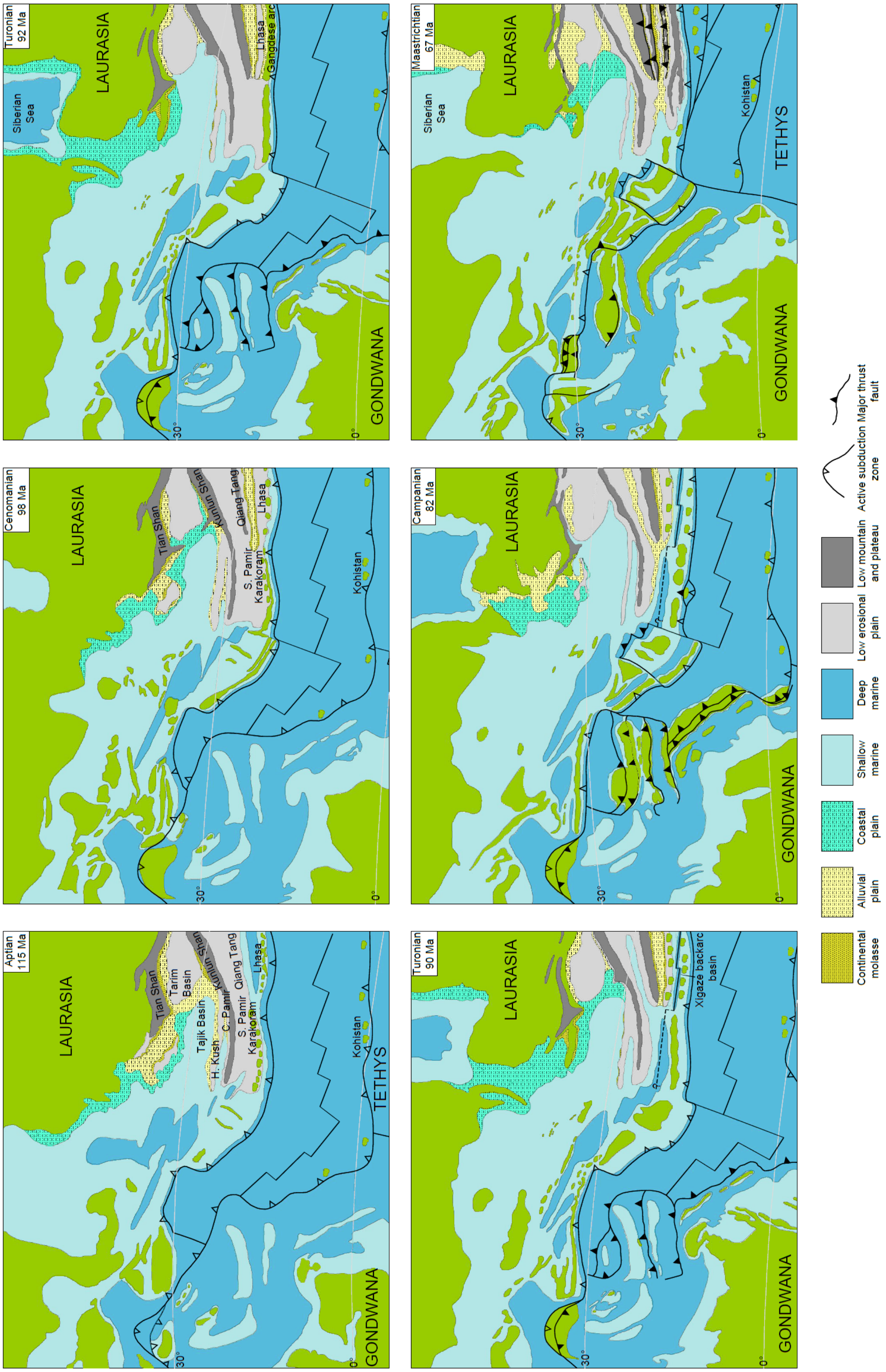
Aptian
115 Ma
LAURASIA
Tian Shan
Tarim Basin
Tajik Basin
Kunlun Shan
H. Kush
C. Pamir
S. Pamir
Karakoram
Qiang Tang
Lhasa
Kohistan
TETHYS
GONDWANA
30°
0°
Cenomanian
98 Ma
LAURASIA
Tian Shan
Kunlun Shan
Qiang Tang
S. Pamir
Karakoram
Lhasa
Kohistan
GONDWANA
30°
0°
Turonian
92 Ma
Siberian Sea
LAURASIA
Lhasa
Gangdese arc
GONDWANA
30°
0°
Turonian
90 Ma
LAURASIA
Xigaze backarc basin
GONDWANA
30°
0°
Campanian
82 Ma
LAURASIA
GONDWANA
30°
0°
Maastrichtian
67 Ma
Siberian Sea
LAURASIA
Kohistan
TETHYS
GONDWANA
30°
0°
Continental molasse
Alluvial plain
Coastal plain
Shallow marine
Deep marine
Low erosional plain
Low mountain and plateau
Active subduction zone
Major thrust fault

Figure 3.8 Paleogeographic maps displaying the Cretaceous sea incursions in the Central Asia. Corresponding facies during the transgressions and regressions are indicated.

3.5.3. Evidence for Early Maastrichtian Cooling

As mentioned in section 4.4, fossil-bearing carbonate rocks in the Nurek and Khirmanjo sections contain foramol (mollusk and small benthic foraminifera-rich), bryomol (bryozoan-rich) or echinofor (echinoderm-rich) grain association types. Heterozoan bryomol and echinofor grain association types are abundant in non-tropical, mostly cool- and cold-water environments on high-energy open shelves and ramps, whereas foramol type of grain associations are indicative of non-tropical, warm-temperate environments (Flügel, 2004). Modern day calcifying reef-building and carbonate platform phototrophs (i.e. corals and larger benthic foraminifera) are found in waters with winter surface temperatures above 20ºC, whereas bryozoan-rich heterotrophic communities become dominant in cool waters (<20ºC) or in warm settings below the photic zone (Jaramillo-Vogel et al., 2016 and references therein). In terms of trophic conditions, phototrophs, with the exception of red algae, thrive in oligotrophic to slightly mesotrophic conditions while heterotrophs generally dominate in nutrient-rich environments (Jaramillo-Vogel et al., 2016 and references therein).

This temperature-related distribution of heterozoan and photozoan biota might explain the abrupt replacement of mollusks and benthic foraminifera by bryozoan-dominated limestones (bryomol grain association type of Nelson, 1988) at ca. 1260 m in the Khirmanjo section and by echinoderm-rich limestones at ca. 1560 m in the Nurek section (Figure 3.5 & S 3.7). At this level, the proportion of the echinoderm and bryozoan bioclasts rapidly increases up to ca. 60% and dominates the carbonate lithofacies in the Nurek and Khirmanjo sections, respectively. At the top of the Khirmanjo section, ca. 1325 m, heterozoan bryozoa-rich biota were replaced by photozoan reefal biota (bearing corals, rudists and red algae) indicating a recovery in the carbonate factory. Species-level determination of the bryozoan microfossils could further constrain interpretation of seawater temperature changes through recognition of cool- or warm-water species (Jaramillo-Vogel et al., 2016; Moisette, 2000). Unfortunately, we were not able to perform taxonomic analysis at the species level on bryozoan microfossils due to their fragmented appearance in thin sections. However, relative percentages of photozoan biota and non-skeletal grains (i.e. ooids, oncoids, peloids etc.) provide some qualitative constraints regarding the seawater temperatures (Halfar et al., 2004). Halfar et al. (2004) concluded that true cold-water heterozoan grain associations contain less than 1% of photozoan components, irrespective of nutrient concentration. In addition, we utilized the presence and abundance of ooid grains which have been shown preferential occurrence in tropical/warmer climates as a warmer sea-water indicator (Flügel, 2004). To adjust for the controlling effect of clastic/nutrient input on the development of grain associations, fluctuations of the clastic content were also evaluated within the Nurek and Khirmanjo sections (Figure 3.5).

We find that the bryozoan- and echinoderm-rich carbonate beds lack photozoan biota and typical warm-water components (i.e. ooids and aggregate grains). One explanation for the absence of photozoan organisms and ooids as well as the outnumbering appearance of the bryozoan and echinoderm beds may be a sudden deepening of the environment. However, the deepest environments indicated by the presence of calcisphaerulids are recognized below stratigraphic levels ca. 1250 m within the Khirmanjo section and ca. 1510 m within the Nurek section. For a deepening event, an increase in calcisphaerulids would also be expected in the bryozoan- and echinoderm-rich beds, but the bryozoan- and echinoderm-dominated facies do not contain calcisphaerulids or any other evidence (e.g. an increase in planktonic foraminifera) for a deepening event. The input of clastics and associated nutrients decreases both for the Nurek and Khirmanjo sections in the bryozoan- and echinoderm-rich beds which are mostly pure limestones lacking siliciclastics (Figure 3.5). Therefore, the terrigenous clastic input had no major effect on the grain association change within the Nurek and Khirmanjo sections. The sheer dominance of heterozoan grain associations and absence of photozoan components strongly suggests that the bryozoan- and echinoderm-rich beds recorded in the Tajik Basin correspond to a cold-water heterozoan association. Alternatively, fluctuations in nutrient concentrations could lead to predominance of heterozoan or photozoan associations (Hallock & Schlager, 1986), and might also have played a role in the formation of the bryozoan- and echinoderm-rich facies in the study area. However, only the clastic input could be evaluated and the influence of other nutrient sources remains unresolved. Future work revealing nutrient fluctuations e.g. evolution of the total phosphorus, (Jaramillo-Vogel et al., 2016) may elucidate the definitive role of nutrients, irrespective of their source.

Intriguingly, the appearance of the heterozoan association coincides with the early Maastrichtian global cooling (ca. 71-70 Ma, Friedrich et al., 2012; Linnert et al., 2014; Miller et al., 1999) (Figure 3.5). We interpret this as evidence for the Late Cretaceous cooling in Central Asia, which was previously documented in terrestrial settings of eastern China including the Xining-Minhe, Sichuan, Songliao and Nanxiaong basins (Gao et al., 2015; Li et al., 2018; Ma et al., 2018; Wang et al., 1990; Wang et al., 2013). The observations align well with Maastrichtian climatic fluctuations observed in intermediate and deep waters of different oceanic basins, and indicate parallel climatic evolution between deeper ocean waters and the sea surface waters of the epicontinental proto-Paratethys Sea.

The final Maastrichtian appearance of photozoan reefal biota at the top of the Khirmanjo section could signal the partial recovery of the carbonate factory, which in turn maybe connected to the late Maastrichtian warming (e.g. Li & Keller, 1998; Linnert et al., 2014; Robinson et al. 2009) (Figure S 3.7). Collectively, shifts in the association types in our studied sections closely follow the global climate trends during the Maastrichtian.

3.6. Conclusions

Our new age constraints reveal that the proto-Paratethys Sea invaded into the Tajik Basin during the Early Cretaceous, yet it did not reach into the Tarim Basin where transitional to non-marine deposition continued. We interpret the invasion of the sea into the Tajik Basin as a result of the increased tectonic subsidence. This subsidence is linked to coeval compressive deformation in the Pamir, resulting from the Lhasa-Qiangtang collision and inception of a subduction zone in the Neo-Tethys.

The 1st major sea incursion that did extend into the Tarim Basin occurred during the Cenomanian-early Turonian (ca. 100-92? Ma). We find this sea incursion was driven mainly by increased subsidence due to tectonics and likely amplified by eustatic highstand, collectively resulting in the maximum geographic extent of the proto-Paratethys Sea during Cretaceous time. The following major regression in the Tajik and Tarim basins occurred during the late Turonian-Coniacian and was likely driven by the eustasy. A change in tectonic regime in the Pamir from compression to extension resulted in a decrease in subsidence and a relative tectonic quiescence at ca. 90 Ma in the Tajik and Tarim basins. The 2nd major sea incursion during the Santonian-Maastrichtian (ca. 86-68? Ma) was controlled predominantly by the eustasy during this period of tectonic quiescence as evidenced by likely coeval fluctuations in the West Siberian Basin. A marked lithofacies change in the Tajik Basin from mollusk-rich limestones to bryozoan-rich and echinoderm-rich limestones coincides the global Early Maastrichtian cooling event, suggesting a causal link. Collectively, our integrated data reveal a complex interplay between global sea levels and regional tectonic processes alternating control on the Cretaceous proto-Paratethys Sea incursions in Central Asia.

3.7. Supplementary Information

3.7.1. Introduction

This file contains the details of the sedimentological, sequence stratigraphic, biostratigraphic and magnetostratigraphic methods and the detailed description of the facies and facies associations. Figures showing sequence stratigraphic correlation of the sections from the Tarim Basin (Figure S 3.1), field photographs (Figure S 3.2), microfacies microphotographs (Figure S 3.3), Zijderveld plots and stereo plots of characteristic directions (Figure S 3.4), NRM vs Magnetic susceptibility and IRM acquisition graphs (Figure S 3.5) obtained from paleomagnetic analysis, generated paleo-water depth curves for the Nurek and Khirmanjo sections (Figure S 3.6) and observed facies change due to the Early Maastrichtian cooling (Figure S 3.7) are also provided. Plates (A to D) of dinocysts, nannofossils, ostracods and foraminifera are provided separately. Tables for descriptions of the siliciclastic (Table S 3.1) and carbonate facies (Table S 3.2), description of facies associations, their related facies/microfacies and depositional environments (Table S 3.3) and mean paleomagnetic results (Table S 3.4) are also included.

3.7.2. Text S1. Sedimentological methods

We observed thirteen facies based on lithology, thickness, geometry, sedimentary structures and fossil content in the field (Table S 3.1). Detailed microfacies analysis was conducted for the samples from the thick carbonate successions in the Khirmanjo and Nurek sections and from the interbedded carbonate beds in the Kuzigongsu, Kezi, Mine, Ka Latale 2 and Ka Latale 1 sections by examining mineralogical components, fossil assemblages and the rock texture in thin sections. In total 562 thin sections were analyzed (363 thin sections from the Khirmanjo section, 125 thin sections from the Nurek section, 23 thin section from the Kuzigongsu section, 21 thins sections from the Mine section, 13 thin sections from the Kezi section, 5 thin sections from the Ka Latale 1 section, and 12 thin sections from the Ka Latale 2 section). Fifteen microfacies (MF) were recognized for the carbonate rocks (Table S 3.2). Individual facies and microfacies were grouped into facies associations (FA) each of which characterizes a specific depositional environment (Table S 3.3).

3.7.3. Text S2. Sequence stratigraphic methods

A variety of surfaces indicative of a seaward or landward shifts of the successive facies belts were recognized and defined as sequence boundaries, transgressive surfaces and maximum flooding surfaces. These surfaces bound different systems tracts as lowstand, transgressive and highstand systems tracts composing the depositional sequences (Catuneanu, 2006 and references therein). A regional stratigraphic architecture was proposed in the results section based on the correlations of these surfaces between the studied sections in the Tajik and Tarim basins (Figure 3.4 & S 3.1).

Key bounding surfaces

Erosional (subaerial) unconformities

The erosional unconformities are characterized by erosional surfaces associated with abrupt facies changes, marking clear downward (seaward) shifts in the overlying facies belts. They can be subaerial in a landward direction or marine and conformable in a seaward direction.

The erosional unconformities are exposed in the field as sharp, erosive surfaces at the base of fluvial channel belts downcutting the grey-green gypsiferous silty claystones of the intertidal to coastal plain environments (e.g. sequence boundary (SB) 4 in the Khirmanjo section, Figure 3.4) or conformable surfaces showing sharp facies contrasts between the intertidal and coastal plain or subtidal deposits (e.g. SB 2 in the Nurek section or SB6 in all sections and SB4 and SB5 in the Nurek section, Figure 3.4).

Maximum flooding surfaces (MFs)

Maximum flooding surfaces are represented as ferrigenous and phosphatic hardgrounds (e.g. MFS at the top of the TST.5.2 in the Khirmanjo sections and MFs at the top of the TST.5.1 in the Nurek section) or sharp changes from deepening up to shallowing up facies tracts (e.g. MFs at the top of the TST.6.2 in the Khirmanjo and Nurek sections, Figure 3.4).

Transgressive surfaces (TSs)

Transgressive surfaces are sharp, occasionally erosional surfaces, characterized by abrupt deepening or landward shifts of the overlying facies belts. We observed TSs in the field as: (1) surfaces marking the sharp facies change from coastal or alluvial plain to intertidal/subtidal deposits (e.g. Ts at the base of the TST.2.1 in the Nurek and Khirmanjo sections, Figure 3.4); (2) hardground surfaces displaying a change from shallowing up to deepening up facies (e.g. Ts at the base of the TST.5.2 in the Nurek section, Figure 3.4).

Sedimentary architecture

The lowstand systems tracts (LSTs) are bounded below by erosional unconformities or their lateral conformities and above by transgressive surfaces. LTSs are composed of progradational to aggradational sets of deposits represented by (1) coastal plain gypsiferous deposits of FA2 (e.g. LST.2.1 in the Nurek section and LST.6.1 in all sections); (2) intertidal deposits of FA2 (e.g. LST.4.1 and LST.5.1 in the Nurek section, Figure 3.4).

The transgressive systems tracts (TSTs) are bounded below by transgressive surfaces and above by maximum flooding surfaces. TSTs are composed of deepening upward, retrogradational sets of deposits and represented by (1) shallow intertidal (FA2) and low-energy subtidal facies (FA4) capped by high-energy subtidal (FA5) and offshore facies of FA6 (e.g. TST.4.1 in the Khirmanjo section); (2) upsection deepening in the intertidal facies of FA2 (e.g. TST.1.1 in the Nurek section); upsection deepening of the *intertidal* (FA2) and low-energy subtidal (FA4) above the coastal plain deposits (FA2) (e.g. TST.2.1 in the Nurek section); (3) upsection deepening in the subtidal deposits of FA4 and FA5 (e.g. TST.3.1 in the Nurek section, Figure 3.4).

The highstand systems tracts (HSTs) are bounded below by maximum flooding surfaces and above by erosional unconformities (or their lateral conformity surfaces). The HSTs consist of shallowing upward, progradational sets of deposits and represented by (1) upsection shallowing in the intertidal deposits of FA2 (e.g. HST.1.1 in the Nurek section) or in the subtidal deposits of FA4 (e.g. HST.2.1 and HST.3.1 in the Nurek section); (2) offshore deposits (FA6) overlaid by high-energy (FA5) and low-energy subtidal deposits (FA4) (e.g. HST.6.2 in the Nurek and Khirmanjo sections, Figure 3.4).

3.7.4. Text S3. Biostratigraphic methods

Calcareous nannofossils

Sample preparation was performed following standardized calcareous nannofossil techniques (Bown & Young, 1998). Smear slides were analyzed with a light microscope at 1250 magnification. Due to the scarcity of the specimens in most of the examined samples, at least 600 field of views were observed. Fossiliferous samples were referred to the biostratigraphic schemes of Burnett (1998) and Sissingh (1977). The nannofossils were identified following the taxonomy given in Perch-Nielsen (1985), and the Nannotax website (Young, Bown, & Lees, 2019).

Dinoflagellate cysts

Samples were processed at Palynological Laboratory Services, Holyhead, UK, using standard palynological (acid) treatment procedures. We used approximately 50g of dry sediment for each sample. Strong acids, concentrated HCl and HF, were added to the sample material to remove carbonates and silicates respectively. Organic residues were pH-neutralized and sieved over a 10 um mesh to remove small particles. Some samples required short ultrasonic treatment or mild oxidation with HNO3. Residues were subsequently mounted on a microscope slide using glycerine jelly and analyzed at 400x magnification under a light-transmitting microscope (Olympus CX41). Each slide was scanned entirely for rare species. Dinoflagellate cyst taxonomy follows Fensome & Williams (2004).

Foraminifera

To identify foraminifera, a total of 185 thin-sections from the carbonate samples of the Nurek and Khirmanjo sections were examined under light-transmitting microscope (Olympus BH2). Benthic and planktonic foraminifera were identified following the taxonomy given by Loeblich & Tappan (1988), Boudagher-Fadel (2018) and Mikrotax website (Young, Wade & Huber, 2019).

Ostracods

Due to high degree of cementation, 200-300 g from all samples was boiled in a sulphate anhydrous solution (Na2SO4 - “Glauber salt”), followed by several freeze/thaw cycles. Many samples remained mostly unsegregated after this procedure and required the use of mechanical methods. Finally, samples were washed using a battery of sieves (0.250, 0.125 and 0.63 mm). Washed samples have been picked using a black tray with horizontal and vertical lines and a ZEISS – GSZ microscope. For illustration of the fossil remains, we used a ZEISS – Stemi SV11 microscope with a NIKON Coolpix 980 digital camera adapted for it.

3.7.5. Text S4. Magnetostratigraphic methods

We collected 2.5 cm diameter paleomagnetic core samples from the Khirmanjo, Mine, and Ka Latale 1 sections, sampling at a stratigraphic resolution of 0.5 - 1 meter where possible. A standard portable electric drill and a magnetic compass mounted on an orientation stage were used for sampling. Samples were cut into cylindrical specimens of ca. 2.2 cm in length then analyzed in the Paleomagnetic Laboratory of the Geosciences Department at the University of Rennes 1 with a 2G cryogenic magnetometer hosted in a magnetically shielded room.

The specimens were thermally demagnetized in a shielded oven in 9 to 18 temperature steps of up to 680ºC after the initial measurements of natural remanent magnetization (NRM). The remanent magnetization and the bulk magnetic susceptibility were measured after each demagnetization step.

ChRM directions were calculated by application of principal component analysis (Kirschvink, 1980) on orthogonal demagnetization plots. The line-fits were applied on a minimum of four temperature steps. Virtual Geomagnetic Poles (VGPs) were calculated from the ChRM directions. The VGPs cluster into only one group (normal) for all sections.

Isothermal remanent magnetization (IRM) acquisition followed by the thermal demagnetization of the IRM was done to better describe the magnetic properties of the samples (Figure S 3.5).

3.7.6. Text S5. Description of facies and facies associations

For the Nurek, Khirmanjo, Kozigongsu and Kezi sections, we describe in the following the various facies associations (Table S 3.1 and S 3.2) and their respective depositional environment interpretations (Table S 3.3, Figure 3.3). The evolution of these environments was illustrated along the logs of the studied stratigraphy in Figure 3.4 & S 3.1.

Facies association 1 (FA1) – Reddish brown sandstones, siltstones and claystones of fluvial, playa and lacustrine environments

Description - FA1 consists mainly of facies Sl, Sc, Sa, Ch, Ml, Ms, Mp and Mg. It crops out in the red clastics of the Gashion Group, in the lower part of the Baldzhuvon Group and Kukebai Formation at the Khirmanjo and Kezi sections, respectively and in the fine clastics of the Wuyitake Formation at the Kuzigongsu and Kezi sections. FA1 contains dm- to m-thick and 10's of meters large medium- to coarse-grained, trough cross-bedded (Sc), erosive-based sandstone channels (Ch) with few bioturbation, dewatering structures and occasional clay chips at the base. Occasionally there are some cm- to dm-thick pebble lags at the base of channels. The channels are overlain by m-scale, fine-grained cross- or parallel-bedded sandstones (Sc, Sl) with asymmetrical ripples (Sa). Red mudstones and siltstones interbedded with fine sandstones (Ms) include asymmetrical ripples, occasional bioturbation, carbonate nodules and wood debris. This sedimentary sequence is encased into 5 to 25 m-thick, massive, occasionally horizontally laminated and bioturbated red (Ml) or green-brown siltstones and claystones (Mp) with very rare root traces and occasionally alternated with gypsum nodules/layers (Mg). No fossil fauna/macroflora was observed in this facies association.

Interpretation - The concave-up, erosive-based, fining-upward, medium- to coarse-grained sandstone succession corresponds to channel deposits in a fluvial environment. A fluvial origin was interpreted due to the trough cross-bedding and medium to coarse granulometry in these channels, indicative of the migration of high energy, 3D megaripples in unidirectional flow direction (Harms et al., 1982). The small size of pebbly channels alternating with fine-grained red sandstones indicates an ephemeral stream deposition (Figure S 3.2a). The red siltstones and claystones with rare root traces and bioturbation correspond to flood plain deposits. Adjacent to the channel beds, laterally extensive thin beds of fining upward, medium to fine-grained sandstones with asymmetrical ripples and occasional bioturbation encased in the red siltstones and mudstones were interpreted as rapid deposition from unconfined flow in overbank or waning flood, therefore as crevasse splay deposits (e.g. Gulliford et al., 2017). Horizontally laminated green-brown claystones and siltstones with occasional bioturbation represent the settling of fine-grained particles from suspension in a standing body of water such as a pond/lake on the flood plain (Figure S 3.2b). The presence of gypsum nodules/layers within these fine-grained deposits implies a semi-arid/arid climatic setting with ponds/lakes in a continental playa.

Facies association 2 (FA2) – Massive-layered gypsum, red-brown claystones, siltstones and sandy limestones of coastal plain, supratidal and intertidal environments

Description - FA2 consists of facies Mp, Mg, Gl, Sa and microfacies MF1, MF2, MF6, MF9, MF10. It crops out at the base of the Baldzhuvon Group, in most parts of the Muzrabat Formation and at base of the Akdjar Formation, and at the top of the Gashion Group of the Nurek and Khirmanjo sections. FA2 comprises of dm- to m-scale, massive, locally layered gypsum strata (Gl) interbedded at random with cm-scale or m-scale, red-brown, grey, green claystones (Mp), laminated siltstones and very fine-grained siliciclastics (Sa), dolomites (MF9b) and dolomitic limestones (MF9a), beige mudstones (MF1), wackestones (MF2), oodial grainstones with radial-fibrious ooids (MF6), gypsum sand and sandy-silty limestones (MF10) with occasional intense bioturbation, desiccation cracks, load casts, algal mats (Figure S 3.2c, d) and gypsum nodules (Mg). The siliciclastic, very fine sandstones and siltstones can be fining upward and planar laminated with clay drapes at the top while the beige mudstones show more consistent laminae/interlaminae couplets. The sandy-silty limestones show trough cross-bedding, herringbone structures and cm-scale sets of fine- and coarse-grained doublets with wave ripples (Figure S 3.2e). The dolomitic beds show crystal-supported planar-e dolomite textures (Sibley & Gregg, 1987) in which most dolomite crystals are euhedral rhombs. Their intercrystalline areas are filled by micrite and occasionally by fine clastics (MF9). The wackestone beds include rare bivalve shells whereas mudstones and sandy-silty limestones include no fauna or macroflora.

Interpretation – Nearshore deposition was interpreted by the altogether presence of wave ripples, desiccation cracks, dolomitization, intense bioturbation and laminae/interlaminae couplets in the siltstones and claystones, as well as herringbone structures in the sandy-silty limestones formed by bidirectional currents in tidal channels characteristic of intertidal deposition. Ooidal grainstones with radial-fibrous ooids (mostly type 4 and 5 with lower amounts of type 3 ooids of Strasser, 1986) indicate also shallow marine, low-energy environment with frequent stirring-up of the sediment with nearby hypersaline deposits. In places, cm-scale, thin to thick sets of relatively coarse- to fine-grained doublets with current ripples represent tidal rhythmites deposited on a tidal flat (Tessier, 1993) as a result of neap-spring tide alternations (Figure S 3.2f). The massive, locally layered gypsum was interpreted to be deposited in a subaqueous environment close to the sea such as a coastal salina [see e.g. the modern marine evaporites of Warren & Kendall (1985) occurring in subaqueous salina setting]. However, red-brown gypsiferous siltstones, claystones and desiccation cracks imply subaerial deposition as a result of fluctuating ground water levels, probably in a sabkha environment (Warren & Kendall, 1985). This indicates deposition in a near shore, coastal plain environment with a semi-perennial water table including supratidal sabkhas and salinas, and intertidal settings similar to the Facies Zone 9A of Wilson (1975) defined for an arid, evaporitic platform interior setting including calcareous, dolomitic mud or sands with nodular, wavy gypsum and interlayers of red beds.

Facies association 3 (FA3) – Red sandstones of a high-energy shoreface to shoal/beach environment

Description – FA3 consists of metric to pluri-metric, fine- to medium-grained reddish-pinkish sandstones (Ss). It crops out at the base of the Baldzhuvon Group of the Khirmanjo section. The reddish-pinkish sandstones show wave ripples, hummocky to swaley cross-stratification with low-angle truncation surfaces, trough cross-beddding and intense bioturbation including vertical burrows and box-works of the Skolithos ichnofacies.

Interpretation – The hummocky to swaley cross-stratified and trough cross-bedded sandstones with low-angle truncation surfaces are typical of high energy 3D megaripples formed in shallow marine wave-dominated environment such as in shoreface to shoal and beach/barrier settings (Strasser, 1986; Proust et al., 2001; Flügel, 2004).

Facies association 4 (FA4) – Micrite-dominated carbonates and gray, blue siltstones, mudstones and fine-grained sandstones of proximal low energy subtidal

Description - FA3 is composed of facies Mp, Sa, Ss, Cq and decimetric to plurimetric carbonates represented by microfacies MF1, MF2, MF3, MF5, MF9a, MF11 and MF12 (Table S 3.3). It crops out in the Kukebai/Baldzhuvon and Yigeziya/Argankun formations/groups. FA3 includes (1) m-scale, gray, bioturbated siltstones and mudstones with planar lamination, clay drapes, ripple-forms and wavy and flaser bedding (Mp), (2) poor to moderately sorted, fine-grained, dm- to m-scale sandstones with ripple laminations and bioturbation (Sa, Ss) interbedded with (3) carbonates and m-scale patchy oyster bioherms (boundstones and floatstones, MF5 and Cq, Figure S 3.2j). Carbonates interbedded with the fine-grained clastics are composed either of micritic mudstone (MF1), dolomitic limestone (MF9b) or bioclastic wackestone to packstone including miliolid foraminifera (MF2 and MF3) and some mixed siliciclastic-carbonate microfacies (MF11, MF12).

Interpretation – Planar laminated fine-grained clastics and micrite-dominated carbonates with occasional intense bioturbation are characteristic of deposition in a low-energy, quiet environment rich in nutrients. Meter-scale boundstone/floatstone lenses of bivalves occurring in the carbonates represent oyster patch reefs. The presence of dolomite crystals, peloids, miliolid foraminifera and biota with a reduced diversity also indicate a restricted, low-energy environment. We interpreted FA3 as a low energy, restricted subtidal depositional environment.

Facies association 5 (FA5) – Grain-supported carbonates of proximal high energy subtidal

Description – FA5 is composed of thick-bedded, occasionally massive and erosive-based, grain-supported bioclastic carbonates (MF3, MF4, MF7 and MF8) and sandy carbonates/calcareous sandstones (MF12, MF13, MF15) interlayered with m-scale mudstones and marls (Mr) and cm-scale patchy oyster bioherms (Cq) at its transition to the offshore environment. It crops out in the Kukebai/Baldzhuvon and Yigeziya/Argankun formations/groups. The grain-supported carbonates are occasionally trough cross-bedded and may contain considerable bioclastic allochems as bivalves, gastropoda, serpulids, bryozoa, echinoid and coral fragments and benthic foraminifera indicating a diverse community. Red algae-coral boundstones (MF8) (Figure S 3.3c, d) and stylolitic carbonate breccias with fragments of corals, sponges, rudists, bryozoa and encrusting algae (MF7) replace the bioclastic packestones and grainstones in the upper levels (ca. 1325 m) of the Argankun Group carbonates in the Khirmanjo section (Figure S 3.2i).

Interpretation – The abundance of trough cross-bedded, grain-supported and sparry calcite cemented carbonates is indicative for a high energy wave-effective subtidal environment, such as in Zone Y of Irwin (1965) and in the grainy, skeletal facies of Lukasik et al. (2000) on an epeiric platform. Red algae-coral boundstones and stylolitic carbonate breccias with bioclastic fragments point to reefal and fore-reefal environments, respectively.

Facies association 6 (FA6) – Laminated dark gray, green mudstones, marls and micrite-dominated carbonates of distal low energy zone-offshore

Description – FA6 consists of interlayering of m-scale, finely laminated, locally calcareous and shelly, bioturbated dark gray, green mudstones and marls (Mp, Mr, Figure S 3.2h), m-scale carbonates and dm- to m-scale poorly bedded to massive oyster bioherms (Cq). FA6 crops out in the Baldzhuvon and Argankun groups of the Nurek and Khirmanjo sections. The m-scale carbonates may show erosive bases with gutter casts and bioturbated tops with iron oxide-impregnated hardground layers (Figure S 3.2g). The carbonates occasionally include fine-grained siliciclastics on a micritic matrix (MF12, MF13). Some of these carbonates with fine siliciclastics also include low-angle lamination and hummocky cross-stratifications (Ts). M-scale carbonates contain variable bioclastic allochems as shell fragments, bryozoa, serpulids, calcisphaerulids, rare planktonic foraminifera and echinoderm fragments indicating a diverse community (MF3). Other carbonates interbedded with mudstones and marls are bioclastic wackestones (MF2) including bivalves, foraminifera, calcisphaerulids, echinoderm fragments and unidentified bioclasts.

Interpretation - Fine-grained siliciclastics and micrite-dominated carbonates indicate a quiet, low-energy marine environment below the fair weather wave base, which is also corroborated by the macro- and micro- fossil assemblages. The presence of highly diverse fossil assemblages containing bivalves, serpulids, bryozoa, echinoderm fragments, calcisphaerulids, planktonic and benthic foraminifera also supports an open marine, offshore environment. Erosive-based silty carbonates with low-angle laminations and hummocky cross-stratification were interpreted to be the result of episodic storm wave action on the sea-floor (Handford, 1986) or tempestites (Ts) indicating an upper offshore environment between the storm wave base and fair weather wave base.

3.7.7. Text S6. Details of biostratigraphic analyses

Calcareous nannofossils

Nurek section

Most of the collected samples were barren or yielded solely few speciemens of Cretaceous taxa with a wide biostratigraphic distribution (Table S 3.6; Figure 3.2).

We detected in samples NR-B21, NR-B22, NR-B24, a few speciemens of *Watznaueria barnesiae*, a ubiquitous coccolith with opportunistic ecology (Lees et al., 2006).

Khirmanjo section

Samples collected along this section were largely barren (Table S 3.7). In samples KR-B21, KR-B29 and KR-B30, we detected a few specimens of *Watznaueria barnesiae*, a Cretaceous species with a wide stratigraphic distribution. Other samples (KR-B42 and KR-B49) are only characterized by the very rare presence of *Braarudosphaera bigelowii*, a species often linked to neritic environments and considered an opportunistic taxon tolerating dynamic or perturbed conditions (Bown & Young, 2019).

Dinoflagellates cyst

Tarim Basin

Mine Section

Samples from the Kukebai and Yigeyiza Formation at the Mine section contain some well-preserved dinocysts and allow to constrain the age of this section to Late Cretaceous (see main manuscript and Table 3.2, Figure 3.2, Table S 3.8).

Ka Latale 1 Section

Only two samples (KL1-B01 and KL1-B06) from the Ka Latale 1 section yielded dinocysts (see the main manuscript and Table S 3.10 for details).

Ka Latale 2 Section

Sixteen samples spanning the Kukebai and Wuyitake formations from the Ka Latale 2 Section were analyzed (Table S 3.9). Dinocyst yield for the Kukebai samples was generally excellent, but the abundance was low for the Wuyitake samples, possibly as a result of poor preservation.

Tajik Basin

Nurek Section

Around half of the 30 analyzed samples from the Nurek section were barren of dinocysts (see the main manuscript and Table S 3.11 for details).

Khirmanjo Section

For the Khirmanjo section, a few samples yielded abundant dinocysts but in most analyzed samples dinocysts were rare or completely absent (see the main manuscript and Table S 3.12 for details).

Foraminifera

Nurek Section

40 carbonate thin section samples were examined throughout the section (see main manuscript and Table 3.2 for the whole list of identified foraminifera).

Khirmanjo Section

A total of 145 carbonate thin section samples were analysed and three main foraminiferal assemblages were determined throughout the section.

The first assemblage from the interval between samples KR-C34 and KR-C109 is characterized by rare specimens of *Charentia cuvillieri*, *Cuneolina pavonia*, *Cuneolina* sp., *Nezzazzata* sp., *Quinqueloculina* sp., *Textularia* sp., *Lenticulina* sp., verneulinids, gavelinellids, nodosarids, discorbids, miliolids.

The second assemblage from the interval between samples KR-C210 and KR-C228 is mainly characterized by the calcisphaerulids, particularly *Calcisphaerula innominate*, and some miliolids.

The third assemblage from the interval represented by the samples KR-C252 and KR-C344 contains larger benthic foraminifera indicating a Santonian-Maastrichtian age. The foraminiferal assemblage is characterized by *Siderolites* cf. *calcitrapoides*, *Praesiderolites douvillei*, *Pseudosiderolites vidali*, *Sirtina orbitoidiformis*, *Pseudorbitoides* sp., *Orbitoides* sp., *Sivasella* sp., *Lepidorbitoides* sp., *Historbitoides* sp., *Planorbulina* sp., *Vaughanina* sp., *Sulcoperculina* sp., *Nummoallotia* sp., *Goupilloudina* sp., *Cibicidoides* ? sp., miliolid forms, and unidentified larger agglutinated forms.

Ostracods

In general, the ostracod fauna is poorly preserved, most of the specimens being fragmented, filled with hard cemented material or affected by recrystallization which make precise identification of the species very difficult. Only five samples (KR-B36, KR-B42, KR-B46, KR-B49 from the Khirmanjo section in the Tajik Basin and MI-B08 from the Mine section in the Tarim Basin) provided an ostracod assemblage (Figure 3.2).

Tajik Basin

Khirmanjo section

The common recorded ostracods species from the interval including samples KR-B36, KR-B42 and KR-B46 are *Cytherella ovata* (Roemer), *Cytherelloidea hindei* Kaye, *Bairdia* aff. *pseudoseptentrionalis* (Mertens) *Schuleridea* aff. *jonesiana* (Bosquet), *Dolocytheridea* (Paracytheridea) aff. *crassa* Damotte, *Hamocythere harrsiana* (Jones), *Cornicythereis bonnemai* (Triebel), *Isocythereis grossouvrensis* (Donze & Thomel) and *Neocythere* aff. *inornata* Colin.

Sample KR-B49, beside the few ostracod species already mentioned above, contains also taxa like *Veenia donzei* Babinot, *Cytherelloidea granulosa* (Jones), *Veeniacythereis begudensis* (Babinot), *Imhotepia marssoni multipapillata* (Pokorný), *Paijenborchella* (*Eopaijenborchella*) *marssoni* Triebel, *Neocythere* aff. *verbosa* (Damotte), *Dolocytheridea* (*Paracytheridea*) sp. and *Paracypris* sp., indicating a Turonian-Maastrichtian age.

Tarim Basin

Mine section

The abundance of *Fossocytheridea* that forms almost a monospecific population in sample MI-B08 suggests a marginal, restrictive environment. Other ostracods in sample MI-B08 seems to belong to *Xestoleberis* sp. and *Dolocytheridea* sp..

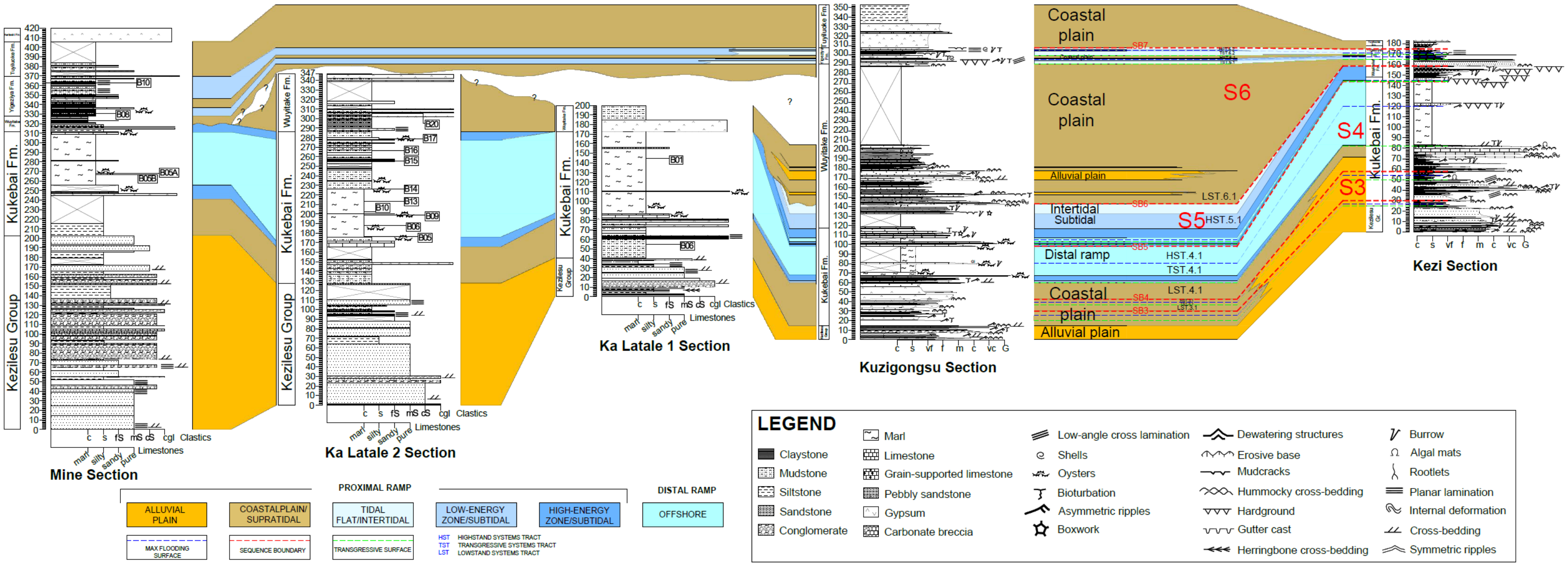
Mine Section
Ka Latale 2 Section
Ka Latale 1 Section
Kuzigongsu Section
Kezi Section
Kezilesu Group
Kukebai Fm.
Wuyitake Fm.
Tuyiluoke Fm.
Clastics
Limestones
c s fS mS cS cgl
marl silty sandy pure
c s vf f m c vc G
Coastal plain
Alluvial plain
Intertidal
Subtidal
Distal ramp
S3
S4
S5
S6
SB3
SB4
SB5
SB6
SB7
LST 4.1
TST 4.1
HST 4.1
HST 5.1
LST 6.1
B01
B05
B05A
B05B
B06
B08
B09
B10
B13
B14
B15
B16
B17
B20
?
PROXIMAL RAMP
DISTAL RAMP
ALLUVIAL PLAIN
COASTALPLAIN/ SUPRATIDAL
TIDAL FLAT/INTERTIDAL
LOW-ENERGY ZONE/SUBTIDAL
HIGH-ENERGY ZONE/SUBTIDAL
OFFSHORE
MAX FLOODING SURFACE
SEQUENCE BOUNDARY
TRANSGRESSIVE SURFACE
HST HIGHSTAND SYSTEMS TRACT
TST TRANSGRESSIVE SYSTEMS TRACT
LST LOWSTAND SYSTEMS TRACT
LEGEND
Claystone
Mudstone
Siltstone
Sandstone
Conglomerate
Marl
Limestone
Grain-supported limestone
Pebbly sandstone
Gypsum
Carbonate breccia
Low-angle cross lamination
Shells
Oysters
Bioturbation
Asymmetric ripples
Boxwork
Dewatering structures
Erosive base
Mudcracks
Hummocky cross-bedding
Hardground
Gutter cast
Herringbone cross-bedding
Burrow
Algal mats
Rootlets
Planar lamination
Internal deformation
Cross-bedding
Symmetric ripples

Figure S 3.1 Correlations in the Tarim Basin between the stratigraphic logs of the Mine, Ka Latale 1, Ka Latale 2, Kuzigongsu and Kezi sections. Kuzigongsu and Kezi sections are correlated based on the sequence stratigraphic relationships and interpretations (for details see Figure 3.3). Mine, Ka Latale 1, Ka Latale 2 and Kuzigongsu sections are correlated by the lithostratigraphic and biostratigraphic observations/results.

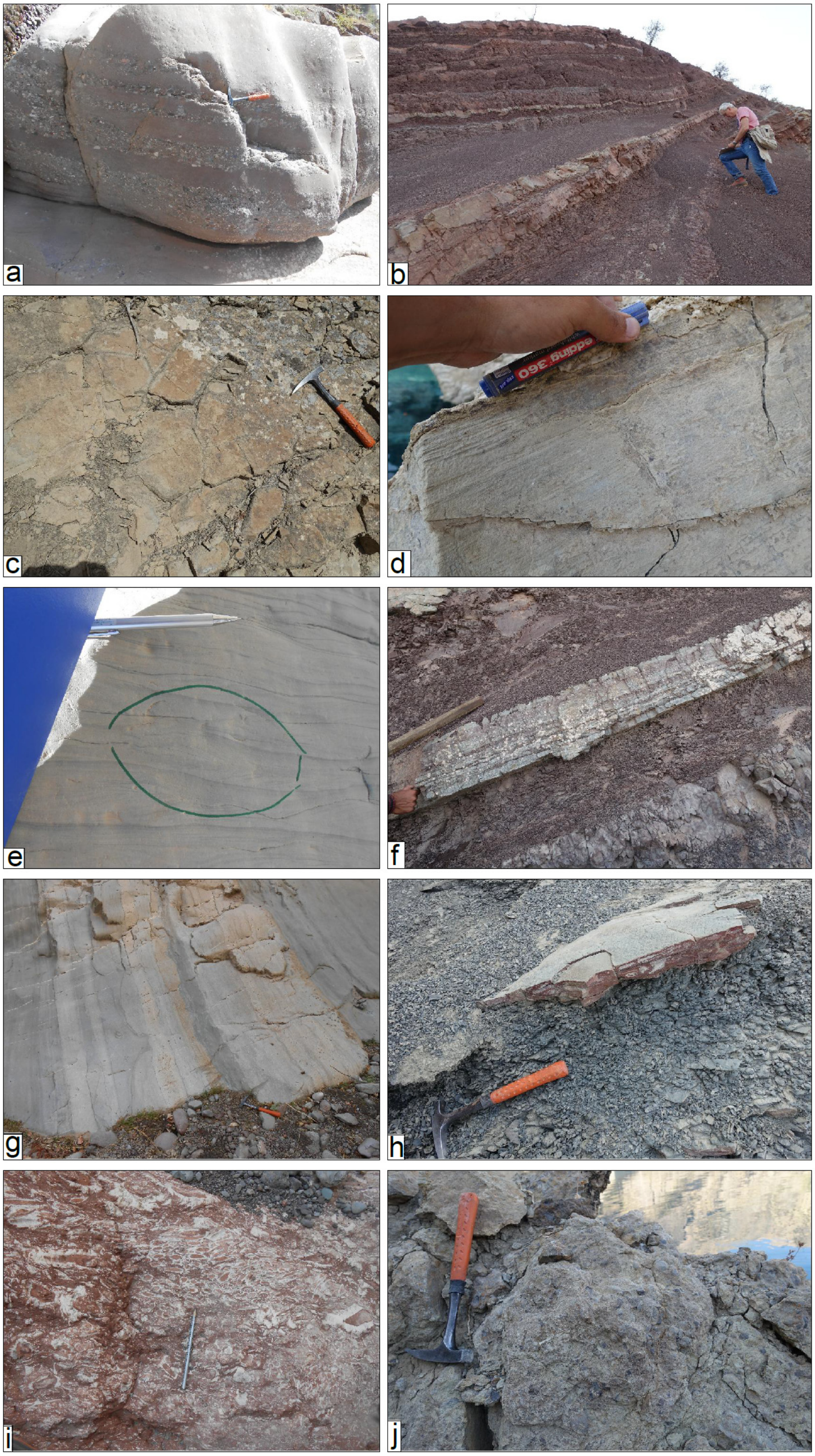
a
b
c
d
e
f
g
h
i
j

Figure S 3.2 Field photographs of some sedimentological features. (a) Ephemeral stream deposits, Gashion Group, Khirmanjo section. (b) Horizontally laminated fine-grained lacustrine deposits, Gashion Group, Nurek Section. (c) Mud cracks, Gashion Group, Nurek section. (d) Algal mats, base of the Baldzhuvon Group, Nurek section. (e) Herringbone cross-stratification, Muzrabat Formation, Khirmanjo section. (f) tidal rhythmites, Baldzhuvon Group, Nurek section. (g) hardground surfaces, Argankun Group, Khirmanjo section. (h) hard ground on offshore marls, Baldzhuvon Group, Nurek section. (i) rudistic limestone, Argankun Group, Khirmanjo section. (j) oyster patch reef, Baldzhuvon Group, Nurek section.

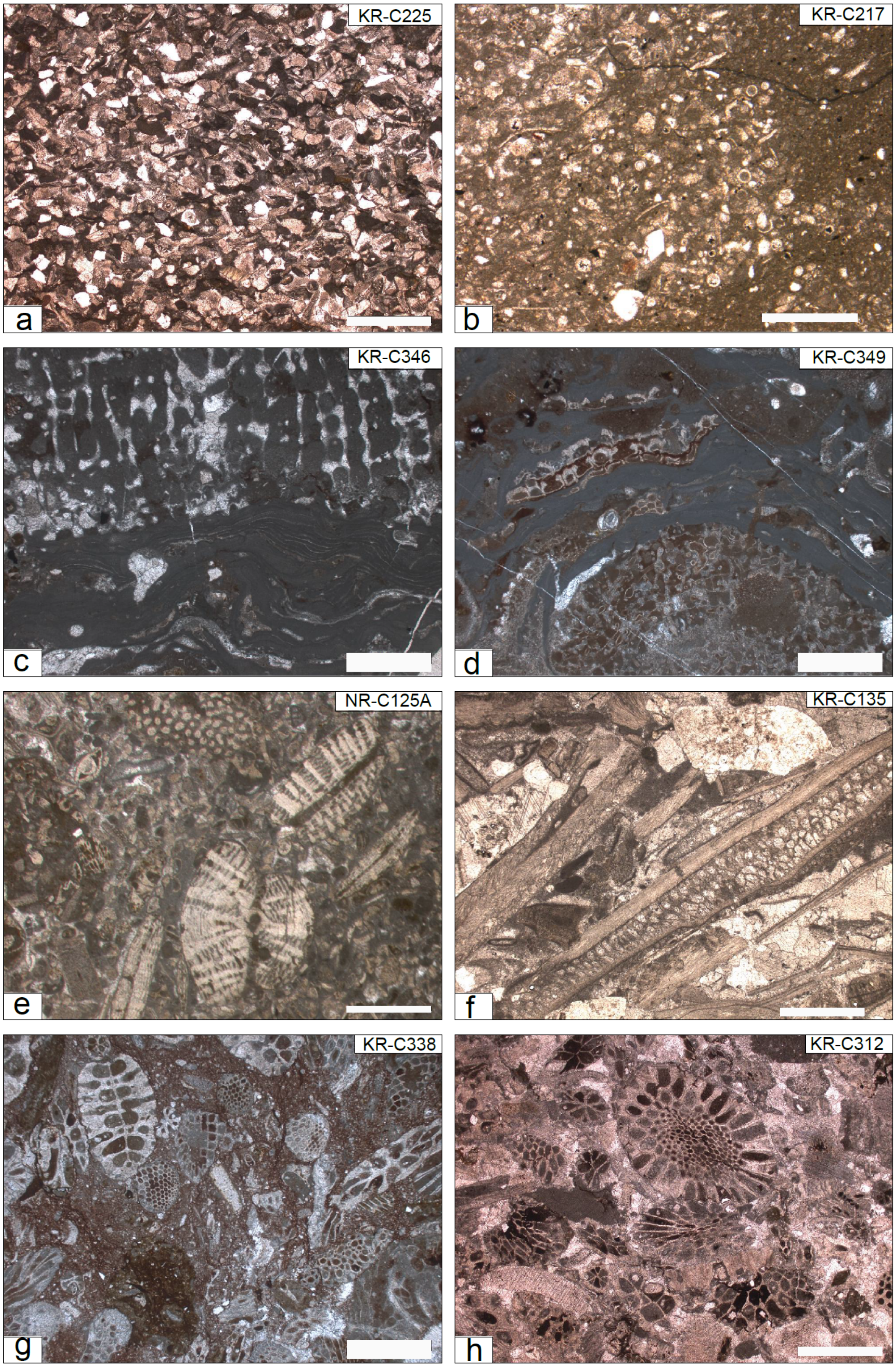
KR-C225
a
KR-C217
b
KR-C346
c
KR-C349
d
NR-C125A
e
KR-C135
f
KR-C338
g
KR-C312
h

Figure S 3.3 Photomicrographs of some microfacies. (a) Echinoderm-rich microfacies. (b) calcisphaerulid-rich offshore microfacies. (c) reefal microfacies with corals and algal encrusters. (d) algae-rich microfacies, red algae encrusting a sponge-like microfossil. (e) foraminifera-rich microfacies, orbitoids and rotalids. (f) mollusk-rich microfacies, bivalve shells. (g, h) bryozoa-rich microfacies. Scale bars: 500 µm.

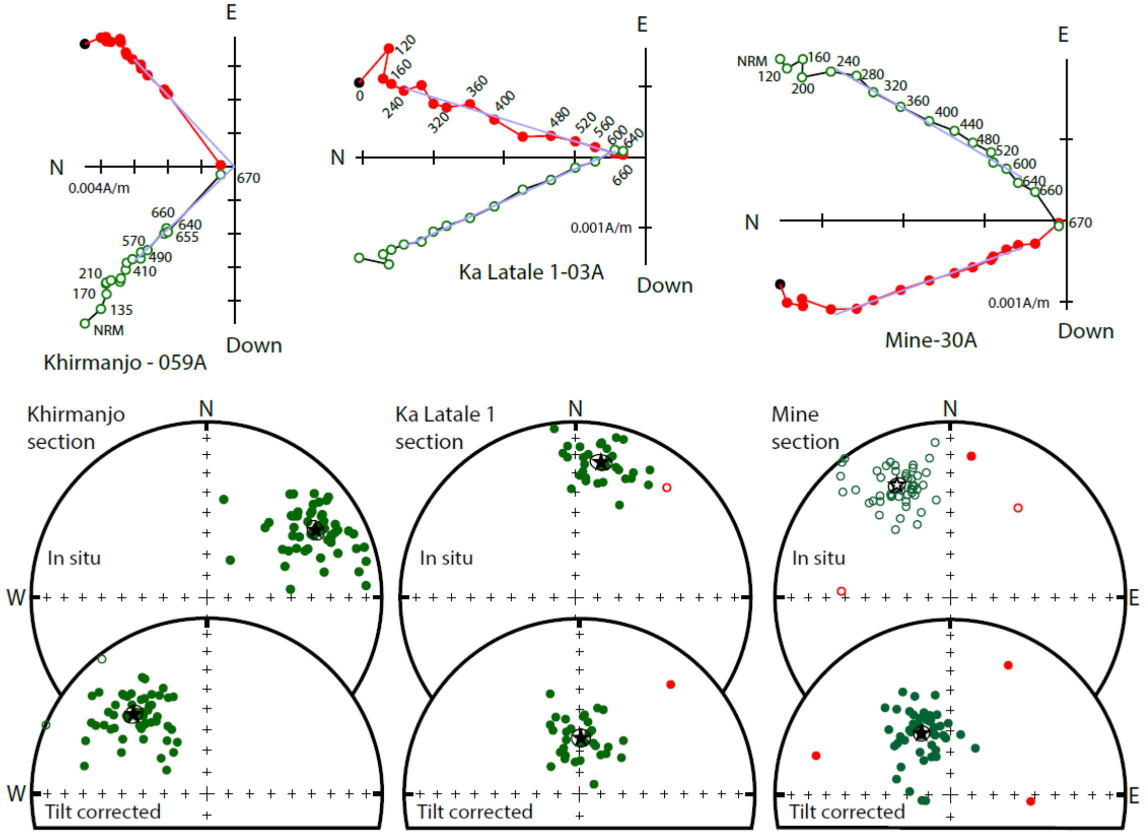

Figure S 3.4 ***(Above)*** **Orthogonal plots of the thermal demagnetization data for one sample of each section. Open/filled symbols are projections in the vertical/horizontal planes. The light blue lines correspond to the ChRMs identified in each samples. (Below) Stereonets of the ChRMs for each section in in situ and tilt corrected directions. Filled/open symbols correspond respectively to positive/negative inclinations. Red symbols correspond to data at more than 45° from the mean shown with a star and corresponding angle of confidence at 95%.**

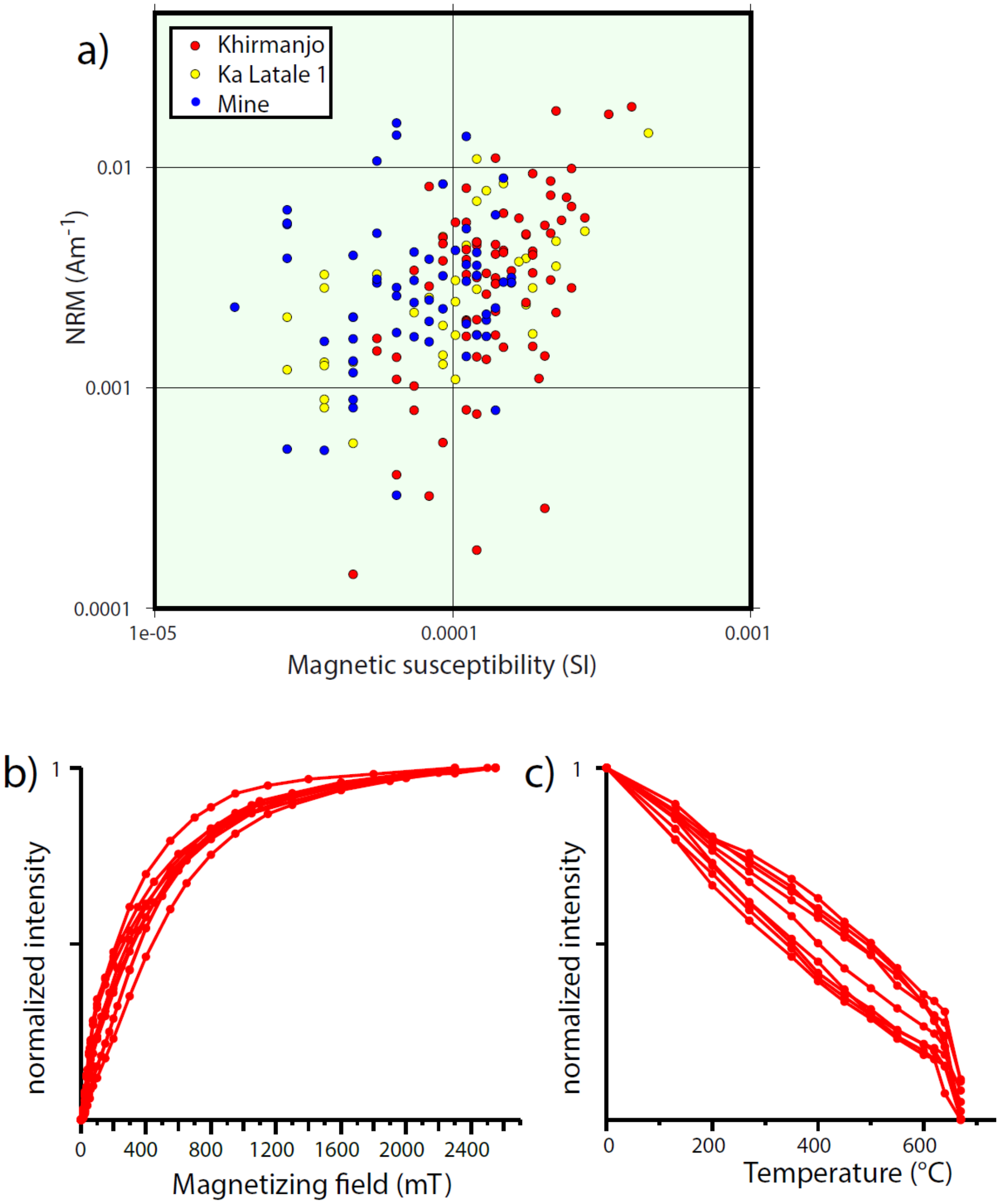

Figure S 3.5 a) Plot of the NRM versus the magnetic susceptibility for samples of the Khirmanjo, Mine and Ka Latale 1 sections. b) IRM acquisition for samples of the Khirmanjo section and c) plot of the normalized intensity of the magnetization during the progressive thermal demagnetization of the IRM acquired at 2.4T.

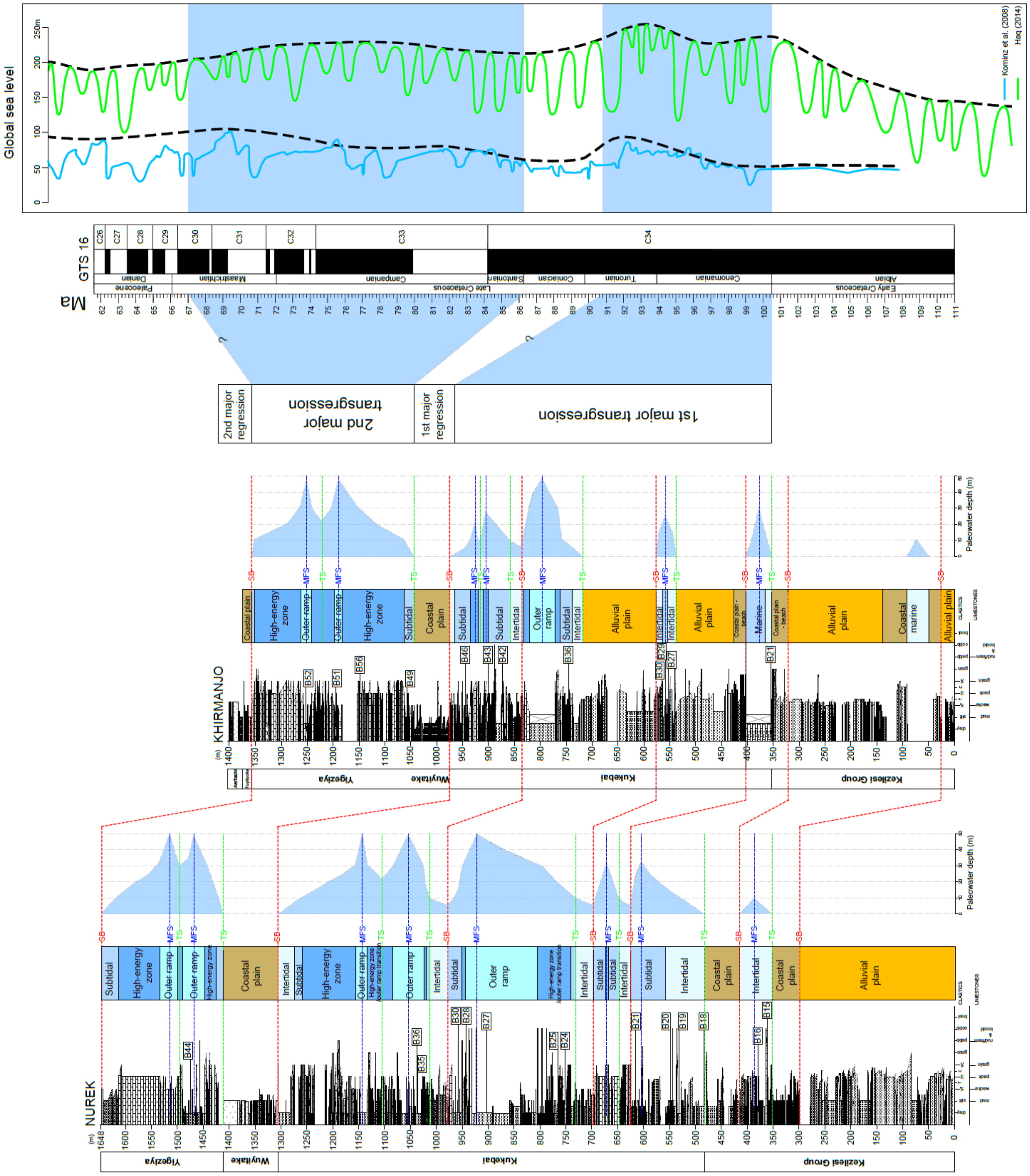
Global sea level
Kominz et al. (2008)
Haq (2014)
GTS 16
Ma
Paleocene
Late Cretaceous
Early Cretaceous
Danian
Maastrichtian
Campanian
Santonian
Coniacian
Turonian
Cenomanian
Albian
1st major transgression
1st major regression
2nd major transgression
2nd major regression
KHIRMANJO
NUREK
Paleowater depth (m)
Yigeziya
Wuyitake
Kukebai
Kezilesi Group
SB
MFS
TS

Figure S 3.6 Paleo-water depths & inferred relative sea level curves for the Nurek and Khirmanjo sections compared to the global sea level curve of Kominz et al. (2008) and Haq (2014). The blue shaded areas highlight the major sea incursions, which have been dated in this study.

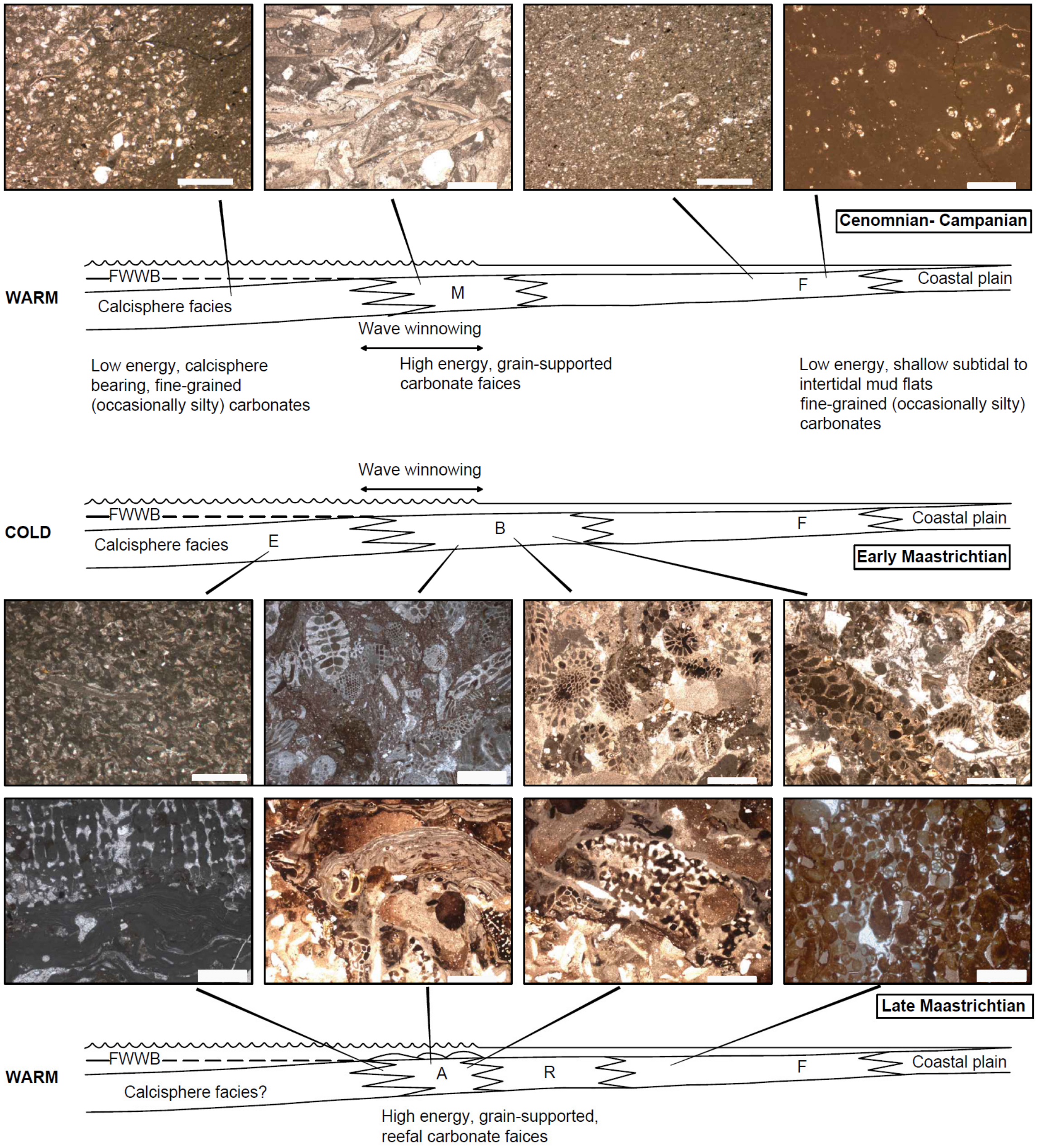

Figure S 3.7 The shift in the lithofacies during the Maastrichtian. Relatively warm Cenomanian-Campanian interval is represented by mollusk-rich facies. Early Maastrichtian cooling is evidenced by the dominance of bryozoa-rich facies without any photozoan components. The following warming pulse is represented by the appearance of heterozoan reefal organisms. M: mollusk-rich facies, F: foraminifera-rich facies, B: bryozoa-rich facies, E: echinoderm-rich facies, A: algae-rich facies, R: reefal facies. Scale bars: 500 µm.

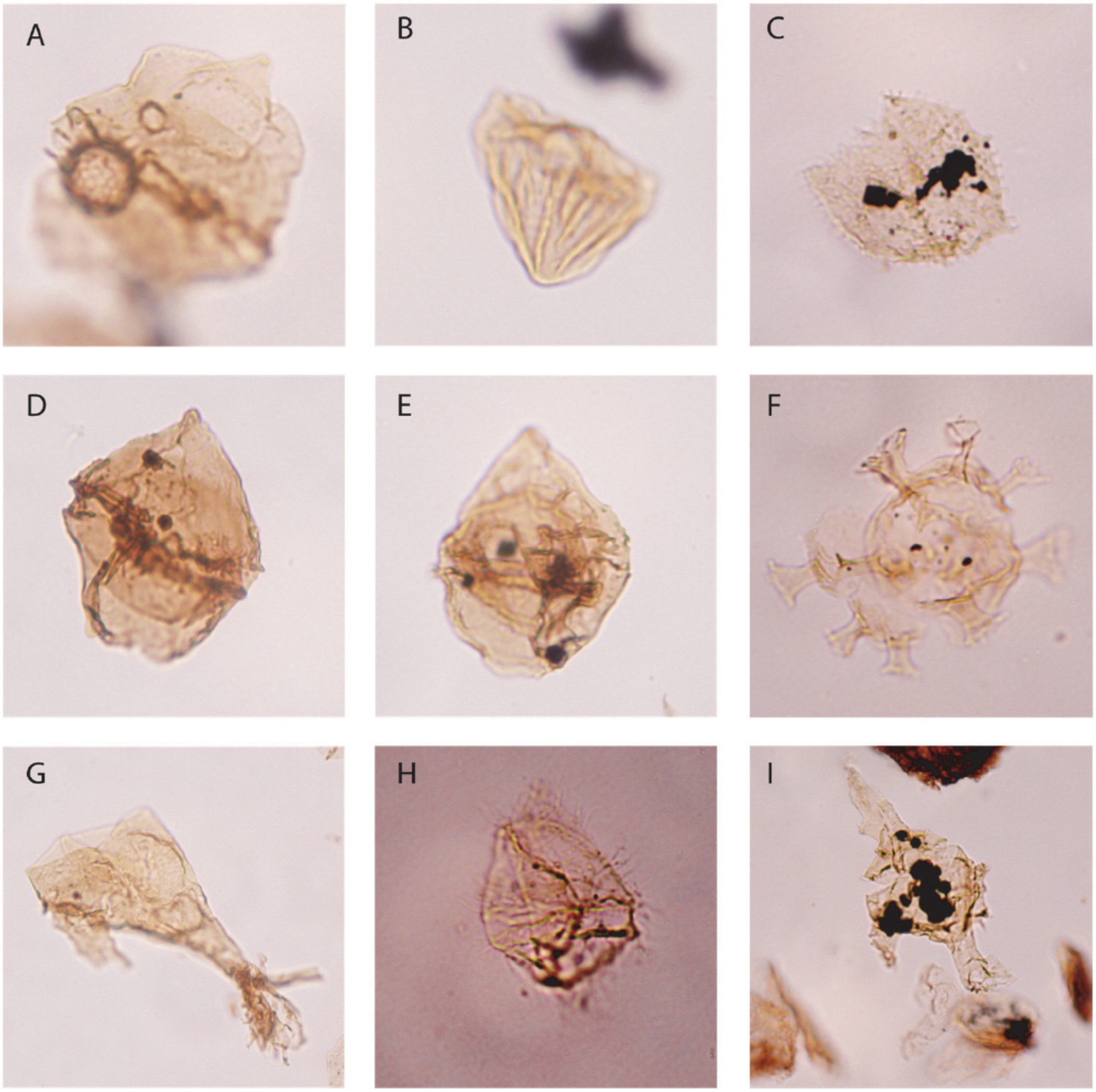

PLATE A Selected dinocyst taxa with sample and England finder coordinates. A. *Chatangiella* spp. (Nurek section, NR-B43 - P45/2). B. *Dinogymnium* spp. (Khirmanjo section, KR-B56 – K37/2) C. *Epilosphaeridium spinosa* (Khirmanjo section, KR-B29 - D25/3) D-E. *Isabelidinium* spp. (Nurek section, NR-B39 – S24/2 and S25/1) F. *Oligosphaeridium albertense* (Ka Latale 1 section, KL1-B06 – J24/2) G. *Odontochitina* cf. *costata* (Ka Latale 1 section, KL1-B06 – K25/2) H. *Palaeohystrichophora infusorioides* (Ka Latale 1 section, KL1-B06 – K26/1) I. *Xenascus ceratoides* (Ka Latale 2 section section, KL2-B15 – B42/3). Note the field of view is approximately 100x100 um, except for G and I, which are ca. 200x200um.

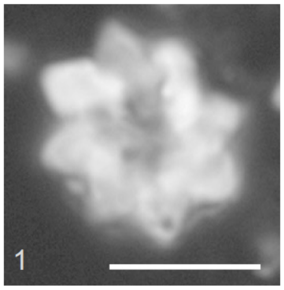
1

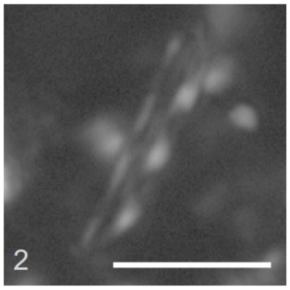
2

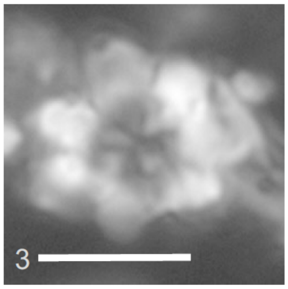
3

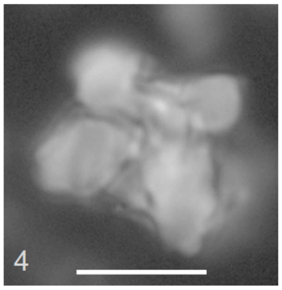
4

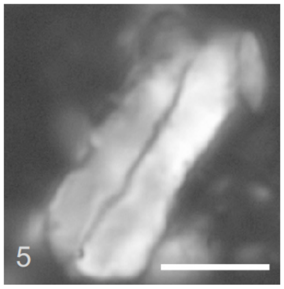
5

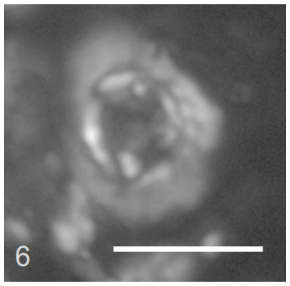
6

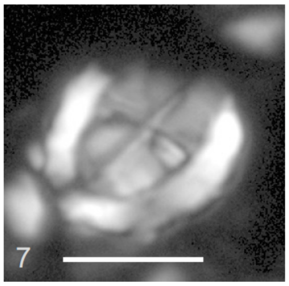
7

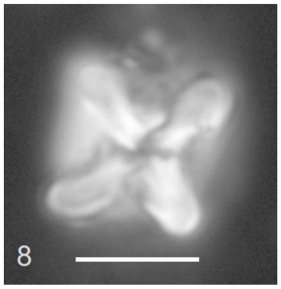
8

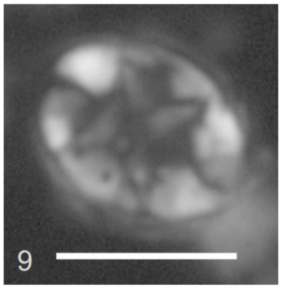
9

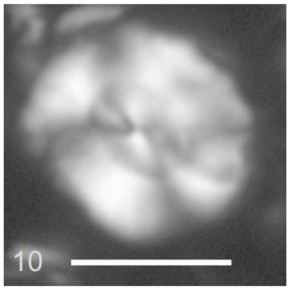
10

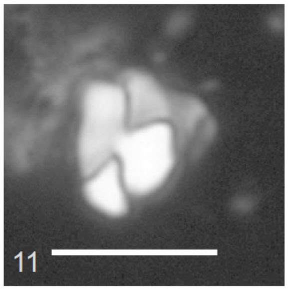
11

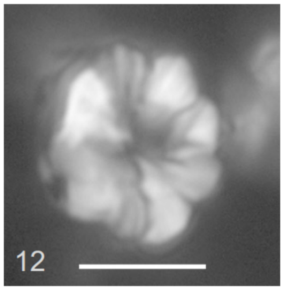
12

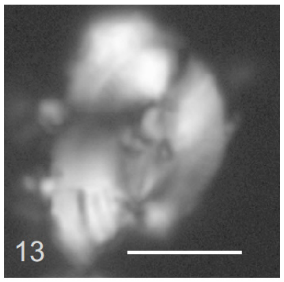
13

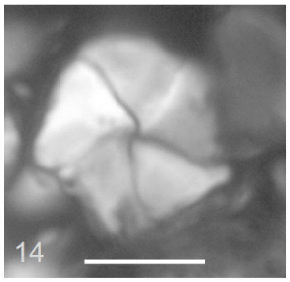
14

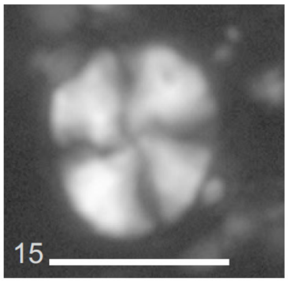
15

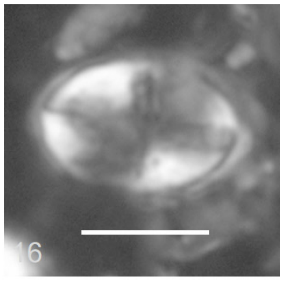
16

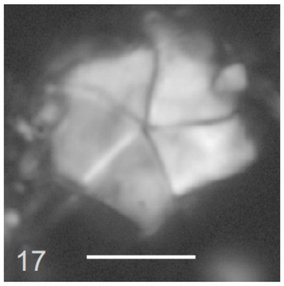
17

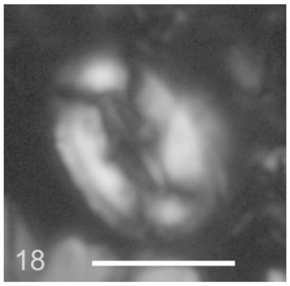
18

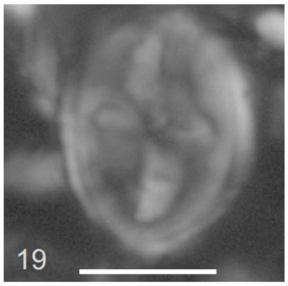
19

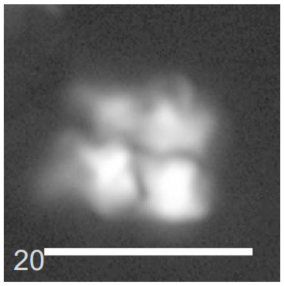
20

PLATE B Light microscope (crossed nicols) images of selected calcareous nannofossil taxa from Nurek and Kirmanjo sections. Scale bar 5µm. 1. *Eprolithus octopetalus* (Nurek section, NR-B27); 2. *Microrhabdulus decoratus* (Nurek section, NR-B27); 3. *Eprolithus moratus* (Nurek section, NR-B30); 4. *Uniplanarius gothicus* (Khirmanjo section, sample KR-B51); 5. *Lucianorhabdus cayeuxii* (Nurek section, NR-B44); 6. *Cylindralithus biarcus* (Nurek section, NR-B27); 7. *Arkangelskiella cymbiformis* (Khirmanjo section, KR-B52); 8. *Micula staurophora* (Nurek section, NR-B35); 9. *Eiffellithus turriseiffelii* (Nurek section, NR-B27); 10. *Watznaueria barnesiae* (Nurek section, NR-B27); 11. *Calculites obscurus* (Nurek section, NR-B44); 12. *Eprolithus floralis* (Nurek section, NR-B27); 13. *Broinsonia parca constricta* (Khirmanjo section, KR-B52); 14. *Micrantolithus* sp. (Nurek section, NR-B44); 15. *Cyclagelosphaera margerelii* (Nurek section, NR-B27); 16. *Eiffellithus eximius* (Nurek section, NR-B44); 17. *Braarudosphaera bigelowii* (Nurek section, NR-B44); 18. *Broinsonia signata* (Nurek section, NR-B44); 19. *Gartnerago segmentatum* (Nurek section, NR-B25); 20. *Quadrum gartneri* (Nurek section, NR-B36).

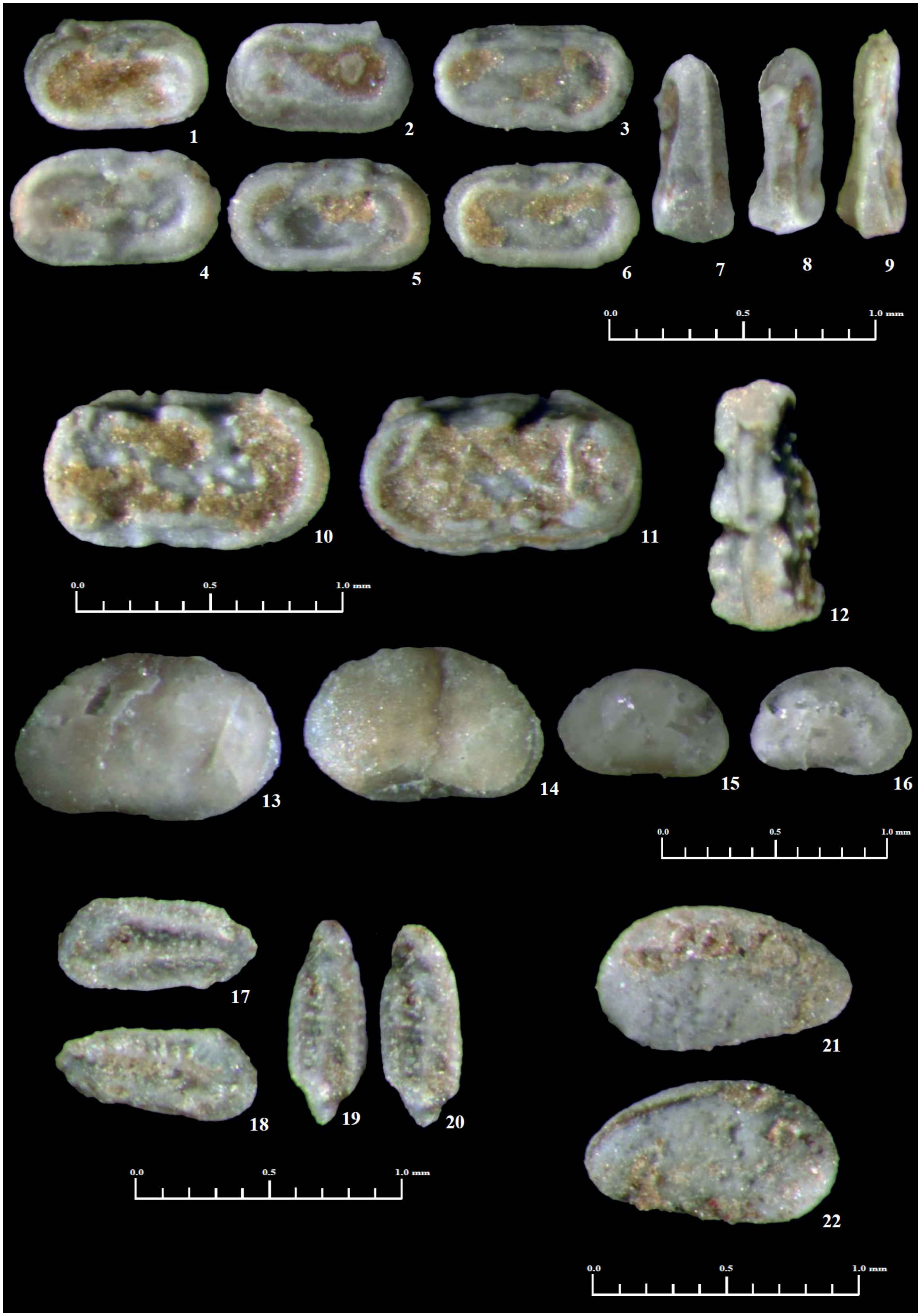
1
2
3
4
5
6
7
8
9
0.0
0.5
1.0 mm
10
11
12
0.0
0.5
1.0 mm
13
14
15
16
0.0
0.5
1.0 mm
17
18
19
20
21
22
0.0
0.5
1.0 mm
0.0
0.5
1.0 mm

PLATE C Images of selected ostracods from the Khirmanjo and Mine sections. 1-9 *Cytherelloidea hindei* (Kaye, 1964) (Khirmanjo section, KR-B49). 10-12 *Cytherelloidea granulosa* (Jones, 1849) (Khirmanjo section, KR-B49). 13-16 *Fossocytheridea* sp. 15-16-juveniles (Mine section, MI-B08). 17-20 *Isocythereis grossouvrensis* (Donze & Thomel, 1972) (Khirmanjo section, KR-B42). 21-22 *Schuleridea* sp. aff. S. jonesiana (Bosquet, 1852) (Khirmanjo section, KR-B36).

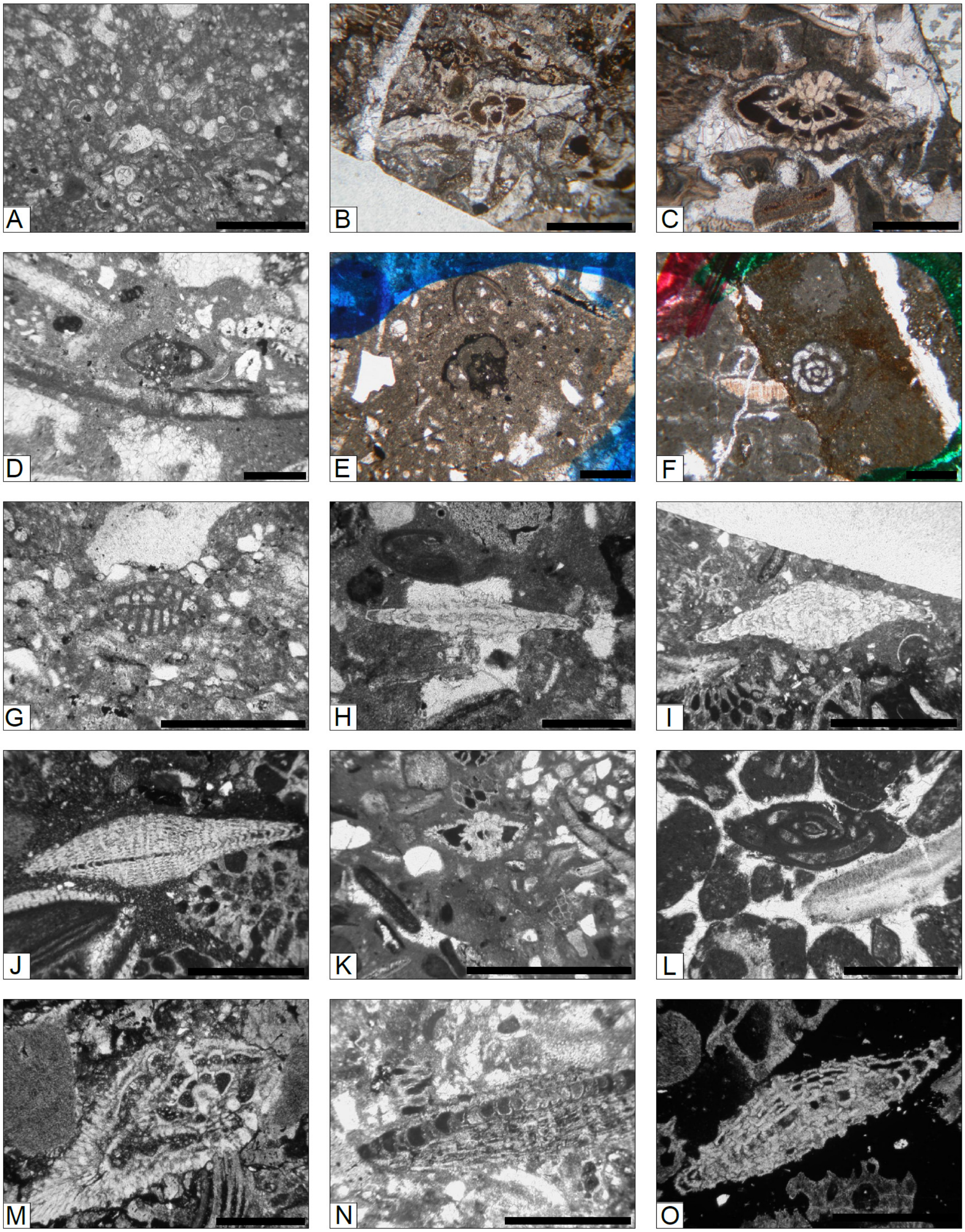
A
B
C
D
E
F
G
H
I
J
K
L
M
N
O

PLATE D Images of selected foraminifera from the Khirmanjo section. A. *Calcispaerula innominata* (KR-C210), scale bar: 250 µm; B. *Pseudosiderolites* sp. (KR-C301), scale bar: 500 µm; C. *Pseudosiderolites vidali* (KR-C300), scale bar: 500 µm; D, E, F. *Charentia cuvillieri* (KR-C39, KR-C51), scale bar: 500 µm; G. *Cuneolina pavoni* (KR-C36), scale bar: 250 µm; H. *Goupilloudina* sp. (KR-C327), scale bar: 250 µm; I. *Pseudorbitoides* sp. (KR-C304), scale bar: 250 µm; J. *Lepidorbitoides* sp. (KR-C337), scale bar: 500 µm; K. *Praesiderolites douvillei* (KR-C252), scale bar: 500 µm; L. *Quinqueloculina robusta* (KR-C347), scale bar: 500 µm; M. *Siderolites calcitropoides* (KR-C301), scale bar: 250 µm; N. *Sivasella* sp. (KR-C304), scale bar: 250 µm; O. *Vaughanina* sp. (KR-C304), scale bar: 250 µm.

Facies code	Lithology	Sedimentary structures/Other features	Interpretation
Sl	Poorly to moderately sorted coarse- to medium-grained sandstones	Horizontal lamination	Saltation transport of sand in rivers at high flow velocities in the upper flow regime
Sc	Poorly to moderately sorted coarse- to medium-grained sandstones	Cross-bedding	Migration of dunes in rivers at high flow velocities in the lower flow regime
Ss	Poorly to moderately sorted fine-grained sandstones	Symmetrical ripples, bioturbation, lenticular bedding	Wave reworking, migration of ripples
Sa	Poorly to moderately sorted fine-grained sandstones	Asymmetrical ripples	Current reworking, migration of ripples
Ch	Poorly sorted, grain-supported conglomerate, granules and pebbles, poorly sorted medium- to coarse-grained sandstone	Erosive-base, Scour-fill structures, rip-up clasts, megaripples, cross-bedding	Deposition in channels
Mp	Siltstones, mudstones	Horizontal lamination, ripples, bioturbation, dewatering structures, algal mats, wavy & flaser bedding	Suspension settling out of fine-grained sediments in a subaqueous (pond, lake)/submarine environment
Ml	Siltstones, mudstones	Horizontal lamination or massive	Suspension settling out of fine-grained sediments from flood waters carried into the flood plain
Mg	Siltstones, claystones, mudstones with gypsum nodules or/and gypsum layers	Horizontal lamination or massive, presence of some sand layers	Suspension settling out of fine-grained sediments with gypsum precipitation in pond/lake
Ms	Siltstones, mudstones alternating with fine-grained sandstones	Sometimes with carbonate nodules, bioturbation, ripples	Crevasse splay deposits, sedimentation from both saltation and suspension on flood plain and levees
Gl	Thick gypsum (occasionally interbedded with limestones and mudstones)	Lamination and nodular structures, occasionally massive, some cases with an erosional base	Gypsum precipitation in a hypersaline lagoon (pond) with occasional carbonate precipitation and suspension settling of fine material
Cq	Coquina shell bed	Poorly bedded to massive, abundant bivalves forming a bioherm, calcareous cement-matrix	High energy environment, deposition above wave base
Ts	Tempestites, alternation of storm and shelf mudstones	Graded shell beds and detrital carbonates with low-angle laminations, lenticular bedding, intense bioturbation in shelf mudstones	Suspension settling of fine material during fair weather phase and storm influenced deposition during storms
Mr	Mudstones, marls	Horizontal lamination or massive, some shelly layers at some levels, some carbonate layers	Suspension settling out of fine-grained sediments with carbonate precipitation in marine environment

Table S 3.1 Descriptions of siliciclastic facies

Facies code	Type	Lithology	Main components	Interpretation
MF1	Pure carbonates	Mudstone	Micrite, rare dolomite crystals, unidentified allochems	Low energy environment, deposition below wave base or in a protected environment
MF2		Wackestone	Bivalves, shell fragments, serpulids, echinoderm fragments, calcispheres	Low energy environment, deposition below wave base or in a protected environment
MF3		Packstone	Gastropoda, foraminifera, peloids, serpulids, echinoderm fragments, shell fragments, bryozoa	Deposition in varying energy levels
MF4		Grainstone	Bivalves, gastropoda, shell fragments, foraminifera, bryozoa	High energy environment, deposition above wave base
MF5		Floatstone/rudstone	Bivalves, shell fragments, foraminifera, echinoderm fragments	Allochems coarser than 2 mm are not bounded during deposition, floatstone matrix supported, rudstone grain-supported
MF6		Ooidal grainstone	Radial-fibrious ooids, low amount of other bioclasts	Shallow marine, low-energy environment
MF7		Carbonate breccia	Stylolites, fragments of corals, sponges and rudists, bryozoa and encrusting algae	Deposition in a fore-reefal environment
MF8		Boundstone	Corals, encrusting red algae, sponges, echinoid fragments, foraminifera	Reef-building organisms are bounded during deposition
MF9a	Dolomite bearing	Dolomitic limestone	Partly dolomitization of the cement, calcite is still the common mineral	Secondary dolomitization
MF9b		Dolomite	Dolomite is the common mineral	Complete or nearly complete dolomitization
MF10	Mixed with siliciclastics	Muddy micrite	Micrite with siliciclastic muds	Mixing of siliciclastics and carbonates, transport of tidal flat and near shore siliciclastics into deeper, subtidal environments by storm-surge ebb, wind forcing etc. (Punctuated mixing of Mount, 1984)
MF11		Muddy allochem limestone	Siliciclastic muds and dominating allochems	Mixing of siliciclastics and carbonates, transport of tidal flat and near shore siliciclastics into deeper, subtidal environments by storm-surge ebb, wind forcing etc. (Punctuated mixing of Mount, 1984)
MF12		Sandy allochem limestone	Bivalves, gastropoda, foraminifera, bryozoa, serpulids	Mixing of siliciclastics and carbonates, transport of tidal flat and near shore siliciclastics into deeper, subtidal environments by storm-surge ebb, wind forcing etc. (Punctuated mixing of Mount, 1984)
MF13		Sandy micrite	Micrite with siliciclastic sands	Mixing of siliciclastics and carbonates, transport of tidal flat and near shore siliciclastics into deeper, subtidal environments by storm-surge ebb, wind forcing etc. (Punctuated mixing of Mount, 1984)
MF14		Micritic mudrock	Micrite and fine silicilastics	Mixing of siliciclastics and carbonates, transport of tidal flat and near shore siliciclastics into deeper, subtidal environments by storm-surge ebb, wind forcing etc. (Punctuated mixing of Mount, 1984)
MF15		Micritic sandstone	Micrite and siliciclastic sand	Mixing of siliciclastics and carbonates, transport of tidal flat and near shore siliciclastics into deeper, subtidal environments by storm-surge ebb, wind forcing etc. (Punctuated mixing of Mount, 1984)

Table S 3.2 Descriptions of carbonate microfacies

Sedimentary environment	Facies association	Facies
Alluvial plain (Fluvial, playa, lacustrine)	FA1	Sl, Sc, Sa, Ch, Ml, Ms, Mp, Mg
Coastal plain (Supratidal including sabkha and coastal salina, intertidal)	FA2	Mp, Mg, Gl, MF1, MF1, MF2, MF6, MF9, MF10
High-energy shoreface to shoal/beach	FA3	Ss, Sc
Low-energy Subtidal	FA4	Mp, Sa, Ss, Cq MF1, MF2, MF3, MF5, MF9a, MF11, MF12
High-energy Subtidal	FA5	MF3, MF4, MF7, MF8, MF12, MF13, MF15
Offshore	FA6	Ts, Cq, Mp, Mr, MF2, MF3, MF12, MF13

Table S 3.3 Facies associations and their related facies/microfacies and depositional environments

Section	N	Dec. IS	Inc. IS	Dec. TC	Inc. TC	α95	k	Lat.	Long.
Mine	49	334.6	-29.8	335.0	58.2	3.6	33.5	70.7	349.7
Ka Latale 1	32	10.7	22.7	1.4	63.8	4.2	37.6	84.3	84.5
Khirmanjo	55	58.4	27.7	317.2	38.3	4.1	23.2	49.8	328.6

Table S 3.4 Mean paleomagnetic results. N, number of samples used in the calculation of the mean direction, Dec. and Inc. are the declination and inclination of the mean direction in in situ (IS) and after tilt correction (TC). k is the precision parameter of the Fisher statistics (Fisher, 1953). Lat., Long. are the latitude and longitude of the virtual geomagnetic pole determined from the tilt corrected mean direction.

sample	Line or Plane	anchored	Demag type	nb points	step min	step max	Dec IS	inc IS	Dec TC	inc TC	mad value	VGP Long	VGP Lat	Height (m)
15MINE01A	L	n	D	11	240	640	341.3	-33.2	344.4	54.1	5.9	326.61	76.55	0
15MINE02A	L	n	D	11	240	640	89.9	-25.7	36.7	-24	6.1	213.38	27.49	0.2
15MINE03A	L	n	D	11	240	640	340.5	-35.2	342.7	52.3	4.9	323.35	74.47	0.3
15MINE04A	L	n	D	11	240	640	323.8	-32.8	319.4	53.9	4.7	348.01	57.47	19.5
15MINE05A	L	n	D	11	240	640	319.3	-29.8	311.3	55.2	3.8	354.28	51.77	20.2
15MINE06A	L	n	D	11	240	640	342.1	-33.7	345.4	53.6	6	322.98	77.04	39.3
15MINE07A	L	n	D	11	240	640	336.1	-16.8	339.9	71.1	10	41.02	69.4	41.8
15MINE08R	L	n	D	11	240	640	337.3	-36.8	338.2	51.1	4.7	326.71	70.64	46.5
15MINE09A	L	n	D	8	360	640	340.3	-26.1	345.8	61.2	6.7	1.95	79.03	48.5
15MINE10A	L	n	D	11	240	640	335.4	-33.3	336	54.7	5.5	338.44	70.48	50.4
15MINE11A	L	n	D	10	280	640	334.5	-31	334.7	57	8.6	346.09	70.2	52.2
15MINE12A	L	n	D	11	240	640	340.2	-34.6	342.4	52.9	6.9	325.66	74.54	53
15MINE13A	L	n	D	11	240	640	337.3	-19.6	342.1	68.1	5.4	32.82	73.17	57.1
15MINE14A	L	n	D	11	240	640	344.9	-29	351.7	57.4	6.7	331.33	83.29	59
15MINE15A	L	n	D	11	240	640	343.9	-24.3	353.4	62	9	21.13	84.01	61.7
15MINE16A	L	n	D	10	280	640	334	-17.7	333.7	70.3	5	32.83	67.17	62.5
15MINE17A	L	n	D	10	280	640	332.9	-35.7	332.5	52.3	6.8	335.68	66.9	67.5
15MINE18A	L	n	D	9	240	560	351.5	-20.9	9.8	61.4	6.1	141.38	82.16	69.5
15MINE19A	L	n	D	11	240	640	8.5	19.8	94.5	52	5.8	135.99	17.14	73
15MINE21A	L	n	D	11	240	640	330	-32.6	328	55.2	6.2	345.47	64.52	92.3
15MINE22A	L	n	D	10	280	640	336.6	-22.7	339.6	65.2	6.8	17.95	73.53	93
15MINE23A	L	n	D	11	240	640	329.9	-22.1	324.7	65.6	6.7	13.73	63.58	97
15MINE24A	L	n	D	10	240	600	322.7	-0.6	256.8	78.3	7.4	48.55	31.66	106.3
15MINE25A	L	n	D	11	240	640	339.9	-36.6	341.5	51	5.2	321.67	72.97	108.4
15MINE27A	L	n	D	8	440	670	329.6	-33.8	327.8	54	8.1	343.01	63.95	122
15MINE28A	L	n	D	11	240	640	349.1	-28.4	358.4	56.4	4.8	278.5	86.86	126.6
15MINE29A	L	n	D	11	240	640	339.9	-27.3	344.5	60.2	10.1	355.69	78.16	128.5
15MINE30A	L	n	D	11	240	640	340.4	-28.7	344.8	58.8	3.5	347.89	78.31	129
15MINE31A	L	n	D	12	280	670	330.3	-33.5	328.6	54.3	9	343.11	64.67	131
15MINE32A	L	n	D	8	360	640	314.4	-15.3	286.4	63.9	8	16.64	37.55	131.1
15MINE35A	L	n	D	11	240	640	334.2	-29.1	334.2	58.9	6.2	352.28	70.23	137.7

15MINE36A	L	n	D	11	240	640	334	-42	334	46	2.9	322.36	65.15	138
15MINE37A	L	n	D	12	240	660	319.2	-38.1	316.7	47.6	9.9	340.67	52.92	138.5
15MINE38A	L	n	D	11	240	640	321.3	-30.3	314.4	55.4	10.2	353.11	54.19	140.5
15MINE39A	L	n	D	7	480	670	335.6	-52.4	335.2	35.6	7.4	308.32	60.71	148.5
15MINE40A	L	n	D	11	320	670	321.2	-1.5	259.3	76.6	11.1	44.91	31.14	149
15MINE41A	L	n	D	14	240	675	273.2	-37.8	286.3	21.3	4.8	342.7	19.52	153
15MINE42A	L	n	D	14	240	675	341.1	-47.6	340.2	40	6.8	304.85	66.06	163.2
15MINE43A	L	n	D	12	320	675	318.6	-19.5	299.5	63.6	13.4	12.25	46.14	163.5
15MINE45A	L	n	D	12	240	660	327.6	-45.8	328	41.9	9.2	323.92	58.91	170
15MINE46A	L	n	D	11	240	640	325.3	-30.3	320.2	56.6	5	352.5	59	170.2
15MINE48A	L	y	D	11	280	660	354.4	-12.3	28.2	65.3	5.2	134.77	68.38	172.5
15MINE49A	L	n	D	12	240	660	351.8	-43.3	351.4	42	4.4	281.95	72.79	180.2
15MINE50A	L	n	D	7	440	660	321	-48.9	323.2	37.9	13.7	324.82	53.64	182.1
15MINE51A	L	n	D	9	360	660	317.8	-7.6	274.8	71.1	11.4	31.47	34.4	185.4
15MINE52A	L	n	D	12	240	660	37.2	-36.2	24.1	20.1	5.3	211.93	53.58	186.5
15MINE53A	L	n	D	12	240	660	344.3	-22.7	355.5	63.4	6.4	42.96	83.91	188.5
15MINE54A	L	n	D	11	240	640	346.4	-34.5	350.6	51.7	5.2	302.69	79.33	190.2
15MINE56A	L	n	D	12	240	660	340.9	-38.3	342.3	49.2	8.1	315.91	72.57	195.5
15MINE57A	L	n	D	12	240	660	335.2	-39.7	335.3	48.3	4.8	324.6	67.2	199.2
15MINE58A	L	n	D	12	240	660	341.8	-29.7	346.5	57.5	4.5	339.49	79.38	203
15MINE59A	L	n	D	12	240	660	329.9	-17.8	322.4	69.8	3.1	25.78	61.23	210.2
15MINE60A	L	n	D	11	240	640	342.9	-35.9	345.5	51.3	4.5	315.08	75.89	212.6
15WFAL01A	L	n	D	11	240	640	357.8	38.1	313.9	71.6	7.1	29.28	55.91	0.5
15WFAL02A	L	n	D	11	240	640	13.5	33	1.3	74.4	4.1	76.46	68.99	1
15WFAL03A	L	n	D	11	240	640	17.3	23.4	15.2	65.4	3.6	124.59	76.62	1.3
15WFAL04A	L	n	D	10	280	640	14.7	17.9	10.9	59.7	3.1	156.17	81.65	2
15WFAL05A	L	n	D	11	240	640	5.1	19.3	352.6	59.2	4.6	348.74	84.32	3
15WFAL06A	L	n	D	11	240	640	24.9	22.7	31.5	64.3	6.5	138.95	66.28	3.9
15WFAL08A	L	n	D	12	240	660	357	14.7	342.9	52.1	4.1	322.69	74.52	5.8

15WFAL09 A	L	n	D	13	240	670	30.3	17	39.4	57.6	12.5	154.83	59.6	7
15WFAL10 A	L	n	D	13	240	670	33	24.6	49.1	64.1	8.3	138.51	54.07	8.4
15WFAL11 A	L	n	D	12	240	660	11.9	14.4	6.7	55.9	6.5	195.23	83.74	9.4
15WFAL13 A	L	n	D	11	240	640	5.1	33.8	337.5	72.3	11.4	42.65	67.16	11.5
15WFAL14 A	L	n	D	11	240	640	14.3	6.7	11.9	48.5	11.9	207.73	75.78	12.5
15WFAL15 A	L	n	D	11	240	640	355	18.6	337.1	54.7	9.6	337.72	71.32	13
15WFAL16 A	L	n	D	11	240	640	1.7	15.2	349.5	54.2	3.1	316.61	80.23	14
15WFAL17 A	L	n	D	11	240	640	25.2	26.1	33.5	67.5	12	129.23	64.39	16.5
15WFAL19 A	L	n	D	10	240	600	356.7	21.1	337.4	57.7	3.2	347.1	72.44	20.2
15WFAL21 A	L	n	D	13	240	670	16.9	6.6	15.8	48.6	3.2	198.25	73.49	25
15WFAL22 A	L	n	D	10	240	600	9.6	11.5	3.6	52.6	9.9	230.04	82.76	29
15WFAL23 A	L	n	D	12	240	660	18.8	24.3	18.5	66.3	4.9	124.56	74.11	31.5
15WFAL24 A	L	n	D	13	240	670	25.5	41.3	55.6	81.9	12.9	94.14	47.28	33
15WFAL26 A	L	n	D	12	240	660	4.9	32.1	340	70.8	4	40.36	69.72	38
15WFAL27 A	L	n	D	11	320	670	352.8	3.6	343.7	40.2	14.7	298.74	68.17	40.2
15WFAL29 A	L	n	D	13	200	660	11.4	25.1	1.6	66.3	5.6	81.47	81.03	47
15WFAL30 A	L	n	D	13	240	670	11	34.2	352.4	75	11.2	65.28	67.53	49
15WFAL31 A	L	n	D	13	240	670	22.9	27.5	28.5	69.3	5.4	121.15	66.62	51.5
15WFAL33 A	L	n	D	13	240	670	2	31.1	335.3	68.6	3.5	28.3	69.14	56.5
15WFAL34 A	L	n	D	12	240	660	3.4	28.9	341	67.4	3.6	28.93	73.1	58
15WFAL35 A	L	n	D	13	240	670	3.9	24.9	346.3	64	3.5	19.58	78.37	59.8
15WFAL36	L	n	D	13	240	670	13.1	24.2	5.7	65.7	6	99.66	80.93	61.6

A														
15WFAL37A	L	n	D	10	320	660	3.2	21.2	348.1	60.3	7.7	357.42	80.85	62.8
15WFAL40A	L	n	D	11	280	660	13.8	19.6	8.7	61.3	3.7	140.36	82.96	71
15WFAL41A	L	n	D	12	240	660	39.8	-19.7	39.8	19.8	3.3	193.61	43.96	72.5
15WFAL42A	L	n	D	11	240	640	9.2	12.5	2.7	53.5	7.7	233.37	83.84	81.3
16KHC006A	L	y	D	12	330	670	57.1	21.3	324.7	41.4	2.2	325.27	56.83	108.2
16KHC009A	L	y	D	10	330	655	57.8	24	321.3	40.2	1.6	327	53.74	140
16KHC010A	L	y	D	11	290	655	61.5	41.2	303.7	30.2	1.4	332.53	36.3	145.2
16KHC011A	L	y	D	11	290	655	53.3	28.7	319.8	34.1	1.4	322.76	50.16	147.7
16KHC012A	L	y	D	14	290	680	60.2	30.2	313.6	37.7	1.6	330.84	46.8	154
16KHC013A	L	y	D	11	290	655	58.8	31	314	36.3	0.8	329.37	46.58	163.5
16KHC014A	L	y	D	6	570	670	66.7	9.5	331.2	55.7	3	344.89	67.05	168
16KHC015A	L	y	D	11	290	655	77.9	31.9	295.7	45	2.7	348.24	35.51	174.5
16KHC016A	L	y	D	14	290	680	65	11.5	329.9	53.3	3.1	339.9	65.39	181.2
16KHC017A	L	y	D	14	290	680	51.2	24.8	325	34.9	1	318.47	54.35	186.5
16KHC022A	L	y	D	9	490	680	49	20.4	330.9	35.5	1.2	312.44	58.84	229.2
16KHC023A	L	y	D	8	530	680	59.8	26.2	317.6	40.2	2.2	330.04	50.88	232.5
16KHC024A	L	y	D	5	530	655	50.8	23.3	326.8	35.4	3.3	317.04	55.88	238.5
16KHC025A	L	y	D	8	490	670	57.8	47.5	301.5	23.7	9.4	330.32	32.3	240
16KHC026A	L	y	D	7	530	670	84.5	50.2	282.7	29.1	5.4	345.1	19.38	241
16KHC029A	L	y	D	7	410	640	10	42.8	322	-3.1	5.2	300.76	37.22	258.7
16KHC030A	L	y	D	9	490	680	54.8	20.9	326.7	39.8	1.3	321.55	57.67	264
16KHC031A	L	y	D	7	490	660	50.6	10.9	340.9	41.2	6.2	304.45	68.34	269
16KHC032A	L	y	D	14	210	660	51.4	36.3	314.1	28.2	2.5	323.41	43.59	278.7
16KHC033A	L	y	D	9	490	680	72.4	6.2	330.1	62.3	2.2	3.85	66.78	282.2
16KHC034A	L	y	D	11	410	680	66.2	23.4	314.7	46.3	9.4	338.6	50.95	292.5
16KHC035A	L	y	D	8	530	680	68.5	50.2	293.5	25.5	7.7	336.61	26.65	295.8
16KHC038A	L	y	D	7	410	640	32.6	69.5	293.1	-0.2	8.1	325.39	17.97	320
16KHC040A	L	y	D	7	450	655	72	11	323	59	2.1	355.57	61.32	332
16KHC042A	L	y	D	10	410	670	54.5	19.9	328	40.2	2.8	320.65	58.81	339.5
16KHC045A	L	y	D	11	290	655	57	36.9	310.1	31.1	4.4	328.5	41.6	350

16KHC048A	L	y	D	5	290	450	80.5	12.8	307.7	63	5	6.89	50.78	360
16KHC049A	L	y	D	7	290	530	57.6	26.4	319.1	38.5	3.6	327.2	51.37	370
16KHC050A	L	y	D	8	290	570	59.8	23.1	320.7	42.2	2.9	329.62	54.07	380
16KHC051A	L	y	D	10	370	660	40.1	46.9	310.4	15.1	5.5	319.19	36.08	390
16KHC052A	L	y	D	12	370	680	39.9	43.7	313.2	16.7	2.8	317.64	38.7	395
16KHC054A	L	y	D	8	530	680	57.8	23.7	321.7	40.4	4.5	326.86	54.13	413.5
16KHC055A	L	y	D	8	490	670	39	25.3	330.9	25.1	2.8	304.25	54.23	418
16KHC056A	L	y	D	4	570	655	49.8	17	334.2	37.8	4.5	310.57	62.18	422.5
16KHC057A	L	y	D	8	530	680	51.1	13	338	40.7	7.3	308.57	66.17	431.8
16KHC058A	L	y	D	6	490	655	46.1	15.8	337.5	35.2	2.6	303.06	63.1	444.4
16KHC059A	L	y	D	7	490	660	46.9	32.8	319.8	27.4	0.9	317.85	47.52	451.6
16KHC060A	L	y	D	9	490	680	71	31.7	302.9	42.3	1.2	341.88	40.13	458.3
16KHC061A	L	y	D	7	530	670	62.9	17	324.9	48.3	3.6	334.21	59.72	465
16KHC063A	L	y	D	5	490	640	46.1	33.3	319.7	26.5	1.4	317.35	47.1	480.5
16KHC064A	L	y	D	9	490	680	64.5	36.1	305.3	35.6	1.8	335.07	39.52	487.2
16KHC065A	L	y	D	9	490	680	71.5	22	310.6	50.6	2.8	346.2	49.29	494.5
16KHC066A	L	y	D	5	490	640	47	29.4	322.9	29.3	2.2	316.15	50.52	503.2
16KHC067A	L	y	D	5	490	640	60.5	45.3	301.5	26.6	3.4	331.91	33.31	511.5
16KHC068A	L	y	D	9	490	680	40.1	24	331.6	26.6	1.8	304.36	55.34	520.7
16KHC069A	L	y	D	9	490	680	48.2	31.2	320.6	29.1	3.1	318.25	48.77	525
16KHC070A	L	y	D	7	490	660	63.3	19.2	321.9	47.2	2	334.83	56.96	531
16KHC071A	L	y	D	6	490	655	77.3	7.4	321	65.3	11.6	11.3	60.15	536.2
16KHC073A	L	y	D	6	490	655	64.8	37.9	303.8	34.4	13.5	335.22	37.9	548
16KHC075A	L	y	D	4	490	610	64.2	22	318.1	45.9	7.8	335.86	53.48	557
16KHC078A	L	y	D	6	490	655	60.5	16.7	327.2	46.6	3.7	329.77	60.87	567.5
16KHC080A	L	y	D	8	490	670	63.6	21.6	319	45.8	4.1	335.1	54.15	578
16KHC081A	L	y	D	6	490	655	64.7	24.4	315.2	44.6	2.8	336.34	50.7	580.5
16KHC082A	L	y	D	9	490	680	85.8	9.6	300.3	68.3	6	18.43	46.77	588

Table S 3.5 Paleomagnetic data per sample

NUREK SECTION																									
SAMPLE	Abundance	*W. barnesiae*	*Eiffellithus* sp.	*T. orionatus*	*G. segmentatum*	*L. carniolensis*	*E. antiquus*	*E. turriseiffelii*	*E. eximius*	*M. decoratus*	*E. floralis*	*E. octopetalus*	*E. moratus*	*R. biarcus*	*Staurolithithes* sp.	*G. segmentatum*	*Braarudosphaera* sp.	*Rucinolithus* sp.	*Q. gartneri*	?*Micula* sp.	*M. staurophora*	*L. cayeuxi*	*Arkangelskiella* sp.	*U.* cf. *sissinghi*	*C. obscurus*
NR-B8	B																								
NR-B9	B																								
NR-B10	B																								
NR-B11	B																								
NR-B12	B																								
NR-B13	B																								
NR-B14	B																								
NRB15	B																								
NR-B16	B																								
NR-B17	B																								
NR-B17b	B																								
NR-B18	B																								
NR-B19	B																								
NR-B20	VR	x																							
NR-B21	B																								
NR-B22	VR	x																							
NR-B23	B																								
NR-B24	VR	x	x																						
NR-B25	VR	x		x	x																				
NR-B26	VR	x																							
NR-B27	R	x	x	x	x	x	x	x		x	x	x		x	x	x									
NR-B30	VR	x				x		x		x			cf.			x									
NR-B31	B																								
NR-B32	B																								
NR-B33	B																								
NR-B34	VR	x															x								
NR-B35	R	x											x x				x								
NR-B36	VR	x											x				x	x	x						
NR-B37	VR					x							x				x			x					

NR-B38	VR												x				x								
NR-B39	B																								
NR-B40	VR	x																							
NR-B41	B																								
NR-B42	B																								
NR-B43	B																								
NR-B44	R	x							x								x				x	x	x	x	x

Table S 3.6 Nannofossils range chart for the Nurek section

KHIRMANJO SECTION												
SAMPLE	Abundance	*W. barnesiae*	*B. bigelowii*	*C. obscurus*	*M. staurophora*	*E. gorkae*	*E. eximius*	*L. cayeuxi*	*U. gothicus*	*A. cymbiformis*	*C. litterarius*	*C. ehrenbergii*
KR-B52	VR	x			x		x			x	x	x
KR-B51	VR	x		x	x	x		x	x			
KR-B50	B											
KR-B49	VR		x									
KR-B48	B											
KR-B47	B											
KR-B46	B											
KR-B45	B											
KR-B44	B											
KR-B43	B											
KR-B42	VR		x									
KR-B41	B											
KR-B40	B											
KR-B39	B											
KR-B38	B											
KR-B37	B											
KR-B36	B											
KR-B35	B											
KR-B34	B											
KR-B33	B											
KR-B32b	B											
KR-B32	B											
KR-B31	B											
KR-B30	VR	x										
KR-B29	VR	x										
KR-B28	B											
KR-B27	B											
KR-B26	B											
KR-B25	B											
KR-B24	B											
KR-B23	B											
KR-B22	B											
KR-B21	VR	x										

Table S 3.7 Nannofossils range chart for the Khirmanjo section

Sample	**Formation name**	**Dinocyst abundance**	**Pollen abundance**	**Dinoflagellate age estimate**	**Based on:**	**Notes**
MI-B01	Tuyiluoke FM		-			No dinocysts, very few pollen, some plant material.
MI-B05A	Kukebai FM	x	xx	Albian-Turonian	*Palaeohystrichophora infusorioides*	Few marker species. More terrestrial OM than sample below.
MI-B05B	Kukebai FM	xxx	-	Albian(?)-Cenomanian	*Litosphaeridium siphoniphorum*, *Palaeohystrichophora infusorioides*	
MI-B06	Kukebai FM					
MI-B07	Wuyitake FM	-	-			Almost barren, preservation poor
MI-B08	Yigeziya FM	xx	xx		*Xenascus ceratoides*, *Florentinia* spp., *Alterbidinium* spp., *Spinidinium echinoideum*	
MI-B09	Yigeziya FM					No dinocysts or pollen, some plant material.
MI-B10	Tuyiluoke FM	o	-	late Cretaceous	*O. pulcherrimum* / *O. poculum*(?)	low diversity assemblage with frequent *Pediastrum*

Abundance:	xxx	very abundant
	xx	abundant
	x	common
	o	rare
	-	very rare
		absent

Table S 3.8 Dinocyst range chart for the Mine section

Sample	Formation name	Dinocyst abudance	Pollen abundance	Dinoflagellate age estimate	Based on:	Notes:
KL2-B01	Kukebai FM	xx	o	Cenomanian or younger	*Apteodinium deflandrei*	somewhat similar to the upper Kukebai FM samples
KL2-B02	Kukebai FM	o	x	?		poor preservation, terrestrial fraction seems less affected (post depositional oxidation?)
KL2-B03	Kukebai FM	o	o	?		
KL2-B05	Kukebai FM	xxx	o	Albian-Cenomanian or younger	Abundant *P. infusorioides*	No Albian or Turonian markers observed, very likely Cenomanian
KL2-B06	Kukebai FM	xxx	o	Albian-Cenomanian or younger	Abundant *P. infusorioides*	No Albian or Turonian markers observed, very likely Cenomanian
KL2-B09	Kukebai FM	xxx	o	Albian-Cenomanian or younger	Abundant *P. infusorioides*	No Albian or Turonian markers observed, very likely Cenomanian
KL2-B10	Kukebai FM	x	x	Albian-Cenomanian or younger		No Albian or Turonian markers observed, very likely Cenomanian
KL2-B13	Kukebai FM	xx	x	Albian-Cenomanian or younger		No Albian or Turonian markers observed, very likely Cenomanian
KL2-B14	Kukebai FM	xx	x	Albian-Cenomanian or younger		No Albian or Turonian markers observed, very likely Cenomanian
KL2-B15	Kukebai FM	xxx	o	Cenomanian or younger	*Apteodinium deflandrei*	No Turonian markers observed, very likely Cenomanian
KL2-B16	Kukebai FM	xx	x	Cenomanian or younger		
KL2-B17	Kukebai FM	x	x	Cenomanian or younger	*P. infusorioides*	assemblage of almost exclusively *P. infusiroides*
KL2-B22	Wuyitake FM	o	o	?		very few dinocysts
KL2-B21	Wuyitake FM	o	x	?		AOM and some pollen, very few dinocysts
KL2-B20	Wuyitake FM	x	xx	late Cretaceous	*P. infusorioides* *Oligosphaeridium complex*, *Canningia* spp.	mostly non-diagnostic dinos, pollen assemblage relatively diverse
KL2-B19	Wuyitake FM	-	-			very poor preservation

Table S 3.9 Dinocyst range chart for the Ka Latale 2 section

Sample no.	Dinocyst yield	Pollen/other organics	Approximate age	Based on:	Dominant/Important secondary species
KL1-B01	xxx			*P. infusorioides*	*Oligosphaeridium poculum*, *Oligosphaeridium albertense*, *Oligosphaeridium pulcherrimum*, *Odontochitina costata*
KL1-B02					
KL1-B03					
KL1-B04					
KL1-B05					
KL1-B06	xxx		~98Ma	*P. infusoroides* (abundant), *Trithyrodinium suspectum*, *Oligosphaeridium albertense*	*X. perforata*, *ceratoides* / *Diphyes spinulum*(?)/ *P. infusorioides* / *O. pulcherrimum*/*D. cladoides*/ *Odon. costata/ F. mantelli*, *C. cooksoniae(?)/Tanyosphaeridium*

Table S 3.10 Dinocyst range chart for the Ka Latale 1 section

Sample no.	**Dinocyst yield**	**Pollen/other organics**	**Approximate age**	**Based on:**	**Other remarks**	**Dominant/Important secondary species**
NR-B15	o	o	late Cretaceous	*Cyclonephelium distinctum*		*Pediastrum*
NR-B16	o	o	late Cretaceous	*Kleithriasphaeridium*?		*Pediastrum*, *Conosphaeridium* spp.
NR-B17	-	x	?			Mostly pollen & plant debris. Potentially non-marine
NR-B17B	-	o	?			as above
NR-B18	xx	x	late Cretaceous	*O. porifera*, *Florentinia* spp, *O. pulcherrimum*		*Trichodinium* / *Cribroperidium edwardsii*, *Tanyosphaeridium xanthiopydixes*?
NR-B19	x	-	late Cretaceous	*Cyclonephelium distinctum*		
NR-B20	x	-	late Cretaceous	*Cyclonephelium distinctum*, *Conosphaeridium*, *Apteodinium*, ?*Canningia senonica*		
NR-B21	o	-	late Cretaceous	*O. pulcherrimum*, *P. infusorioides*		
NR-B22	-	-	?		some mature plant debris	
NR-B23	o	o		*P. infusorioides*	mature plant debris common	
NR-B24	xx	-	late Cretaceous	*P. infusorioides* (very abundant), *Florentinia* spp., *Apteodinium*, *O. albertense*, *Xenascus ceratoides*, *C. colleveri*?		
NR-B25	xx	-	late Cretaceous (Cenomanian/ Turonian)	*Florentinia* spp. (cf. *cooksoniae*)		
NR-B26	x	o		*P. infusorioides*		
NR-B27	xx			*P. infusorioides* abundant, *Dinopterygium cladoides*, *Cribroperidinium*/*T. castanea*? *O. poculum* (cf), *Tany*osphaeridium spp.		
NR-B28	xx		Likely Turonian	*D. cladoides*, *Xenascus ceratoides*, *O. costata*, *O. complex*, *Chatangiella granulifera*(?)		
NR-B30	xx			*O. poculum*, *D. cladoides*		
NR-B31	xx	x		*Chatangiella* spp., *P. infusoroides*		*Pediastrum*
NR-B32	x	-		*P. infusorioides*	very abundant AOM	
NR-B33	x	-	few diagnostic			
NR-B34	xx			*D.cladoides*, *P. infusorioides*, *O. pulcherrimum*		
NR-B35	x	x	few diagnostic			
NR-B36	x	x	few diagnostic			
NR-B37	xx	o	few diagnostic	*Chatangiella*/*Isabelidinium*/*Alterbidinium* dominated assemblage		
NR-B38	-	-			some mature plant	

					debris	
NR-B39	xx	o	few diagnostic	*Chatangiella*/*Isabelidinium*/*Alterbidinium* dominated assemblage, *Conosphaeridium*, *Xenascus ceratoides*		
NR-B40	x		as above			
NR-B41	xxx	-		*Chatangiella* cf. *granulifera*, *Chatangiella*/*Alterbidinium*/*Isabelidinium* dominated		*Pediastrum*
NR-B42	x	-		*T. suspectum*		
NR-B43	xx	-		*T. suspectum*, *Chatangiella*/*Isabelidniium*/*Alterbidinium*		*Pediastrum*
NR-B44	xxx	-	oldest possible = Cenomanian?	*T. suspectum*, *O. pulcherrimum*, *Chichouadinium vestitum*?, *Spinidinium echinoideum*		*Tanyosphaeridium xanthiopyxides*, *Cerodinium* spp?

Table S 3.11 Dinocyst range chart for the Nurek section

Sample no.	**Dinocyst yield**	**Pollen/other organics**	**Approximate age**	**Based on:**	**Other remarks**	**Dominant/Important secondary species**
KR-B56	o	-	> 90 Ma or younger	*Dinogymnium* spp., *Cannosphaeropsis utinensis*		
KR-B55	o					
KR-B54	o					
KR-B53	o					
KR-B52	-					
KR-B51	-					
KR-B50	-	o				
KR-B48	/	o				
KR-B47	-					
KR-B46	/					
KR-B45	-					
KR-B44	x					
KR-B43	xx		Most likely Cenomanian/Turonian; assemblages very similar to Peyrot (2011) (Spain)	Assemblage		
KR-B42	xx			*Callaiosphaeridium assymettricum*? *X. ceratoides*, *F. buspina*(?),*F. mayi*(?)		
KR-B40	/				barren	
KR-B39	xx			*D. cladoides*, *P. infusorioides*, *O coronifera*(?). *F. clavigera*? *Trigonopydia ginella*		
KR-B38	/				barren	
KR-B37	/				barren	
KR-B36	o					
KR-B34	o					
KR-B31	/					
KR-B29	o		Cenomanian	*Epilosphaeridium spinosa*		
KR-B27	o		Cenomanian	as above		
KR-B24	-					
KR-B23	/				barren	
KR-B21	/		early Cenomanian	*P. infusorioides* & *P. paleoinfusa* abundant		

Table S 3.12 Dinocyst range chart for the Khirmanjo section

Study area	
X	652.4792
Y	262.539
Z	3km

Sections	X	Y
Nurek	10.70123	59.93686
Khirmanjo	83.07411	7.73679
Kosigongsu	531.326	233.546
Kezi	636.8794	88.48455

unit name	Start age	End age
Tylk	67	65
Ygzya	86.3	67
Wytk	91	86.3
Kkb	100.5	91
Kzlsu	105	100.5

Well name	x	y	Total depth	Top of basement	Top of Kzlsu	Top of Kkb	Top of Wytk	Top of Ygzya	Top of Tylk
Nurek	10.70123	59.93686	2.484	2.484	1.434	0.604	0.4995	0.265	0
Khirmanjo	83.07411	7.73679	2.429	2.429	1.029	0.4155	0.3375	0.0235	0
Kosigongsu	531.326	233.546	1.318	1.318	0.338	0.231	0.088	0.0725	0
Kezi	636.8794	88.48455	0.478	0.478	0.158	0.035	0.018	0.008	0

Stratigraphic unit	init. Porosity	c	waterdepth	sea level	sed. Density	uplift
Tylk	0.49	0.27	0	30	2.65	
Ygzya	0.7	0.71	40	70	2.71	
Wytk	0.49	0.27	0	50	2.65	
KKb	0.63	0.51	50	90	2.72	
K1k2	0.49	0.27	0	0	2.65	

Table S 3.13 Input data for subsidence analysis

Well name	**x**	**y**	**Total depth**	**Top of basement**	**Top of Kzlsu**	**Top of Kkb**	**Top of Wytk**	**Top of Ygzya**	**Top of Tylk**
well 3/34	14.70123	52.93686	2.128	2128	1.104	0.601	0.499	0.066	0
well 10/43	11.70123	50.93686	1.259	1.259	0.609	0.27	0.175	0.027	0

Thickness	**Well 3/34**	**Well 10/43**
Tylk	66	27
Ygzya	433	148
Wytk	102	95
KKb	503	339
Kz1	571	220
Kz2	58	78
Kz3	146	124
Kz4	249	228
Total kezilesu	1024	650
total	2128	1259

Parameters					
Stratigraphic unit	**init. Porosity**	**c**	**waterdepth**	**sea level**	**sed. Density**
Tylk	0.49	0.27	0	30	2.65
Ygzya	0.7	0.71	50	70	2.71
Wytk	0.49	0.27	0	50	2.65
KKb	0.63	0.51	80	90	2.72
Kz1	0.7	0.71	50	50	2.71
Kz2	0.49	0.27	0	50	2.65
Kz3	0.49	0.27	30	50	2.65
Kz4	0.49	0.27	0	60	2.65

Stratigraphic units		
Tylk	67	65
Ygzya	86.3	67
Wytk	91	86.3
Kkb	100.5	91
Kz1	125	100.5
Kz2	130	125
Kz3	132.9	130
Kz4	145	132.9

Table S 3.14 Input data for subsidence analysis from Burtman (2000)

Chapter 4

4. The Eurasian Epicontinental Sea, a major carbon sink of the Paleocene-Eocene Thermal Maximum

ABSTRACT

The Paleocene-Eocene Thermal Maximum (PETM; ca. 56 Ma) offers a primary analogue for future global warming and carbon cycle recovery. Yet, where and how massive PETM carbon emissions were mitigated remains largely unknown. Here we show that organic carbon (C_{org}) burial in the vast epicontinental seaways that extended over Eurasia during the PETM, provided a major carbon sink. We coupled new and existing stratigraphic analyses to a detailed paleogeographic framework and using spatiotemporal interpolation calculated ca. 550-1000 Gt C_{org} excess burial, focused in the eastern parts of the Eurasian epicontinental seaways. A much larger amount (>7000 Gt C) could have been sequestered in similar environments globally. We also found that most of the C_{org} burial occurred before the recovery of the PETM, suggesting part of the massive carbon release was mainly buffered by C_{org} burial. With the disappearance of most epicontinental seas since the PETM, an effective negative carbon cycle feedback also disappeared making the modern carbon cycle critically dependent on much slower feedbacks.

4.1. Introduction

The Paleocene-Eocene Thermal Maximum (PETM), a global warming event ca. 56 million years ago (Ma), was associated with geologically rapid release (<<10 kyr) of thousands of petagrams of ^{13}C-depleted carbon into the ocean-atmosphere system (Dickens et al., 1995; Zeebe et al., 2009, 2016). The characteristic global negative Carbon Isotope Excursion (CIE) shows a rapid "onset" lasting a few kyrs, low and stable $\delta^{13}C$ values constituting the "body" of the CIE for about 70-80 kyrs, and ending by a gradual (ca. 100 kyr) "recovery" (e.g. McInerney and Wing, 2011). The event is marked by strongly elevated atmospheric pCO_2, substantial shoaling of the calcite compensation depth (CCD), as well as surface ocean acidification, and accelerated hydrologic and weathering cycles (e.g. Pagani et al., 2006; Penman et al., 2014; Zachos et al., 2005).

Previous studies have provided evidence for carbon removal either through weathering as evidenced by stable Os isotopes (e.g. Ravizza et al., 2001), biogenic silica and carbonate (C_{carb}) accumulation in the deep ocean (e.g. Penman et al., 2016a) and burial of organic carbon (C_{org}) in terrestrial and marine sediments (e.g. Bowen and Zachos, 2010; John et al., 2008). Thorough analyses of sedimentary records can help constrain the timing, processes and amounts of carbon buried, and the role these processes played in the mitigation of past carbon emissions.

Importantly, organic carbon accumulation in shallow marine settings (epicontinental seas and continental shelves) has been suggested to provide significant carbon sinks for the PETM and Mesozoic Oceanic Anoxic Events (OAEs) (e.g. Gavrilov et al., 2019; Jenkyns, 2010; John et al., 2008). We focus on the vast Eurasian Epicontinental Sea (EES) that extended from the Mediterranean Tethys to the margin of the Tibetan Plateau through the proto-Paratethys Sea and up to the Arctic through the West Siberian sea (e.g. Kaya et al., 2019) (Figure 4.1). Organic carbon-rich facies widely developed in the EES during the PETM (e.g. Gavrilov et al., 2003; Table S1). Here we estimate the amount and timing of organic carbon sequestered in the EES during the PETM using previously studied PETM records (e.g. Gavrilov et al., 1997, 2003, 2009; Shcherbinina et al., 2016; Dickson et al., 2014, 2015; Bolle et al., 2000; Frieling et al., 2014). In addition, we generate new multi-proxy data for a recently identified section from the easternmost EES (Kaya et al., 2019). The results allow a more complete view of the carbon cycle behaviour, and its potential impact on Cenozoic climatic events and future carbon cycle recovery.

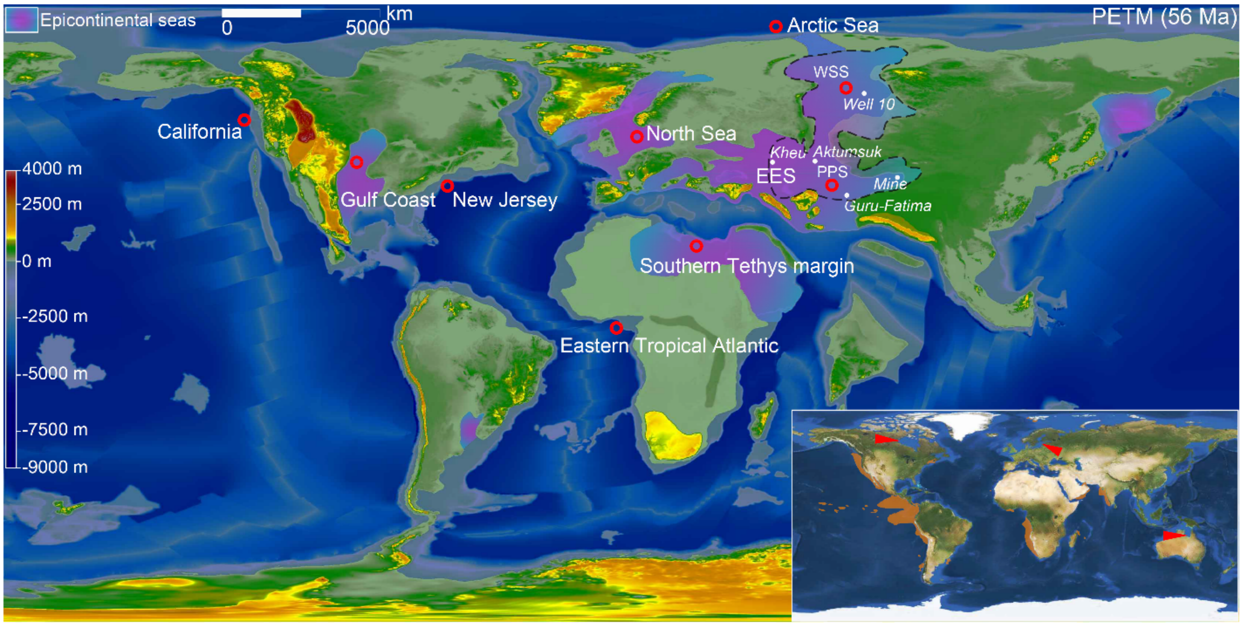

Figure 4.1 (a) Paleogeography during the PETM (modified from Poblete et al., in revision). Until the Late Eocene isolation, the Eurasian Epicontinental Sea (EES) extended across Eurasia from the Mediterranean Tethys to the Tarim Basin in western China (Kaya et al., 2019). This study focuses on the central and eastern EES (delineated by black dashed line) consisting mostly of the West Siberian Sea (WSS) and the proto-Paratethys (PPS) that were connected via the Turgai Strait. Red circles show locations of the areas with enhanced organic carbon burial during the PETM. Black dashed line indicates the study area with enhanced organic carbon burial in EES. The inset shows the modern day epicontinental seas (red triangles; Hudson Bay, Baltic Sea and Gulf of Carpentaria) and regions with high organic carbon concentrations (ca. 1.5% or more) in marine sediments (orange shaded regions, modified from Keil, 2017).

4.2. Results

4.2.1. PETM record from the EES

We previously identified a Paleocene-Eocene record from the EES based on biostratigraphy of calcareous nannofossils, dinocysts and foraminifera (Mine section, 39° 50.860'N, 74° 30.124'E) in NW Tarim Basin, in West China (Kaya et al., 2019; Figure 4.2, S4.1). Here, we use stable carbon isotope analyses of bulk organic matter ($\delta^{13}C_{org}$) and carbonate ($\delta^{13}C_{carb}$), to locate the characteristic PETM CIE (Figure 4.2). The PETM onset is broadly expanded over ca. 2 m thickness indicating exceptionally high accumulation rates (>50 cm kyr^{-1}) given its short duration

(<4 kyr, e.g. Zeebe et al., 2016). The following interval represents the CIE body ($\delta^{13}C_{org}$ values ca.-30‰) and is characterized by organic carbon-rich sapropel beds (Figure 4.2). The onset of the recovery period is placed at ca. 11.3 m height when the bulk $\delta^{13}C_{carb}$ and $\delta^{18}O_{carb}$ values start to increase although $\delta^{13}C_{org}$ remains low (Figure S4.3, see SI 4.4.2.1 for further geochemical and stratigraphic data presentation).

The expression of the PETM in the Tarim Basin is similar to shallow marine sections on the southern fringes of the Tethys (e.g. Speijer & Wagner, 2002) and elsewhere in the EES basin (e.g. Gavrilov et al., 2003). The most remarkable feature is a dramatic increase in organic carbon (TOC) content (Figure S4.2), roughly coincident with a drop in carbonate ($CaCO_3$) content during the onset. Biomarker distributions, δD n-alkanes showing a drop from -143‰ to -164‰ in C_{29} and from -139‰ to -154‰ in C_{31} (SI 4.4.2.3; Table S4.2), and microfossil data across this interval signals higher siliciclastic, nutrient and fresh-water input, suggesting the drop in carbonate content is related to dilution and potentially reduced calcification (SI 4.4.2.5; Figure 4.2).

The observed increase in freshwater and terrestrial input implies the shift to extensive sapropel deposition supports the hypothesis that the CIE is most likely related to increased productivity, the formation of a freshwater lid and the development and sea-wide expansion of anoxic conditions (e.g. Dickson et al., 2014). Enhanced preservation of fish debris in sapropel layers suggests a shift in reactive phosphorus (P) sink in sediments during oxygen-depleted periods, when burial of other forms of reactive P is limited (Slomp & Van Cappellen, 2006; Tsandev & Slomp, 2009). Such conditions have been also described in other anoxic PETM EES sections (Kheu River and Guru-Fatima), where high C_{org}/P ratios indicate preferential phosphorus regeneration (Dickson et al., 2014). Two thinner black organic-rich layers near the top of the CIE have lower TOC values ca. 1.2 % defining a cut-off of ≥1.2% C_{org} for the sapropels. We treat all TOC values ≥1.2% as sapropel beds.

During the recovery phase, microfossil assemblages are still dominated by low-salinity and high-nutrient taxa. Intriguingly, across this phase, there is an increase in $CaCO_3$, but not TOC, in the EES, suggesting persistent elevated carbonate precipitation in shallow seas (John et al., 2008) as well as in deep ocean records (e.g. Penman et al., 2016b).

The extensive EES organic carbon burial appears to be concentrated in the body of the CIE, likely enabled by the presence of oxygen-depleted/anoxic conditions (e.g. Dickson et al, 2014) and delivery of terrestrial lithogenic particles and nutrients into EES area. Stratification due to freshwater lids was probably important as well, because without ventilation of the water column oxygen-depleted waters easily developed and persisted.

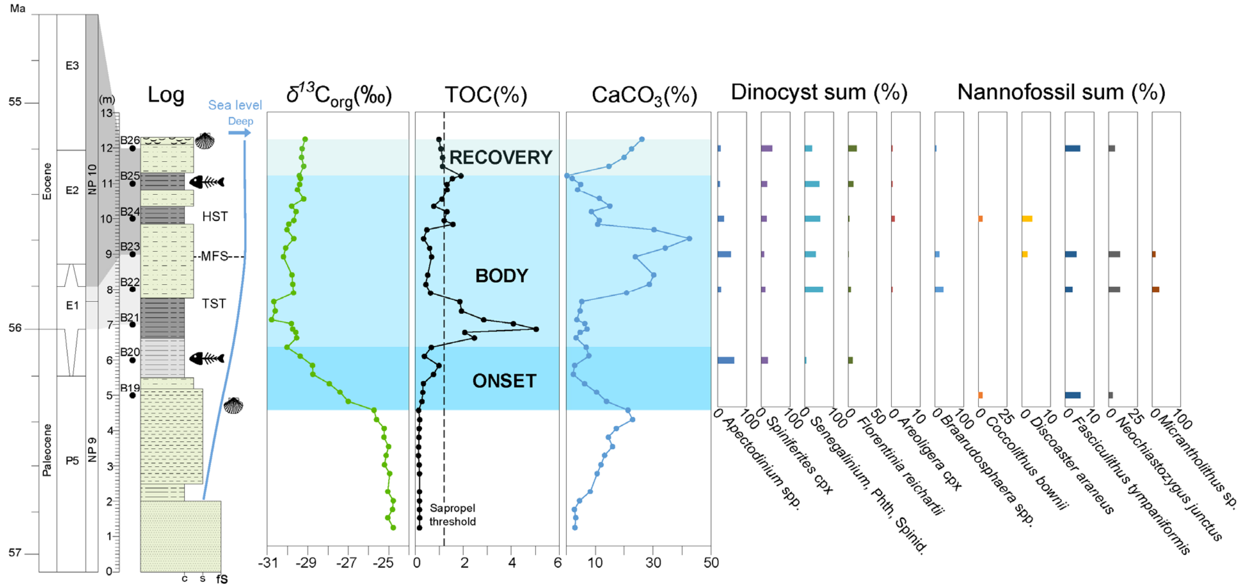

Figure 4.2 The PETM record from the Mine section in the Tarim Basin. Timescale (Ogg et al., 2016) indicates biostratigraphic zonations of planktonic foraminifera (P5, E1, E2 and E3) and calcareous nannofossils (NP9 and NP10). Stratigraphic log of the section shows lithologic distribution (c:clay, s:silt, fS:fine sand, sapropels in dark grey shading) with occurrences of bivalve and fish bone, biostratigraphic sample, and schematic relative sea level (blue line) interpreted from sequence stratigraphy (MFS: maximum flooding surface, TST: Transgressive systems tract, HST: Highstand systems tract). Isotopic values of $\delta^{13}C_{org}$ record the onset but not the recovery of the CIE. Total Organic Carbon (TOC) values peak just after the onset and are linked to sapropel deposition above a 1.2% threshold. Wt%$CaCO_3$ decreases at the onset, fluctuate during CIE body, and increases at the recovery. Relative abundance (%) of dinocyst and nannofossil assemblages indicate paleoenvironmental conditions. The Senegalinium group is often interpreted to be low-salinity tolerant, and likely had a preference for relatively high nutrients levels. Apectodinium and Florentinia reichartii are thermophilic dinocyst taxa and abundant Spiniferites indicates influence of open marine conditions (e.g. Frieling & Sluijs, 2018). Nannofossil Neochiastozygus junctus is an opportunist species indicative of high-productivity conditions (e.g. Self-Trail et al., 2012). Braarudosphaera bigelowii and Micrantholithus are indicative of nutrient-rich or low-salinity waters (e.g. Bown, 2005; Bown & Pearson, 2009).

4.2.2. C_{org} burial in the EES during the PETM

We estimate the amount of total organic carbon burial in the central and eastern EES based on the following equation (Xu et al., 2017).

(1) M = Area * Thickness * Density * TOC

In its simplest application, average values were used for input parameters (i.e. average thickness and TOC) for the estimation of the total amount of organic carbon burial (Xu et al., 2017). Here, we refine this approach by including spatial variation of organic carbon burial throughout the central and eastern EES. We applied an Inverse Distance Weighted method (Watson & Philip, 1985) and interpolated the spatial distribution of both thickness (Figure 4.3a) and TOC (Figure 4.3b) based on new and previously analyzed sections (Table S4.1). The organic carbon content of sapropel-rich horizons was estimated at each section based on integrating TOC values over their thicknesses that range from 0.2 m to 2.3 m in thickness and from 0.7 to 17% in TOC values.

Background pre-CIE TOC values are ca. 0.1-0.2%. The central and eastern EES extent and area (ca. 8.5 x 10^6 km^2; Figure 4.3a, b) were determined from a review of land-sea distribution data (Kaya et al., 2019 and references therein) over a 60 Ma paleogeographic reconstruction (Poblete et al., in revision). We used a broad range of well-established bulk density values (from 2.1 x 10^{12} to 2.7 x 10^{12} kg/km^3) proposed for organic shales (Vernik & Milovac, 2011).

We applied equation (1) for each grid cell (1 km x 1 km) throughout the study area using interpolated thickness and TOC with range of densities and area (i.e., area of grid cell). For a mean density value of 2.4 x 10^{12} kg/km^3 the amount of organic carbon burial varies from 3.0×10^{-6} to 3.0×10^{-4} Gt/km^2 (Figure 4.3c). The cumulative amount of organic carbon burial for the entire analyzed area of the EES ranges between 665 Gt and 855 Gt. The southeastern sector, represented by Guru-Fatima, Kurpai and Mine sections in the Tajik and Tarim basins, yield the highest organic carbon burial values per km^2. This likely relates to higher sediment accumulation rates for these sections in the proximity to the Pamir/Tibetan Plateau orogenies providing high lithogenic input. Depositional setting, sediment accumulation and bottom water oxygenation seem to play a major role for the organic carbon burial/preservation efficiency reflecting the importance of the balance between constructive and destructive processes (Bianchi et al., 2018).

The substantial regional differences highlight the need for good geographical coverage and spatial interpolation techniques. To this end, the study area was divided into sub-sections (polygons) and the amount of total organic carbon burial per each sub-section was examined separately. We applied Equation (1) for each polygon accounting for variations in thickness, TOC and density. This results in a total amount of organic carbon burial ranging between 555 Gt (1st quartile) and 996 Gt/km^2 (3rd quartile) with a mean value of 764 Gt in the central and eastern parts of the EES during the CIE of the PETM (Figure 4.3d).

The obtained ca. 550-1000 Gt range can be almost entirely regarded as excess burial, as the pre-CIE C_{org} accumulation rate is very low with TOC values ca. 0.1- 0.2% (cumulative <40 Gt C for the same duration).

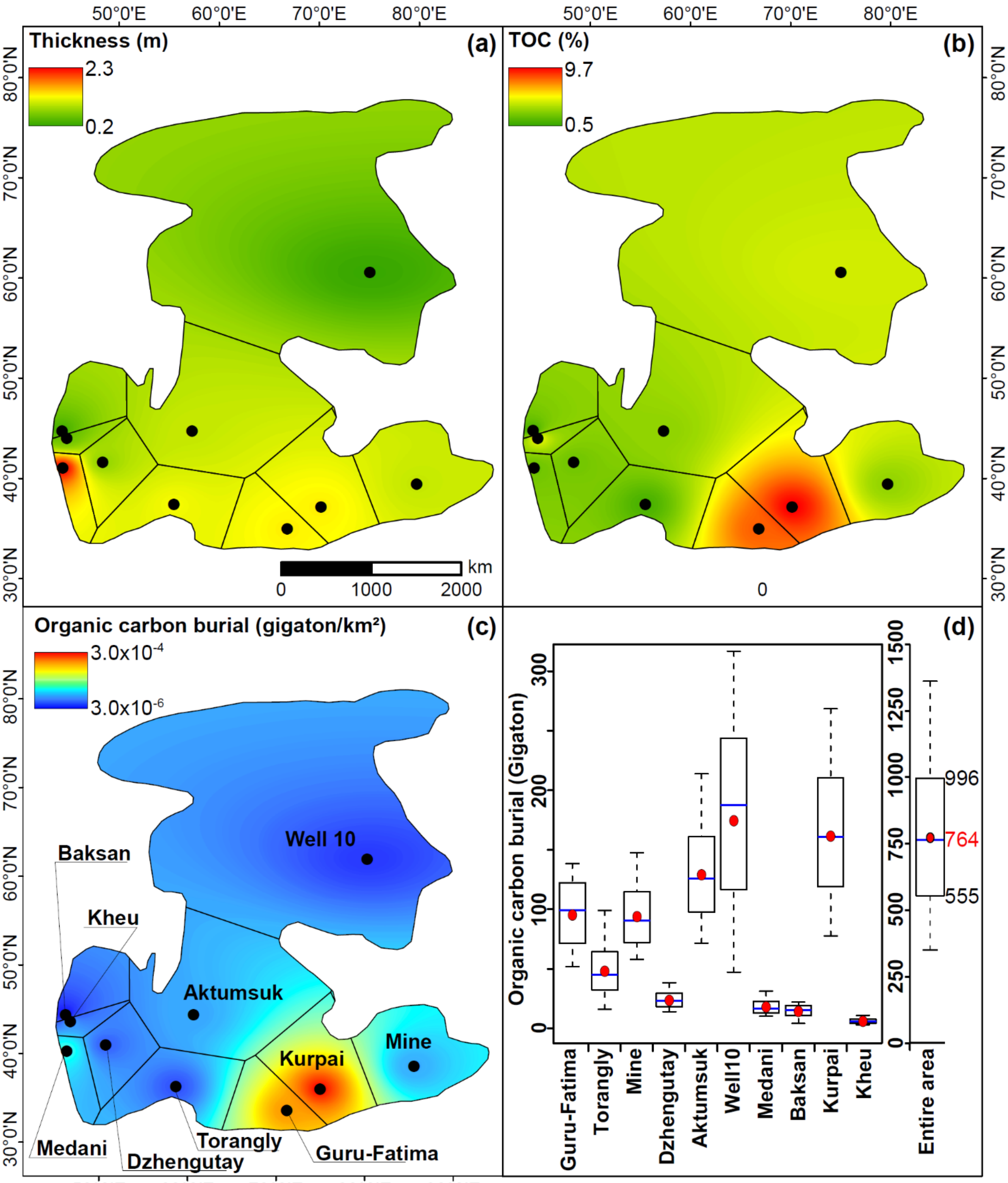

Figure 4.3 Spatial distribution of (a) sapropel thickness, (b) TOC values and (c) estimated total organic carbon burial (using 2.4 x 10^{12} kg/km^3 density) in the proto-Paratethys and West Siberian basins. Black dots show the locations of the studied sections/wells (Mine section, this study; Well 10, Frieling et al., 2014; Kheu, Baksan, Medani, Torangly, Aktumsuk, Guru-Fatima and Kurpai sections, Gavrilov et al., 1997; 2003; Dzhengutay section, Gavrilov et al., 2009). Constructed Thiessen polygons indicate sub-sections with a

reference section/well. (d) Box-and-whisker plots showing estimated total organic carbon burial for each sub-section and entire area. Lower and upper limits of the boxplots indicate 1st and 3rd quartiles, respectively. Red dots and blue lines inside the boxes show the mean and median values, respectively. A broad range of bulk density values (from 2.1 x 10^{12} to 2.7 x 10^{12} kg/km^3) proposed for organic shales (Vernik & Milovac, 2011) was used for the estimation.

4.2.3. Epicontinental seas as C_{org} burial factories

The warm Paleogene epicontinental seas were susceptible to widespread anoxia (e.g. Dickson et al., 2014) and as such provided ideal environments for the sequestration of organic carbon. In the vicinity of an orogeny, C_{org} burial appears to be further promoted by increased runoff leading to (1) stratification and (2) weathering and/or erosion of terrestrial material feeding organic carbon, lithogenic sediments and nutrient influxes (Figure 4.4a).

Low C_{org} percentages (< 1.2%) in the Mine section indicate the oxygen minimum zone weakened intermittently. Remarkably dinocysts and nannofossil assemblages for those intervals still indicate high nutrient levels. The continued presence of oligotrophic taxa (*Spiniferites*) could imply transport from nearby open marine conditions. Variations in circulation may have provided occasional ventilation (Figure 4.4b) in line with previously identified cyclic variations in trace metal enrichments and lycopene concentrations (e.g. Dickson et al., 2014).

We thus identify three main factors governing oxygenation and in turn burial efficiency of epicontinental seas; nutrient levels, circulation and freshwater runoff. Further positive feedbacks, including P-regeneration (e.g. Tsandev & Slomp, 2009; Dickson et al., 2014) are also likely and have been argued to significantly affect the global carbon cycle (e.g. Komar & Zeebe, 2017).

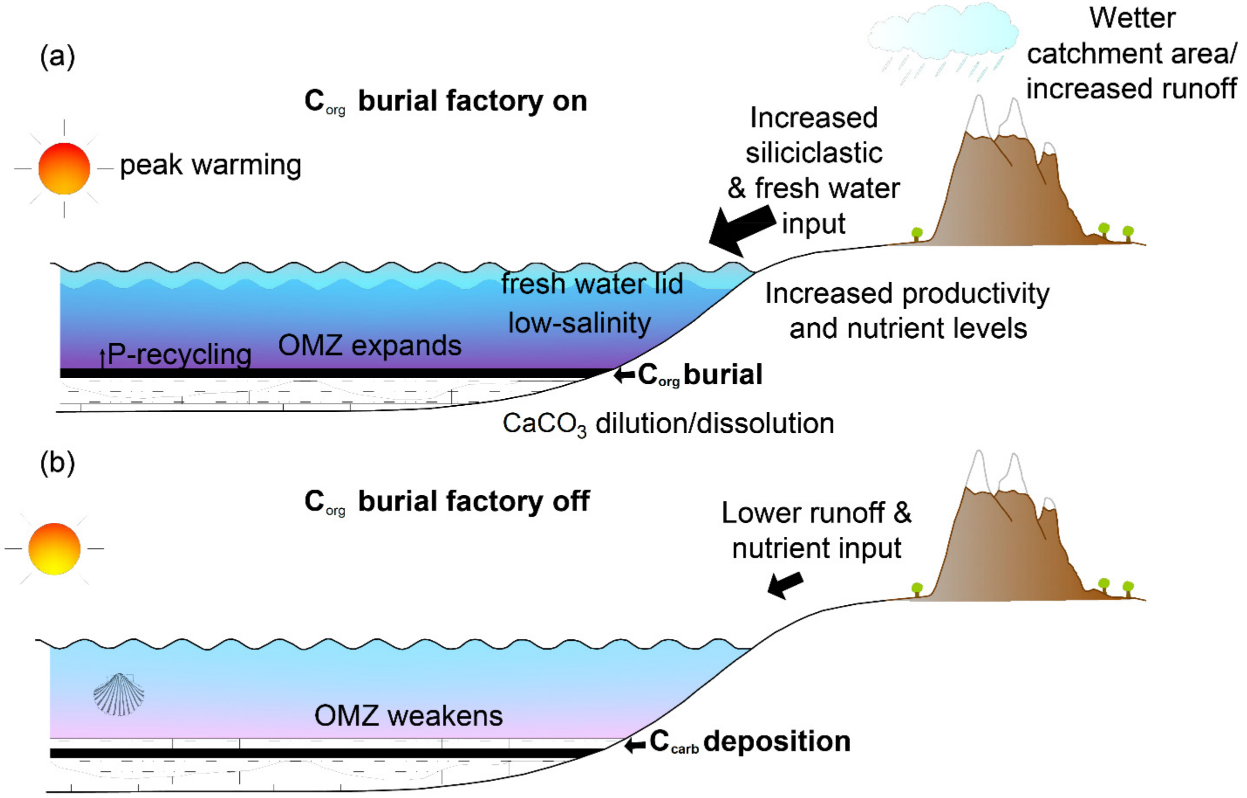

Figure 4.4 Schematic representation of paleoecological and paleoenvironmental changes during the C_{org} (a) and C_{carb} (b) deposition in the EES. OMZ: Oxygen minimum zone.

4.3. Discussions

4.3.1. Contribution to the global PETM carbon budget

The total global amount of carbon released during the PETM has been estimated to range from 4500 Gt (e.g. Zeebe et al., 2009) to more than 10000 Gt (e.g. Gutjahr et al., 2017) based on modelling of paleoenvironmental constraints (e.g. pH, CCD) and $\delta^{13}C$ records.

Our estimates over the central and eastern EES indicate ca. 550-1000 Gt C_{org} burial during the PETM CIE. While this is perhaps 5-20% of the total released carbon, the area of central and eastern EES (ca. 8.5 x 10^6 km^2) is only about 30% of the global late Paleocene epicontinental sea surface area (ca. 30 x 10^6 km^2; Figure 1). Continental shelves and epicontinental seaways that have been analysed also show elevated C_{org} burial across this period, warranting the extrapolation of our results. On a global scale, this amounts to ca. 1650-3000 Gt excess C_{org} burial in epicontinental seas. If accurate, this implies the carbon burial in epicontinental seas alone may have sequestered 30-50% of carbon emissions. Crucially, that estimate is still without C_{org} burial in the Arctic Ocean (estimated 770 Gt C in Sluijs et al., 2008) and on continental shelves.

Continental shelves were previously recognized as potentially important carbon sinks, and have been estimated to sequester 2200 to 2900 Gt C_{org} (John et al., 2008). However, these estimates were based on present-day shelf areas, and high Paleocene sea level triple the global shelf area. We estimate a total shelf area of ca. 92 x 10^6 km^2 based on the paleogeographic reconstruction in Figure 1, which when extrapolating the results of John et al. (2008), would imply an additional C_{org} sink of ca. 7400 to 10300 Gt.

These extrapolations to gross global burial carry significant uncertainties. Our analyses show that epicontinental seas are inherently variable in C_{org} burial efficiency during the PETM and the same holds for the continental shelves. Nevertheless, the order of magnitude of the C_{org} burial clearly shows that epicontinental seas provided a proportionally and quantitatively major C sink. Combined with epicontinental seas, continental shelves, which previously have been designated as the largest sink for organic carbon (Figure 4.1 inset, Blair et al., 2004), would have had the potential to mitigate the even the high-end estimates of carbon release during the PETM. At face value, this could support modelling studies for these emission scenarios, which suggested silicate weathering was likely insufficient to account for the CIE recovery and force this with enhanced C_{org} burial (e.g. Bowen & Zachos, 2010; Gutjahr et a., 2017).

4.3.2. Timing of C_{org} and C_{carb} burial

However, when looking in more detail, our estimates indicate the bulk of the organic carbon sequestration took place during the CIE body, just after the CIE onset, whereas C_{carb} burial appears to increase somewhat later. The exact same trends are recorded on continental shelves, where carbon sequestration also appears to occur mainly before the CIE recovery (John et al., 2008). Intriguingly, a major C_{org} sink during the CIE body requires a larger and more $\delta^{13}C$-depleted continuous carbon release compared to previous estimates (e.g. Gutjahr et al., 2017). The enhanced C_{org} burial hence seems to allow large fluxes of both light carbon from surface and heavy carbon from mantle reservoirs into the exogenic carbon cycle during the body phase (e.g. Komar & Zeebe, 2017).

Following this line of reasoning, the presence of sapropel layers in the EES up until the end of the CIE could suggest anomalous carbon release was active until that time and that recovery started soon after the release halted. During the recovery, disappearance of sapropel beds and the predominance of C_{carb} sedimentation indicate that C_{org} burial in the EES did not account for significant organic carbon sequestration. The CIE recovery should rather be ascribed to silicate weathering or terrestrial organic carbon storage, which would involve relatively lower organic carbon sequestration in line with previous estimates (from 1700 Pg C to 2900 Pg C, averaging around 2000-2500 Gt; Komar & Zeebe, 2017; Gutjahr et al., 2017; Bowen & Zachos, 2010).

4.3.3. Role of epicontinental seaways from OAEs to ongoing warming

Our results highlight that during the PETM the EES and other epicontinental seas, provided an effective carbon sink mitigating the massive carbon injection. This mitigation through C_{org} burial must have played a dynamic role, governed by eustatic and relative sea level fluctuations throughout the geologic history of the EES (Kaya et al., 2019, 2020) and its sapropel-rich sedimentary record (e.g. Gavrilov et al., 2019).

Before the PETM, Mesozoic sedimentary successions of the EES record several intervals with C_{org}-rich deposits associated with the Jurassic and Cretaceous OAEs (e.g. Gavrilov et al., 2019). Most importantly, the Eocene Oligocene Transition (EOT) is coeval with the EES retreat and restriction of Paratethyan basins (Schulz et al., 2005), followed by deposition of black shales with km-scale thickness and TOC values as high as 24% over vast areas from the Vienna Basin in Austria to the Caspian Sea (e.g. Sachsenhofer et al, 2018). However, the C_{org} sink provided by the epicontinental seas must have been significantly reduced after the disappearance of the Paratethys and global sea level drop in the Oligo-Miocene (e.g. Sant et al., 2017). This suggests other mechanisms such as C_{carb} sedimentation and silicate weathering are more efficient carbon sinks in the Late Cenozoic icehouse state.

The paucity of modern analogues with the geographic extent of the ancient epicontinental seas and reduced inundated continental shelf area as a result of much lower sea levels (Figure 1 inset) clearly limits the potential for organic carbon burial and consequently the drawdown of atmospheric carbon dioxide. This is amplified by an anticipated decrease in global carbon burial in wetland dominated coastal systems and overall carbon preservation in the modern ocean due to anthropogenic forcing and climate change (e.g. Keil, 2017; Hopkinson et al., 2012; Syvitski et al., 2005). In addition, estimated Paleogene weatherability is comparatively low (e.g. Caves et al., 2016) and recovery from these ancient carbon cycle perturbations can be expected to considerably differ mechanistically and temporally from similar perturbations imposed on the modern carbon cycle. Specifically, the modern carbon cycle recovery may be considered critically dependent on slower negative feedbacks such as silicate weathering, perhaps until rising sea levels eventually lead to the expansion of epicontinental seas with efficient C_{org} burial factories.

4.4. Supplementary information

4.4.1. Methods

4.4.1.1. Lithostratigraphy and sampling

A lithostratigraphic section was studied and measured in the NW Tarim Basin, in West China (Figure 4.2, S4.1, and S4.3). The Mine section (39° 50.860'N, 74° 30.124'E) was chosen for excellent exposure of the Thanetian-Ypresian lower member of the Qimugen Formation and organic-rich sapropel bed unit. The lower member of the Qimugen Formation, representing the 1st Paleogene marine transgression in the Tarim Basin (Figure S1), mainly consists of grey-to-green mudstone and marls intercalated with thin-bedded shelly limestone beds (Kaya et al., 2019). The stratigraphic thickness of the observed units was measured to a cm-level. Samples were collected with a sampling interval of 25 cm for geochemical analysis and with a sampling interval of 1 m for biostratigraphic analysis. Dinoflagellate cyst (dinocysts), calcareous nannofossils and foraminifera were used to constrain the age of the studied interval.

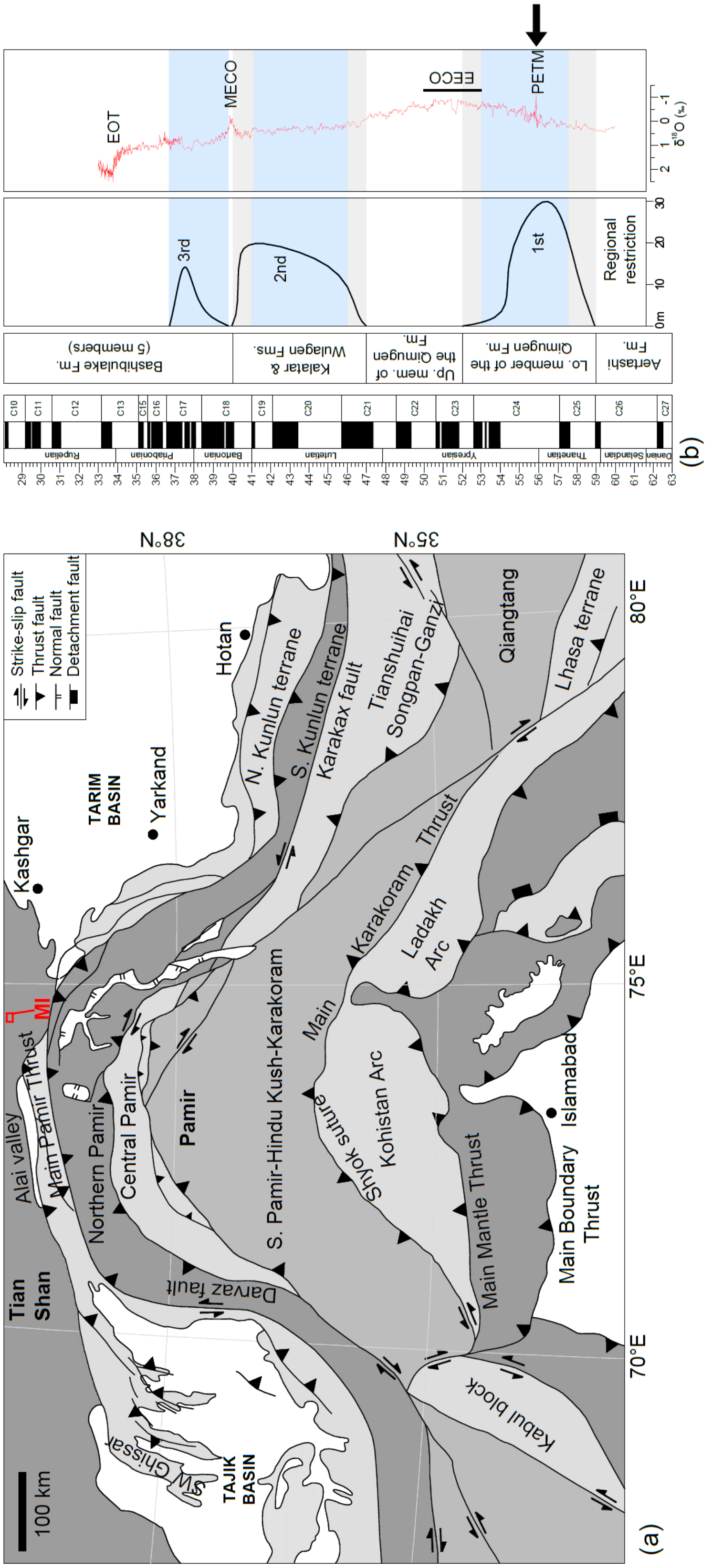
(a)
100 km
Strike-slip fault
Thrust fault
Normal fault
Detachment fault
Tian Shan
Kashgar
TARIM BASIN
Yarkand
Hotan
TAJIK BASIN
SW Ghissar
Alai valley
Main Pamir Thrust
MI
Northern Pamir
Central Pamir
Pamir
Darvaz fault
S. Pamir-Hindu Kush-Karakoram
N. Kunlun terrane
S. Kunlun terrane
Karakax fault
Tianshuihai
Songpan-Ganzi
Qiangtang
Lhasa terrane
Main Karakoram Thrust
Shyok suture
Kohistan Arc
Ladakh Arc
Main Mantle Thrust
Main Boundary Thrust
Islamabad
Kabul block
70°E
75°E
80°E
38°N
35°N
(b)
Ma
GTS16
Rupelian
Priabonian
Bartonian
Lutetian
Ypresian
Thanetian
Selandian
Danian
C10
C11
C12
C13
C15
C16
C17
C18
C19
C20
C21
C22
C23
C24
C25
C26
C27
Bashibulake Fm. (5 members)
Kalatar & Wulagen Fms.
Up. mem. of the Qimugen Fm.
Lo. member of the Qimugen Fm.
Aertashi Fm.
Tarim sea level
3rd
2nd
1st
Regional restriction
0m
10
20
30
Global climate
EOT
MECO
EECO
PETM
δ18O (‰)
2
1
0
-1

Figure S 4.1 *(a)* **Location of the studied section (MI: Mine) on a schematic map of major tectonic domains within the Pamir and western Tibet (modified from Cowgill, 2010). (b) Paleogene sea incursions in the Tarim Basin (Kaya et al., 2019) and global climate events (benthic $\delta^{18}O$ record of Cramer et al., 2009).**

4.4.1.2. Total Carbon (TC), Total Organic Carbon (TOC), Total Inorganic Carbon (TIC), $CaCO_3$ content and bulk organic $\delta^{13}C$ analyses

For the TC determination, ca. 3 mg of sample material were loaded in tin capsules (5x9 mm) and finally wrapped and measured.

The TOC content and $\delta^{13}C_{org}$ values were determined on in-situ decalcified samples. Around 6 mg of sample material were weighted into 5x9 mm Ag-capsules, dropped with 20% HCl, heated for 3 hours at 75°C, and finally wrapped and measured.

Analyses of elemental content and isotopic composition were performed using an elemental analyser (EA) (NC2500 CarloErba) coupled with a ConFlo III interface on a DELTAplusXL isotopic ratio mass spectrometer (IRMS) (ThermoFischer Scientific) at the GeoForschungsZentrum in Potsdam, Germany.

The isotopic composition is given in standard delta notation: δ (‰) = $[(R_{sample} - R_{standard})/R_{standard})] \times 1000$. The ratio (R) and standard for carbon is $^{13}C/^{12}C$ and VPDB (Vienna PeeDee Belemnite). The TC and TOC content were calibrated using Urea and the results were verified with a soil reference sample (Boden3, Hekatech). The calibration for isotopic ratios was performed using certified isotope standards (USGS24, IAEA CH-7), and verified with Pepton and a soil reference sample (Boden3, Hekatech). The reproducibility for replicate analyses is 0.2 % for carbon content and 0.15 ‰ for $\delta^{13}C_{org}$, respectively.

The TIC content was calculated using the difference between TC and TOC. With the TIC content we calculated the $CaCO_3$ content using the factor 8.33.

4.4.1.3. Bulk carbonate $\delta^{13}C$ & $\delta^{18}O$ analyses

Bulk sedimentary carbonate isotope analyses were performed at Utrecht University following standard procedures. Briefly, ca. 0.5g of freeze-dried sediments were homogenized and a sedimentary weight yielding approximately 100 µg of pure carbonate was analysed. CO_2 was generated from the carbonate by adding phosphoric acid (H_3PO_4) at 70ºC using continuous flow GC-IRMS. Both internal (Naxos) and external (IAEA-CO-1) carbonate standards were run along samples to obtain absolute stable carbon and oxygen isotope values. Reproducibility of the $\delta^{13}C_{carb}$ and $\delta^{18}O_{carb}$ were in the order of 0.1‰ or better, except for samples with very low carbonate content. $\delta^{13}C_{carb}$ and $\delta^{18}O_{carb}$ values are reported relative to the VPDB standard.

4.4.1.4. Biomarker analysis

Samples were crushed using dichloromethane (DCM)-cleaned equipment and pulverized (ca. 40 to 60 µm) in a shatterbox with agate grinding chamber. Soluble organic matter was extracted from samples (ca. 100 g) at the GFZ Potsdam using an accelerated solvent extractor (ASE350, Dionex Crop., Sunnyvale, USA) with a dichloromethane/methanol mixture of 9:1 at 100°C and

1500 psi. Total extracts of three 18-minute cycles were captured in 250 ml bottles, concentrated to 4 ml in a Turbovap, and then separated on silica gel using a solid phase extraction (SPE). SPE-columns preparation included the use of 1.5 g of silica gel (0.040-0.063 mesh; Alfa Aesar, Ward Hill, USA) filled into 6 ml glass columns (Macherey-Nagel, Düren, Germany). Columns were cleaned with three times the column volume of acetone and DCM and then dried overnight at 60°C. The column was again flushed with three times the column volume of acetone, DCM, and hexane prior to transferal of the total lipid extract onto the column. n-Alkanes and alcohols were eluted in 15 ml hexane and DCM, respectively, and the remaining substances were flushed with 15 ml methanol. Two out of three separated fractions were stored for later analysis. The remaining n-alkane fraction was treated with 6 µg 5-androstane standard for gas chromatographic quantification. The identification and quantification of individual compounds was performed using a gas chromatograph with a coupled flame ionization and mass-selective detector (GC-FID/MSD Agilent 7890A GC, 5975C MSD, Agilent Technologies, Palo Alto, USA) flushed with helium carrier gas. Temperatures in the GC oven were programmed to increase at a rate of 12°C/min starting from 70°C to 320°C at which temperatures were held constant for 21 min. The PTV injector had a split ratio of 5:1 at an initial temperature of 70°C. The injector was heated up to 300°C at a programmed rate of 7.2°C/min and held constant at this temperature for 2.5 min. The n-alkane FID-peak areas were compared with the previously added 5-androstane standard from which n-alkane concentrations were calculated. For all samples δ13Cwax were measured using a coupled gas chromatography-isotope ratio mass spectrometer (GC-IRMS) Delta V Advantage (ThermoFisher Bremen, Germany) at the University of Connecticut. The n-alkane fractions were concentrated to 60 µg/µl in hexane for $\delta^{13}C$ measurements. The n-alkane fraction was injected (1 µl) into an TRACE 1310 Gas Chromatograph equipped with an Agilent DB-5 column, 30 m x 0.25 mm x 25 µm film. The injector was operated in splitless mode at 300°C and the oven was held at 70°C for 2 min. The oven was heated at 15°C/min until 150°C, and then heated with 5°C/min to 320°C. The final temperature was held for 10 min. The column effluent was transferred via a ConFlo IV interface (ThermoFisher, Bremen, Germany) into an isotope ratio mass spectrometer after conversion to H_2 in a high-temperature oven at 960 °C. Duplicates were measured for each sample and a CO2 gas with known isotopic composition was used as reference gas. The same n-alkane standard mixtures (A3-5 and B2 standard) were used as for δD measurements with the same standard setup in the measured sequence. Only duplicate analysis for each sample was performed. The standards were used to correct the analysed samples to Vienna Standard Pee Dee Belemnite scale (VPDB). A Linear regression was produced using the known vs. measured values of the A4 and A5 standards and linear regression had a slope of 1 ± 0.14 for all analysed standards. The results are reported in delta notation in permil (‰). The analytical precision of each single measurement had a typical standard deviation of ± 0.5‰. We report all measured samples with a standard deviation of ±1‰, which represents the total variability in all measured n-alkane standard mixtures of the A3-5 standards and is more than the analytical standard deviation of ± 0.5‰.

4.4.1.5. Biostratigraphy

Dinoflagellate cysts

Samples were processed at Palynological Laboratory Services, Holyhead, UK, using standard palynological treatment procedures. We used approximately 50g of dry sediment for each sample. Concentrated HCl and HF, were added to the sample material to remove carbonates and silicates respectively. Organic residues were pH-neutralized and sieved over a 10 µm mesh to remove small particles. Some samples required short ultrasonic treatment or mild oxidation with HNO3. Residues were subsequently mounted on a microscope slide using glycerine jelly and analysed at 400x magnification under a light-transmitting microscope (Olympus CX41). Each slide was scanned entirely for rare species. Dinoflagellate cyst taxonomy follows Fensome & Williams (2004) and Bijl et al. (2016) for Wetzellielloid species.

Calcareous nannofossils

Samples for calcareous nannofossils analyses were processed following the standard smear-slide techniques (Bown & Young, 1998) and quantitative analyses were performed using a Zeiss Axioskop 40 microscope under crossed-polarized and plane-transmitted light at 1250x magnification, scanning at least three transverses of each slide (~600 fields of view). Nannofossil specimens were identified following the taxonomy given in Perch-Nielsen (1985), and Agnini et al. (2014). The biostratigraphic attribution is based on the scheme proposed by Martini (1971) and on the recognition of secondary nannofossil bioevents (Bralower, 2002; Bown, 2005; Raffi et al., 2005; Agnini et al., 2014; Shcherbinina et al., 2016).

Foraminifera

For the benthic foraminiferal taxonomy, we followed Loeblich & Tappan (1988) at generic level. Due to poor state of preservation and low abundance, identification at species level was fairly limited. Whenever possible, benthic foraminifera species were identified mainly by following the species concepts of Cushman (1951), LeRoy (1953), Berggren and Aubert (1975) and Speijer (1994). The taxonomy and biostratigraphic attribution of planktonic foraminifera were based on Olsson et al. (1999), Pearson et al. (2006) and Young et al. (2018).

4.4.1.6. Relative Sea-level

Sedimentary facies and micropaleontologic assemblages have been used to reconstruct water depths and recognize sea level rise (or fall) generally expressed by a shift to offshore (or inshore) characteristics (e.g. Catuneanu, 2006). The distribution and relative abundance of planktonic and benthic foraminifera have been used to further identify relative sea-level variations (e.g. BouDagher-Fadel, 2012; Murray. 2006). Relative abundance of terrestrially derived palynomorphs and other organic material, along with grain size of the deposited sediments, were inspected to assess coastal proximity (e.g. Sluijs et al., 2008).

4.4.1.7. Mass balance calculations

We used equation (1) to estimate the amount of total organic carbon burial in the EES.

M = Area * Thickness * Density * TOC

The same equation has been used by Xu et al. (2017) applying the average values for the input parameters (i.e. average thickness and TOC) for the estimation of the total amount of organic carbon burial in the Sichuan Basin during the Early Jurassic Toarcian oceanic anoxic event. We aimed estimating not only the total amount of organic-carbon burial but also its spatial variation throughout the EES. To do so, we applied Inverse Distance Weighted method (Watson & Philip, 1985) and estimated the spatial distribution of both thickness (Figure 3a) and TOC (Figure 4.3b) based on observed values from previous studies and this study (Table S4.1).

In addition, due to spatial variations obtained from the Inverse Distance Weighted method, as a second method, we constructed Thiessen polygons (Thiessen, 1911) using the values from the measured sections/wells as reference. These polygons were identified in such a way that all the points located inside each polygon are closer to the associated reference point than to any other. Then the interpolated thickness and TOC values as ranges of values which are most likely to be observed within each polygon were obtained. In turn, the range of total organic carbon burial amount for the entire area was summed for each polygon and its associated range (Figure 4.3c, d).

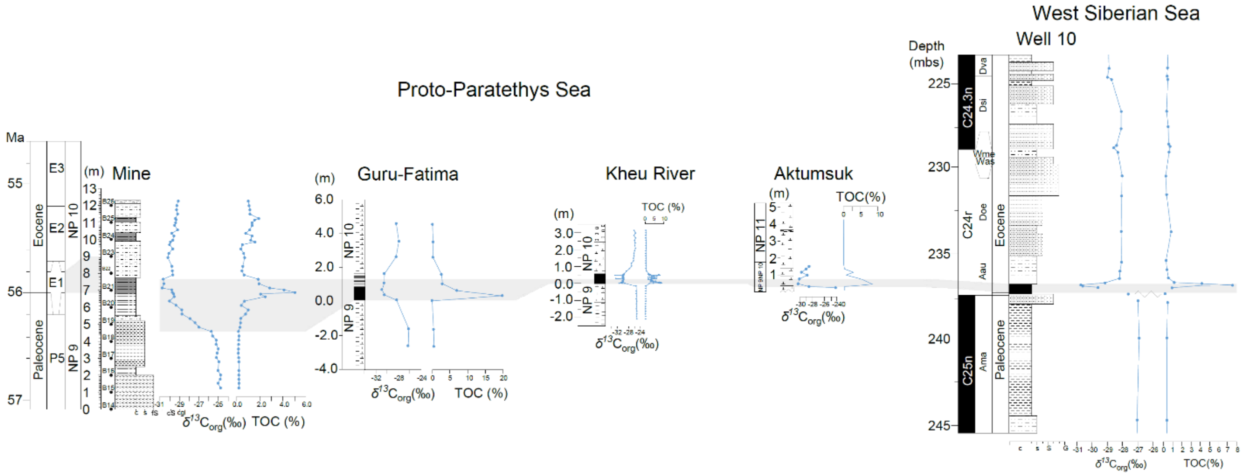

Figure S 4.2 Correlation of the C_{org}-rich sapropel interval (grey shaded area) with high TOC peak values from different sections studied in the EES (Mine section, this study; Guru-Fatima and Kheu River sections from Dickson et al., 2014; Aktumsuk section from Bolle et al., 2000), and WSS (Well 10 from Frieling et al., 2014). The age correlation at the Mine section based on foraminifera assemblage is shown by light grey shading corresponding to E1 planktonic foraminifera zonation.

Table S 4.1 Data used in this study

Section/well	Location	Study	Sample	TOC (%)	Avg. TOC (%)	Max. TOC (%)	Sapropel Thickness (m)
Kheu	Central Caucasus	Gavrilov et al. (1997; 2003)	11a	7.9	5.30	7.9	0.58
			11b	6.3			
			11c	1.01			
			11d	6			
Baksan			54a	1.07	0.5	1.07	0.25
			54b	0.3			
			54c	0.12			
Aktumsuk	Western Aral Sea, Uzbekistan		101	0.95	2.85	6.5	1.00
			103	6.5			
			104	0.54			
			106	3.4			
Torangly	Western Kopetdag Mountains, Turkmenistan		10	1.81	1.06	1.81	1.20
			11	1.02			
			13	1.42			
			14	0.75			
			15	0.32			
Guru-Fatima	Tajikistan		7	15.5	7.98	15.5	1.30
			7a	6.4			
			7b	2.04			
Kurpai	Tajikistan		15	7.45	9.73	17.0	1.30
			17	1.16			
			18	13.3			
			19	17.0			
Medani	Transcaucasia, Georgia		5	0.48	2.03	3.30	2.30
			6	0.5			
			8	1.92			
			10	2.65			
			11	3.30			
			12	3.30			
Well 10	Southwestern Siberia, Russia	Frieling et al. (2014)	236.85	7.54	4.24	7.54	0.20
			236.9	4.23			
			237	0.96			
Mine	Tarim Basin, Western China	Kaya et al. (2019), this study	975	2.5	2.90	5.00	1.00
			990	2.1			
			1000	5.0			
			1015	4.1			
			1025	2.9			
			1050	1.9			
			1075	1.9			
Dzhengutay	Dagestan, East Caucasus	Gavrilov et al. (2009)		4.92	2.11	4.92	0.76
				0.44			
				0.52			
				2.57			
				1.03			
				1.95			
				1.16			
				5.9			
				0.52			

4.4.2. Results

4.4.2.1. Total Organic Carbon (TOC), $CaCO_3$ content and bulk organic $\delta^{13}C_{org}$ analyses

The lowermost grey-greenish sandstone, claystone, siltstone and mudstone beds have relatively low TOC values (≤ 1.0%) in the Mine section compared to the higher TOC values of the dark grey-black sapropel beds (Figure 4.2). The sapropel beds deposited during the early CIE body show the highest TOC values (up to 5%), whereas the ones in the late CIE show relatively lower TOC values (up to 1.9 %). Previous works have demonstrated increased organic carbon accumulation with TOC values up to 17% in the sapropel beds of the central and eastern EES during the PETM (Gavrilov et al., 1997, 2003, 2009; Shcherbinina et al., 2016; Dickson et al., 2014, 2015; Bolle et al., 2000; Frieling et al., 2014; Rudmin et al., 2018), bearing similarities to older OAEs (Jenkyns, 2010) (Figure S2).

The $CaCO_3$ content increases at the base of the Mine section in the grey-greenish siltstones and mudstones (reaching up to 23%, ca. 4.3 m) and then decreases towards the base of the sapropel beds. In the sapropel beds during the CIE onset and body, $CaCO_3$ content persists below 10%. The drop in carbonate content during the onset is most likely related to an increase in freshwater and terrestrial input. Biomarker analyses and δD n-alkane values show increased terrestrial input with a wetter catchment area (samples B19 and B20) during the onset of the PETM which is also evidenced by an increase in eutrophic and low-salinity tolerant dinocysts and nannofossil taxa (Figure 2; See SI 2.3 and 2.4). Microfossil assemblages also indicate elevated fresh water input, nutrient levels and productivity through the CIE onset and during CIE body which might be associated with continuous delivery of terrigenous detritus with riverine systems (See SI 4.5.2.5). The drop in carbonate content is thus interpreted to relate dilution by siliciclastic material, although reduced carbonate production due to fresh water input and resulting low salinities is likely a contributing factor as well. $CaCO_3$ content increases up to 20.7% within the CIE body in the grey-greenish siltstones (ca. 7.8 m). These grey-greenish calcareous siltstone beds in the CIE body show the highest values for the $CaCO_3$ content reaching up to 42% (ca. 9.4 m). Then $CaCO_3$ content declines up section dropping to 0.2% with the deposition of sapropel beds during the late CIE. The $CaCO_3$ content in the uppermost siltstone beds (ca. 11.3 m) then recovers and increases up to 26% at onset of the recovery phase.

The grey-greenish sandstone, claystone and siltstone beds at the base of the section underlying the organic carbon-rich dark grey-black sapropel beds show a gradual decrease in $\delta^{13}C_{org}$ from -24.8‰ to -25.7‰. The $\delta^{13}C_{org}$ decreases to -27.0‰ then to -30.0‰ marking the CIE onset. During the CIE body, $\delta^{13}C_{org}$ values very slightly increase up to -29.5‰ (coinciding with the increasing TOC values), then declines to the most negative value as -30.8‰ and show a quasi-steady-state around -30.7‰ during the early CIE.

The later stage of the CIE body starts with the deposition of the calcareous siltstone beds overlying the sapropels (ca. 7.8 m) showing an increase in $\delta^{13}C_{org}$ values up to -29.7‰. Further up the section, during the late CIE, toward the top of the section $\delta^{13}C_{org}$ increases gradually up to -29.1‰ with slight fluctuations.

We define the start of the recovery period at ca. 11.3 m when the bulk carbonate $\delta^{13}C_{carb}$ and $\delta^{18}O_{carb}$ values start to increase (Figure S3). The $\delta^{13}C_{carb}$ values goes back to pre-PETM values at ca. 15.3 m, however, $\delta^{18}O$ values stays lower than the pre-PETM values during recovery (Figure S3).

4.4.2.2. Bulk carbonate $\delta^{13}C_{carb}$ & $\delta^{18}O_{carb}$ analyses

A few samples (at ca. 5.85 m, 6.85 m and 7.15 m) at the Mine section have too low $CaCO_3$ content to reliably measure the bulk carbonate isotopes. For the rest of the samples, we were able to obtain reliable results for the bulk carbonate isotopes (Figure S4.3).

During the CIE, $\delta^{13}C_{carb}$ values within the calcareous siltstone beds (between ca. 7.8 to 9.9 m) range between -5‰ and -2.7‰, whereas overlying sapropel beds with low $CaCO_3$ content show $\delta^{13}C_{carb}$ values ranging between -3.1‰ and -4.9‰. This is followed by a rapid increase at ca. 11.7 m to -3‰ in the uppermost siltstones. This $\delta^{13}C_{carb}$ profile mimics the $\delta^{13}C_{org}$ profile which shows the original trends are retained. However, $\delta^{13}C_{carb}$ values are relatively depleted suggestive of a diagenetic overprint or local lower $\delta^{13}C_{carb}$ of dissolved inorganic carbon. $\delta^{13}C_{carb}$ values gradually decrease by ca. -5‰ to reach minimum values at ca. 8.10 m. In addition to being more $\delta^{13}C$ depleted, the magnitude of the CIE is large (ca. -5‰) compared to most other marine bulk $\delta^{13}C_{carb}$ records. We therefore rely on the $\delta^{13}C_{org}$ profile to identify the CIE stages.

$\delta^{18}O_{carb}$ values show similar trends with $\delta^{13}C_{carb}$ values, but they are very depleted which likely indicates a diagenetic/meteoric signal. They also show a massive anomaly during the CIE body (down to –8‰ from –2.5‰). Increased fresh water input, which is also evidenced by microfossil assemblage, could be a factor for these very low values in addition to diagenetic overprinting.

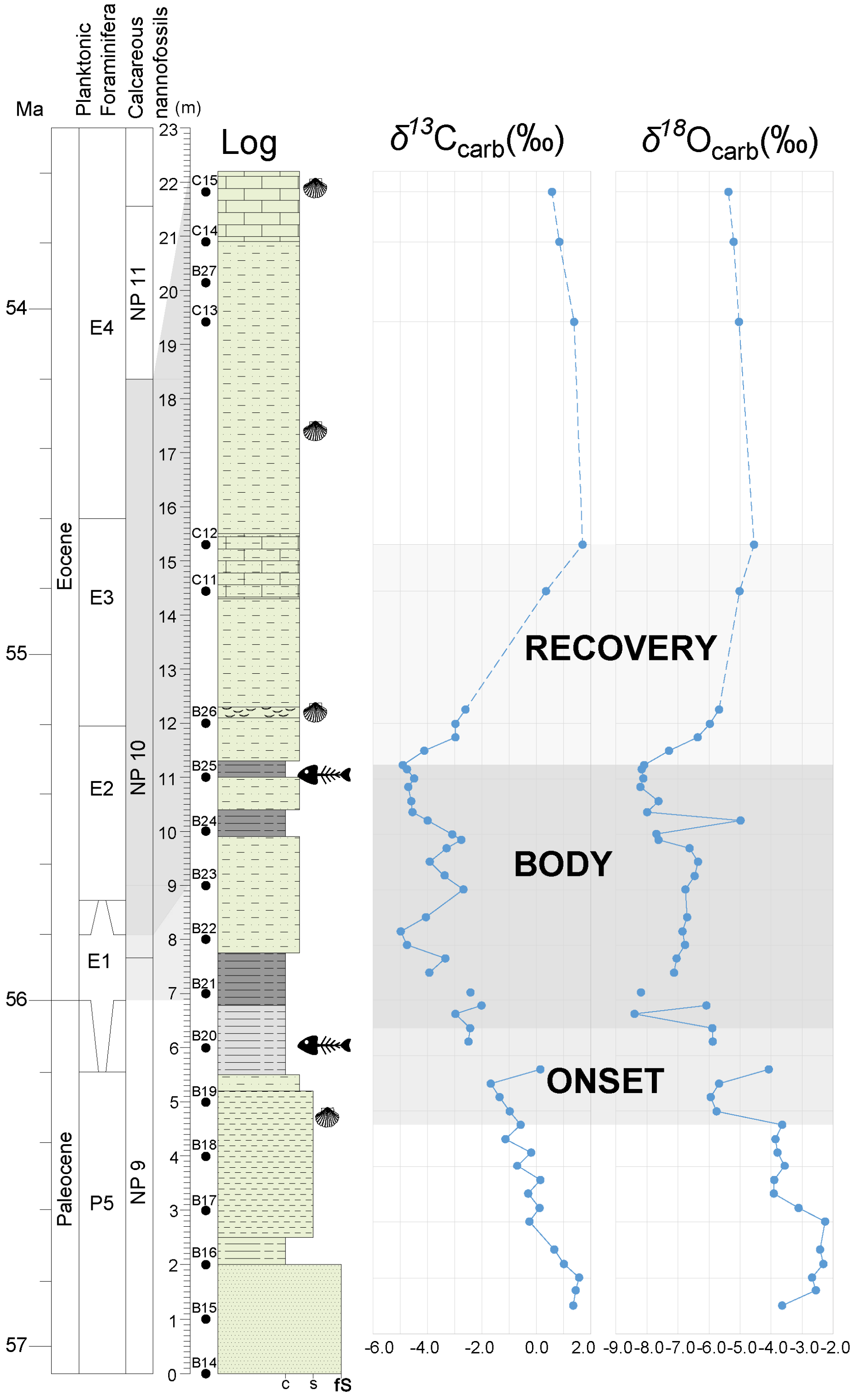

Figure S 4.3 Bulk carbonate isotope records ($\delta^{13}C_{carb}$ and $\delta^{18}O_{carb}$) across the Paleocene-Eocene boundary interval including the PETM in the Mine section.

4.4.2.3. Biomarker analysis

Here we present the results of two samples (B19 and B20) for compound-specific biomarker analysis. In both samples the most prominent n-alkanes include C_{27}-C_{33} with a peak in C_{29}-C_{31} suggesting a dominance of higher terrestrial land plants as a source for carbon at the onset of the PETM (Table S4.2). The δD values of C_{29} and C_{31} change between samples B19 and B20 and show a decline from -143‰ to -164‰ and 139‰ to -154‰, respectively. This suggests an increased hydrological cycle or wetter climate within the terrestrial catchments for the onset of the PETM.

Table S 4.2 Results of hydrogen isotope analysis of n-alkane lipid biomarkers from the Mine section

Sample #	Stratigraphic height (m)	ACL (C25-C37)	CPI	Hydrogen δD results													
				C27	St. dev.	C28	St. dev.	C29	St. dev.	C30	St. dev.	C31	St. dev.	C32	St. dev.	C33	St. dev.
B19	5.0	30.3	2.3	-141.1	0.2	-131.8	0.6	-143.2	0.5	-131.0	1.1	-139.4	5.2	-121.1	2.4	-136.7	2.3
B20	6.0	30.2	2.5	-149.7	5.0	-164.6	5.0	-164.8	5.0	-169.4	5.0	-154.5	5.0			-165.0	5.0

4.4.2.4. Biostratigraphy

Dinoflagellate cysts

The biostratigraphy of the Mine Section was published in Kaya et al. (2019). Briefly, we identify several late Paleocene – early Eocene taxa in the Mine section. The lowermost analyzed samples (B03, B11, 17 meters below log in Figure 4.2, see Kaya et al., 2019) contain sparse *Alisocysta circumtabulata, Melitasphaeridium pseudorecurvatum* and *Deflandrea denticulata*. *A. circumtabulata* in the North Sea has a last appearance in the uppermost Paleocene. *M. pseudorecurvatum* had a calibrated first appearance in the early Eocene (~55 Ma) (e.g. Williams et al. 2004), but this species is also recorded in the uppermost Paleocene of the New Jersey shelf (Sluijs & Brinkhuis, 2009). *Deflandrea denticulata* has a first occurrence at the base of the Thanethian in the North Sea (Powell, 1992). The assemblages here recorded are very similar to those in the North Atlantic and North Sea, and we therefore argue these species firmly establish the presence of upper(most) Paleocene sediments. Above these samples we find superabundant *Apectodinium* (~50% of the total assemblage in B20 and B23) in combination with the marker species *Wilsonidium pechoricum* (Iakovleva & Heilmann-Clausen, 2007), indicating the CIE we record must represent the PETM.

Calcareous nannofossils

The base of the investigated section, below the onset of the PETM (samples B14 to B17, Figure S3), yields very sparse assemblages, but the presence of *Discoaster delicatus* (sample B14), enable us to narrow the age of the investigated section down to the Late Paleocene. In fact, the first appearance of this species is considered an additional bioevent occurring at the top of NP8 (calibrated age of 57.42Ma, Agnini *et al.*, 2016).

Despite the poor preservation and abundance of the assemblage, the occurrence of *Discoaster multiradiatus* before the onset of the PETM (from sample B18) suggests an age that is not older than NP9. The first occurrence of this species has a calibrated age of 57.21 Ma (Gradstein *et al*., 2012; Agnini *et al*., 2016).

The presence of *Coccolithus bownii* (from sample B19 upwards) indicates the onset of the hyperthermal event. This species has been detected in a number of settings and is regarded as an excursion taxon in the PETM (Bown & Pearson, 2009, Bown, 2010, Self-Trail *et al*., 2012). It occurs below the lower sapropel bed and was detected in a similar position in the Caucasus area (Shcherbinina *et al*., 2016). A nannofossil excursion taxon is also considered to be *Bomolithus supremus* which usually occurs following the onset of the CIE (Angori *et al*., 2007; Self-Trail *et al*., 2012, Hollis et al., 2015). In our section this species was also detected in very low abundances in the CIE (sample B23). During the CIE, we also document the occurrence of the lowermost Eocene "long arm" *Rhomboaster* and "malformed" *Discoaster* (*D*.cf. *araneus*), (Bown & Pearson, 2009; Self-Trail *et al*., 2012; Agnini *et al*., 2016). The short-lived *Rhomboaster* lineage and the asymmetrical *Discoaster araneus* were identified for the first time in the Tethys (Kahn & Aubry, 2004) and restricted to the PETM interval. They are considered the best nannofossil proxy for this event (Gavrilov *et al*., 2003; Tremolada & Bralower, 2004; Cao *et al*., 2018), occurring shortly after the onset of the CIE.

The top of the investigated section still correlates to the earliest Eocene, on the basis of the presence of *Fasciculithus tympaniformis,* which usually became extinct shortly after the Paleocene-Eocene boundary (Self-Trail *et al*., 2012, Agnini *et al*., 2016).

Foraminifera

Eight washed samples (B20 to B27) from the lower member of the Qimugen Formation were analyzed. The samples yielded a poorly preserved and low diversified benthic foraminiferal assemblage, including *Anomalinoides* spp., *Anomalinoides aegyptiacus*, *Haplophragmoides* sp., *Trochammina* sp., Trochamminids with flattened tests, *Recurvoides* ? sp., *Lagenammina* sp., *Baggina* spp., *Nonionella africana*, *Nonionella* spp., *Nonion* sp., *Stainforthia* sp., *Bolivina* sp., *Cancris* spp., *Cibicidoides* spp., *Spiroplectinella* spp., *Osangularia* sp., *Eponides* sp..

On the other hand, planktonic foraminiferal assemblage has been recognized from the same samples consisting of *Morozovella aequa*, *Morozovella subbotinae*, *Morozovella* spp., *Parasubbotina inaequispira*, *Subbotina* sp., *Acarinina multicamerata* and *Acarinina* spp..

In addition to the foraminifera, the samples also yielded ostracoda, fish teeth, echinoid spines, and burrows mold.

Although the recorded benthic foraminifers have long stratigraphic ranges, a precise earliest Eocene age is assigned to samples (B22 and B23) based on the presence of *Acarinina multicamerata.* This form, together with *A.sibaiyaensis, A. Africana* and *Morozovella* *allisonensis*, constitute an assemblage of small, morphologically distinct taxa that are characteristic for the PETM (Berggren et al. 2006). *Acarinina multicamerata* has a larger number of chambers, and a gradually increased chamber size than those of *A. sibaiyaensis.* Since *Acarinina multicamerata* is regarded as an excursion taxon during the PETM (Guasti & Speijer, 2008), the Paleocene-Eocene (P-E) boundary might be delineated below the sample B22.

4.4.2.5. Paleoenvironment

Dinoflagellates

The latest Paleocene assemblages in the Mine Section are marked by abundant *Spiniferites* spp. suggesting a relatively oligotrophic open marine setting. *Apectodinium* is rare in the latest Paleocene. During the PETM CIE, assemblages are dominated by *Apectodinium*, a thermophilic, potentially heterotrophic or mixotrophic, and possibly euryhaline genus (Frieling & Sluijs, 2018; Sluijs & Brinkhuis, 2009; Frieling *et al*., 2014). The first *Apectodinium* acme is often recognized at the PETM, possibly driven by warming in higher latitudes, but here and in other mid-latitude localities, factors other than temperature are likely more important (Frieling *et al*., 2014; Sluijs & Brinkhuis, 2009).

Florentinia reichartii is present in the late Paleocene in low abundances and becomes more abundant concomitant with *Apectodinium*. Similar to *Apectodinium*, *Florentinia reichartii* is thermophilic, but possibly had an even higher optimum temperature (>30ºC) (Frieling & Sluijs, 2018). Above the *Apectodinium* acme, *Senegalinium*, a low-salinity tolerant genus (e.g. Barke *et al*., 2012), becomes very abundant, indicating more fresh water influence and below marine salinities. Both the *Apectodinium* and *Senegalinium* dominated assemblages are likely indicative of increased productivity and nutrient levels (Sluijs *et al*., 2005). The continued high proportion of oligotrophic taxa (*Spiniferites*) in most of these samples indicates transport from nearby open marine conditions or otherwise (seasonally) variable salinity and nutrient loading. Inner neritic taxa (here mainly *Areoligera*) are more abundant in the latest Paleocene and later stages of the PETM CIE, suggesting most distal conditions are associated with the peak of the PETM CIE. This is consistent with previous studies and provides further support for the hypothesized global sea level rise (Sluijs et al. 2008).

The sequence of dinocyst assemblage events across the late Paleocene and PETM in the Mine Section suggests an evolution from an oligotrophic open marine, normal salinity environment to a more nutrient-rich, fresh-water dominated, stratified system, likely driven in part by the strong (~5 ºC) global warming that marks the PETM (Dunkley Jones et al., 2013; Frieling *et al*., 2017).

Calcareous nannofossils

The nannofossil assemblages show a very low abundance and diversity all along the investigated section. *Discoaster, Coccolithus and Fasciculithus,* considered dissolution-resistant taxa (*e.g.* Raffi *et al*., 2009, Monechi *et al*., 2000), are relatively common in the productive samples, pointing to some carbonate dissolution affecting the nannofossil assemblages. The presence of the eutrophic taxa *Chiasmolithus danicus* and *Neochiastozygus junctus* at the onset of the PETM, suggests an increased nutrient input. Indeed, *N. junctus* exhibits a relatively high abundance from sample B19 upwards and is considered an opportunist species indicative of high-productivity conditions (Jiang & Wise, 2006; Self-Trail *et al*., 2012).

The calcareous pentalith *Braarudosphaera bigelowii* shows a peak in the CIE, (samples B22 and B23). High percentages of this species have already been reported from a PETM section of the Tajik depression (Guru Fatima section, Gavrilov *et al*., 2003). This species usually indicates relatively shallow-water conditions (*e.g.* Bown, 2005; Bolle *et al*., 2000), and is regarded as indicative of nutrient-enriched or low-salinity waters (Siesser *et al*., 1992; Thierstein *et al*., 2004), and related to high environmental stress (Wade & Bown, 2006; Auer *et al*., 2014). A similar peak (samples B22 and B23) was also recorded for *Micrantholithus* sp., which seems to have the same paleoecological preferences (Street & Bown, 2000; Bown & Pearson, 2009).

Therefore, the nannofossil assemblages identified in the Mine section across the PETM interval, are indicative of a stressed and high-nutrient environment.

Foraminifera

The presence of non-calcareous cemented taxa, *Haplophragmoides* spp. characteristic for the low-oxygen conditions in organic rich mud facies and relatively high abundance of trochamminids (B20) may reflect an environmental stress condition at the base of CIE interval during the PETM (Alegret *et al*., 2005; Stassen *et al*., 2009 and references therein).

The high abundance of *Anomalinoides aegyptiacus* and *Anomalinoides* sp. in the sample B25 also suggests the presence of high environmental stress conditions. The same bio-event was recorded reflecting an opportunistic strategy in sapropel beds during Paleocene-Eocene transition at Gebel Duwi, Egypt (middle neritic environment) indicating high environmental stress at the bottom surface (Speijer et al., 1996).

The benthic foraminiferal assemblage from the top of the section (B27, ca. 8 meters above top of the log in Figure 4.2, see Figure S4.3) indicates a recovery phase of benthic foraminifera, since *Cibicidoides* spp., *Spiroplectinella* spp. and *Osangularia* sp. reappear in the populations of benthic foraminifers.

4.4.2.6. Relative Sea-level fluctuations

An overall transgressive trend of the Mine section during the PETM has been interpreted based on microfossil assemblages and lithologies which is consistent with other proto-Paratethys and global records (e.g. Gavrilov et al., 2003; Sluijs et al., 2008). A transgression is interpreted based on the fining upward trend from the lowermost fine sandstones to mudstones/siltstones and the increase in the $CaCO_3$ content (Figure 4.2). This is also supported by the appearance of bivalve fossils in the siltstone between samples B18 and B19. A Maximum Flooding Surface (MFS) is placed around 9 m based on the presence of planktonic foraminifera in samples B22 and B23 and their absence below and above those samples. Above, samples B24 and B25 lack planktonic foraminifera and present only opportunistic benthic foraminifera in the sapropel deposits. In addition to a shallowing, the lack of planktonic foraminifera above samples B22 and B23 might be attributed to low-salinities, given the co-occurrence of abundant low-salinity tolerant dinocysts. Open marine conditions are re-instated at the top of the section based on the reappearance of bivalve fossils, oligotrophic dinocyst assemblages and more diverse population of benthic foraminifera together with the increase in the $CaCO_3$ content (Figure S4.3).

Chapter 5

5. Discussion of the main findings

5.1. Overview of the proto-Paratethys Sea incursions

Here, we provide a synopsis of the Cretaceous-Paleogene sea incursions in Central Asia in detail for their timing, controlling mechanisms and effects on regional/global paleoenvironment and paleoclimate taking full account of the most recent relevant publications and the main finding of this thesis. Recently some other studies have also applied precision and integrated dating techniques to improve the inaccuracies in dating (e.g. Zhang et al., 2018; Chapman et al., 2019; Sun et al., 2020). We try to provide the recent progress and still-existing questions and conflictions on these issues and set out some of the main challenges for the future research as well.

5.1.1. Cretaceous sea incursions

5.1.1.1. 1st Cretaceous sea incursion

The 1st major Cretaceous sea incursion into Central Asia occurred during the Early Cretaceous (Late Barremian - Aptian) shortly after the initiation of the subduction related magmatism along the southern Eurasian margin (Chapter 3 this study; Naidin et al., 1980). This was a transgression from the west into the western Tajik Basin represented by neritic carbonate, marl, sandstone and gypsum deposition, however not reaching into the eastern Tajik Basin and Tarim Basin due to the infilling represented by the red clastic units of the Gashion Group and Kezilesu Group (Burtman, 2000; Kaya et al., 2020a). The Tajik and Tarim basins located north of the Pamir orogeny are commonly interpreted as retro-arc foreland basins at this time due to widespread shortening and crustal thickening within the Pamir related to the Neo-Tethyan subduction and collisional events along the southern margin of Eurasia.

Before this major sea incursion in Central Asia, records of minor sea incursions (limited in geographic extent) have been also documented during the Valanginian-Hauterivian and Barremian in the western and central Tajik Basin, respectively (Burtman, 2000; Naidein et al., 1980). The Valanginian-Hauterivian incursion was represented by the deposition of neritic carbonates and gypsum in the western Tajik Basin (Zone D of Burtman, 2000). Marl, claystones and gypsum were laid down in the western (Zone D of Burtman, 2000) and central (Zone C of Burtman, 2000) Tajik Basin during the Barremian minor sea incursion. In the Tarim Basin an Early Cretaceous sea incursion has been interpreted by Hao et al. (1998) and Guo (1991) based on the presence of marine trace fossils *Ophiomorpha* and *Thalassinioides*, foraminifera *Saccammina globose* and glauconite abundance data in the Kezilesu Group deposits. However, none of the following studies, including this thesis, have reported any evidence supporting this early Cretaceous sea incursion in the Tarim Basin. Further studies might be conducted to document clearly this Early Cretaceous sea incursion in the Tarim Basin which might be correlated to the one of the Early Cretaceous minor sea incursions in the Tajik Basin.

An eustatic driving mechanism for the Late Barremian - Aptian major sea incursion was proposed previously (e.g. Naidin et al., 1980), however as explained in detail in Chapter 3 here it has been linked to an increase in tectonic subsidence due to the crustal thickening and shortening occurring along the southern margin of the Pamir (ca. 130-90 Ma) related to Lhasa-Qiangtang collision and the collision of the Central Afghan blocks with the south Eurasian margin.

The ages of early Cretaceous sea incursions (major and minor ones) and that of the terrigenous deposits of the Kezilesu Group in the Tarim Basin and the correlated Gashion Group in the Tajik Basin have been poorly constrained mainly relying on old studies of the Russian geologists (see Burtman, 2000 and references therein), lithostratigraphic correlations and relative age determinations (e.g. Baratov et al., 1976) and still remains to be improved. Recently Chapman et al. (2019) interpreted the maximum depositional age of the Gashion Group clastics as 99±6 Ma based on the detrital Zircon Fission Track (ZFT) data from the Dashtijum section in the SE Tajik Basin. However, this depositional age constraint might be likely older as this sample with the ZFT data is not at the base of the Gashion Group clastics. Having improved age constraints is required for future research to better understand the driving mechanisms and regional impacts of these early Cretaceous sea incursions. Nonfossiliferous terrestrial red clastic rocks of the Kezilesu Group in the Tarim Basin and those of the correlated Gashion Group in the Tajik Basin are good candidates for magnetostratigraphic dating, however deposition within the Cretaceous normal polarity super chron (C34n; ca. 126-84 Ma. Ogg et al., 2016) hampers determination of a high-resolution age constraint, particularly for the uppermost rock units (see Chapter 3).

5.1.1.2. 2nd Cretaceous sea incursion

There is a consensus on the age of the 2nd Cretaceous sea incursion which has been assigned as Cenomanian – early Turonian by several studies (ca. 100 -92? Ma, Guo et al., 2015; Hao et al., 1982; He, 1991; Pa, 1991; Sobel, 1995; Wang et al., 1990; Yang, 1991; Zhang, 1992). The onset of the sea incursion has been relatively well constrained to the early Cenomanian (ca. 100 Ma) in this study (see Chapter 2), however the onset of the following regression remains less well defined within early Turonian and might be improved with further studies. We also tried strontium isotope stratigraphy on some bivalve shell samples to date this sea incursion at Max Planck Institute for Chemistry, in Mainz, however due to likely recrystallization and diagenetic effects, the results were not reliable. Red fine clastics of the Wuyitake Formation in the Tarim Basin (and the correlative Musrabat Formation in the Tajik Basin) representing the regression can be sampled for magnetostratigraphic dating however, due to its deposition within the Cretaceous normal polarity super chron (C34n; ca. 126-84 Ma. Ogg et al., 2016) no better ages can be provided. Low diversity fossil content can be explored more in detail; however, it seems very difficult to improve also by biostratigraphic dating.

The 2nd Cretaceous sea incursion recorded in the marls, calcareous mudstones, limestones, siltstones, sandstones and gypsum interlayers of the Kukebai Formation and Baldzhuvon Group in the Tarim and Tajik basins, respectively (Kaya et al., 2020a). Coinciding with the Cenomanian-Turonian eustatic highstand associated with hothouse climates, the 2nd Cretaceous sea incursion extended up to the Tarim Basin resulting in the maximum geographic extent of the sea in Central Asia during Cretaceous times.

It has been previously proposed that this sea incursion was driven mainly by eustasy (Guo et al., 2015; Naidin et al., 1980; Sobel, 1995; Wang et al., 2014; Xi et al, 2016) however we document an additional controlling factor as increased subsidence due to tectonics in this study (Chapter 3).

The record of the Ocean Anoxic Event 2 (OAE2) event during the 2nd Cretaceous sea incursion in Central Asia remains to be explored. During fieldwork in the Tajik Basin, we observed and collected samples of organic-rich black shales at the Nurek section which might be corresponding to the OAE 2 event. However, this must be tested and verified through futures studies.

5.1.1.3. 3rd Cretaceous sea incursion

The suggested age of the 3rd sea incursion ranges from Coniacian to Maastrichtian (Chapman et al., 2019; Guo et al., 2015; Pan, 1991; Sobel, 1995; Sun, 1991; Wang et al., 1990; Xi et al., 2016; 2019; Yang, 1991; Zhang, 1992). The onset of the 3rd sea incursion has been assigned here as Santonian based on biostratigraphic (dinocysts and ostracods) age constraint, however the age of the following regression remains to be less precise within the Maastrichtian. The age of the following regression can be improved by magnetostratigraphic studies considering the proper lithology of the Tuyiluoke Formation (red fine-grained siliciclastic) for paleomagnetic sampling.

The 3rd Cretaceous sea incursion is characterized predominantly by limestones and interlayered sandstones, marls, mudstones and siltstones of the Yigeziya Formation and Argankun Group representing buildup of a carbonate dominated epicontinental ramp system in the Tarim and Tajik basins, respectively (see Chapter 3). Particularly the carbonate rocks are well exposed in the Khirmanjo and Nurek sections in the Tajik Basin and further carbonate sedimentology studies can be conducted on these carbonates.

During the 3rd Cretaceous sea incursion, the global Early Maastrichtian cooling is inferred from the disappearance of mollusk-rich limestones and the dominance of bryozoan-rich and echinoderm-rich limestones in the Tajik Basin. Our observations are in parallel with Maastrichtian climatic fluctuations observed in intermediate and deep waters of different oceanic basins, and indicate parallel climatic evolution between deeper ocean waters and the sea surface waters of the epicontinental proto-Paratethys Sea. This documents the first evidence for the Late Cretaceous cooling event in Central Asia.

Eustasy has been proposed as the main driving mechanism for the 3rd Cretaceous sea incursion in most studies (e.g. Guo et al., 2015; Sobel, 1995; Xi et al., 2016). We agree with that view here. Tectonic regime change in the Pamir from compression to extension related to a slab rollback (ca. 90 Ma) resulted in a decrease in tectonic subsidence and a relative tectonic quiescence in Central Asia, hence eustasy became the main driving mechanism for the 3rd Cretaceous sea incursion. The coeval fluctuations in the West Siberian Basin (Kontorovich et al., 2014) supports an eustatic controlling mechanism for the 3rd Cretaceous sea incursion in Central Asia, as well.

5.1.1.4. Early Paleogene Restriction event

The last Cretaceous sea incursion was followed by a major restriction event marked by exceptionally thick evaporitic deposits, known as the Aertashi Formation in the Tarim Basin and the equivalent thinner correlative Akdjar Formation in the Tajik Basin. The age of this restriction event has commonly been assigned as Danian-Selandian (ca. 63 – 59 Ma, Chinese Bureau of Stratigraphy, 1981; Hao et al., 1982; Jia et al., 2004; Tang et al., 1989; Wan et al., 2014). Here, we have obtained age constraint for this restriction event supporting this age assignment (Chapter 2).

Two controlling mechanisms have been proposed for this regional restriction event: hydrographic isolation from the open sea due to creation of a tectonic barrier (Zhang et al., 2018; 2019) or an eustatic barrier as explained in detail in Chapter 2. The early Paleogene northward indentation and uplift of the Pamir related to the India-Asia collision onset, including increased subsidence and formation of a topographic barrier and contemporaneous local conglomerate deposition has been revoked as one mechanism to explain the isolation of the Tarim Basin (Zhang et al, 2018; 2019). Opposing the tectonic barrier view, the isolation of the Tajik and Tarim basins has been explained by the creation of an exposed barrier, in the west, composed of shoals and rudist build-up due to a relative sea-level fall at the end of the Cretaceous in this study. The presence of thick gypsum deposits of the Akdjar Formation west of the Pamir in the Tajik Basin, local presence of the conglomerates merely in the Tarim Basin weaken the tectonic barrier hypothesis. Both of these hypotheses might be tested with further detailed studies of the Aertashi and Akdjar formations in the Tarim and Tajik basins, respectively.

5.1.2. Paleogene sea incursions

5.1.2.1. 1st Paleogene sea incursion

The age of the 1st Paleogene sea incursion representing the maximum eastward extent of the proto-Paratethys Sea in Central Asia has commonly assigned as Paleocene to Early Eocene in previous studies (e.g. Mao & Norris, 1988; Sobel, 1995; Wang et al., 1990) In more recent studies the age of the 1st Paleogene sea incursion has been determined as Selandian-Thanetain (Wan et al., 2014) or Thanetain (Zhang et al., 2018). We assigned a Thanetian-Ypresian (ca. 59-52 Ma) age here in this study (see Chapter 2). Additionally, we tried strontium isotope stratigraphy on some bivalve shell samples to support our age constraint, however we could not obtain reliable results due to likely recrystallization and diagenesis.

Marls, mudstones and limestones of the lower member of the Qimugen Formation and Tabakch - Arukfan – Karatag – Givar - (lower member) Jukar formations are associated with the 1st Paleogene sea incursion in the Tarim and Tajik basins, respectively. Sapropelitic, organic rich deposits laid down during this sea incursion record some significant global climatic events such as the PETM (e.g. Cao et al., 2018; Gavrilove et al., 2003; Jiang et al., 2018; Kaya et al., 2020b) and likely the other Early Eocene hyperthermal events. The paleoenvironmental and paleoecological conditions in the Tarim Basin during the PETM shows similarities with the other peri-Tethyan records (see Chapter 4). The proto-Paratethys basin together with the West Siberian basin act as an important carbon sink during the PETM sequestering large amounts of organic carbon presented in detail in Chapter 4.

We also analyzed a selection of PETM samples on the presence of glycerol dibiphytanyl glycerol tetraether (GDGT) concentrations at the Organic Geochemistry Lab, at the University of Utrecht to reconstruct paleotemperature, however, the content was too low and insufficient for the temperature record. Other than the PETM samples, during our fieldwork in the Tajik Basin we have also observed and sampled some other organic-rich sapropelitic beds (above the PETM interval) at the Khirmanjo section. Preliminary biostratigraphic results document these are most likely related to the Early Eocene hyperthermal events; however further studies are required to reveal the presence and details of the records of these events.

Eustasy has been interpreted as the main controlling mechanism for the 1st Paleogene sea incursion (e.g. this study; Wang et al., 2014), however the ca. 53-52 Ma following regression has been linked to the far-field effects of early Eocene Indo-Asia collision in this study (see Chapter 2).

5.1.2.2. 2nd Paleogene sea incursion

An Early–Middle Eocene age has been generally assigned for the age of the 2nd Paleogene sea incursion (e.g. Mao & Norris, 1988; Sobel, 1995; Wang et al., 1990). Recent works provided more precise ages as early Lutetian (ca. 47-41 Ma, this study; Wan et al., 2014) or late Ypresian (Zhang et al., 2018). The age of the onset of the following regression has been dated more precisely for several studies as Bartonian (41-40 Ma, Bosboom et al., 2017, 2014a, 2014b; this study). We further tried strontium isotope stratigraphy on bivalve shell samples, however similar to the other bivalve shell samples from other intervals the results were not reliable due to likely recrystallization and diagenesis.

This sea incursion represents generation of a shallow carbonate ramp system in Central Asia for the second time after the 2nd Cretaceous sea incursion. The carbonate ramp deposition is characterized by the massive limestones, marls, mudstones and interlayered gypsum rocks of the Kalatar and Wulagen formations and the correlative (upper member) Jukar – Beshkent – (lower member) Tochar formations in the Tarim and Tajik basins, respectively.

An eustatic control on the long-term trend of the 2nd Paleogene sea incursion has been commonly accepted (e.g. Kaya et al., 2019; Wang et al., 2014). The following regression, however, has been linked to both tectonism (ca. 40 Ma) related to Pamir and Tibetan Plateau uplift and eustasy (e.g. Bosboom et al., 2014a; Kaya et al., 2019).

5.1.2.3. 3rd Paleogene sea incursion

The third and final Paleogene sea incursion has been previously dated as Late Eocene - Oligocene (e.g. Sobel, 1995; Wang et al., 1990). However more recent studies have provided better age constraints and generally assigned a late Bartonian – early Priabonian (ca. 40 – 37 Ma, Bosboom et al., 2014b, Kaya et al., 2019) age. It has been determined as ca. 39 Ma by Carrapa et al. (2015), however the marine interval of Carrapa et al. (2015) seems to correspond to the 2nd Paleogene sea incursion (Bosboom et al., 2017). Indeed, more recently, the same group dated the 2nd and 3rd Paleogene sea incursions as ca. 41 Ma and ca. 37 Ma, respectively (Wang et al., 2019). Sun et al. (2020) determined the age of the final sea retreat in central Tajik Basin as ca. 39 Ma and interpreted that it is coeval with ca. 41 Ma sea retreat in the Tarim Basin (Bosboom et al., 2014a; Sun et al., 2016). However, once again it should be noted that the ca. 41 Ma age of Bosboom et al. (2014a) corresponds to the 2nd Paleogene sea retreat in the Tarim Basin, not the last one.

The 3rd sea incursion was recorded in the marls, mudstones and shelly calcareous sandstones of the 2nd, 3rd and 4th members of the Bashibulake and Kushan – Sanglak - Hissarak formations in the Tarim and Tajik basins, respectively. It was geographically limited and less extended far eastward in the Tarim Basin (Bosboom et al., 2014b; Kaya et al., 2019), however it can be well-correlated and recognized in the Tajik, Tarim, Fergana and Alai Valley basins (e.g. Bosboom et al., 2017; Kaya et al., 2019).

It has been interpreted that the 3rd and final Paleogene sea incursion was not primarily driven by eustasy but rather related to tectonic subsidence creating accommodation space overcoming basin infilling in the Tajik and Tarim basins (Kaya et al., 2019). The final retreat of the sea has been generally related to (1) tectonism and related basin infilling (Burtman, 2000; Burtman & Molnar, 1993), (2) eustasy (Dupont-Nivet et al., 2007; Sobel & Dumitru, 1997) or (3) combined effects of both tectonism and global sea level (Bosboom et al., 2017, 2014a, 2011; Zhang et al., 2018). Agreeing with the 3rd view, we relate the final retreat to the combined effects of tectonism and eustasy (Chapter 2).

After this last sea incursion, the connection of the Tarim and Tajik basins with the retreated Paratethys Sea remains elusive (Bosbbom et al., 2014a). Some studies documented the occasional occurrence of brackish-marine conditions during Oligocene-Miocene based on foraminifera and ostracod fossils and negative oxygen isotope shifts (e.g. Zheng et al., 1999; Gao et al., 2000; Graham et al., 2005). Recently, Oligocene sea incursion of the Paratethys into the Junggar Basin, located north of the Tarim Basin and the Tian Shan Mountains, has been interpreted based on the isotope composition of a dolomitization fluid likely derived from the Paratethys seawater (Li et al., 2020). However, continental deposition was prevalent in the Tarim and Tajik basins during this time and younger incursions, if occurred, should still be confirmed.

5.2. Effects of sea incursions on regional climate: Role of the proto-Paratethys sea as a moisture source and a carbon sink

5.2.1. The proto-Paratethys Sea as a moisture source

The subtropical climate of Central Asia shifted to more arid conditions with the onset of inland deserts during the Cenozoic (e.g. Guo et al., 2008), however the controlling mechanisms of this aridification remain elusive. Generally three mechanisms, all occurring during the Eocene epoch, have been called upon: (1) the growth of the Himalaya and Tibetan Plateau in response to the India-Asia collision (e.g. Kutzbach et al., 1993; Li et al., 2018; Manabe& Broccoli, 1990), (2) the global cooling during the Cenozoic (e.g. Dupont-Nivet et al., 2007; Lu et al., 2010), and (3) the westward retreat of the proto-Paratethys Sea (e.g. Bosboom et al., 2014a; Carrapa et al., 2015; Ramstein et al., 1997; Wang et al., 2016; Zhang et al., 2007). Recent proxy and model data have shown that the Asian Aridification was linked to a decrease in the westerly moisture flux (e.g. Caves et al., 2015). Modulating the moisture governed by the westerlies, the proto-Paratethys Sea fluctuations have been frequently proposed as a major moisture source for the Asian interior, and also a trigger for setting up the Siberian High resulting in winter monsoonal circulation and associated dust storms, hence a major contributor to the Asian aridification (e.g. Bougeois et al., 2018; Kaya et al., 2019; Meijer et al., 2019, 2020a). The long-term westward retreat of the sea (starting ca. 53-52 Ma and ending ca. 36.7 Ma) likely removed a potentially significant moisture source to Central Asia (Bosboom et al., 2014a; Bougeois et al., 2018; Graham et al., 2005; Kent-Corson et al., 2009; Ramstein et al., 1997; Zhang et al., 2012). Recent proxy and model data also show that the retreat of the proto-Paratethys Sea was noninfluential on the intensification/generation of the Asian monsoons due to its very shallow water depths (e.g. Bougeouis et a., 2018; Licht et al., 2014, 2016; Roe et al., 2016; Zhang et al., 2012).

The influence of the proto-Paratethys Sea incursions on Asian aridification has been documented recently by the correlation of relatively wetter (saline lake) phases in the Qaidam and Xining basins with the highstands of the proto-Paratethys Sea (Kaya et al., 2019; Meijer et al., 2019). These correlations suggest that moisture was governed by the proto-Paratethys sea incursions in that region. However, the oldest one of these wet phases in the Xining Basin representing an intensified Asian hydrological cycle has been dated later as 50.9 Ma and linked to the global warmth of the Early Eocene Climatic Optimum (EECO) (Meijer et al., 2020b). This suggests that even though the proto-Paratethys sea was an important moisture source, it was not the only driver on the evolution of atmospheric moisture.

Sensitivity climate simulations show that the Asian climate is sensitive to the coeval retreat of the proto-Paratethys and the Siberian seas (Zhang et al., 2007). Supporting this, the increased continentality due to retreating proto-Paratethys and Siberian seas (ca. 40 Ma) has been interpreted to have triggered the onset of an atmospheric high pressure system developing over Siberia resulting in a shift to predominant steppe-desert vegetation and appearance of a loess-like dust in the grain-size record coeval with the onset of obliquity cycles in the Xining Basin (Meijer et al., 2020a). Other mechanisms such as the Tibetan Plateau uplift and global cooling may have likely contributed to the setting up the long-term boundary conditions, however the sea retreat has been interpreted to have been acted as the critical trigger at 40 Ma (Meijer et al., 2020a).

In parallel with above mentioned studies (Bosboom et al., 2014a; Bougeois et al., 2018; Graham et al., 2005; Kent-Corson et al., 2009; Meijer et al., 2019; Ramstein et al., 1997; Zhang et al., 2012), we show evidence for the correlation between the proto-Paratethys sea incursions and the Asian aridification in this thesis (Chapter 2). However, we think that the overall aridification might be best explained by the combined effects of the sea retreat, global climate and Tibetan uplift. We argue that superimposing on the long-term effects of the Tibetan Plateau uplift and global cooling, the proto-Paratethys sea played a major role as a moisture source on the Asian aridification. Further evidence, which can be provided by future work, is still needed to better understand and differentiate the contributions of the proto-Paratethys Sea incursions, Tibetan Plateau uplift and global cooling on Asian aridification.

The proto-Paratethys Sea as a carbon sink

During most of the Mesozoic - Cenozoic short-term or long-term global paleoclimatic and paleoecological events (e.g. Cretaceous OAEs, PETM, early Eocene hyperthermals, Eocene-Oligocene climate transition), the proto-Paratethys and (then Paratethys during Oligocene and thereafter) Basin acted as a carbon sink well represented by the extensive deposition of organic-rich sapropel layers (Gavrilov et al., 2019) (Figure 5.1). Many of these events are also associated with large sea-level fluctuations making the proto-Paratethys sea incursions and their impact on the regional/global climate more significant.

The TOC-rich sediments of the eastern Caucasus corresponding to the late Cenomanian OAE2 event has been studied and well documented in the west proto-Paratethys area (Gavrilov et al., 2009, 2013, 2019), however no studies have been conducted yet on the Cretaceous OAEs in the eastern part of the proto-Paratethys Basin and remains to be explored. The paleoenvironmental/paleoecological conditions in the Tarim Basin and the efficient role of the proto-Paratethys as a carbon sink during the PETM was explained in Chapter 4. There are still unprocessed samples from several PETM sections in the Tarim Basin which were collected during our field studies. These samples can help to further constrain the paleoenvironmental/paleoecological conditions in the Tarim Basin during the PETM.

Here we will revisit an old idea that the Paratethys Sea can be a significant carbon sink during the Eocene-Oligocene cooling trend and the inception of the Antarctic glaciation, contributing to the decline of atmospheric $p\mathrm{CO}_2$. We propose some further work that can be done to test the contribution and efficiency of the proto-Paratethys (and later Paratethys) basin on the regional/global climate.

5.2.2. Role of the proto-Paratethys & Paratethys as a carbon sink on the Eocene-Oligocene climate transition and rapid Antarctic ice sheet expansion – Kuma Formation & Maikop series

The Eocene-Oligocene transition (EOT) from the greenhouse to the icehouse conditions represents one of the most pronounced periods of global cooling during the Cenozoic (Pagani et al., 2011). Mainly two events have been thought to have contributed to the long term Eocene-Oligocene cooling trend and glaciation of Antarctica (Lear & Lunt, 2016). The first one is the widening and deepening of Drake Passage that led to the development of the Antarctic Circumpolar Current resulting in the thermal isolation of Antarctica and growth of ice sheets (e.g. Kennett, 1977). The second one is the inferred long-term reduction in atmospheric carbon dioxide levels (e.g. Zachos et al., 1996). However, since the pioneering work of DeConto &

Pollard (2003) the first "gateway hypothesis" by Kennett (1997) has been out of favor (Lear & Lunt, 2016) and precedence has been given to falling CO_2 hypothesis as the main driver (Kennedy et al., 2015).

During the long-term Eocene-Oligocene transition, the expansion of continental ice sheets on Antarctica was abrupt (occurring less than 50 kyr) and prominent and is well documented in oxygen isotope and glaciomarine sediment records (Zachos & Kump, 2005 and references therein). In each record the same elevated pattern in $\delta^{18}O$ has been observed between 33.7 and 33.5 Ma followed by a partial return to less ^{18}O-enriched values at 33.0 Ma (Zachos & Kump, 2005).

For drawing down of atmospheric carbon dioxide and pCO_2 two mechanisms operating on different timescales are generally called upon: (1) increased burial of organic carbon operating on kyrs time scales and (2) increased weathering of silicate rocks operating on Myrs time scales (Spofforth et al., 2010). Given the scale of the climate transition and abrupt ice sheet expansion on Antarctica during the earliest Oligocene (33.7 Ma, <50 kyr), it has been previously proposed and documented that increased export production and burial of organic carbon together with a globally higher organic carbon/$CaCO_3$ burial ratio would have accelerated the removal of carbon from the surface and deep ocean resulting a reduction in atmospheric pCO_2 (Zachos et al., 1996 and references therein).

After the final westward retreat of the proto-Paratethys from Central Asia and its isolation as the Paratethys, the initial deposition during the Oligocene and early Miocene in this restricted basin is represented by the oxygen-poor, dark, organic carbon-rich claystones/shales with fish remains named as the 'Maikop Series' (van der Boon, 2017) (Figure 5.1). Beginning with the early Oligocene, the entire Paratethys basin was isolated/restricted and consequently oxygen-depleted for millions of years resulting in the deposition of black shales over vast areas from the Vienna basin in Austria to the Caspian Sea (van der Boon, 2017). The thickness of the Maikop deposits can be very thick as 3 km in offshore Azerbaijan whereas in the Western Black Sea it is up to 2 km (van der Boon et al., 2018). TOC values of the black shales with 10-25m thickness in the Austrian Molasse Basin reaches up to 12 %, whereas in the Western Carpathians it is around 5.1-5.9 % (Sachsenhofer et al., 2018). In the Eastern Carpathians the average TOC content of the shaly lithologies is 9.8 % with maximum values as 24 % (Sachsenhofer et al, 2018).

Oxygen-depleted conditions already occurred before the isolation of the Paratethys during the PETM (e.g. Dickson et al., 2014; Gavrilov et al., 2003; see also Chapter 4) and around the Middle Eocene Climatic Optimum (MECO) (Beniamovski et al., 2003; van der Boon et al., 2019) represented by the organic carbon-rich (between 2 and 15 wt%) deposits of the Kuma Formation (Figure 5.1). Kuma Formation can be traced over 2000 km, extending from the northwest coast of the Black Sea in the west to the Aral Sea in the east (Beniamovski et al., 2003). Its thickness varies between 20 and 50 m (Beniamovski et al., 2003).

The high TOC and thickness values in the nearly entire Paratethys basin indicate enhanced preservation and burial of organic carbon which could have provided a major sink for carbon and lowered atmospheric pCO_2. Previously Paratethys has been considered as a significant carbon sink however without linking to the cooling (Vetö, 1987). Vetö (1987) estimated 1.2 X 10^{13} t (12000 gigaton) organic carbon accumulation during the deposition of the Maikop deposits. We speculate that enhanced organic carbon burial over much of the proto-Paratethys and later Paratethys during the deposition of the Kuma Formation and Maikop series, repectively, may have majorly contributed to drawdown of atmospheric carbon dioxide before and during the EOT cooling and glaciation of Antarctica. Indeed, it was previously estimated that 6 x 10^{16} g (60 gigaton) organic carbon was accumulated in the dysoxic-anoxic Peri-Tethyan basin during the deposition of the Kuma Formation (Beniamovski et al., 2003) which deemed one of the causes of lowered atmospheric CO_2 and consequent global cooling and Antarctic glaciation. This is indeed an intriguing argument which has to be further tested with the question of "Was the Paratethys an important carbon sink and contributor to the EOT global cooling?". If yes, "How much and to what extent did it contribute?".

Precise age constraints for the onset of the deposition of the Kuma Formation and the Maikop Series (and the equivalent deposits) become important and required to reveal the contribution of organic carbon burial in the Paratethys on the reduction of atmospheric CO_2. Recent and previous studies have provided major contribution for the development of a solid stratigraphic framework of the Maikop series (see Popov et al., 2019a and references therein). The onset of the deposition of the Maikop Series has been dated around the base of chron C13n at ca. 33.7 Ma in North Caucasus, Russia (van der Boon et al., 2019) and ca. 37.7 Ma in Azerbaijan (van der Boon et al., 2017). However, it remains as a question whether the Pirembel Formation in Azerbaijan truly represents the equivalent of the classic Maikop Series (van der Boon et al., 2017). This should be confirmed or refuted by further studies.

Kuma Formation has also been studied comprehensively (e.g. Beniamovski et al., 2003; Popov et al., 2019b) and has been dated recently between 42.1 and 38.4 Ma (van der Boon et al., 2019).

Considering we already have a solid stratigraphic framework for the Maikop series and the Kuma Formation thanks to above mentioned studies, the next step would be obtaining the spatial distribution of the thickness and TOC values in order to estimate accurately the role of proto-Paratethys as a carbon sink. By following a similar methodology as in Chapter 4, we can better estimate the amount of organic carbon burial in the Proto-Paratethys (and Paratethys) basin during the deposition of the Kuma Formation and the Maikop series. For the PETM study in Chapter 4, we had a limited number of values for the entire area (particularly for the West Siberian Sea) and we were able to apply two methods (Inverse Distance Weighted & Thiessen polygons) for the interpolation with relatively low-resolution. By having more values, the estimation would have been more precise and representative, and several interpolation methods could have been applied for comparison. For the Maikop series and the Kuma Formation, this can be achieved by gathering sufficient amount of data both from the field and preexisting literature. Therefore, after a comprehensive literature survey, field studies might be required if there are insufficient data for some regions.

To better understand the role of the proto-Paratethys as a carbon sink and its effect on global climate, all records (PETM, OAEs, EOT, EECO etc.) can be further studied with better paleogeographic constraints provided by this thesis. Despite the presence of their records, these events are poorly documented particularly for the eastern proto-Paratethys (in the Tajik and Tarim basins). Comparing the records of these paleoclimate events can provide insight on the paleoenvironmental/paleoecological conditions and mechanisms during different paleoclimatic/paleoecological events. These future studies can also be conducted to better understand the recovery from these ancient carbon cycle perturbations and then compared to similar perturbations imposed on the modern system.

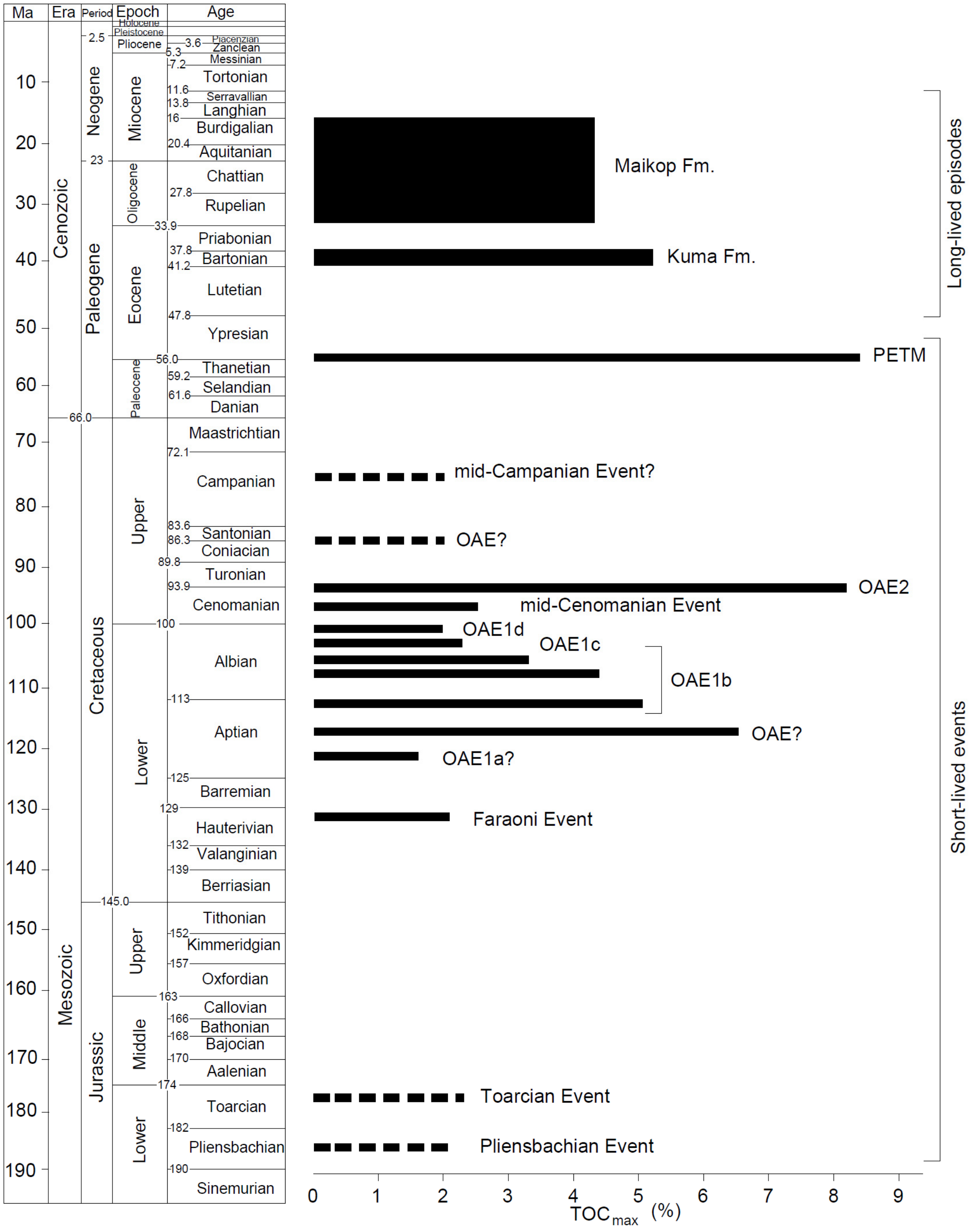

Figure 5.1 The TOC-rich sediments of the proto-Paratethys/Paratethys Basin during the Mesozoic and Cenozoic. Dashed lines indicate uncertain intervals of TOC enrichment. (modified from Gavrilov et al., 2019).

6. Acknowledgement

During the last 5 years, I have experienced the greatest adventure of my life until now with several social and academic events forming my PhD Journey. All these experiences were very instructive indeed and taught me a lot and shaped my worldview and perception of myself. Not all of them were nice, sometimes unpleasant and nerve-wracking, however as a whole, they were parts of my PhD adventure. This was my motivation all the time to overcome any issue not only academic but also social.

It's all started in Vienna in April 2015 when I met Guillaume, my supervisor, for the first time. Guillaume was looking for PhD students for his ERC project at that time. On my side however, I had already started my PhD in Turkey, even passed my qualification exam. I was not aware what this meeting will bring new to my life when I was introduced to Guillaume by Arda Özacar, a professor from my previous university in Turkey. It brought me the opportunity of doing my PhD in a super exciting project in Germany. Therefore, I should thank Arda Özacar and also Nuretdin Kaymakçı for introducing me to Guillaume. When I was listening Guillaume's EGU talk at that time, I admired the provided conditions and opportunities of his ERC project, but more attracted by the opportunity of working in Central Asia. In the end, I couldn't resist quitting my PhD in Turkey, which I was halfway through, and accepted Guillaume's offer to involve in his project as a PhD student. Three months later in August 2015, I found myself piggybacking my first samples in a rice bag during the fieldwork in China.

Right after the first year fieldwork, the adventure continued when I moved to Germany in November 2015. Before bothering you with my early desperate times in Germany, I should mention about "Işık Family", my family in Berlin. I had never met the members of Işık Family before I came to Germany. I knew them from other acquaintances in Turkey, but not personally. They hosted me warmly for a month in their house, and helped me literally with everything. Without their presence, their help and support, I would not be able to overcome the difficulties during my early desperate times in Germany, indeed. Therefore, I would like to thank all the members of Işık Family; Ayhan Işık, Berrin Işık, Selma Işık, Selçuk Işık, Aykut Işık for accepting me as one of them and for their help and support when needed.

During my first arrival to Germany, I had to come alone because the application process for my wife Sema's visa took three months to complete. Those three months alone, literally were not the best start for my PhD journey. I had to tackle with several issues, which would be easy to solve daily problems somewhere else, such as finding a flat, opening a bank account, extending my temporary visa and then extending my contract. However, they form a vicious circle in Germany as they are all interconnected. You have to accomplish one to continue with the rest, but that was indeed a pain in the neck. You would always get a question from the landlord such as, "Do you have a residence permit?" when you go for an appointment to see a flat. In order to get your residential permit, you need to find a flat, which requires an everlasting search. Or a bank would ask for your residential registration, when you apply for opening a bank account. Apparently, you need to find a flat to extend your temporary visa and you need an extended visa to extend your work contract. If a potential future international PhD student, who needs a visa, is reading this, then here is a warning for you; If you don't have the devil's luck or if you don't have an acquaintance/friend to help you with all these troubles, get ready for tough sledding. I did not have the devil's luck but I was still lucky to meet the best people to help me.

Of course, finishing this thesis would have never been possible without the help and support of a number of people I would like to thank here. In light of this, I would like to make following acknowledgements:

Primarily I should thank Guilllaume Dupont-Nivet as my supervisor who provided me a valuable guidance and the freedom to carry out this project independently. His constant encouragement and support throughout my PhD enabled me successfully complete this project. His easygoing approach to problem solving was crucial for the improvement of the project. I owe many skills I learned during my PhD to him, such as conducting paleomagnetic analyses, being efficient and productive in the field, writing convincing research papers, and dealing with the harsh reviewers.

I would like to thank Jean-Noël Proust who made a valuable contribution to the project. I learned many skills from his extensive experience on sedimentology and sequence stratigraphy. His drawings of logs in his tidy field books, which were very artistic indeed, showed me another way of logging in the field.

I would like to thank Pierrick Roperch for his help and support for the project. He taught me how to perform paleomagnetic analysis in the lab in Rennes which I spent at least 4 months through my PhD years. He also helped me with many issues from accommodation to transportation during my stays in Rennes. I also thank Fernando Poblete for the discussions on the paleogeography, and hosting me in his house during one of my stays in Rennes when I was late to pick up the key for the university guesthouse.

I would like to thank all the biostratigraphers who did a large amount of work during the project. Joost Frieling, Chiara Fioroni, Sevinç Özkan Altıner, Ezgi Vardar and Marius Stoica have been involved from the beginning of the project to the end and provided valuable data. I want to thank particularly Joost Frieling who provided the most constructive suggestions and motivating discussions on many topics. I thank to pollen specialist Natasha Barbolini who contributed to the first manuscript. I also thank to Laurie Bougeois for fruitful discussions and sharing her data from her PhD research. With the data provided, she contributed significantly to the first manuscript.

Of course I also thank to my examination committee members, Edward Sobel, Maria Mutti, Manfred Strecker and reviewers, Wout Krijgsman and Anne Bernhardt for their precious time and valuable reviews on my thesis.

I would like to thank Niels Meijer who assisted me so much during the second year fieldwork in China and Tajikistan. He was a great support for collecting gigantic amount of samples and was a great fun to work with. Also, I am grateful for our constructive discussions with Niels in the office during our Potsdam days. I thank to Alexander Rohrmann for his contribution to the third manuscript with biomarker analysis and for our discussions in the office. I would like to thank

Verónica Torres Acosta for her administrative and organisational contribution to the project. I also thank her for the warm friendship and for the encouraging and motivating talks we had.

At University of Potsdam I would like to thank particularly Edward Sobel for fruitful discussions and advice, and also for providing me the old Chinese books which were difficult to reach. Other people I would like to name from University of Potsdam include Christine Fischer, Christina Günter and Tanja Klaka-Tauscher. I would like to thank Christine Fischer and Christina Günter for their support and help during my labworks. Tanja deserves special thanks for her immediate administrative help and support when needed. From GFZ in Potsdam, I would like to thank Birgit Plessen and Norbert Nowaczyk for their help and guidance during my labworks.

Of course my gratitude also goes to our field assistants Mehmut Mamtimin, Sohibnazar Ashuraliev, Sodik Yatimov and Jovid Aminov. I especially thank to my brothers in Tajikistan, Sohibnazar Ashuraliev, Sodik Yatimov and Jovid Aminov, who were very friendly and helpful during my field works. They introduced the Tajik culture to me and hosted me warmly in their home with some delicious Tajik food, which I have already missed a lot.

I would like to thank to my friends in Berlin, Görkem Sivri, Gamze Koç, Can Kuseyri and Zeynep Çokuğraş-Kuseyri for their warm friendship. It was very nice to have their friendship during the tough times of my PhD and I owe them many thanks for the encouraging and motivating talks we had. I also would like to thank my musician friends from my bands Carnal Tomb and Vapor Void. They all helped me to forget about the academic struggle during the times we made music and shared the stage. Among them, I particularly thank to Alexander Ruoff for his warm friendship.

Among my friends, Hakan Tanyaş deserves a place for gratitude particularly. Our paths have come across many times during the last 10 years and I hope they will again soon. We spent many hours of speaking to motivate each other during our PhDs, to find solutions to our academic and social problems.

Finally, I would like to thank to my beloved wife Sema Bagci-Kaya and my dear family. I would like to express my gratitude to Hidayet Kaya, Yurdal Kaya, Sait Bağcı, Nuray Bağcı, Murat Yüksel Kaya, Başak Şener Kaya, Duru Kaya and Derya Bağcı for their never-ending, unconditional support and love. It would not have been possible to accomplish this project without any of you.

7. References

Abels, H. A., Dupont-Nivet, G., Xiao, G., Bosboom, R., & Krijgsman, W. (2011). Step-wise change of Asian interior climate preceding the Eocene-Oligocene Transition (EOT). *Palaeogeography, Palaeoclimatology, Palaeoecology*, *299*(3–4), 399–412. https://doi.org/10.1016/j.palaeo.2010.11.028.

Agnini, C., E. Fornaciari, L. Giusberti, P. Grandesso, L. Lanci, V. Luciani, G. Muttoni, H. Pälike, D. Rio, D. J. A. Spofforth, C. Stefani (2011). Integrated biomagnetostratigraphy of the Alano section (NE Italy): A proposal for defining the middle-late Eocene boundary. *Geological Society of America Bulletin* 123, 841–872. doi:10.1130/B30158.1.

Agnini, C., Fornaciari, E., Raffi, I., Catanzariti, R., Pälike, H., Backman, J., Rio, D. (2014). Biozonation and biochronology of Paleogene calcareous nannofossils from low and middle latitudes. *Newsletters on Stratigraphy*, 47/2, 131-181. doi:10.1127/0078-0421/2014/0042.

Agnini, C., Spofforth, D.J.A., Dickens G.R., Rio, D., Pälike, H., Backman, J., Muttoni, G., Dallanave, E. (2016). Stable isotope and calcareous nannofossil assemblage record of the late Paleocene and early Eocene (Cicogna section). *Clim. Past*, 12, 883-909.

Akhmetiev, M.A. & Beniamovski, V.N. (2009). Paleogene floral assemblages around epicontinental seas and straits in Northern Central Eurasia: proxies for climatic and paleogeographic evolution. *Geologica Acta*, 7, 297-309.

Akhmetiev, M.A., Zaporozhets, N.I., Iakovleva, A.I., Aleksandrova, G.N., Benyamovskiy, V.N., Oreshkina, T.V., Gnibidenko, Z.N., Dolya, Z.A. (2010). Comparative analysis of marine Paleogene sections and biota from west Siberia and the Arctic Region. *Stratigraphy and Geological Correlation,* 18, 635-659.

Akhmetiev, M.A., Zaporozhets, N.I., Benyamovskiy, V.N., Aleksandrova, G.N., Iakovleva, A.I., Oreshkina, T.V. (2012). The Paleogene history of the western Siberian seaway – A connection of the Peri-Tethys to the Arctic Ocean. *Austrian Journal of Earth Sciences*, 105, 50-67.

Alegret, L., Ortiz, S., Arenillas, I., & Molina, E. (2005). Palaeoenvironmental turnover across the Palaeocene/Eocene boundary at the Stratotype section in Dababiya (Egypt) based on benthic foraminifera. *Terra Nova*, 17(6), 526–536.

Allmon, W. D. (2007). Cretaceous marine nutrients, greenhouse carbonates, and the abundance of turritelline gastropods. *The Journal of Geology*, *115*(5), 509-523.

Amidon, W.H., Hynek, S.A. (2010). Exhumational history of the north central Pamir. *Tectonics*, 29, TC5017.

Aminov, J., Ding, L., Mamadjonov, Y., Dupont-Nivet, G., Aminov, J., Zhang, L.Y., Yoqubov, S., Aminov, J., & Abdulov, S. (2017). Pamir Plateau formation and crustal thickening before the India-Asia collision inferred from dating and petrology of the 110–92 Ma Southern Pamir volcanic sequence. *Gondwana Research*, *51*, 310-326.

Angori, E., Bernaola, G., and Monechi, S. (2007). Calcareous nannofossil assemblages and their response to the Paleocene-Eocene Thermal Maximum event at different latitudes: ODP Site 690 and Tethyan sections, *Geol. S. Am. S.,* 424, 69–85.

Auer, G., Piller, W.E., Harzhauser, M. (2014). High-resolution calcareous nannoplankton palaeoecology as a proxy for small-scale environmental changes in the Early Miocene. *Mar. micropal.*, 111, 53–65.

Baccelle, L., & Bosellini, A. (1965). *Diagrammi per la stima visiva: della composizione percentuale nelle rocce sedimentarie* (Vol. 4, No. 3). Università degli studi di Ferrara.

Bao, J., Wang, Y., Song, C., Feng, Y., Hu, C., Zhong, S., & Yang, J. (2017). Cenozoic sediment flux in the Qaidam Basin, northern Tibetan Plateau, and implications with regional tectonics and climate. *Global and Planetary Change*, *155*, 56–69. https://doi.org/10.1016/j.gloplacha.2017.03.006.

Baratov, R. B., Budanov, V. I., Budanova, K. T., Vlasov, N. G., & Djakov, J. A. (1976). Subdivisions of Stratified and Intrusive Rocks of Tajikistan. "*Donish" Publishing House,* Dushanbe*,* 269 p. (in Russian).

Barke, J., van der Burgh, J., van Konijnenburg-van Cittert, J.H.A., Collinson, M.E., Pearce, M.A., Bujak, J., Heilmann-Clausen, C., Speelman, E.N., van Kempen, M.M.L., Reichart, G.-J., Lotter, A.F., Brinkhuis, H. (2012). Coeval Eocene blooms of the freshwater fern Azolla in and around Arctic and Nordic seas. *Palaeogeogr. Palaeoclimatol. Palaeoecol.* 337–338, 108–119. doi:10.1016/j.palaeo.2012.04.002.

Barrier E., Vrielynck, B., Brouillet J.F. & Brunet M.F. (Contributors : Angiolini L., Kaveh F., Poisson A., Pourteau A., Plunder A., Robertson A., Shekawat R., Sosson M. and Zanchi A.) (2018). Paleotectonic Reconstruction of the Central Tethyan Realm. Tectonono-Sedimentary-Palinspastic maps from Late Permian to Pliocene. CCGM/CGMW, Paris, http://www.ccgm.org. Atlas of 20 maps (scale: 1/15 000 000).

Beniamovski, V. N., Alekseev, A. S., Ovechkina, M. N., & Oberhaensli, H. (2003). Middle to upper Eocene dysoxic-anoxic Kuma Formation (northeast Peri-Tethys): biostratigraphy and paleoenvironments. *Special Paper of the Geological Society of America*, *369*, 95-112.

Berggren, W. A., & Aubert, J. (1975). Paleocene benthonic foraminiferal biostratigraphy, paleobiogeography and paleoecology of Atlantic-Tethyan regions: Midway-type fauna. *Palaeogeography, Palaeoclimatology, Palaeoecology,* 18(2), 73–192.

Bjerrum, C. J., Bendtsen, J., & Legarth, J. J. F. (2006). Modeling organic carbon burial during sea level rise with reference to the Cretaceous. *Geochemistry, Geophysics, Geosystems*, *7*(5).

Bian, W., Yang, T., Ma, Y., Jin, J., Gao, F., Zhang, S., Wu, H., & Li, H. (2017). New Early Cretaceous palaeomagnetic and geochronological results from the far western Lhasa terrane: Contributions to the Lhasa-Qiangtang collision. *Scientific reports*, *7*(1), 16216.

Bianchi, T. S., Cui, X., Blair, N. E., Burdige, D. J., Eglinton, T. I., & Galy, V. (2018). Centers of organic carbon burial and oxidation at the land-ocean interface. *Organic Geochemistry*, *115*, 138-155.

Bijl, P.K., Sluijs, A., Brinkhuis, H. (2013). A magneto- and chemostratigraphically calibrated dinoflagellate cyst zonation of the early Paleogene South Pacific Ocean, *Earth-Sci. Rev*., 124, 1-31.

Bijl, P.K., Brinkhuis, H., Egger, L.M., Eldrett, J.S., Frieling, J., Grothe, A., Houben, A.J.P., Pross, J., Śliwińska, K.K., Sluijs, A. (2016). Comment on "Wetzeliella and its allies – the 'hole' story: a taxonomic revision of the Paleogene dinoflagellate subfamily Wetzelielloideae" by Williams *et al*. (2015). *Palynology* 6122, 1–7. doi:10.1080/01916122.2016.1235056.

Blayney, T., Najman, Y., Dupont-Nivet, G., Carter, A., Millar, I., Garzanti, E., Sobel, E.R., Rittner, M., Andò, S., Guo, Z., & Vezzoli, G. (2016). Indentation of the Pamirs with respect to the northern margin of Tibet: Constraints from the Tarim basin sedimentary record. *Tectonics*, *35*(10), 2345-2369.

Blayney, T., Dupont-Nivet, G., Najman, Y., Proust, J.N., Meijer, N., Roperch, P., Sobel, E.R., Millar, I., & Guo, Z. (2019). Tectonic evolution of the Pamir recorded in the western Tarim Basin (China): sedimentologic and magnetostratigraphic analyses of the Aertashi section. *Tectonics*, *38*(2), 492-515.

Blum, M. D., & Törnqvist, T. E. (2000). Fluvial responses to climate and sea-level change: A review and look forward. *Sedimentology*, *47*(SUPPL. 1), 2–48. https://doi.org/10.1046/j.1365-3091.2000.00008.x

Bolle, M. P., Pardo, A., Hinrichs, K. U., Adatte, T., Von Salis, K., Burns, S., Keller, G., & Muzylev, N. (2000). The Paleocene–Eocene transition in the marginal northeastern Tethys (Kazakhstan and Uzbekistan). *International Journal of Earth Sciences*, *89*(2), 390-414.

Borneman, N. L., Hodges, K. V., Soest, M. C., Bohon, W., Wartho, J. A., Cronk, S. S., & Ahmad, T. (2015). Age and structure of the Shyok suture in the Ladakh region of northwestern India: implications for slip on the Karakoram fault system. *Tectonics*, *34*(10), 2011-2033.

Bosboom, R., Dupont-Nivet, G., Grothe, A., Brinkhuis, H., Villa, G., Mandic, O., … Guo, Z. J. (2014b). Timing, cause and impact of the late Eocene stepwise sea retreat from the Tarim Basin (west China). *Palaeogeography, Palaeoclimatology, Palaeoecology*, *403*, 101–118. https://doi.org/10.1016/j.palaeo.2014.03.035.

Bosboom, R., Dupont-Nivet, G., Grothe, A., Brinkhuis, H., Villa, G., Mandic, O., … Krijgsman, W. (2014a). Linking Tarim Basin sea retreat (west China) and Asian aridification in the late Eocene. *Basin Research*, *26*(5), 621–640. https://doi.org/10.1111/bre.12054.

Bosboom, R., Ables, H.A., Hoorn, C., van den Berg, B.C..J., Guo, Z., Dupont-Nivet, G. (2014c). Aridification in continental Asia after the Middle Eocene Climatic Optimum (MECO). *Earth and Planetary Science Letters,* 389, 34-42.

Bosboom, R. E., Dupont-Nivet, G., Houben, A. J. P., Brinkhuis, H., Villa, G., Mandic, O., … Krijgsman, W. (2011). Late Eocene sea retreat from the Tarim Basin (west China) and concomitant Asian paleoenvironmental change. *Palaeogeography, Palaeoclimatology, Palaeoecology*, *299*(3–4), 385–398. https://doi.org/10.1016/j.palaeo.2010.11.019.

Bosboom, R., Mandic, O., Dupont-Nivet, G., Proust, J.-N., Ormukov, C., & Aminov, J. (2017). Late Eocene palaeogeography of the proto-Paratethys Sea in Central Asia (NW China, southern Kyrgyzstan and SW Tajikistan). *Geological Society, London, Special Publications*, *427*(1), SP427-11. https://doi.org/10.1144/SP427.11.

BouDagher-Fadel, M. K. (2012). *Biostratigraphic and geological significance of planktonic foraminifera* (Vol. 22). Newnes.

Boudreau, B. P., Middelburg, J. J., & Luo, Y. (2018). The role of calcification in carbonate compensation. *Nature Geoscience*, *11*(12), 894-900.

Bougeois, L. (2014). Paleogene seasonal variability in Central Asia: constrains from high-resolution geochemistry on oyster shells, PhD dissertation, University of Rennes.

Bougeois, L., de Rafélis, M., Reichart, G. J., de Nooijer, L. J., & Dupont-Nivet, G. (2016). Mg/Ca in fossil oyster shells as palaeotemperature proxy, an example from the Palaeogene of Central Asia. *Palaeogeography, Palaeoclimatology, Palaeoecology*, *441*, 611–626. https://doi.org/10.1016/j.palaeo.2015.09.052.

Bougeois, L., Dupont-Nivet, G., de Rafélis, M., Tindall, J. C., Proust, J.-N., Reichart, G.-J., … Ormukov, C. (2018). Asian monsoons and aridification response to Paleogene sea retreat and Neogene westerly shielding indicated by seasonality in Paratethys oysters. *Earth and Planetary Science Letters*, *485*, 99–110. https://doi.org/https://doi.org/10.1016/j.epsl.2017.12.036.

Boudaugher-Fadel, M. K. (2018). *Evolution and geological significance of larger benthic foraminifera*. UCL Press.

Bouilhol, P., Jagoutz, O., Hanchar, J. M., & Dudas, F. O. (2013). Dating the India–Eurasia collision through arc magmatic records. *Earth and Planetary Science Letters*, *366*, 163-175.

Bowen, G. J., Beerling, D. J., Koch, P. L., Zachos, J. C., & Quattlebaum, T. (2004). A humid climate state during the Palaeocene/Eocene thermal maximum. *Nature*, *432*(7016), 495.

Bowen, G. J., & Zachos, J. C. (2010). Rapid carbon sequestration at the termination of the Palaeocene–Eocene Thermal Maximum. *Nature Geoscience*, *3*(12), 866.

Bown, P. R., & Young, J.R. (1998) Introduction. In: Bown, P.R. (Ed.), Calcareous Nannofossil Biostratigraphy: *British Micropalaeontology Society Series*. Chapman and Hall, London, pp. 1–15.

Bown, P. R., (2005). Palaeogene calcareous nannofossils from the Kilwa and Lindi areas of coastal Tanzania (Tanzania Drilling Project 2003-4). *Journal of Nannoplankton Research,* 27, 21-95.

Bown, P., Pearson, P. (2009). Calcareous plankton evolution and the Paleocene/Eocene thermal maximum event: new evidence from Tanzania. *Marine Micropaleontology* 71, 60–70.

Bown, P. (2010). Calcareous nannofossils from Paleocene/Eocene Thermal Maximum interval of southern Tanzania (TDP Site 14). *J. Nannoplankton Res*., 31(1), 11-38.

Bown, P. R., & Young, J.R. (2019). The fossil record of coastal coccolithophores. J. *Nannoplankton Res*., 4, 73-80.

Bralower, T.J. (2002). Evidence of surface water oligotrophy during the Paleocene–Eocene thermal maximum: nannofossil assemblage data from Ocean Drilling Program Site 690, Maud Rise,Weddell Sea. *Paleoceanography* 17 (2), 1–11.

Brinkhuis, H., 1994. Late Eocene to Early Oligocene dinoflagellate cysts from the Priabonian type-area (northeast Italy): Biostratigraphy and paleoenvironmental interpretation. *Palaeogeogr. Palaeoclimatol. Palaeoecol.* 107, 121–163.

Brookfield, M. E., & Hashmat, A. (2001). The geology and petroleum potential of the North Afghan platform and adjacent areas (northern Afghanistan, with parts of southern Turkmenistan, Uzbekistan and Tajikistan). *Earth-Science Reviews*, *55*(1-2), 41-71.

Burchette, T. P., & Wright, V. P. (1992). Carbonate ramp depositional systems. *Sedimentary Geology*, *79*(1–4), 3–57. https://doi.org/10.1016/0037-0738(92)90003-A.

Burg, J. P. (2011). The Asia–Kohistan–India collision: review and discussion. In Brown, D. & Ryan P. D., eds., *Arc-continent collision* (pp. 279-309). Springer, Berlin, Heidelberg.

Burg, J. P., Jagoutz, O., Dawood, H., & Hussain, S. S. (2006). Precollision tilt of crustal blocks in rifted island arcs: structural evidence from the Kohistan Arc. *Tectonics*, *25*(5).

Burnett, J.A. (1998). Upper Cretaceous. In: Bown, P.R. (Ed.), Calcareous Nannofossil Biostratigraphy: *British Micropalaeontology Society Series*. Chapman and Hall, London, pp. 1–15.

Burtman, V. S., & Molnar, P. (1993). Geological and Geophysical Evidence for Deep Subduction of Continental Crust Beneath the Pamir. *Geological Society of America Special Papers*. https://doi.org/10.1130/SPE281

Burtman, V. S. (2000). Cenozoic crustal shortening between the Pamir and Tien Shan and a reconstruction of the Pamir-Tien Shan transition zone for the Cretaceous and Palaeogene. *Tectonophysics*, *319*(2), 69–92. https://doi.org/10.1016/S0040-1951(00)00022-6.

Cao, K., Wang, G. C., Bernet, M., van der Beek, P., & Zhang, K. X. (2015). Exhumation history of the West Kunlun Mountains, northwestern Tibet: Evidence for a long-lived, rejuvenated orogen. *Earth and Planetary Science Letters*, *432*(December 2015), 391–403. https://doi.org/10.1016/j.epsl.2015.10.033.

Cao, W., Xi, D., Melinte-Dobrinescu, M.C., Jiang, T., Wise, S.W.Jr., Wan, X. (2018). Calcareous nannofossil changes linked to climate deterioration during the Paleocene-Eocene thermal maximum in Tarim Basin, NW China. *Geoscience Frontiers*, 1465-1478.

Carannante, G., Esteban, M., Milliman, J. D., & Simone, L. (1988). Carbonate lithofacies as paleolatitude indicators: problems and limitations. *Sedimentary Geology*, *60*(1-4), 333-346.

Carannante, G., Graziano, R., Ruberti, D., & Simone, L., (1997). Upper cretaceous temperatetypeopen shelves from northern (sardinia) and southern (apennines-apulia) Mesozoic tethyan margins. In: James, N.P., Clarke, J.A.D. (Eds.), *Cool-Water Carbonates. vol. 56.* SEPM Special Publication, pp. 309‐325.

Carmichael, M. J., Inglis, G. N., Badger, M. P., Naafs, B. D. A., Behrooz, L., Remmelzwaal, S., ... & Dickson, A. J. (2017). Hydrological and associated biogeochemical consequences of rapid global warming during the Paleocene-Eocene Thermal Maximum. *Global and Planetary Change*, *157*, 114-138.

Carrapa, B., DeCelles, P.G., Wang, X., Clementz, M.T., Mancin, N., Stoica, M., Kraatz, B., Meng, J., Abdulov, S., & Chen, F. (2015). Tectono-climatic implications of Eocene Paratethys regression in the Tajik basin of central Asia. *Earth and Planetary Science Letters*, *424*, 168-178.

Catuneanu, O. (2004). Retroarc foreland systems—evolution through time. *Journal of African Earth Sciences*, *38*(3), 225-242.

Catuneanu, O. (2006). *Principles of Sequence Stratigraphy. Elsevier.* https://doi.org/10.5860/CHOICE.44-4462.

Caves, J. K., Winnick, M. J., Graham, S. A., Sjostrom, D. J., Mulch, A., & Chamberlain, C. P. (2015). Role of the westerlies in Central Asia climate over the Cenozoic. *Earth and Planetary Science Letters*, *428*, 33–43. https://doi.org/10.1016/j.epsl.2015.07.023.

Caves, J. K., Jost, A. B., Lau, K. V., & Maher, K. (2016). Cenozoic carbon cycle imbalances and a variable weathering feedback. *Earth and Planetary Science Letters*, *450*, 152-163.

Chapman, J.B., Robinson, A.C., Carrapa, B., Villarreal, D., Worthington, J., DeCelles, P.G., Kapp, P., Gadoev, M., Oimahmadov, I., & Gehrels, G. (2018a). Cretaceous shortening and exhumation history of the South Pamir terrane. *Lithosphere*, *10*(4), 494-511.

Chapman, J. B., Scoggin, S. H., Kapp, P., Carrapa, B., Ducea, M. N., Worthington, J., … Gadoev, M. (2018b). Mesozoic to Cenozoic magmatic history of the Pamir. *Earth and Planetary Science Letters*, *482*, 181–192. https://doi.org/10.1016/j.epsl.2017.10.041.

Chapman, J.B., Carrapa, B., DeCelles, P.G., Worthington, J., Mancin, N., Cobianchi, M., Stoica, M., Wang, X., Gadoev, M., & Oimahmadov, I. (2019) The Tajik Basin: a composite record of sedimentary basin evolution in response to tectonics in the Pamir. *Basin Research,* https://doi.org/10.1111/bre.12381.

Chen, X., Chen, H., Lin, X., Cheng, X., Yang, R., Ding, W., Gong, J., Wu, L., Zhang, F., Chen, S., & Zhang, Y. (2018). Arcuate Pamir in the Paleogene? Insights from a review of stratigraphy and sedimentology of the basin fills in the foreland of NE Chinese Pamir, western Tarim Basin. *Earth-Science Reviews*, *180*, 1-16.

Chinese Bureau of Stratigraphy. (1981). Stratigraphic tables for Xinjiang Autonomous Region, 496 p

Clark, M. K., Farley, K. A., Zheng, D., Wang, Z., & Duvall, A. R. (2010). Early Cenozoic faulting of the northern Tibetan Plateau margin from apatite (U-Th)/He ages. *Earth and Planetary Science Letters*, *296*(1–2), 78–88. https://doi.org/10.1016/j.epsl.2010.04.051.

Clarke, L. J., & Jenkyns, H. C. (1999). New oxygen isotope evidence for long-term Cretaceous climatic change in the Southern Hemisphere. *Geology*, *27*(8), 699-702.

Cobbold, P.R., Davy, P., Gapais, D., Rossello, E.A., Sadybakasov, E., Thomas, J.C., Biyo, J.T., & De Urreiztieta, M. (1993). Sedimentary basins and crustal thickening. *Sedimentary Geology*, *86*(1-2), 77-89.

Cowgill, E. (2010). Cenozoic right-slip faulting along the eastern margin of the Pamir salient, northwestern China. *Bulletin of the Geological Society of America*, *122*(1–2), 145–161 https://doi.org/10.1130/B26520.1

Cramer, B.S., Toggweiler, J.R., Wright, J.D., Katz, M.E., Miller, K.G. (2009). Ocean overturning since the Late Cretaceous: Inferences from a new foraminiferal isotope compilation. *Paleoceanography*, 24, PA4216, doi:10.1029/2008PA001683

Crouch E.M., Heilmann-Clausen, C., Brinkhuis, H., Morgans, H.E.G., Rogers, K.M., Egger, H., Schmitz, B. (2001). Global dinoflagellate event associated with the late Paleocene thermal maximum. *Geology*, 29, 315-318

Cushman, J.A. (1951). Paleocene foraminifera of the Gulf coastal region of the United States and adjacent areas. U.S. Geol. Surv., Prof. Pap., 232, 75 pp.

Dayem, K. E., Molnar, P., Clark, M. K., & Houseman, G. A. (2009). Far-field lithospheric deformation in Tibet during continental collision. *Tectonics*, *28*(6). https://doi.org/10.1029/2008TC002344.

Dedow, R., Franz, M., Szulc, A., Schneider, J. W., Brückner, J., Ratschbacher, L., ... & Oimahmadov, I. (2020). Tajik Basin and Southwestern Tian Shan, Northwestern India-Asia Collision Zone: 3. Pre-to Syn-orogenic Retro-foreland Basin Evolution in the Eastern Tajik Depression and Linkage to the Pamir Hinterland. *Tectonics*.

Dercourt, J., Gaetani, M., Vrielynck, B., Barrier, E., Biju-Duval, B., Brunet, M. F., … Sandulescu, M. (2000). Peri-Tethys Paleogeographical Atlas.

Dickson, A. J., Rees-Owen, R. L., März, C., Coe, A. L., Cohen, A. S., Pancost, R. D., ... & Shcherbinina, E. (2014). The spread of marine anoxia on the northern Tethys margin during the Paleocene-Eocene Thermal Maximum. *Paleoceanography*, *29*(6), 471-488.

Dickson, A. J., Cohen, A. S., Coe, A. L., Davies, M., Shcherbinina, E. A., & Gavrilov, Y. O. (2015). Evidence for weathering and volcanism during the PETM from Arctic Ocean and Peri-Tethys osmium isotope records. *Palaeogeography, Palaeoclimatology, Palaeoecology*, *438*, 300-307.

Dunkley Jones, T., Lunt, D.J., Schmidt, D.N., Ridgwell, A.J., Sluijs, A., Valdes, P.J., Maslin, M.A. (2013). Climate model and proxy data constraints on ocean warming across the Paleocene–Eocene Thermal Maximum. *Earth-Science Rev.* 125, 123–145. doi:http://dx.doi.org/10.1016/j.earscirev.2013.07.004.

Dunkley Jones, T., Manners, H.R., Hoggett, M., Kirtland Turner, S., Westerhold, T., Leng, M.J., Pancost, R.D., Ridgwell, A., Alegret, L., Duller, R. and Grimes, S.T. (2018). Dynamics of sediment flux to a bathyal continental margin section through the Paleocene–Eocene Thermal Maximum. *Climate of the Past, 14*(7), pp.1035-1049.

Dupont-Nivet, G., Krijgsman, W., Langereis, C. G., Abels, H. A., Dai, S., & Fang, X. (2007). Tibetan plateau aridification linked to global cooling at the Eocene–Oligocene transition. *Nature*, *445*(7128), 635–638. https://doi.org/10.1038/nature05516

Dupont-Nivet, G., Lippert, P.C., van Hinsbergen, J.J.D., Meijers, M., Kapp., P. (2010). Palaeolatitude and age of the Indo-Asia collision: palaeomagnetic constraints. Geophysical Journal International, 182, 1189-1198.

Dupont-Nivet, G., & Krijgsman, W. (2011). Magnetostratigraphic methods and applications. *Tectonics of Sedimentary Basins: Recent Advances*, 80-94.

Dzhalilov, M.R., Alekseev, M.N., Andreev, Y.N., Salibaev, G.K. (1982). Mesozoic and Cenozoic deposits of the northern part of the Afghano-Tajik Basin. In: Stratigraphic Correlation Between Sedimentary Basins of the ESCAP Region, Volume 8. ESCAP Atlas of Stratigraphy 3 – Australia, Bangladesh, Fiji, India, Indonesia, Nepal, Solomon Islands, Tajikistan. Mineral Resources Development Series, 48. United Nations (Economic and Social Commission for Asia and the Pacific), New York, 24-32.

Eldrett, J.S., Harding, I.C., Firth, J.V., Roberts, A.P. (2004). Magnetostratigraphic calibration of Eocene-Oligocene dinoflagellate cyst biostratigraphy from the Norwegian-Greenland Sea. *Marine Geology*, 204, 91-127

Faisal, S., Larson, K. P., Cottle, J. M., & Lamming, J. (2014). Building the Hindu Kush: monazite records of terrane accretion, plutonism and the evolution of the Himalaya–Karakoram–Tibet orogen. *Terra Nova*, *26*(5), 395-401.

Fensome, R.A., Williams, G.L. (2004). The Lentin and Williams Index of Fossil Dinoflagellates 2004 Edition, 909 pp. *Am.Assoc.of Strat. Coll. Station.* Tex.

Fisher, R. A. (1953). Dispersion on a sphere. *Proceedings of the Royal Society of London. Series A. Mathematical and Physical Sciences*, *217*(1130), 295-305.

Flügel, E. (2004). *Microfacies of carbonate rocks: analysis, interpretation and application*. Berlin: Springe.

Fraser, J. E., Searle, M. P., Parrish, R. R., & Noble, S. R. (2001). Chronology of deformation, metamorphism, and magmatism in the southern Karakoram Mountains. *Geological Society of America Bulletin*, *113*(11), 1443-1455.

Friedrich, O., Norris, R. D., & Erbacher, J. (2012). Evolution of middle to Late Cretaceous oceans—a 55 my record of Earth's temperature and carbon cycle. *Geology*, *40*(2), 107-110.

Frieling, J., Iakovleva, A.I., Reichart, G.-J., Aleksandrova, G.N., Gnibidenko, Z.N., Schouten, S., Sluijs, A. (2014). Paleocene-Eocene warming and biotic response in the epicontinental West Siberian Sea. *Geology* 42, 767–770.

Frieling, J., Gebhardt, H., Huber, M., Adekeye, O.A., Akande, S.O., Reichart, G.-J., Middelburg, J.J., Schouten, S., Sluijs, A. (2017). Extreme warmth and heat-stressed plankton in the tropics during the Paleocene-Eocene Thermal Maximum. *Sci. Adv.* 3, e1600891. doi:10.1126/sciadv.1600891

Frieling, J., & Sluijs, A. (2018). Towards quantitative environmental reconstructions from ancient non-analogue microfossil assemblages: Ecological preferences of Paleocene–Eocene dinoflagellates. *Earth-Science Reviews*, *185*, 956-973.

Frieling, J., Reichart, G. J., Middelburg, J. J., Röhl, U., Westerhold, T., Bohaty, S. M., & Sluijs, A. (2018). Tropical Atlantic climate and ecosystem regime shifts during the Paleocene–Eocene Thermal Maximum. *Climate of the Past*, *14*(1), 39-55.

Fornaciari, E., Agnini, C., Catanzariti, R., Rio, D., Bolla, E.M., Valvasoni, E. (2010). Mid-latitude calcareous nannofossil biostratigraphy, biochronology and evolution across the middle to late Eocene transition. *Stratigraphy* 7, 229-264.

Gao, Y., Ibarra, D. E., Wang, C., Caves, J. K., Chamberlain, C. P., Graham, S. A., & Wu, H. (2015). Mid-latitude terrestrial climate of East Asia linked to global climate in the Late Cretaceous. *Geology*, *43*(4), 287-290.

Gao, Z., Chen, K., & Wei, J. (2000). The Lithostratigraphic Dictionary of China. *The Press of Geological University, Beijing*, *627*.

Gavrilov, Y. O., Kodina, L. A., Lubchenko, I. Y., & Muzylev, N. G. (1997). The late Paleocene anoxic event in epicontinental seas of Peri-Tethys and formation of the sapropelite unit: Sedimentology and geochemistry. *Lithology and mineral resources c/c of litologiia i poleznye iskopaemye*, *32*, 427-450.

Gavrilov, Y.O., Shcherbinina, E.A., Oberhänsli, H. (2003). Paleocene/Eocene Boundary Events in the Northeastern Peri-Tethys. In: Wing, S.L., Gingerich, F.D., Schmitz, B., Thomas, E. (Eds.), Causes and Consequences of Globally Warm Climates in the Early Paleogene. Boulder, Colorado, *Geological Society of America Special Paper vol.* 369, pp. 147–168.

Gavrilov, Y.O., Shcherbinina, E.A., Golovanova, O., & Pokrovsky, B. (2009). A variety of PETM records in different settings, northeastern Peri-Tethys. In *Climatic and Biotic Events of the Paleogene [CBEP 2009], Extended Abstracts From an International Conference in Wellington, New Zealand, GNS Science Miscellaneous Series* (Vol. 18, pp. 67-70).

Gavrilov, Y.O., Shcherbinina, E.A., Aleksandrova, G.N. (2019). Mesozoic and Early Cenozoic Paleoecological events in the sedimentary record of the NE Peri-Tethys and adjacent areas: an overview. *Lithology and Mineral Resources*, 54(6), 524-543.

Gradstein, F. M., Ogg, J. G., Schmitz, M., & Ogg, G. (Eds.). (2012). *The geologic time scale 2012*. elsevier.

Graham, S. A., Chamberlain, C. P., Yue, Y., Ritts, B. D., Hanson, A. D., Horton, T. W., … Feng, X. (2005). Stable isotope records of cenozoic climate and topography, Tibetan plateau and Tarim basin. *American Journal of Science*, *305*(2), 101–118. https://doi.org/10.2475/ajs.305.2.101.

Guasti, E., Speijer, R.P. (2008). *Acarinina multicamerata* n. sp. (Foraminifera): a new marker for the Paleocene-Eocene thermal maximum. *Journal of Micropalaeontology*, 27, 5-12

Guilmette, C., Hébert, R., Dostal, J., Indares, A., Ullrich, T., Bédard, É., & Wang, C. (2012). Discovery of a dismembered metamorphic sole in the Saga ophiolitic mélange, South Tibet: Assessing an Early Cretaceous disruption of the Neo-Tethyan supra-subduction zone and consequences on basin closing. *Gondwana Research*, *22*(2), 398-414.

Gulliford, A. R., Flint, S. S., & Hodgson, D. M. (2017). Crevasse splay processes and deposits in an ancient distributive fluvial system: The lower Beaufort Group, South Africa. *Sedimentary Geology*, *358*, 1–18. https://doi.org/10.1016/j.sedgeo.2017.06.005.

Guo, R., Li, S., Yu, S., Dai, L., Liu, Y., Peng, Y., Zhou, Z., Wang, Y., Liu, Y., & Wang, Q. (2019). Collisional processes between the Qiangtang Block and the Lhasa Block: Insights from structural analysis of the Bangong–Nujiang Suture Zone, central Tibet. *Geological Journal*, *54*(2), 946-960.

Guo, F., Yang, D., Eriksson, K. A., & Guo, L. (2015). Paleoenvironments, stratigraphic evolution and reservoir characteristics of the Upper Cretaceous Yingjisha Group, southwest Tarim Basin. *Marine and Petroleum Geology*, *67*, 336–355. https://doi.org/10.1016/j.marpetgeo.2015.05.023

Guo, X. (1991). The depositional environment of the Cretaceous Kizilsu Group in Xinjiang - with a discussion of the lowermost marine horizon of the Cretaceous in the western Tarim Basin. *Acta Geologica Sinica 4*, 441-453.

Guo, X. (1990). Study on marine Cretaceous-Tertiary boundary in the western Tarim Basin. *J. China Univ. Geosci.*, 15, 325-335

Guo, Z.T., Sun, B., Zhang, Z.S., Peng, S.Z., Xiao, G.Q., Ge, J.Y., Hao, Q.Z., Qiao, Y.S., Liang, M.Y., Liu, J.F., Yin, Q.Z., Wei, J.J. (2008). A major reorganization of Asian climate by the early Miocene. *Clim. Past.*, 4, 153-174.

Gutjahr, M., Ridgwell, A., Sexton, P. F., Anagnostou, E., Pearson, P. N., Pälike, H., ... & Foster, G. L. (2017). Very large release of mostly volcanic carbon during the Palaeocene–Eocene Thermal Maximum. *Nature*, *548*(7669), 573.

Halfar, J., Godinez-Orta, L., Mutti, M., Valdez-Holguín, J. E., & Borges, J. M. (2004). Nutrient and temperature controls on modern carbonate production: an example from the Gulf of California, Mexico. *Geology*, *32*(3), 213-216.

Hallock, P., & Schlager, W. (1986). Nutrient excess and the demise of coral reefs and carbonate platforms. *Palaios*, 389-398.

Hamburger, M. W., Sarewitz, D. R., Pavlis, T. L., & Popandopulo, G. A. (1992). Structural and seismic evidence for intracontinental subduction in the Peter the First Range, central Asia. *Geological Society of America Bulletin*, *104*(4), 397-408.

Handford, C.R. (1986). Facies and bedding sequences in shelf-storm-deposited carbonates – Fayetteville shale and Pikin limestone (Mississippian), Arkansas. *Journal of Sedimentary Petrology*, 56 (1), 123-137.

Hao, Y. C., Guo, X. P., Ye, L. S., Yao, P. Y., Fu, D. R., Li, H. M., & Ruan, P. H. (2001). *The boundary between the marine Cretaceous and Tertiary in the southwest Tarim Basin*. Bejing: Geological Publishing House.

Hao, Y., & Guo, X. (1990). Cretaceous ‐ Paleocene foraminiferal communities from the western Tarim basin and their environmental significance. *Journal of China University of Geosciences*, *1*, 34‐42.

Hao, Y., Zeng, X., & Guo, X. (1988). The marine Cretaceous in the western part of the Tarim Basin of Xinjiang and its depositional environments [J]. *Acta Geologica Sinica*, *1*.

Hao, Y., & Zeng, X. (1984). On the evolution of the west Tarim gulf from Mesozoic to Cenozoic in terms of characteristics of foraminiferal fauna. *Acta Micropalaeotologica Sinica*, 1, 1-18.

Hao Y., Zeng X., & Li H. (1982). Late Cretaceous and Tertiary strata and foraminifera in western Tarim Basin. Earth Science. "*Papers on Paleontology I*", No.2 (vol.17), pp 1-161 (in Chinese).

Harms, J.C., Southard, J.B., & Walker, R.G., (1982), Structures and Sequences in Clastic Rocks, *Soc. Econ. Paleontologists and Mineralogists Short Course No. 9*, Tulsa, Oklahoma.

Haq, B.U., Hardenbol, J., Vail. P.R. (1987). Chronology of fluctuating sea levels since the Triassic (250 million years ago to present). *Science*, 235, 1156-1167.

Haq, B. U. (2014). Cretaceous eustasy revisited. *Global and Planetary change*, *113*, 44-58.

Hayton, S., Nelson, C. S., & Hood, S. D. (1995). A skeletal assemblage classification system for non-tropical carbonate deposits based on New Zealand Cenozoic limestones. *Sedimentary geology*, *100* (1-4), 123-141.

He, J., Kapp, P., Chapman, J. B., DeCelles, P. G., & Carrapa, B. (2019). Structural setting and detrital zircon U–Pb geochronology of Triassic–Cenozoic strata in the eastern Central Pamir, Tajikistan. *Geological Society, London, Special Publications*, *483*(1), 605-630.

He, C. (1991). Late Cretaceous-Early Tertiary Microphytoplankton from the Western Tarim Basin in southern Xinjiang, China. *Najing Institute of Geology and Palaeontology, Academia Sinica*, *235*.

Hefu, L. (1986). Geodynamic scenario and structural styles of Mesozoic and Cenozoic basins in China. *AAPG Bulletin*, *70*(4), 377-395.

Hendrix, M. S., Graham, S. A., Carroll, A. R., Sobel, E. R., McKnight, C. L., Schulein, B. J., & Wang, Z. (1992). Sedimentary record and climatic implications of recurrent deformation in the Tian Shan: Evidence from Mesozoic strata of the north Tarim, south Junggar, and Turpan basins, northwest China. *Geological Society of America Bulletin*, *104*(1), 53-79.

Hollis, C. J., Hines, B. R., Littler, K., Villasante-Marcos, V., Kulhanek, D. K., Strong, C. P., Zachos, J. C., Eggins, S. M., Northcote, L., Phillips, A. (2015). The Paleocene-Eocene Thermal Maximum at DSDP Site 277, Campbell Plateau, southern Pacific Ocean. *Clim. Past*, 11, 1009-1025.

Hoorn, C., Straathof, J., Abels, H. A., Xu, Y., Utescher, T., & Dupont-Nivet, G. (2012). A late Eocene palynological record of climate change and Tibetan Plateau uplift (Xining Basin, China). *Palaeogeography, Palaeoclimatology, Palaeoecology*, *344–345*, 16–38. https://doi.org/10.1016/j.palaeo.2012.05.011.

Hopkinson, C. S., Cai, W. J., & Hu, X. (2012). Carbon sequestration in wetland dominated coastal systems—a global sink of rapidly diminishing magnitude. *Current Opinion in Environmental Sustainability*, *4*(2), 186-194.

Hu, X., Garzanti, E., Wang, J., Huang, W., An, W., & Webb, A. (2016). The timing of India-Asia collision onset – Facts, theories, controversies. *Earth-Science Reviews*, *160*(July 2016), 264–299. https://doi.org/10.1016/j.earscirev.2016.07.014

Hudson, J. D. (1977). Stable isotopes and limestone lithification. *Zl Geol. Soc. Lond.*, *133*, 637–660.

Iakovleva, A.I., Heilmann-Clausen, C., 2007. *Wilsonidium pechoricum* new species—A new dinoflagellate species with unusual asymmetry from the Paleocene/Eocene transition. *J. Inf.* 81, 1020-1030

Iakovleva, A.I., Heilmann-Clausen, C., 2010. Eocene dinoflagellate cyst biostratigraphy of research borehole 011-BP, Omsk Region, southwestern Siberia. *Palynology* 34, 37–41. doi:10.1080/01916121003629974.

Imrecke, D.B., Robinson, A.C., Owen, L.A., Chen, J., Schoenbohm, L.M., Hedrick, K.A., Lapen, T.J., Li, W., & Yuan, Z. (2019). Mesozoic evolution of the eastern Pamir. *Lithosphere*, *11*(4), 560-580.

Irwin, M. L. (1965). General theory of epeiric clear water sedimentation. *Aapg Bulletin*, *49*(4), 445-459.

James, N.P. (1997). The cool-water carbonate depositional realm. In: James, N.P., Clarke, J.A.D. (Eds.), Cool-water Carbonates 56. SEPM Special Publication, Tulsa, pp. 1–22.

Jagoutz, O., Müntener, O., Ulmer, P., Pettke, T., Burg, J. P., Dawood, H., & Hussain, S. (2007). Petrology and mineral chemistry of lower crustal intrusions: the Chilas Complex, Kohistan (NW Pakistan). *Journal of Petrology*, *48*(10), 1895-1953.

Jaramillo-Vogel, D., Bover-Arnal, T., & Strasser, A. (2016). Bryozoan beds in northern Italy as a shallow-water expression of environmental changes during the Oligocene isotope event 1. *Sedimentary geology*, *331*, 148-161.

Jaramillo-Vogel, D., Strasser, A., Frijia, G., & Spezzaferri, S. (2013). Neritic isotope and sedimentary records of the Eocene–Oligocene greenhouse–icehouse transition: The Calcare di Nago Formation (northern Italy) in a global context. *Palaeogeography, Palaeoclimatology, Palaeoecology*, *369*, 361-376.

Jenkyns, H. C. (2010). Geochemistry of oceanic anoxic events. *Geochemistry, Geophysics, Geosystems*, *11*(3).

Ji, J., Zhang, K., Clift, P.D., Zhuang, G., Song, B., Ke, X., Xu, Y. (2017). High-resolution magnetostratigraphic study of the Paleogene-Neogene strata in the Northern Qaidam Basin: Implications for the growth of the Northeastern Tibetan Plateau. *Gondwana Research*, 46, 141-155

Jia, C.Z., Zhang, S.B., Wu, S.Z. *et al*. (2004). Stratigraphy of the Tarim Basin and Adjacent Areas, Science Press, Beijing, 427 p (In Chinese with English abstract).

Jiang, S., Wise Jr., S.W. (2006). Surface-water chemistry and fertility variations in the tropical Atlantic across the Paleocene/Eocene Thermal Maximum as evidenced by calcareous nannoplankton from ODP Leg 207, Hole 1259B. *Revue de Micropaleontologie* 49, 227–244.

Jin, C., Liu, Q., Liang, W., Roberts, A. P., Sun, J., Hu, P., … Yuan, S. (2018). Magnetostratigraphy of the Fenghuoshan Group in the Hoh Xil Basin and its tectonic implications for India–Eurasia collision and Tibetan Plateau deformation. *Earth and Planetary Science Letters*, *486*, 41–53. https://doi.org/10.1016/j.epsl.2018.01.010.

Joachimski, M. M., & Buggisch, W. (1993). Anoxic events in the late Frasnian—Causes of the Frasnian-Famennian faunal crisis?. *Geology*, *21*(8), 675-678.

John, C. M., Bohaty, S. M., Zachos, J. C., Sluijs, A., Gibbs, S., Brinkhuis, H., & Bralower, T. J. (2008). North American continental margin records of the Paleocene-Eocene thermal maximum: Implications for global carbon and hydrological cycling. *Paleoceanography*, *23*(2).

Jolivet, M. (2017). Mesozoic tectonic and topographic evolution of Central Asia and Tibet: a preliminary synthesis. *Geological Society, London, Special Publications*, *427*(1), 19-55.

Jolivet, M., Brunel, M., Seward, D., Xu, Z., Yang, J., Roger, F., … Wu, C. (2001). Mesozoic and Cenozoic tectonics of the northern edge of the Tibetan plateau: Fission-track constraints. *Tectonophysics*, *343*(1–2), 111–134. https://doi.org/10.1016/S0040-1951(01)00196-2

Jolivet, M., Heilbronn, G., Robin, C., Barrier, L., Bourquin, S., Guo, Z., … Fu, B. (2013). Reconstructing the Late Palaeozoic - Mesozoic topographic evolution of the Chinese

Tian Shan: Available data and remaining uncertainties. *Advances in Geosciences*, *37*, 7–18. https://doi.org/10.5194/adgeo-37-7-2013.

Junium, C.K., Dickson, A.J. and Uveges, B.T. (2018). Perturbation to the nitrogen cycle during rapid Early Eocene global warming. *Nature communications, 9*(1), pp.1-8.

Kahn, A., Aubry, M.-P., 2004. Provincialism associated with the Paleocene/Eocene thermal maximum: temporal constraint. *Marine Micropaleontology* 52, 117–131. doi:10. 1016/j.marmicro.2004.04.003.

Kapp, P., & DeCelles, P. (2019). Mesozoic-Cenozoic geological evolution of the Himalayan-Tibetan orogeny and working tectonic hypotheses. *American Journal of Science*, 319, 159-254.

Kapp, P., Murphy, M. A., Yin, A., Harrison, T. M., Ding, L., & Guo, J. (2003). Mesozoic and Cenozoic tectonic evolution of the Shiquanhe area of western Tibet. *Tectonics*, *22*(4).

Kapp, P., DeCelles, P. G., Gehrels, G. E., Heizler, M., & Ding, L. (2007). Geological records of the Lhasa-Qiangtang and Indo-Asian collisions in the Nima area of central Tibet. *Geological Society of America Bulletin*, *119*(7-8), 917-933.

Kaya, M. Y., Dupont-Nivet, G., Proust, J. N., Roperch, P., Bougeois, L., Meijer, N., Frieling, J., Fioroni, C., Altıner, S. A., Vardar, E., Barbolini, N., Stoica, M., Aminov, J., Mamtimin, M., & Guo, Z. (2019). Paleogene evolution and demise of the proto-Paratethys Sea in Central Asia (Tarim and Tajik basins): Role of intensified tectonic activity at ca. 41 Ma. *Basin Research, 31*(3), 461-486.

Keil, R. (2017). Anthropogenic forcing of carbonate and organic carbon preservation in marine sediments. *Annual review of marine science*, *9*, 151-172.

Kent-Corson, M. L., Ritts, B. D., Zhuang, G., Bovet, P. M., Graham, S. A., & Page Chamberlain, C. (2009). Stable isotopic constraints on the tectonic, topographic, and climatic evolution of the northern margin of the Tibetan Plateau. *Earth and Planetary Science Letters*, *282*(1–4), 158–166. https://doi.org/10.1016/j.epsl.2009.03.011.

Khan, S. D., Walker, D. J., Hall, S. A., Burke, K. C., Shah, M. T., & Stockli, L. (2009). Did the Kohistan-Ladakh island arc collide first with India?. *Geological Society of America Bulletin*, *121*(3-4), 366-384.

Kindler, P., & Wilson, M. E. (2010). Carbonate grain associations: their use and environmental significance, a brief review. *Carbonate systems during the Oligocene-Miocene climate transition. International Association of Sedimentologists Special Publications Wiley-Blackwell, Chichester (West Sussex)*, 35-48.

Kirschvink, J. L. (1980). The least-square line and plane and the analysis of paleomagnetic data. *Geophysical Journal of the Royal Astronomical Society*, *62*, 699–718.

Klocke, M., Voigt, T., Kley, J., Pfeifer, S., Rocktäschel, T., Keil, S., & Gaupp, R. (2017). Cenozoic evolution of the Pamir and Tien Shan mountains reflected in syntectonic deposits of the Tajik Basin. *Geological Society, London, Special Publications*, *427*(1), 523-564.

Koch, P. L., Zachos, J. C., & Gingerich, P. D. (1992). Correlation between isotope records in marine and continental carbon reservoirs near the Palaeocene/Eocene boundary. *Nature*, *358*(6384), 319.

Komar, N., & Zeebe, R. E. (2017). Redox-controlled carbon and phosphorus burial: A mechanism for enhanced organic carbon sequestration during the PETM. *Earth and Planetary Science Letters*, *479*, 71-82.

Kominz, M. A., Browning, J. V, Miller, K. G., Sugarman, P. J., & Mizintseva, S. (2008). Late Cretaceous to Miocene sea-level estimates from the New Jersey and Delaware coastal plain coreholes : an error analysis, *Basin Research,* 20, 211–226. https://doi.org/10.1111/j.1365-2117.2008.00354.x

Kontorovich, A.E., Ershov, S.V., Kazanenkov, V.A., Karogodin, Y.N., Kontorovich, V.A., Lebedeva, N.K., Nikitenko, B.L., Popova, N.I., & Shurygin, B.N. (2014). Cretaceous paleogeography of the West Siberian sedimentary basin. *Russian Geology and Geophysics*, *55*(5-6), 582-609.

Köthe, A. (2012). A revised Cenozoic dionflagellate cyst and calcareous nannoplankton zonation for the German sector of the southeastern North Sea Basin. *Newsletters on Stratigraphy*, 45, 189-220

Kufner, S.K., Schurr, B., Sippl, C., Yuan, X., Ratschbacher, L., Ischuk, A., Murodkulov, S., Schneider, F., Mechie, J., & Tilmann, F. (2016). Deep India meets deep Asia: Lithospheric indentation, delamination and break-off under Pamir and Hindu Kush (Central Asia). *Earth and Planetary Science Letters*, *435*, 171-184.

Kutzbach, J.E., Prell, W.L., Ruddiman, W.F. (1993). Sensitivity of Eurasian climate to surface uplift of the Tibetan Palteau. *The Journal of Geology*, 101, 177-190.

Lan, X., & Wei, J. (1995). Late Cretaceous–early Tertiary marine bivalve fauna from the western Tarim Basin. *Chinese Science House, Beijing*, 212.

Lebedeva, N. K. (2006). Dinocyst biostratigraphy of the Upper Cretaceous of northern Siberia. *Paleontological Journal*, *40*(5), S604-S621.

Lebedeva, N.K., Aleksandrova, G.N., Shurygin, B.N., Ovechkina, M.N., & Gnibidenko, Z.N. (2013). Paleontological and magnetostratigraphic data on Upper Cretaceous deposits from borehole no. 8 (Russkaya Polyana District, Southwestern Siberia). *Stratigr. Geol. Correl*. 21, 48–78. doi:10.1134/S086959381301005X.

Lee, K. Y. (1985). Geology of the Tarim Basin with special emphasis on petroleum deposits, Xinjiang Uygur Zizhiqu, Northwest Chin. *US Geological Survey Open-File report (No. 85-616).*

Lee, E. Y., Novotny, J., & Wagreich, M. (2016). BasinVis 1.0: A MATLAB®-based program for sedimentary basin subsidence analysis and visualization. *Computers and Geosciences*, *91*(May), 119–127. https://doi.org/10.1016/j.cageo.2016.03.013.

Lees, A., & Buller, A. T. (1972). Modern temperate-water and warm-water shelf carbonate sediments contrasted. *Marine Geology*, *13*(5), M67-M73.

Lees J.A., Bown, P.R., & Young, J.R. (2006). Photic zone palaeoenvironments of the Kimmeridge Clay Formation (Upper Jurassic, UK) suggested by calcareous nannoplankton palaeoecology. *Palaeogeogr., Palaeoclimatol., Palaeoecol.*, 235, 110-134.

LeRoy, LW., 1953. Biostratigraphy of the Maqfi section, Egypt. *GSA, Mem.*, 54: 73 pp

Leith, W. (1985). A mid-Mesozoic extension across Central Asia?. *Nature*, *313*(6003), 567.

Li, Y. (1990). An Apparent Polar Wander Path from the Tarim Block, China. *Tectonophysics*, *181*, 31–41. https://doi.org/10.1111/j.1755-6724.1990.mp3001001.x

Li, J., Wen, X., & Huang, C. (2018). Lower and upper Cretaceous paleosols in the western Sichuan Basin, China: Implications for regional paleoclimate. *Geological Journal*. 1-19. https://doi.org/10.1002/gj.3423

Li, L., & Keller, G. (1998). Abrupt deep-sea warming at the end of the Cretaceous. *Geology*, *26*(11), 995-998.

Li, X., Zhang, R., Zhang, Z., Yan, Q. (2018). What enhanced the aridity in Eocene Asian inland: Gglobal cooling or early Tibetan Plateau uplift?. *Palaeogeography, Palaeoclimatology, Palaeoecology (510),* 6-14. https://doi.org/10.1016/j.palaeo.2017.10.029.

Li, Q., Li, L., Zhang, Y., & Guo, Z. (2020). Oligocene incursion of the paratethys seawater to the Junggar Basin, NW china: insight from multiple isotopic analysis of carbonate. *Scientific reports*, *10*(1), 1-7.

Licht, A., Dupont-Nivet, G., Pullen, A., Kapp, P., Abels, H. A., Lai, Z., … Giesler, D. (2016). Resilience of the Asian atmospheric circulation shown by Paleogene dust provenance. *Nature Communications*, *7*(August), 12390. https://doi.org/10.1038/ncomms12390

Licht, A., van Cappelle, M., Abels, H. A., Ladant, J. B., Trabucho-Alexandre, J., France-Lanord, C., … Jaeger, J. J. (2014). Asian monsoons in a late Eocene greenhouse world. *Nature*, *513*(7519), 501–506. https://doi.org/10.1038/nature13704\rhttp://www.nature.com/nature/journal/v513/n7519/abs/nature13704.html#supplementary-information

Linnert, C., Robinson, S.A., Lees, J.A., Bown, P.R., Pérez-Rodríguez, I., Petrizzo, M.R., Falzoni, F., Littler, K., Arz, J.A., & Russell, E.E. (2014). Evidence for global cooling in the Late Cretaceous. *Nature Communications*, *5*, 4194.

Loeblich, A.R. Jr., & Tappan, H. (1988). Foraminiferal genera and their classification, von Nostrand Reinhold Company, New York, 2 volumes, 970 p.

Long, X., Wilde, S. A., Wang, Q., Yuan, C., Wang, X. C., Li, J., … Dan, W. (2015). Partial melting of thickened continental crust in central Tibet: Evidence from geochemistry and geochronology of Eocene adakitic rhyolites in the northern Qiangtang Terrane. *Earth and Planetary Science Letters*, *414*, 30–44. https://doi.org/10.1016/j.epsl.2015.01.007.

Lu, H., Wang, X., Li, L. (2010). Aeolian sediment evidence that global cooling has driven late Cenozoic stepwise aridification in central Asia. *Geological Society London Special Publications*, 342, 29-44.

Luo, Y., Boudreau, B. P., Dickens, G. R., Sluijs, A., & Middelburg, J. J. (2016). An alternative model for CaCO3 over-shooting during the PETM: biological carbonate compensation. *Earth and Planetary Science Letters*, *453*, 223-233.

Lukasik, J. J., James, N. P., McGowran, B., & Bone, Y. (2000). An epeiric ramp: low-energy, cool-water carbonate facies in a Tertiary inland sea, Murray Basin, South Australia. *Sedimentology*, *47*(4), 851-881.

Ma, A., Hu, X., Garzanti, E., Han, Z., & Lai, W. (2017). Sedimentary and tectonic evolution of the southern Qiangtang basin: Implications for the Lhasa-Qiangtang collision timing. *Journal of Geophysical Research: Solid Earth*, *122*(7), 4790-4813.

Ma, M., Liu, X., & Wang, W. (2018). Palaeoclimate evolution across the Cretaceous–Palaeogene boundary in the Nanxiong Basin (SE China) recorded by red strata and its correlation with marine records. *Climate of the Past*, *14*(3), 287-302.

Manabe, S., Broccoli, A.J. (1990). Mountains and arid climates of Middle latitudes. *Science*, 247, 192-195.

Mao, S., & Norris, G. (1988). *Late Cretaceous-early Tertiary dinoflagellates and acritarchs from the Kashi area, Tarim Basin, Xinjiang Province, China*. Toronto ON: Royal Ontario Museum Life Sciences Publications.

Marc S. Hendrix, Stephan A. Graham, Alan R. Carroll, Edward R. Sobel, Cleavy L. McKnight, Benjamin J. Schulein, Z. W. (1992). Sedimentary record and climatic implications of recurrent deformation in the Tian Shan: Evidence from Mesozoic strata of the north Tarim, south Junggar, and Turpan basins. *Geological Society of America Bulletin*, *104*, 53–79

Martini, E., 1971. Standard Tertiary and Quaternary calcareous nannoplankton zonation. In: Farinacci, A. (Eds.), *Proceedings 2nd International Conference Planktonic Microfossils* Roma, 2, 739-785.

McFadden, P. L., & McElhinny, M. W. (1988). The combined analysis of remagnetization circles and direct observations in palaeomagnetism. *Earth and Planetary Science Letters*, *87*(1–2), 161–172. https://doi.org/10.1016/0012-821X(88)90072-6.

McInerney, F. A., & Wing, S. L. (2011). The Paleocene-Eocene Thermal Maximum: A perturbation of carbon cycle, climate, and biosphere with implications for the future. *Annual Review of Earth and Planetary Sciences*, *39*, 489-516.

Meijer, N., Dupont-Nivet, G., Abels, H., Kaya, Mustafa Y.K., Licht, A., Xiao, M., Zhang, Y., Roperch, P., Poujol, M., Zhongping, L., Guo, Z. (2019). Central Asian moisture modulated by proto-Paratethys Sea incursions since the early Eocene. Manuscript submitted for publication to *Earth Palnet. Sci. Lett. (510),* 73-44.

Meijer, N., Dupont-Nivet, G., Barbolini, N., Woutersen, A., Rohrmann, A., Zhang, Y., Liu, X.-J., Licht, A., Abels., H.A., Hoorn, C., Tjallingii, R., Andermann, C., Dietze, M., Nowaczyk, N. (2020a). Asian dust appearance at 40 Ma. *Global and Planetary Change* (submitted).

Meijer, N., Dupont-Nivet, G., Licht, A., Abels, H.A., Roperch, P., Nowaczyk, N., Meyer, H., Liu, X.-J., Woutersen, A., Rohrmann, A. (2020b). Hydroclimatic shifts during the Early Eocene Climatic Optimum (EECO) recorded in the Xining Basin, NE Tibet. (in preparation).

Michel, J., Borgomano, J., & Reijmer, J. J. (2018). Heterozoan carbonates: When, where and why? A synthesis on parameters controlling carbonate production and occurrences. *Earth-science reviews*.

Miller, K. G., Barrera, E., Olsson, R. K., Sugarman, P. J., & Savin, S. M. (1999). Does ice drive early Maastrichtian eustasy?. *Geology*, *27*(9), 783-786.

Miller, K. G., Wright, J. D., & Browning, J. V. (2005). Visions of ice sheets in a greenhouse world. *Marine Geology*, *217*(3-4), 215-231.

Moissette, P. (2000). Changes in bryozoan assemblages and bathymetric variations. Examples from the Messinian of northwest Algeria. *Palaeogeography, Palaeoclimatology, Palaeoecology*, *155*(3-4), 305-326.

Monechi, S., Angori, E., Speijer, R. (2000). Upper Paleocene biostratigraphy in the Mediterranean region: zonal markers, diachronism, and preservational problems. *GFF 122*, 108–110.

Montenat, C. (2009). The Mesozoic of Afghanistan. *GeoArabia*, *14*(1), 147-210.

Mount, J. (1985). Mixed siliciclastic and carbonate sediment: a propose First ordeder textural and compositional classificatión. *Sedimrntology*, *32*, 432–435. https://doi.org/10.1111/j.1365-3091.1985.tb00522.x

Mudge, D.C., Bujak, J.P. (1996). Palaeocene biostratigraphy and sequence stratigraphy of the UK central North Sea. *Mar. Pet. Geol.* 13, 295–312. doi:10.1016/0264-8172(95)00066-6.

Murray, J. W. (2006). *Ecology and applications of benthic foraminifera*. Cambridge University Press.

Naidin, D.P., Sasonova, I.G., Pojarkova, Z.N., Djalilov, M.R., Papulov, G.N., Senkovsky, Y., Benjamovsky, V.N., & Kopaevich, L.F. (1980). Cretaceous transgressions and regressions on the Russian Platform, in Crimea and Central Asia. *Cretaceous Research*, *1*(4), 375-387.

Negredo, A. M., Replumaz, A., Villaseñor, A., & Guillot, S. (2007). Modeling the evolution of continental subduction processes in the Pamir-Hindu Kush region. *Earth and Planetary Science Letters*, *259*(1–2), 212–225. https://doi.org/10.1016/j.epsl.2007.04.043

Nelson, C. S. (1988). An introductory perspective on non-tropical shelf carbonates. *Sedimentary geology*, *60*(1-4), 3-12.

Nelson, C. S., & Smith, A. M. (1996). Stable oxygen and carbon isotope compositional fields for skeletal and diagenetic components in New Zealand Cenozoic nontropical carbonate sediments and limestones: A synthesis and review. *New Zealand Journal of Geology and Geophysics*, *39*(September 1995), 93–107. https://doi.org/10.1080/00288306.1996.9514697.

Nikolaev, V. G. (2002). Afghan-Tajik depression: Architecture of sedimentary cover and evolution. *Russian Journal of Earth Sciences*, *4*(6).

Ogg, J. G., Ogg, G. M., Gradstein, F. M. (2016). A concise geological time scale. Elsevier. 240pp

Okada, H., Bukry, D., 1980. Supplementary modification and introduction of code numbers to the low latitude coccolith biostratigraphic zonation. *Mar.Micropal.* 5, 321-325. doi:10.1016/0377-8398(80)90016-X

Olsson, R.K., Hemleben, C., Berggren, W.A. and Huber, B.T. (eds.) (1999) Atlas of Paleocene Planktonic Foraminifera, *Smithsonian Contributions to Paleobiology* 85, 1-252.

Opreanu, G. (2003). Porosity density and other physical properties of deep-sea sediments from the Black Sea. *GEO-ECO-MARINA* 9-10/2003-2004.

Ostrander, C. M., Owens, J. D., & Nielsen, S. G. (2017). Constraining the rate of oceanic deoxygenation leading up to a Cretaceous Oceanic Anoxic Event (OAE-2:~ 94 Ma). *Science advances, 3*(8), e1701020.

Otto, S. C. (1997). Mesozoic-Cenozoic history of deformation and petroleum systems in sedimentary basins of Central Asia; implications of collisions on the Eurasian margin. *Petroleum Geoscience*, *3*(4), 327-341.

Ou, Q., Wang, Q., Wyman, D. A., Zhang, H. X., Yang, J. H., Zeng, J. P., … Qi, Y. (2017). Eocene adakitic porphyries in the central-northern Qiangtang Block, central Tibet: Partial melting of thickened lower crust and implications for initial surface uplifting of the plateau. *Journal of Geophysical Research: Solid Earth*, *122*(2), 1025–1053. https://doi.org/10.1002/2016JB013259.

Owens, J. D., Lyons, T. W., & Lowery, C. M. (2018). Quantifying the missing sink for global organic carbon burial during a Cretaceous oceanic anoxic event. *Earth and Planetary Science Letters, 499*, 83-94.

Özcan, E. (2007). Morphometric analysis of the genus Omphalocyclus from the Late Cretaceous of Turkey: new data on its stratigraphic distribution in Mediterranean Tethys and description of two new taxa. *Cretaceous Research*, *28*(4), 621-641.

Pagani, M., Pedentchouk, N., Huber, M., Sluijs, A., Schouten, S., Brinkhuis, H., ... & Cronin, T. (2006). Arctic hydrology during global warming at the Palaeocene/Eocene thermal maximum. *Nature*, *442*(7103), 671.

Pan, H. (1991). Marine Late Cretaceous –Early Tertiary Gastropod fossils from Western Tarim Basin. Science Press, Beijing, 1-100.

Pearce, M.A., Jarvis, I., & Tocher, B.A. (2009). The Cenomanian–Turonian boundary event, OAE2 and palaeoenvironmental change in epicontinental seas: New insights from the dinocyst and geochemical records. *Palaeogeogr. Palaeoclimatol. Palaeoecol*. 280, 207–234. doi:10.1016/j.palaeo.2009.06.012.

Pearson, P.N., Olsson, R.K., Huber, B.t., Hemleben, C., and Berggren, W.A. (eds.) (2006). The Atlas of Eocene Planktonic Foraminifera, *Cushman Foundation Special Publication* 41, 514 pp.

Penman, D. E. (2016). Silicate weathering and North Atlantic silica burial during the Paleocene-Eocene thermal maximum. *Geology*, *44*(9), 731-734.

Penman, D. E., Hönisch, B., Zeebe, R. E., Thomas, E., & Zachos, J. C. (2014). Rapid and sustained surface ocean acidification during the Paleocene-Eocene Thermal Maximum. *Paleoceanography*, *29*(5), 357-369.

Perch-Nielsen, K. (1985). Mesozoic Calcareous Nannofossils. In: Bolli, H.M., Saunders, J.B., Perrch-Nielsen, K. (Eds.), *Plankton Straitigraphy*, Cambridge University Press, 329-426.

Perch-Nielsen, K. (1985). Cenozoic calcareous nannofossils. In: Bolli, H. M., Saunders, J. B. Perch-Nielsen, K. (Eds.), *Plankton Stratigraphy*, Cambridge University Press, Cambridge, 427-554.

Peyrot, D. (2011). Late Cretaceous (Late Cenomanian–Early Turonian) dinoflagellate cysts from the Castilian Platform, northern Spain. Palynology 35, 267–300. doi:10.1080/01916122.2010.523987.

Philip, J. M., & Gari, J. (2005). Late Cretaceous heterozoan carbonates: palaeoenvironmental setting, relationships with rudist carbonates (Provence, south-east France). *Sedimentary Geology*, *175* (1-4), 315-337.

Poblete, F., Dupont-Nivet, G., Licht, A., van Hinsbergen, D., Roperch, P., Guillocheau, F., Baby, G., Baatsten, M. (2017) Preliminary global paleogeographic maps through the Greenhouse-Icehouse transition: forcing of the Drake Passage and Asian Monsoons. *EGU General Assembly 2017*, Geophysical Research Abstracts, Vol. 19

Poblete, F., Dupont-Nivet, G., Licht, A., van Hinsbergen, D.J.J., Roperch, P., Mihalynuk, M.G., Johnston, S.T., Guillocheau, F., Baby, G., Fluteau, F., Robin, C., Van der Linden, T.J.M., Ruiz, D. and Baatsen, M., (in revision), Global paleogeographic maps through the Greenhouse-Icehouse transition at 60, 40 and 20 Ma, Earth Science Reviews

Pojarkova, Z. N. (1984). The Cenomanian and Turonian in northeastern Central Asia. *Cretaceous research*, *5*(1), 1-14.

Pomar, L., Brandano, M., & Westphal, H. (2004). Environmental factors influencing skeletal grain sediment associations: a critical review of Miocene examples from the western Mediterranean. *Sedimentology*, *51*(3), 627-651.

Popov, S. V., Rögl, F., Rozanov, A. Y., Steininger, F. F., Shcherba, I. G., & Kovac, M. (2004). Lithological-paleogeographic maps of Paratethys-10 maps Late Eocene to Pliocene. Courier Forschungsinstitut Senckenberg 250, 1-42.

Powell, A.J. (1992). *A Stratigraphic index of dinoflagellate cycts*. British Micropaleontological Society, Publication Series, Chapman & Hall, London, 290 p

Premoli-Silva, I., & Verga, D. (2004). Practical manual of Cretaceous Planktonic Foraminifera. *International School on Planktonic Foraminifera, 3. Course: Cretaceous. Verga & Rettori (eds.) Universities of Perugia and Milan, Tipografia Pontefelcino, Perugia (Italy)*, 283 p.

Proust, J. N., Mahieux, G., & Tessier, B. (2001). Field and seismic images of sharp-based shoreface deposits: Implications for sequence stratigraphic analysis. *Journal of Sedimentary Research*, *71*(6), 944-957.

Qiao, Q., Huang, B., Biggin, A. J., & Piper, J. D. A. (2017). Late Cenozoic evolution in the Pamir-Tian Shan convergence: New chronological constraints from the magnetostratigraphic record of the southwestern Tianshan foreland basin (Ulugqat area). *Tectonophysics*, *717*, 51–64. https://doi.org/10.1016/j.tecto.2017.07.013

Radionova, E. P., Beniamovski, V. N., Iakovleva, A. I., Muzylov, N. G., Oreshkina, T. V., Shcherbinina, E. A., … Kozlova, G. E. (2003). Early Paleogene transgressions: Stratigraphical and sedimentological evidence from the northern Peri-Tethys. *Special Papers-Geological Society of America*, *369*(January 2003), 239–262. https://doi.org/10.1130/0-8137-2369-8.239

Raffi, I., Backman, J., Pälike, H. (2005). Changes in calcareous nannofossil assemblages across the Paleocene/Eocene transition from the paleo-equatorial Pacific Ocean. *Palaeogeography, Palaeoclimatology, Palaeoecology* 226, 93–126.

Raffi, I., Backman, J., Zachos, J. C., and Sluijs, A. (2006). The response of calcareous nannofossil assemblages to the Paleocene Eocene Thermal Maximum at the Walvis Ridge in the South Atlantic, *Marine Micropaleontology,* 70, 201–212, doi:10.1016/j.marmicro.2008.12.005.

Ramstein, G., Fluteau, F., Besse, J., & Joussaume, S. (1997). Effect of orogeny, plate motion and land–sea distribution on Eurasian climate change over the past 30 million years. *Nature*, *386*(6627), 788.

Replumaz, A., Negredo, A. M., Villasenor, A., & Guillot, S. (2010). Indian continental subduction and slab break-off during Tertiary collision. *Terra Nova*, *22*(4), 290-296.

Robertson, A. H., & Collins, A. S. (2002). Shyok Suture Zone, N Pakistan: late Mesozoic–Tertiary evolution of a critical suture separating the oceanic Ladakh Arc from the Asian continental margin. *Journal of Asian Earth Sciences*, *20*(3), 309-351.

Robinson, A. C., Yin, A., Manning, C. E., Harrison, T. M., Zhang, S. H., & Wang, X. F. (2004). Tectonic evolution of the northeastern Pamir: Constraints from the northern portion of the Cenozoic Kongur Shan extensional system, western China. *Geological Society of America Bulletin*, *116*(7-8), 953-973.

Robinson, A. C., Ducea, M., & Lapen, T. J. (2012). Detrital zircon and isotopic constraints on the crustal architecture and tectonic evolution of the northeastern Pamir. *Tectonics*, *31*(2).

Robinson, A. C. (2015). Mesozoic tectonics of the Gondwanan terranes of the Pamir plateau. *Journal of Asian Earth Sciences*, *102*, 170-179.

Robinson, N., Ravizza, G., Coccioni, R., Peucker-Ehrenbrink, B., & Norris, R. (2009). A high-resolution marine 187Os/188Os record for the late Maastrichtian: Distinguishing the chemical fingerprints of Deccan volcanism and the KP impact event. *Earth and Planetary Science Letters*, *281*(3-4), 159-168.

Roe, G. H., Ding, Q., Battisti, D. S., Molnar, P., Clark, M. K., & Garzione, C. N. (2016). A modeling study of the response of Asian summertime climate to the largest geologic forcings of the past 50??Ma. *Journal of Geophysical Research: Atmospheres*, *121*(10), 5453–5470. https://doi.org/10.1002/2015JD024370

Roger, F., Tapponnier, P., Arnaud, N., Schärer, U., Brunel, M., Zhiqin, X., & Jingsui, Y. (2000). An Eocene magmatic belt across Central Tibet: Mantle subduction triggered by the Indian collision? *Terra Nova*, *12*(2), 102–108. https://doi.org/10.1111/j.1365-3121.2000.00282.x.

Rudmin, M., Roberts, A. P., Horng, C. S., Mazurov, A., Savinova, O., Ruban, A., ... & Veklich, M. (2018). Ferrimagnetic Iron Sulfide Formation and Methane Venting Across the Paleocene-Eocene Thermal Maximum in Shallow Marine Sediments, Ancient West Siberian Sea. *Geochemistry, Geophysics, Geosystems*, *19*(1), 21-42.

Rutte, D., Ratschbacher, L., Khan, J., Stübner, K., Hacker, B.R., Stearns, M.A., Enkelmann, E., Jonckheere, R., Pfänder, J.A., Sperner, B., & Tichomirowa, M. (2017a). Building the Pamir-Tibetan Plateau—Crustal stacking, extensional collapse, and lateral extrusion in the Central Pamir: 2. Timing and rates. *Tectonics*, *36*(3), 385-419.

Rutte, D., Ratschbacher, L., Schneider, S., Stübner, K., Stearns, M. A., Gulzar, M. A., & Hacker, B. R. (2017b). Building the Pamir‐Tibetan Plateau—Crustal stacking, extensional collapse, and lateral extrusion in the Central Pamir: 1. Geometry and kinematics. *Tectonics*, *36*(3), 342-384.

Sachsenhofer, R. F., Popov, S. V., Coric, S., Mayer, J., Misch, D., Morton, M. T., ... & Tari, G. (2018). Paratethyan petroleum source rocks: an overview. *Journal of Petroleum Geology, 41*(3), 219-245.

Sant, K., V. Palcu, D., Mandic, O., & Krijgsman, W. (2017). Changing seas in the Early–Middle Miocene of Central Europe: a Mediterranean approach to Paratethyan stratigraphy. *Terra Nova*, *29*(5), 273-281.

Schlanger, S. O., & Jenkyns, H. C. (1976). Cretaceous oceanic anoxic events: causes and consequences. *Geologie en mijnbouw*, *55*(3-4).

Schulz, H. M., Bechtel, A., & Sachsenhofer, R. F. (2005). The birth of the Paratethys during the Early Oligocene: From Tethys to an ancient Black Sea analogue?. *Global and Planetary Change*, *49*(3-4), 163-176.

Schwab, M., Ratschbacher, L., Siebel, W., McWilliams, M., Minaev, V., Lutkov, V., Chen, F., Stanek, K., Nelson, B., Frisch, W., & Wooden, J.L. (2004). Assembly of the Pamirs: Age and origin of magmatic belts from the southern Tien Shan to the southern Pamirs and their relation to Tibet. *Tectonics*, *23*(4).

Scott, R. W., Wan, X., Sha, J., & Wen, S.-X. (2010). Rudists of Tibet and the Tarim Basin, China: Significance to Requieniidae Phylogeny. *Journal of Paleontology*, *84*(3), 444–465 https://doi.org/10.1666/09-137.1.

Self-Trail, J.M., Powars, D.S., Watkins, D.K., Wandless, G.A. (2012). Calcareous nannofossil assemblage changes across the Paleocene–Eocene thermal maximum: evidence from a shelf setting. *Mar. Micropaleontol*. 92–93, 61–80.

Shcherbinina E., Gavrilov, Y., Iakovleva, A., Pokrovsky, B., Golovanova, O., Aleksandrova, G. *et al*. (2016). Environmental dynamics during the Paleocene–Eocene thermal maximum (PETM) in the northeastern Proto-Paratethys revealed by high-resolution micropalaeontological and geochemical studies of a Caucasian key section. *Palaeogeogr. Palaeoclimatol. Palaeoecol.*, 456, 60-81

Sheldon, E., (2002). Palaeogene nannofossil biostratigraphy of the Kangâmiut-1 and Nukik-2 wells, offshore West Greenland. *Marine and Petroleum Geology* 20, 1031–1041.

Sibley, D. F., & Gregg, J. M. (1987). Classification of Dolomite Rock Textures. *SEPM Journal of Sedimentary Research*, *Vol. 57*(January 1987). https://doi.org/10.1306/212F8CBA-2B24-11D7-8648000102C1865D.

Siesser W.G., Bralower T.J., De Carlo E.H. (1992). Mid-Tertiary Braarudosphaera-rich sediments on the Exmouth Plateau. *Proc. Ocean Drill. Program Sci. Results*, 122, 653–663.

Sissingh, W. (1977). Biostratigraphy of Cretaceous calcareous nannoplankton. *Geol. En Minjbouw*, 56, 37-65.

Slomp, C. P., & Van Cappellen, P. (2006). The global marine phosphorus cycle: sensitivity to oceanic circulation. *Biogeosciences Discussions*, *3*(5), 1587-1629.

Sluijs, A., Pross, J., Brinkhuis, H. (2005). From greenhouse to icehouse; organic-walled dinoflagellate cysts as paleoenvironmental indicators in the Paleogene. *Earth-Science Rev.* 68, 281–315. doi:http://dx.doi.org/10.1016/j.earscirev.2004.06.001

Sluijs, A., Röhl, U., Schouten, S., Brumsack, H. J., Sangiorgi, F., Damsté, J. S. S., & Brinkhuis, H. (2008a). Arctic late Paleocene–early Eocene paleoenvironments with special emphasis on the Paleocene-Eocene thermal maximum (Lomonosov Ridge, Integrated Ocean Drilling Program Expedition 302). *Paleoceanography*, *23*(1).

Sluijs, A., Brinkhuis, H., Crouch, E. M., John, C. M., Handley, L., Munsterman, D., ... & Pancost, R. D. (2008b). Eustatic variations during the Paleocene-Eocene greenhouse world. *Paleoceanography*, *23*(4).

Sluijs, A., Brinkhuis, H. (2009). A dynamic climate and ecosystem state during the Paleocene-Eocene Thermal Maximum – inferences from dinoflagellate cyst assemblages at the New Jersey Shelf. *Biogeosciences* 6, 1755–1781. doi:10.5194/bgd-6-5163-2009.

Sluijs, A., Van Roij, L., Harrington, G. J., Schouten, S., Sessa, J. A., LeVay, L. J., ... & Slomp, C. P. (2014). Warming, euxinia and sea level rise during the Paleocene–Eocene Thermal

Maximum on the Gulf Coastal Plain: implications for ocean oxygenation and nutrient cycling. *Climate of the Past*, *10*(4), 1421-1439.

Smith, R. W., Bianchi, T. S., Allison, M., Savage, C., & Galy, V. (2015). High rates of organic carbon burial in fjord sediments globally. *Nature Geoscience*, *8*(6), 450.

Sobel, E.R. (1995). Basin analysis and apatite fission-track thermochronology of the Jurassic-Paleogene southwest Tarim Basin, NW China [Phd dissertation]. Stanford, CA, Stanford University, 308 pp.

Sobel, E. R. (1999). Basin analysis of the Jurassic–Lower Cretaceous southwest Tarim basin, northwest China. *Geological Society of America Bulletin*, *111*(5), 709-724.

Sobel, E.R., Chen, J., & Heermance, R.V. (2006). Late Oligocene-Early Miocene initiation of shortening in the Southwestern Chinese Tian Shan: Implications for Neogene shortening rate variations. *Earth and Planetary Science Letters*, *247*(1–2), 70–81. https://doi.org/10.1016/j.epsl.2006.03.048.

Sobel, E.R., & Dumitru, T.A. (1997). Thrusting and exhumation around the margins of the western Tarim basin during the India-Asia collision. *Journal of Geophysical Research: Solid Earth*, *102*(B3), 5043–5063. https://doi.org/10.1029/96JB03267.

Sobel, E. R., Chen, J., Schoenbohm, L. M., Thiede, R., Stockli, D. F., Sudo, M., & Strecker, M. R. (2013). Oceanic-style subduction controls late Cenozoic deformation of the Northern Pamir orogen. *Earth and Planetary Science Letters*, *363*, 204-218.

Song, B., Zhang, K., Lu, J., Wang, C., Xu, Y., & Greenough, J. (2013). The middle Eocene to early Miocene integrated sedimentary record in the Qaidam Basin and its implications for paleoclimate and early Tibetan Plateau uplift. *Canadian Journal of Earth Sciences*, *50*(2), 183–196. https://doi.org/10.1139/cjes-2012-0048.

Speijer, R. P. (1994). Extinction and recovery patterns in benthic foraminiferal paleocommunities across the Cretaceous/Paleogene and Paleocene/Eocene boundaries. Geologica Ultraiectina (Vol. 124, p. 191). [Faculteit Aardwetenschappen, Universiteit Utrecht].

Speijer R.P., J. van der Zwaan, B. Schmitz. (1996). The impact of Paleocene/Eocene boundary events on middle neritic benthic foraminiferal assemblages from Egypt. *Marine Micropaleontology*, 99-132.

Speijer, R., & Wagner, T. (2002). Sea-level changes and black shales associated with the late Paleocene thermal maximum: Organic-geochemical and micropaleontologic evidence from the southern Tethyan margin (Egypt-Israel). Catastrophic events and mass extinctions: Impacts and beyond, 356, 533-549.

Song, B., Zhang, K., Lu, J., Wang, C., Xu, Y., & Greenough, J. (2013). The middle Eocene to early Miocene integrated sedimentary record in the Qaidam Basin and its implications for paleoclimate and early Tibetan Plateau uplift. *Canadian Journal of Earth Sciences*, *50*(2), 183–196. https://doi.org/10.1139/cjes-2012-0048

Spurlin, M. S., Yin, A., Horton, B. K., Zhou, J., & Wang, J. (2005). Structural evolution of the Yushu-Nangqian region and its relationship to syncollisional igneous activity, east-central Tibet. *Bulletin of the Geological Society of America*, *117*(9–10), 1293–1317. https://doi.org/10.1130/B25572.1.

Stassen, P., Dupuis, C., Morsi, A. M., Steurbaut, E., & Speijer, R. P. (2009). Reconstruction of a latest Paleocene shallow-marine eutrophic paleoenvironment at Sidi Nasseur (Central Tunisia) based on foraminifera, ostracoda, calcareous nannofossils and stable isotopes (δ13C, δ18O). *Geologica Acta*, 7(1–2), 93–112.

Strasser, A. (1986). Ooids in Purbeck limestones (lowermost Cretaceous) of the Swiss and French Jura. *Sedimentology*, 33 (5), 711-727.

Street, C., Bown, P.R. (2000). Palaeobiogeography of Early Cretaceous (Berriasian– Barremian) calcareous nannoplankton. *Mar. Micropaleontol.*, 39 (1–4), 265–291.

Stübner, K., Ratschbacher, L., Rutte, D., Stanek, K., Minaev, V., Wiesinger, M., & Gloaguen, R. (2013a). The giant Shakhdara migmatitic gneiss dome, Pamir, India-Asia collision zone: 1. Geometry and kinematics. *Tectonics*, *32*(4), 948-979.

Stübner, K., Ratschbacher, L., Weise, C., Chow, J., Hofmann, J., Khan, J., Rutte, D., Sperner, B., Pfänder, J.A., Hacker, B.R., & Dunkl, I. (2013b). The giant Shakhdara migmatitic gneiss dome, Pamir, India-Asia collision zone: 2. Timing of dome formation. *Tectonics*, *32*(5), 1404-1431.

Sun, D. (1991). Late Cretaceous Brachiopods from the Western Tarim Basin, South Xinjiang, China. Science Press, Beijing, 133-150.

Sun, J., & Jiang, M. (2013). Eocene seawater retreat from the southwest Tarim Basin and implications for early Cenozoic tectonic evolution in the Pamir Plateau. *Tectonophysics*, *588*, 27–38. https://doi.org/10.1016/j.tecto.2012.11.031

Sun, J., Li, Y., Zhang, Z., & Fu, B. (2009). Magnetostratigraphic data on Neogene growth folding in the foreland basin of the southern Tianshan Mountains. *Geology*, *37*(11), 1051–1054. https://doi.org/10.1130/G30278A.1

Sun, J., Windley, B. F., Zhang, Z., Fu, B., & Li, S. (2016). Diachronous seawater retreat from the southwestern margin of the Tarim Basin in the late Eocene. *Journal of Asian Earth Sciences*, *116*, 222–231. https://doi.org/10.1016/j.jseaes.2015.11.020.

Sun, G., Hu, X., Xu, Y., & BouDagher-Fadel, M. K. (2019). Discovery of Middle Jurassic trench deposits in the Bangong-Nujiang suture zone: Implications for the timing of Lhasa-Qiangtang initial collision. *Tectonophysics*, *750*, 344-358.

Syvitski, J. P., Vörösmarty, C. J., Kettner, A. J., & Green, P. (2005). Impact of humans on the flux of terrestrial sediment to the global coastal ocean. S*cience*, *308*(5720), 376-380.

Şengör, A.M.C., Altiner, D., Cin, A., Ustaomer, T., and Hsu, K.J. (1988). Origin and assembly of the Tethyside orogenic collage at the expense of Gondwana Land. *Geological Society, London, Special Publications*, *37*(1), 119–181. https://doi.org/10.1144/GSL.SP.1988.037.01.09

Şengör, A. M. C., Natal'in, B. A., & Burtman, V. S. (1993). Evolution of the Altaid tectonic collage and Palaeozoic crustal growth in Eurasia. *Nature Letters*, *364*, 299–307.

Şengör, A. M. C. (1979). Mid-Mesozoic closure of Permo-Triassic Tethys and its implications. *Nature*, *279*, 590-593.

Şengör, A. M. C. (1984). The Cimmeride orogenic system and the tectonics of Eurasia. *Geological Society of America Special Paper*, *195*, 82.

Tang, T., Yang, H., Lan, X., Yu, C., Xue, Y., Zhang, Y., Hu, L., Zhong, S., Wei, J. (1989). Marine Late Cretaceous and Early tertiary stratigraphy and Petroleum Geology in Western Tarim Basin, *China, Science Press*, Beijing, 118 p (In Chinese with English abstract).

Tang, W., Zhong, X., Guo, C., Yan, Z., & Ye, L. (1992a). Abnormal event of carbon stable isotope at the boundary between Cretaceous and Tertiary in Altax section in Xinjiang Autonomous region. *Acta Petrolei Sinica*, *13*(2), 209-214.

Tang, T., Xue, Y., & Yu, C. (1992b). Characteristics and sedimentary environments of the Late Cretaceous to early Tertiary marine strata in the western Tarim, China. *Sci. Press, Beijing*.

Tapponnier, P., Mattauer, M., Proust, F., & Cassaigneau, C. (1981). Mesozoic ophiolites, sutures, and arge-scale tectonic movements in Afghanistan. Earth and Planetary Science Letters, 52(2), 355-371.

Tessier, B. (1993). Upper intertidal rhythmites in the Mont-Saint-Michel Bay (NW France): Perspectives for paleoreconstruction. *Marine Geology*, *110*(3–4), 355–367. https://doi.org/10.1016/0025-3227(93)90093-B.

Thierstein H.R., Cortés M., Haidar A.T. (2004). Plankton community behavior on ecological and evolutionary time-scales: when models confront evidence. In: Thierstein H.R., Young J.R., editors. *Coccolithophores*. Springer; Berlin, Heidelberg, pp. 455–479.

Thiessen, A.H. (1911). Precipitation averages for large areas. *Mon. Weather Rev.* 39, 1082–1089.

Thomas, J. C., Chauvin, A., Gapais, D., Bazhenov, M. L., Perroud, H., Cobbold, P. R., & Burtman, V. S. (1994). Paleomagnetic evidence for Cenozoic block rotations in the

Tadjik depression (Central Asia). *Journal of Geophysical Research: Solid Earth*, *99*(B8), 15141-15160.

Thomas, J. C., Cobbold, P. R., Shein, V. S., & Le Douaran, S. (1999). Sedimentary record of late Paleozoic to Recent tectonism in central Asia—analysis of subsurface data from the Turan and south Kazak domains. *Tectonophysics*, *313*(3), 243-263.

Tibert, N. E., Colin, J. P., Leckie, R. M., & Babinot, J. F. (2003). Revision of the ostracode genus Fossocytheridea: Mesozoic ancestral root for the modern eurytopic Cyprideis Jones. *Micropaleontology*, *49*(3), 205-230.

Tremolada, F., Bralower, T. J., (2004). Nannofossil assemblage fluctuations during the Paleocene – Eocene Thermal Maximum at Sites 213 (Indian Ocean) and 401 (North Atlantic Ocean): palaeoceanographic implications. *Marine Micropaleontology* 52, 107–116. doi:10.1016/j.marmicro.2004. 04.002.

Tsandev, I., & Slomp, C. P. (2009). Modeling phosphorus cycling and carbon burial during Cretaceous Oceanic Anoxic Events. *Earth and Planetary Science Letters*, *286*(1-2), 71-79.

van der Boon, A. (2017). *From Peri-Tethys to Paratethys: Basin restriction and anoxia in central Eurasia linked to volcanic belts in Iran* (Doctoral dissertation, University Utrecht).

van Hinsbergen, D.J.J., Lippert, P. C., Dupont-Nivet, G., McQuarrie, N., Doubrovine, P. V., Spakman, W., & Torsvik, T. H. (2012). Greater India Basin hypothesis and a two-stage Cenozoic collision between India and Asia. *Proceedings of the National Academy of Sciences*, *109*(20), 7659–7664. https://doi.org/10.1073/pnas.1117262109

van Hinsbergen, D.J.J., Lippert, P.C., Li, S., Huang, W., Advokaat, E.L., Spakman, W. (2018). Reconstructing Greater India: Paleogeographic, kinematic and geodynamic perspectives. Tectonophysics (in press) https://doi.org/10.1016/j.tecto.2018.04.006

Van Morkhoven, F.P.C.M., Berggren, W.A. and Edwards, A.S., (1986). Cenozoic cosmopolitan deep-water benthic foraminifera. Bull. Centro Rech. Expl.-Prod. Elf-Aquitaine, Mem., 11: 421 pp.

Wade B.S., Bown P.R. (2006). Calcareous nannofossils in extreme environments: the Messinian salinity crisis, Polemi Basin, Cyprus. *Palaeogeogr. Palaeoclimatol. Palaeoecol.* 233(3–4), 271–286.

Wan, X., Jiang, T., Zhang, Y., Xi, D., & Li, G. (2014). Palaeogene marine stratigraphy in China. *Lethaia*, *47*(3), 297–308. https://doi.org/10.1111/let.12071

Wang, D.-N., Sun, X.-Y., & Zhao, Y.-N. (1990). Late Cretaceous to Tertiary palynofloras in Xinjiang and Qinghai, China. *Review of Palaeobotany and Palynology*, *65*(1–4), 95–104. https://doi.org/10.1016/0034-6667(90)90060-V

Wang, Q., Wyman, D. A., Xu, J., Dong, Y., Vasconcelos, P. M., Pearson, N., … Chu, Z. (2008). Eocene melting of subducting continental crust and early uplifting of central Tibet: Evidence from central-western Qiangtang high-K calc-alkaline andesites, dacites and rhyolites. *Earth and Planetary Science Letters*, *272*(1–2), 158–171. https://doi.org/10.1016/j.epsl.2008.04.034

Wang, C., Hong, H., Li, Z., Yin, K., Xie, J., Liang, G., Song, B., Song, E., Zhang, K. (2013). The Eocene-Oligocene climate transition in the Tarim Basin, Northwest China: Evidence from clay mineralogy. *Applied Clay Science*, 74, 10-19

Wang, W., Zheng, W., Zhang, P., Li, Q., Kirby, E., Yuan, D., … Pang, J. (2017). Expansion of the Tibetan Plateau during the Neogene. *Nature Communications*, *8*(May), 1–12. https://doi.org/10.1038/ncomms15887

Wang, X., Carrapa, B., Chapman, J. B., Henriquez, S., Wang, M., DeCelles, P. G., Li, Z., Wang, F., Oimuhammadzoda, I., Gadoev, M., & Chen, F. (2019). Parathethys last gasp in central Asia and late Oligocene accelerated uplift of the Pamirs. *Geophysical Research Letters*, *46*(21), 11773-11781.

Wang, B.D., Wang, L.Q., Chung, S.L., Chen, J.L., Yin, F.G., Liu, H., Li, X.B., & Chen, L.K. (2016). Evolution of the Bangong–Nujiang Tethyan ocean: insights from the geochronology and geochemistry of mafic rocks within ophiolites. *Lithos*, *245*, 18-33.

Wang, X., Sun, D., Chen, F., Wang, F., Li, B., Popov, S.V., Wu, S., Zhang, Y., & Li, Z. (2014). Cenozoic paleo-environmental evolution of the Pamir–Tien Shan convergence zone. *Journal of Asian Earth Sciences*, *80*, 84-100.

Wang, C., Feng, Z., Zhang, L., Huang, Y., Cao, K., Wang, P., & Zhao, B. (2013). Cretaceous paleogeography and paleoclimate and the setting of SKI borehole sites in Songliao Basin, northeast China. *Palaeogeography, Palaeoclimatology, Palaeoecology*, *385*, 17-30.

Wang, D., Sun, X., Zhao, Y., & He, Z. (1990) Palynoflora from Late Cretaceous to Tertiary in some regions of Qinghai and Xinjiang. (The study on the micropaleobotany from Cretaceous-Tertiary of the oil bearing basins in some regions of Qinghai and Xinjiang.) Ministry of Geology and Mineral Resources Institute of Geology, Xinjiang Bureau of Petroleum P. 1- 179.

Warren, J. K., & Kendall, C. G. S. C. (1985). Comparison of Sequences Formed in Marine Sabkha (Subaerial) and Salina (Subaqueous) Settings - Modern and Ancient. *AAPG Bulletin*, *69*(6), 1013–1023.

Warren, J. K. (2010). Evaporites through time: Tectonic, climatic and eustatic controls in marine and nonmarine deposits. *Earth-Science Reviews*, *98*(3–4), 217–268. https://doi.org/10.1016/j.earscirev.2009.11.004.

Watson, D.F., Philip, G.M. (1985). A refinement of inverse distance weighted interpolation. *Geo-processing* 2, 315–327.

Watson, M. P., Hayward, A. B., Parkinson, D. N., & Zhang, Z. M. (1987). Plate tectonic history, basin development and petroleum source rock deposition onshore China. *Marine and Petroleum Geology*, *4*(3), 205-225.

Williams, G.L., Brinkhuis, H., Pearce, M.A., Fensome, R.A., & Weegink, J.W. (2004). Southern Ocean and global dinoflagellate cyst events compared: index events for the Late Cretaceous–Neogene, in: *Proceedings of the Ocean Drilling Program, Scientific Results*. pp. 1–98.

Williams, G.L., & Bujak, J.P. (1989). Mesozoic and Cenozoic dinoflagellates, in: *Plankton Stratigraphy*: Volume 2, Radiolaria, Diatoms, Silicoflagellates, Dinoflagellates and Ichthyoliths. pp. 847–964.

Wilson, J.L. (1975). Carbonate facies in geologic history, Springer-Verlag, Berlin, 471 pp.

Xi, D., Cao, W., Cheng, Y., Jiang, T., Jia, J., Li, Y., & Wan, X. (2016). Late Cretaceous biostratigraphy and sea-level change in the southwest Tarim Basin. *Palaeogeography, Palaeoclimatology, Palaeoecology*, *441*, 516–527. https://doi.org/10.1016/j.palaeo.2015.09.045.

Xi, D., Wan, X., Li, G., & Li, G. (2019). Cretaceous integrative stratigraphy and timescale of China. *Science China Earth Sciences*, *62*(1), 256-286.

Xu, W., Ruhl, M., Jenkyns, H. C., Hesselbo, S. P., Riding, J. B., Selby, D., ... & Idiz, E. F. (2017). Carbon sequestration in an expanded lake system during the Toarcian oceanic anoxic event. *Nature Geoscience*, *10*(2), 129.

Yang, H. Q., Shen, J. W., Yang, H. J., Zhang, L. J., Li, M., & Wang, J. P. (2014). Mixed carbonate-clastic facies in the Eocene Kalatar Formation of the southwest Tarim Basin (NW China): Tectonic and climatic controls. *Facies*, *60*(1), 111–131. https://doi.org/10.1007/s10347-013-0373-1

Yang, W., Dupont-Nivet, G., Jolivet, M., Guo, Z., Bougeois, L., Bosboom, R., … Heilbronn, G. (2015). Magnetostratigraphic record of the early evolution of the southwestern Tian Shan foreland basin (Ulugqat area), interactions with Pamir indentation and India-Asia collision. *Tectonophysics*, *644*, 122–137. https://doi.org/10.1016/j.tecto.2015.01.003.

Yang, Y. (2011). Tectonically-driven underfilled–overfilled cycles, the Middle Cretaceous in the northern Cordilleran foreland basin. *Sedimentary Geology*, *233*(1-4), 15-27.

Yang, Z.Y., Wang, Q., Zhang, C., Yang, J.H., Ma, L., Wang, J., Sun, P., & Qi, Y. (2019). Cretaceous (~ 100 Ma) high-silica granites in the Gajin area, Central Tibet: Petrogenesis and implications for collision between the Lhasa and Qiangtang Terranes. *Lithos*, *324*, 402-417.

Yang, H., Jiang, X., & Lin, S. (1995). Late Cretaceous-early Tertiary ostracod fauna from Western Tarim basin, S. Xinjiang, China. Science Press, Beijing.

Yang, S. (1991). Late Cretaceous and Early Tertiary Echinoids from Tarim Basin. Science Press, Beijing, 101-132.

Yang, H.-R., Tang, T.-F., Lan, X., Hu, L.-Y., Yu, C.-L., Zhang, Y.-Y., Zhong, S.-L., & Wei, J.-M. (1983). A preliminary study of the Upper Cretaceous of the Western Tarim Basin (South Xinjiang, China) with special reference to its transgressions. *Zitteliana, 10*, 115-121.

Ye, D., Tang, W., Wei, J., Xu, D., & Mao, X. (1992). Geochemical markers of the Cretaceous-Tertiary boundary event in the Altax section. *Tarim Basin, Acta Petrolei Sinica*, *13*(2), 202‑208.

Ye, C., Yang, Y., Fang, X., & Zhang, W. (2016). Late Eocene clay boron-derived paleosalinity in the Qaidam Basin and its implications for regional tectonics and climate. *Sedimentary Geology*, *346*, 49–59. https://doi.org/10.1016/j.sedgeo.2016.10.006

Yin, A., Craig, P., & Harrison, T. M. (1998). Late Cenozoic tectonic evolution of the southern Chinese Tian Shan. *Tectonics*, *17*(1), 1–27

Yin, A., & Harrison, T. M. (2000). E Volution of the H Ealth C Are. *Annual Reviews of Earth and Planetary Sciences*, *28*, 211–280. https://doi.org/10.1080/01947641003598252

Yin, A., Rumelhart, P. E., Butler, R., Cowgill, E., Harrison, T. M., Foster, D. A., … Raza, A. (2002). Tectonic history of the Altyn Tagh fault system in northern Tibet inferred from Cenozoic sedimentation. *Bulletin of the Geological Society of America*, *114*(10), 1257–1295. https://doi.org/10.1130/0016-7606(2002)114<1257:THOTAT>2.0.CO;2

Young, J.R., Wade, B.S., & Huber B.T. (eds) pforams@mikrotax website. (2018). URL: http://ww.mikrotax.org/pforams

Young, J.R., Bown P.R., Lees J.A. (eds). Nannotax3 website. International Nannoplankton Association. 21 Apr. 2017. URL: http://ina.tmsoc.org/Nannotax3.

Young, J.R., Wade, B.S., & Huber B.T. (2019). (eds) pforams@mikrotax website. Accessed 18 July 2019. URL: http://www.mikrotax.org/pforams

Young, J.R., Bown P.R., & Lees J.A. (2019). Nannotax3 website. International Nannoplankton Association. Accessed 21 Apr. 2019. URL: http://www.mikrotax.org/Nannotax3.

Zachos, J. C., Röhl, U., Schellenberg, S. A., Sluijs, A., Hodell, D. A., Kelly, D. C., ... & McCarren, H. (2005). Rapid acidification of the ocean during the Paleocene-Eocene thermal maximum. *Science*, *308*(5728), 1611-1615.

Zeebe, R. E., Zachos, J. C., & Dickens, G. R. (2009). Carbon dioxide forcing alone insufficient to explain Palaeocene–Eocene Thermal Maximum warming. *Nature Geoscience*, *2*(8), 576.

Zeebe, R. E., Ridgwell, A., & Zachos, J. C. (2016). Anthropogenic carbon release rate unprecedented during the past 66 million years. *Nature Geoscience*, *9*(4), 325.

Zhang, Z., Wang, H., Guo, Z., Jiang, D. (2007). What triggers the transition of palaeoenvironmental patterns in China, the Tibetan Plateau uplift or the Paratethys Sea retreat?. *Palaeogeography, Palaeoclimatology, Palaeoecology*, 245, 317-331.

Zhang, Z., Flatøy, F., Wang, H., Bethke, I., Bentsen, M., & Guo, Z. (2012). Early Eocene Asian climate dominated by desert and steppe with limited monsoons. *Journal of Asian Earth Sciences*, *44*(January), 24–35. https://doi.org/10.1016/j.jseaes.2011.05.013

Zhang, S., Hu, X., Han, Z., Li, J., & Garzanti, E. (2018). Climatic and tectonic controls on cretaceous-palaeogene sea-level changes recorded in the Tarim epicontinental sea. *Palaeogeography, Palaeoclimatology, Palaeoecology*, 501, 92-110, https://doi.org/10.1016/j.palaeo.2018.04.008.

Zhang, C. L., Zou, H. B., Li, H. K., & Wang, H. Y. (2013). Tectonic framework and evolution of the Tarim Block in NW China. *Gondwana Research*, *23*(4), 1306-1315.

Zhang, K. J., Xia, B. D., Wang, G. M., Li, Y. T., & Ye, H. F. (2004). Early Cretaceous stratigraphy, depositional environments, sandstone provenance, and tectonic setting of central Tibet, western China. *GSA Bulletin*, *116*(9-10), 1202-1222.

Zhang, S. (1992). Calcareous nannofossils from the Upper Cretaceous and Lower Tertiary in the Western Tarim Basin, South Xinjiang, China. *Xinjiang Stratigraphic Res. Ser*, *5*, 1-121.

Zheng, J., He, X., & Liu, S. (1999). Dictionary of Chinese Stratigraphy-Tertiary. Geology Press, Beijing.

Zonneveld, K.A.F., Marret, F., Versteegh, G.J.M., Bogus, K., Bonnet, S., Bouimetarhan, I., Crouch, E., de Vernal, A., Elshanawany, R., Edwards, L., Esper, O., Forke, S., Grøsfjeld, K., Henry, M., Holzwarth, U., Kielt, J.-F., Kim, S.-Y., Ladouceur, S., Ledu, D., Chen, L., Limoges, A., Londeix, L., Lu, S.-H., Mahmoud, M.S., Marino, G., Matsouka, K., Matthiessen, J., Mildenhal, D.C., Mudie, P., Neil, H.L., Pospelova, V., Qi, Y., Radi, T., Richerol, T., Rochon, A., Sangiorgi, F., Solignac, S., Turon, J.-L., Verleye, T., Wang, Y., Wang, Z., Young, M. (2013). Atlas of modern dinoflagellate cyst distribution based on 2405 data points. *Rev. Palaeobot. Palynol.* 191, 1–197. doi:10.1016/j.revpalbo.2012.08.003.